Chapter 2

Detector for the Linear Collider

General Detector Concepts and Detector Performance

Conveners: M. Martinez, D.J. Miller, M. Piccolo

Working Group: A. Andreazza, M. Battaglia, G. Blair, G. Daskalakis, A. Juste, A. Kyriakis, C. Markou, H.U. Martyn, H. Nowak, I. Riu, M. Sachwitz, H.J. Schreiber, D. Schulte, R. Settles, R. Shanidze, C. Shepherd-Themistocleous, S. Shichanin, E. Simopoulou, R. Vuopionperä, C. Troncon

Detector Subsystems

Conveners: M. Mazzucato, D. Saxon, R. Settles

Working Group: S. Aïd, A. Andreazza, P. Bambade, T. Barklow, W. Bartel, M. Battaglia, R. Bellanzzini, S. Bertolucci, G. Blair, R. Brinkmann, I. Brock, R. Brown, J. Bürger, P.J. Bussey, M. Caccia, P. Checchia, G. Coignet, P. Colas, P. Clarke, C. Damerell, M. David, A. De Roeck, E. Elsen, E. Fernandez, Y. Giomataris, T. Greenshaw, R. Heuer, C. Heusch, N. Holtkamp, P. Hüntemeyer, P. Janot, L. Jönsson, F.P. Juster, B.J. King, F. Kircher, V. Korbel, U. Kötz, Y. Kurihara, P. Le Du, M. Leenen, W. Lohmann, C. Luci, L. Mandelli, M. Martinez, C. Meroni, J. Meyer, D. Miller, R. Nahnhauer, O. Napoly, R. Nania, R. Orava, M. Piccolo, M. Pohl, D. Reed, F. Richard, A. Rousarie, H.-G. Sander, U. Schneekloth, H.J. Schreiber, S. Schreiber, D. Schulte, C. Shepherd-Themistocleous, F. Simonetto, K. Sinram, A. Skillman, A. Sopczak, P. Steffen, H. Steiner, J. Steuerer, G. Tonelli, M. Tonutti, C. Troncon, C. VanderVelde, G. Vegni, A. Wagner, N. Walker, M. Weber, W. Wiedenmann, G.W. Wilson, K. Zapfe-Düren

Collider-Experiment Interface

Conveners: N. Holtkamp, M. Leenen, O. Napoly

Working Group: G. Bardin, R. Brinkmann, C. Cavata, S. Drozhdin, J.-P. Jorda, N. Mokhov, M. Sachwitz, H.J. Schreiber, S. Schreiber, D. Schulte, R. Settles, K. Sinram, N. Walker, K. Zapfe-Düren

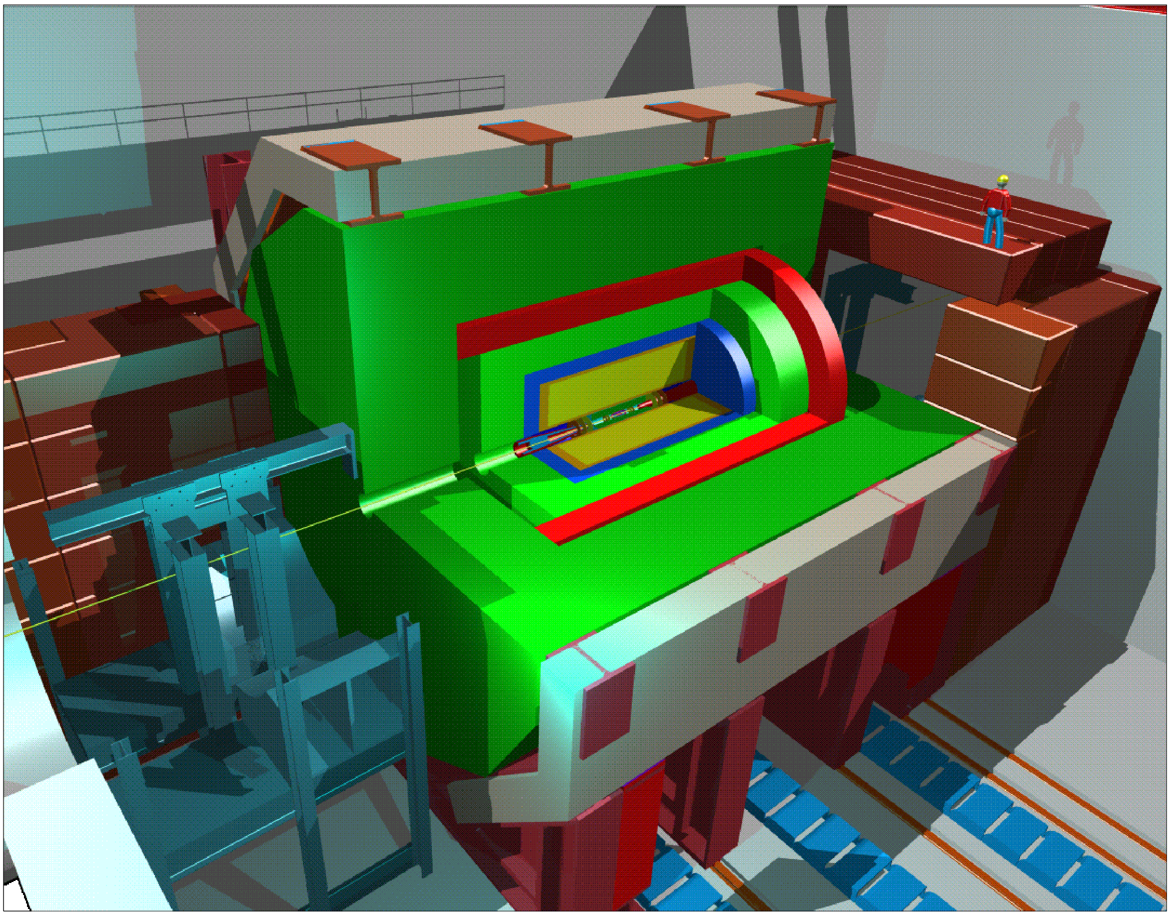

Contents

2.1 General Detector Concept

2.1.1 Introduction

A detector for e^+e^- experiments up to the highest linear collider energies is presented here. It results from one set of choices among many possibilities considered during the *ECFA/DESY Study on Physics and Detectors for the Linear Collider* [1]. As will be shown the detector matches the requirements of the physics analyses and could essentially be built today. The performance of all subsystems can be improved with further R&D, which is also discussed.

Requirements

The physics programme of the linear collider has been the subject of intense investigation in the present [1] and past [2]–[14] studies. A few example experiments listing the analysis aspects needing excellent performance ($\surd$) show that the detector has to meet high demands on quality:

	DETECTOR				
PHYSICS	Missing Energy	Jet-jet Reconstruction	Lepton I.D.	b,c,τ Vertexing	Forward Direction
Higgs branching ratios	$\surd$	$\surd$	$\surd$	$\surd$	$\surd$
Top threshold scan	$\surd$	$\surd$		$\surd$	$\surd$
W-boson couplings	$\surd$	$\surd$	$\surd$		$\surd$
$\tilde{\chi}^{\pm}_j \tilde{\chi}^0_i \tilde{\ell} \tilde{q}$ spectroscopy	$\surd$	$\surd$	$\surd$	$\surd$	

The most essential performance goals for the detector can be summarized as follows:

- Excellent vertex resolution for heavy flavour identification (b, c, τ vertexing).
- Tracking with accurate momentum determination and high redundancy to handle easily the multijet environment (jet-jet reconstruction).
- Good energy-flow measurement given by high granularity in the calorimeters and particle identification in the tracking (jet-jet reconstruction, missing energy).
- Hermetic, with good measurement in the forward direction (missing energy, forward direction).
- Very good lepton identification and e-π separation (lepton identification).
- Flexible trigger – because of possible backgrounds (see below).

Table 2.1.1 lists the major differences in a detector for the linear collider as compared to LEP2.

Difference LEP 2→LC	Possible Improvements to Detector
Smaller beam pipe	Instrumentation down to smaller radius with detectors having higher resolution
Higher multiplicities, more beam-associated background	Pixels essential in vertex detector; minimize mass in whole tracking volume; higher B field
Higher peak track energies (especially leptons)	Better point resolution; more measured points; higher B field
Higher e and γ energies	Thicker electromagnetic calorimeter ECAL
Higher hadron energies	Thicker hadronic calorimeter HCAL
Narrower and/or more jets	Better jet reconstruction; fine granularity; better HCAL; ECAL and HCAL inside coil

Table 2.1.1: *Differences between detectors for LEP and the LC.*

Good vertex resolution is demanded because much of the new physics to be studied involves heavy flavors, especially Higgs and top decays. Only with the best vertex resolution will it be possible to measure charm signals well, so that the beam pipe radius should be as small as possible.

LEP experience has shown how cleanly signals can be recognized and separated by using the redundant information from a many-layered tracker. Even dense high-energy jets can be resolved into individual particles, and at the linear collider this must be possible in the presence of a large number of isolated photon hits. The tracks of primary events must be identified in the main tracker and followed back into the vertex detector. The vertex detector with at least three layers will allow stand-alone tracking to match with the tracks found in the main tracker.

Many of the physics channels for SUSY, top and W^+W^- involve significant amounts of missing energy. The detector has to be hermetic to identify these events. The shielding mask around the mini-beta quadrupoles is a feature specific to the LC. R&D work is needed to develop a way of measuring the energy deposited in it.

The higher energy of the LC will either produce more energetic and narrower jets than LEP (e.g. in W^+W^- production) or events with many more jets to be resolved and measured (e.g. in top-antitop or the production of pairs of SUSY Higgs bosons). It will be essential to measure individual jet energies in order to establish the detailed energy flow for all parts of the event. This involves the measurement of charged tracks and the subtraction of the associated energy from the observed neutral clusters. Fine granularity is needed in both the electromagnetic and the hadronic calorimeter. The major part of all showers must be measured before they reach the coil, which spreads the

Vertexing	$\delta(IP_{r\phi}) \leq 10\,\mu m \oplus \frac{30\,\mu m\ \mathrm{GeV}/c}{p \sin^{3/2}\theta}$ $\delta(IP_z) \leq 20\,\mu m \oplus \frac{30\,\mu m\ \mathrm{GeV}/c}{p \sin^{5/2}\theta}$
Forward Tracking	$\frac{\delta p}{p} < 20\,\%$, $\delta_\theta < 200\,\mu$rad for 100–250 GeV particles down to lowest polar angle θ.
Tracking	$\frac{\delta p_t}{{p_t}^2} \leq 1 \cdot 10^{-4} (\frac{\mathrm{GeV}}{c})^{-1}$ Good particle identification.
Electromagnetic Calorimeter	$\frac{\delta E}{E} \leq 0.10 \frac{1}{\sqrt{E}} \oplus 0.01$ (E in GeV) Granularity $0.9^\circ \times 0.9^\circ$, at least 3 samples in depth.
Hadronic Calorimeter	$\frac{\delta E}{E} \leq 0.50 \frac{1}{\sqrt{E}} \oplus 0.04$ (E in GeV) Granularity $2^\circ \times 2^\circ$, at least 3 samples in depth.
Muon Detector	Fe yoke instrumented as tail catcher and muon tracker. Toroid momentum analysis for forward muons ($\theta < 15^\circ$), $\frac{\delta p}{p} < 20\,\%$.
Energy Flow	$\frac{\delta E}{E} \simeq 0.3 \frac{1}{\sqrt{E}}$ (E in GeV)
Hermetic Coverage	$\|\cos\theta\| < 0.99$

Table 2.1.2: *Detector performance goals.*

clusters and degrade the energy resolution. The LEP detectors are presently gaining experience in handling multijet events at higher energies, and the difficulty of this undertaking is reflected in the emphasis on very good jet resolution for the LC detector.

2.1.2 Layout Concept

The performance goals given in Tab. 2.1.2 are derived from the needs of the physics analysis and match the technical feasibility. The basic layout follows the well-proven concept of tracking in a magnetic field at inner radii and calorimetry at outer radii. Two alternatives were considered: (i) a detector with large solenoid and calorimetry inside the coil and (ii) a compact detector with small solenoid and calorimetry outside the coil. The large detector was chosen in order to achieve better jet resolution and because of the good experience with such detectors at LEP/SLC/HERA.

Figure 2.1.1 shows a schematic cross section through the detector and Fig. 2.1.2 some details of the inner region. Table 2.1.3 gives the subdetector techniques chosen and Tab. 2.1.4 the the subdetector dimensions.

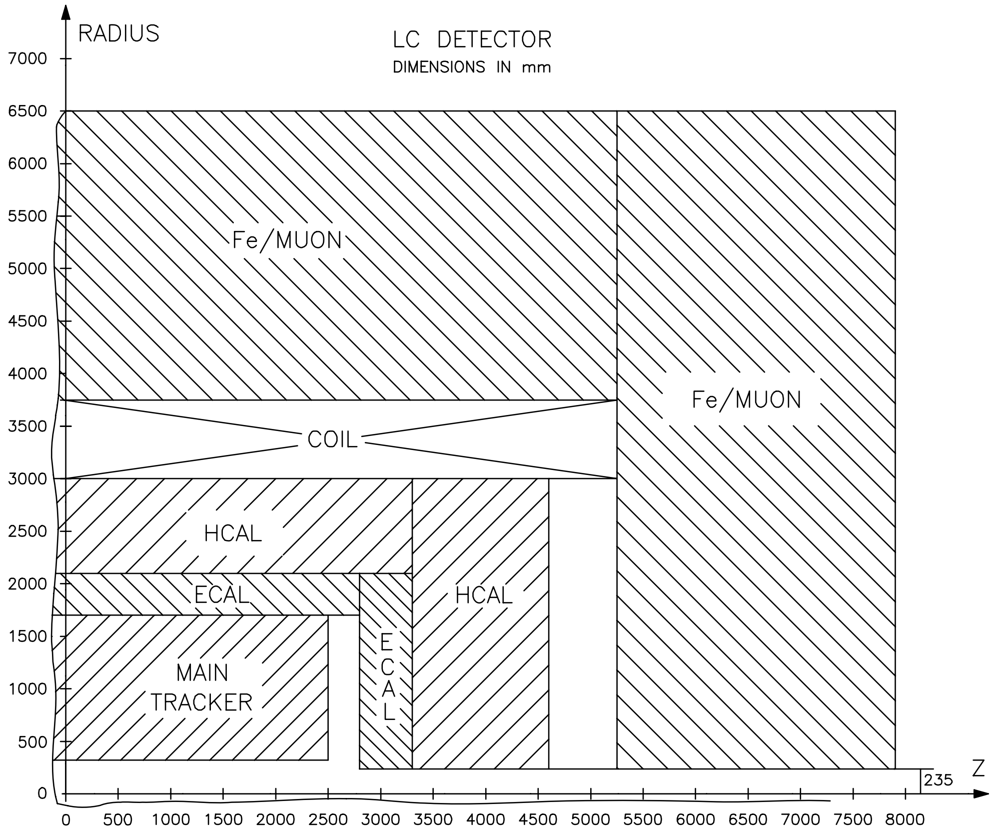

Figure 2.1.1: *Schematical layout of one quadrant of the LC Detector.*

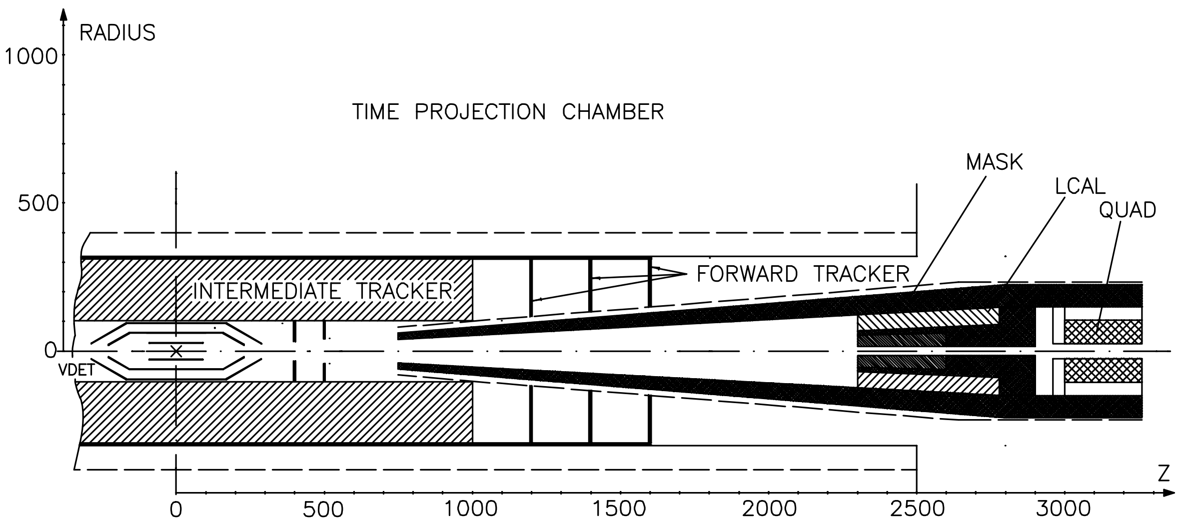

Figure 2.1.2: *Schematic layout of the inner region of the detector.*

Subdetector	Technique chosen (Radiation Lengths)	Alternative techniques
Barrel		
Beam pipe	(0.3 % X_0)	
Vertex detector	CCD or APS (1.6 % or 2.4 % X_0)	Silicon strip
Intermediate tracker	Honeycomb straw tubes (0.23 % X_0)	Scintillating fibers with drift chamber; Silicon strip
Intermediate layer	Double-sided silicon strip (1 % X_0)	
Main tracker	Time projection chamber (3 % X_0 to outer field cage)	MSGC; Silicon strip
(Total thickness to outermost tracking radius = 6.1 % (CCD) or 6.9 % (APS) X_0)		
Presampler	Scintillating fibers	
E-M calorimeter	Pb-scintillator Shashlik cal.	Spaghetti calorimeter; Crystals
Hadron Calorimeter	Cu-scintillator Shashlik	
Tailcatcher, muon identifier	Resistive plate chambers	Limited streamer
Forward		
Luminosity calorimeter	Scintillating fibers in Pb	Spaghetti calorimeter Silicon-tungsten Shashlik
Instrumented mask	Quartz fibers in W	
Forward tracker	Silicon strip and/or pixels	
Forward muon tracker	Toroids with honeycomb tubes	

Table 2.1.3: *Techniques chosen for the LC detector.*

Subdetector	Radial extent		Longitudinal extent	
	r_{min} [mm]	r_{max} [mm]	$\lvert z_{\text{min}}\rvert$ [mm]	$\lvert z_{\text{max}}\rvert$ [mm]
Beam pipe		20		
Vertex detector	25	100		300
			(including endcaps)	
Forward tracker discs			at 400, 500, 1200, 1400, 1600	
Intermediate tracker	120	300		1000
Intermediate Si layer	300	320		1600
Main Tracker (TPC)	320	1700		2800
Sensitive volume	386	1626		2500
ECAL Barrel	1700	2100		2800
ECAL Endcap	235	2100	2800	3300
HCAL Barrel	2100	3000		3300
HCAL Endcap	235	3000	3300	4600
Coil Cryostat	3000	3750		5250
Iron Barrel	3800	6400		5250
Iron Endcap	235	6400	5250	7900
Toroid	400	3000	7900	9400
	Angular range			
	θ_{min} [mrad]	θ_{max} [mrad]		
TESLA Mask	55	80	750	2800
(conical part)	r_{outer}=62 to 225 mm			
SBLC Mask	85	125	750	1800
(conical part)	r_{outer}=62 to 225 mm			
TESLA $\mathcal{L}$cal	30	55	2300	2800
SBLC $\mathcal{L}$cal	30	85	1300	1800

Table 2.1.4: *Dimensions of the LC subdetectors.*

Detector Choices

The techniques chosen for the different subdetectors (Tab. 2.1.3) are reviewed briefly in the following paragraphs and compared with the alternative techniques. The full discussion follows in Section 2.2.

Either Charged Coupled Devices (CCD) or Active Pixel Sensors (APS) could provide the performance required for a vertex detector. They are regarded as alternatives at this stage, with R&D programmes continuing. Both are described in Section 2.2.1 below. The advantages of CCDs are their uniformly small pixel size ($20\,\mu\mathrm{m}^2$, compared with $50\,\mu\mathrm{m}^2$ for APSs) and their thinness ($30\,\mu$m of silicon with very light support structures, giving only $0.12\,\% X_0$ per layer, as compared with $0.8\,\% X_0$ for APS). APSs are presently better matched to the time structure of the machine (though current development of fast-clear facilities will help the CCDs to compete) and are more resistant to the neutron radiation. Silicon strip detectors are shown not to be suitable for the vertex detector because they would have occupancy problems with high multiplicity events and the photon background in the innermost layers. The outer two layers of the vertex detector will taper down conically at 30° at the outer edge of the barrel.

The intermediate tracker needs good position resolution in $r\phi$ to aid linking tracks from the main tracker to the vertex detector, and it also provides the fast track-trigger. Both straw tubes and scintillating fibers have been investigated. The straw-tube "honeycomb chamber" was chosen as having the advantage of better intrinsic resolution and much less material ($0.23\,\%\ X_0$ compared with $1\,\%\ X_0$ per layer for scintillating fibers). The thin walls in the forward direction represent also an important reduction of material for the forward tracking.

An intermediate Si-strip layer provides a precise reference for connecting the intermediate tracker and vertex detector coordinates with those of the TPC system, and it improves the momentum resolution.

The TPC main tracker has a number of advantages over other techniques. It presents the minimum possible amount of material for the conversion of outgoing photons from beam-beam effects ($3\,\%\ X_0$ for the inner field cage plus gas, compared with $10\,\%$ distributed over the whole volume for MSGCs). Its z resolution is better than a jet chamber, and it can be gated to eliminate the distortion due to positive ions from the detector planes drifting into the detector volume.

For the electromagnetic calorimeter, ECAL, the Pb-scintillator Shashlik technique has been chosen since it gives better 3D granularity than a crystal calorimeter. Crystals would give better energy resolution but physics studies have shown that $\lesssim 10\,\%\sqrt{E}$ will be sufficient. Liquid argon would involve large cryostats which would reduce the space for all inner tracking detectors and introduce cracks which compromise the hermeticity. Also being studied studied is a scintillating fiber presampler, with thin layers of lead converter, which will give precise coordinates for shower conversions; detailed simulations are needed to be sure that this will not compromise the overall resolution of the ECAL. The performance goal for the electromagnetic energy resolution (good performance is needed e.g. for measuring the $H \to \gamma\gamma$ branching ratio) does not allow compensation at hardware level for the measurement of hadronic showers, and good granularity enables this to be done in the off-line software.

Also for the hadron calorimeter, HCAL, a Shashlik approach similar to that for the electromagnetic layer but with copper as absorber, has been chosen, with flexibility to optimize the granularity and the sampling in depth and to match the towers to those of the ECAL. There will be at least five interaction lengths of calorimeter within the coil at the equator, with more in the forward and backward towers.

The tail-catcher will use the iron return-yoke of the magnet to measure the leakage of energy which escapes from the back of the hadron calorimeter and through the coil. A powerful muon detector will also result from sampling the muon tracks in the iron. Resistive plate chambers are likely to be cheaper and easier to build than limited streamer tubes for the same performance. Either technique can also provide fast triggering for cosmic ray events.

The luminosity calorimeter, covering from about 30 to 55 (30 to 85) mrad for TESLA (SBLC) from the beam direction inside the tungsten shielding masks, has to measure high energy electron showers – in the presence of intense soft electromagnetic radiation from beam-beam pair production and beamsstrahlung. It is not yet clear how long scintillators or silicon pad detectors would survive under these circumstances. A solution based on Pb with liquid scintillator in quartz fibers is being studied.

The possibility is being studied of instrumenting the tungsten mask with embedded longitudinal quartz fibers in order to obtain the best possible hermeticity. It remains to be verified that the masking function can be maintained in this case.

A sequence of forward tracking detectors will be used to measure tracks close to the outer surface of the mask, especially muons and Bhabha electrons (for acollinearity measurement to give the luminosity spectrum). Discs of pixel and silicon-strip detectors will be inserted inside the intermediate tracker and inside the TPC inner cylinder.

Forward toroids are needed to measure the sign and the momentum of muons at small angles to the beam direction – e.g. in the study of W^+W^- production or for the absolute c.m.s. energy determination. Strawtube honeycomb chambers before and after the toroids would measure the positions and the bending of muons over a range of angles from 35 to 240 mrad from the beam direction. Beyond that, the muons can be tracked and measured in the iron of the yoke.

2.1.3 Layout for Other Machine Options

e^-e^-, $e^-\gamma$, and $\gamma\gamma$Colliders. This report is largely concerned with the initial phase of the programme of a linear collider, running in the e^+e^- mode. There are three important additional modes of operation which would extend the physics potential, as explained in Chapter 1: e^-e^- collisions and the Compton-collider with its $e^-\gamma$ and $\gamma\gamma$

modes. The luminosity in all three cases will be reduced by a factor of between 1/2 to 1/5 from the e^+e^- luminosity. The detector described in this report will do equally well for e^-e^- studies.

Much more special preparation will be needed to provide the backscattered laser facility for $e^-\gamma$ and $\gamma\gamma$ physics. The linac optics of the final focus region need to be optimized in a different way, access must be provided for the intense laser beams and the beam-crossing angle at intersection must be large enough for radiation and pairs from the conversion points to escape past the focusing quadrupoles. It is therefore anticipated that a second interaction point will need to be provided for $e^-\gamma$ and $\gamma\gamma$ collisions, with a different beam delivery section and its own detector. Because the physics channels to be studied in $e^-\gamma$ and $\gamma\gamma$ are not so different from those in e^+e^- [20], most features of the detector could be similar to those described in this report. The essential difference will be in the region of the conical mask around the beam direction. In order to make room for laser optics the mask will have to come out to larger angles – 150 to 200 mrad, compared with 80 to 100 mrad in the detector described here – and the region inside the mask may not have any room for small-angle calorimetry.

Two Interaction Regions. It may be argued that a second interaction region for e^+e^- studies, with its own detector, should be planned as part of the basic linear collider programme, to provide for scientific redundancy, to have complementary detectors, to give competition between alternating teams, or to insure against failure of a single detector. If provision is made for such a second IR in the collider layout plans, then the needs of $e^-\gamma$ and $\gamma\gamma$ must be borne in mind. The detector in such a second region might well be used for all four collider modes, e^+e^-, e^-e^-, $e^-\gamma$, and $\gamma\gamma$. It should be noted, however, that at a linear collider, contrary to storage rings with more than one experiment, the total available luminosity would have to be shared between the experiments.

2.1.4 The Detector Magnet

The magnetic field has two important rôles: it bends charged particles for momentum measurement and it limits beam related background by imposing a cutoff in the transverse momentum of those e^+e^- pairs from beamstrahlung that enter the detector (see Fig.2.4.9).

In order to reduce the beam-pipe diameter, the aperture of the mask, and the background in the detector, a field of at least 2 T is necessary. With higher fields, the pair background in the vertex detector can be further reduced and the momentum measurement by the tracking further improved. Therefore, a field strength of $B = 3\,\mathrm{T}$ was chosen as being a reasonable compromise between high field, large volume and safe technology.

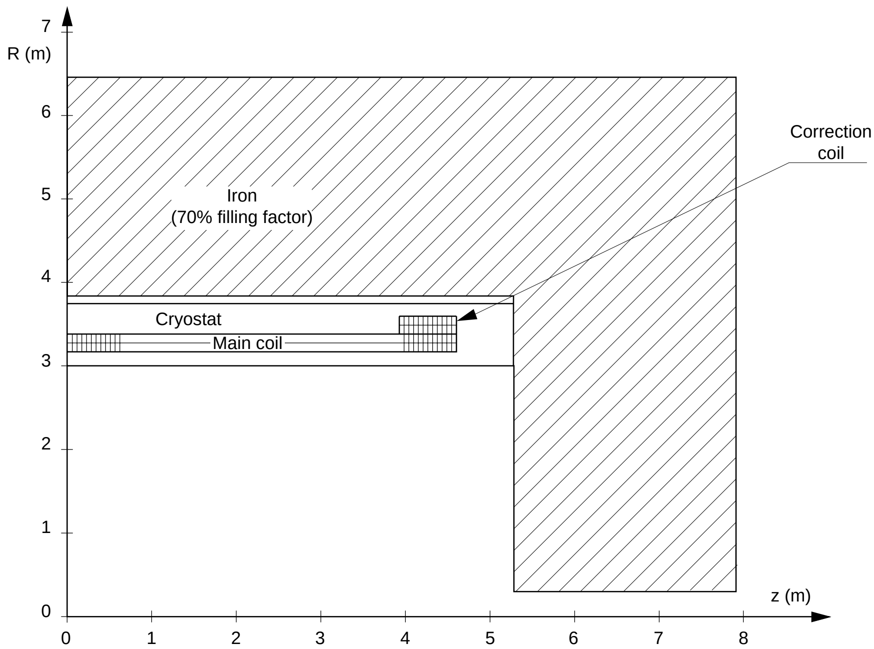

Figure 2.1.3: *Cross section through the magnet.*

The dimensions of the coil are determined by the need to have good momentum resolution and the decision to have the electromagnetic calorimeter and part of the hadronic calorimetry inside the coil. This leads to the choice of an internal coil diameter of 6.0 m. In order to provide good tracking down to $|\cos\theta| = 0.99$, good field homogeneity is required for the TPC in order to reduce $E \times B$ distortions on the electron drift. Thus the length of the magnet was chosen to be 9.2 m.

With these magnet dimensions the last quadrupole doublets are inside the coil. These doublets are superconducting in the case of TESLA, and the 3 T from the main coil is close to but still within a safe margin of their critical field strength.

The large aperture superconducting solenoid selected for this detector is a magnetic configuration which has been used in several previous projects as well as in projects under design. It is more expensive than a compact solenoid would be, but the physics benefits of putting the main calorimetry inside the coil are worth the extra cost. Even with extensive R&D it would not be possible to reduce the thickness of a compact coil to much less than half of a radiation length which would reduce the performance of the calorimeter.

The cross section of the magnet with its iron is shown in Fig 2.1.3. The iron is used both as a magnetic return yoke and as a hadronic tail-catcher and muon filter as described in Section 2.2.6. Table 2.1.5 summarizes the main parameters of the magnet preliminary design.

Dimensions	
Cryostat inner radius (m)	3
Main coil inner radius (m)	3.15
Main coil outer radius (m)	3.35
Correction coil inner radius (m)	3.35
Correction coil outer radius (m)	3.55
Cryostat outer radius (m)	3.75
Iron inner radius (m)	3.8
Iron outer radius (m)	6.4
Iron filling factor (%)	70
Main coil length (m)	9.2
Cryostat overall length (m)	10.5
Magnetic field	
Central field (T)	3
Maximum field at conductor (T)	3.8
Stored energy (MJ)	1 350
Nominal current (A)	15 000
Ampere turns main coil	$21.9 \cdot 10^6$
Ampere turns correction coil	$1.8 \cdot 10^6$
Conductor	
Type	NbTi cable in high purity Al plus mechanical reinforcement
Strand diameter (mm)	1.1
Cu to Sc ratio	1.3
No. of strands in cable	32
Overall dimensions (mm^2)	100×12
Critical current at 4.2 K and 4 T (A)	35 500

Table 2.1.5: *Main characteristics of the superconducting solenoid.*

	BaBar	LHC	LC
Bunch crossing time	4 ns	25 ns	4-708 ns
Level-1 accept rate	2 kHz	100 kHz	<0.1 kHz
Event building	0.4 Gbit/s	20-500 Gbit/s	1 Gbit/s
Processing power	10^3 MIPS	10^6 MIPS	10^5 MIPS

Table 2.1.6: *Comparison of three triggering projects.*

The mechanical and magnetic characteristics of this solenoid lie between those of ALEPH [21] and CMS [22]. Its design will include several features used for these two magnets:

- a high purity aluminum-stabilized conductor, with mechanical reinforcement;
- a compact impregnated winding, with indirect cooling provided by circulating helium at 4.5 K;
- a quench-back protection scheme.

Special features for this magnet are the use of a rather large conductor in order to limit the number of layers to two and the use of correction coils (as in ALEPH) to attain a field homogeneity of better than $\sim 10^{-3}$ in the TPC volume. More details about the design of this solenoid can be found in Ref. [23]. Further optimization of its dimensions will result from studies that follow.

2.1.5 Rates

Trigger and Data Acquisition Overview

This section outlines a functional overview of the event selection and data acquisition (DAQ) systems compatible with both machine proposals (TESLA and SBLC). The trigger structure and data flow are shown in Fig. 2.1.4. At the design luminosity and $\sqrt{s} = 500\,\mathrm{GeV}$, the physics rate to be recorded is expected to be about 0.1 Hz. Backgrounds expected to be rejected by the trigger include those from beam-beam effects (see next Section), beam-gas interactions and cosmic rays. There must be flexibility for adjusting the trigger rate due to background to the needs of the experiment (as is the case at LEP for example).

Extrapolation from previous or recent e^+e^- detectors (LEP detectors and BaBar) as well as advanced studies for LHC experiments allows a realistic model to be proposed based on a two-level scheme that satisfies the basic requirements. Compared to the LHC requirements, the data acquisition for the experiment is not a critical issue (see Tab. 2.1.6)

The DAQ system (see Section 2.2) must deal with

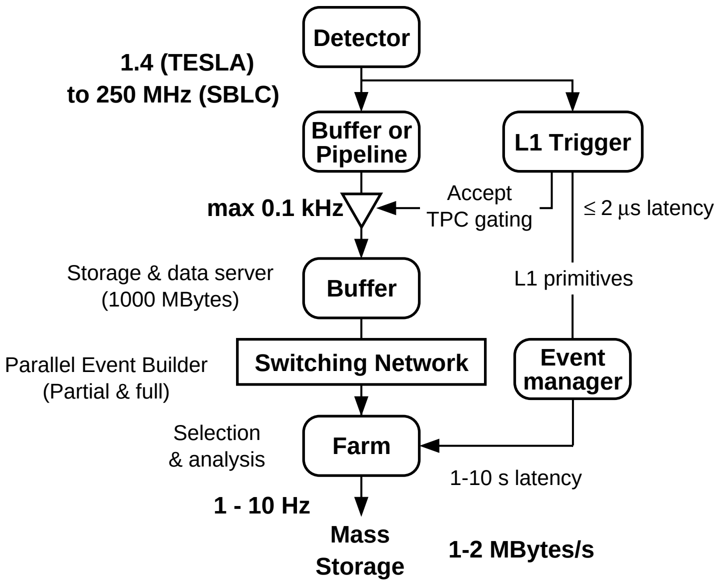

Figure 2.1.4: *Trigger and readout scheme.*

- $2 \cdot 10^7$ ($7 \cdot 10^8$) pixels of APS (CCD) vertex detector which are multiplexed into a few hundred readout channels,
- 10^3 channels of intermediate tracker,
- 10^7 pixels and strips for the forward tracker and intermediate silicon strip layer to be multiplexed into a few hundred channels,
- $7 \cdot 10^8$ TPC pixels read out in 720 k pad channels which will be reduced by multiplexing to a few thousand readout channels,
- 342 k calorimeter readout cells before multiplexing,
- and 200 k muon channels before multiplexing.

The final size of a physics event after zero suppression will be a few hundred kBytes up to about a MByte; the size of background events will be an order of magnitude smaller.

The Level-1 trigger would be adapted to the machine beam/bunch-crossing rate seen in Tab. 2.1.7. A first reduction of the initial background rate to less than 100 Hz can be achieved by fast logic that retains only those events that satisfy simple geometrical, energy deposition or track criteria, as well as pattern matching between subdetectors. Selection algorithms are performed synchronously within $2\,\mu$s latency using a separate stream of coarse dedicated data. Following a Level-1 Accept signal, about 1 GByte/s of front-end raw digitized information produced by the different subdetectors are transferred in parallel to a series of "readout buffers" acting as temporary data storage and server during the next steps of the selection process. Only that level would be affected by the choice of the machine (latency and front-end electronics design). After each Level-1 accept, the TPC signals are digitized during the $50\,\mu$s drift time, introducing a negligible dead time given sufficient front-end buffering. Several techniques will be envisaged, such as triggering the TPC grid at the Level-1 accept rate, or working in a free-running mode if the positive-ion effects in the TPC volume are under control.

Downstream of the Level-1, the second step may combine the event selection and analysis together by using a sequential strategy guided by the Level-1 primitives and trigger flags. At each step, only the event data which is necessary to make a decision is acquired and analyzed. The full event reconstruction (using all calibration constants) is performed only when required for physics analysis. A modern view for an implementation consists of a system with only four standard components: the "sources" data buffers (total capacity of 1000 MBytes), a 1 to 5 Gbit/s network for both protocol and data, the "destination" processing farm (10^5 MIPS) and the event control flow system. The recent development and availability of modern commercial switching network technologies such as ATM already solve the event building aspect, decreasing the complexity of connection and control protocols. Finally, some parameters such as the computing power, the latency and temporary storage buffer size will no longer be critical due to rapid development within the computing industry. After the on-line analysis, a few MBytes/s of data (about 1 % of an LHC typical bandwidth) will be recorded on permanent storage.

Backgrounds

The sources of background, discussed in detail in Section 2.4, are beam-beam effects, synchrotron radiation and debris from the final quadrupoles, and muon backgrounds arising from upstream sources. The main backgrounds are due to beam-beam effects. Table 2.1.7 gives an overview of some machine properties and related background rates.

The bunch crossing time for the two machine options are 6 ns (SBLC) and 708 ns (TESLA) for $\sqrt{s} = 500\,\mathrm{GeV}$. Via the beam-beam interaction, each bunch crossing occurring within the time resolution of the detector may produce particles that can partially obscure a real physics event triggered by a different bunch in the train. The row labeled "Minijet ev./100 ns, $p_T^{\min} = 3.2\,\mathrm{GeV}/c$" gives a measure of the probability of having stiff particles from underlying hadronic events in a good physics event for a typical subdetector with a timing resolution of 100 ns. The last rows show the rates for several physics channels.

	TESLA	SBLC	TESLA	SBLC
[Units in brackets]	0.5 TeV		0.8 TeV	
Beam properties				
Trains/s	5	50	3	50
Bunches/train	1130	333	1130	125
Interbunch spacing	708 ns	6 ns	566 ns	4 ns
$N_{e^\pm}$ per bunch $[10^{10}]$	3.6	1.1	3.6	1.2
$N_{\mathrm{beamstr.}\gamma}$ per $e^\pm$	2.0	1.4	2.4	1.6
$\langle E_{\mathrm{beamstr.}\gamma}\rangle$ [GeV]	3.0	4.7	8.7	11.1
Backgrounds/bunch				
$N_{\mathrm{beamstr.}e^\pm}$/bunch crossing $\theta > 150\,\mathrm{mrad}$, $p_t > 20\,\mathrm{MeV}/c$	31	7	47	17
Hadr.ev./bunch $E_{\gamma\gamma-\mathrm{c.m.s.}} \geq 5\,GeV$	.13	.04	.46	.17
Minijet ev./bunch $[10^{-2}]$ $p_T^{\mathrm{min}} = 3.2\,\mathrm{GeV}/c$	.30	.10	1.6	.66
Backgrounds/100 ns				
$N_{\mathrm{beamstr.}e^\pm}$/100 ns $\theta > 150\,\mathrm{mrad}$, $p_t > 20\,\mathrm{MeV}/c$	31	118	47	425
Minijet ev./100 ns, $p_T^{\mathrm{min}} = 3.2\,\mathrm{GeV}/c$	.003	.017	.016	.16
Physics events per hour				
Bhabha	3200	3000	900	1000
W^+W^-	140	133	34	36
$q\bar{q}$	63	60	19	20
$t\bar{t}$	15	14	5	5
$\nu\nu H_{\mathrm{SM}}$ ($M_{H_{\mathrm{SM}}} = 140$ GeV)	1.4	1.4	2.9	3.0
ZH_{SM}	1.2	1.2	0.4	0.4

Table 2.1.7: *Table of some machine properties and related backgrounds.*

Bibliography

[1] *ECFA/DESY Study of Physics and Detector for a Linear Collider*, http://www.desy.de/conferences/ecfa-desy-lc96.html, proceedings to be published as DESY 97-123E.

[2] *Proceedings of the Workshop on Physics at Future Accelerators*, La Thuile 1987, ed. J.H. Mulvey, CERN 87-07 (1987).

[3] C. Ahn et al., *Opportunities and Requirements for Experimentation at a Very High Energy e^+e^- Collider*, SLAC-Report-329 (1988).

[4] *Proceedings of the Summer Study on High Energy Physics in the 1990s*, Snowmass, 1988, ed. S. Jensen, World Scientific, Singapore, 1989.

[5] Three Workshops on the Japan Linear Collider (1989,1990,1992) resulting in:
JLC Group, *JLC-I*, KEK Report 92-16 (1992).
The latest workshop took place in 1995.

[6] *e^+e^--Collisions at 500 GeV: The Physics Potential, Parts A and B*, Workshops at Munich, Annecy, Hamburg, 1991, ed. P.M. Zerwas, DESY 92-123A&B (1992).

[7] *Physics and Experiments with Linear Colliders, Vols. I and II*, eds. R. Orava, P. Eerola and M. Nordberg, World Scientific, Singapore, 1992.

[8] *Proceedings of the 1992 Workshops on High-Energy Physics with Colliding Beams*, Trilogy of Workshops at Yale, Wisconsin, Santa Cruz, 1992, ed. J. Rogers, SLAC-428 (1993).

[9] *Workshop on Physics and Experiments with Linear e^+e^- Colliders, Vols.I and II*, Waikoloa, Hawaii, 1993, eds. F.A. Harris, S.L. Olsen, S. Pakvasa and X. Tata, World Scientific, Singapore, 1993.

[10] *e^+e^--Collisions at 500 GeV: The Physics Potential, Part C*, Workshops at Munich, Annecy, Hamburg, 1992-1993, ed. P.M. Zerwas, DESY 93-123C (1993).

[11] D.Burke, "Status of the Interregional Collaboration", Opening Session at the *Fifth International Workshop on Next-Generation Linear Colliders*, (LC93, SLAC, October 13-21, 1993), SLAC-436 (1993).

[12] *Proceedings of the Zeuthen Workshop on Elementary Particle Theory – Physics at LEP200 and Beyond*, Teupitz/Brandenburg, Germany, April 1994, eds. T. Riemann and J. Blümlein, Nucl. Phys. B (Proc. Suppl.) 37B (1994).

[13] *Proceedings of the Gamma-Gamma Collider Workshop* Berkeley, March 28-31, 1994, ed. A. Sessler, Nucl. Instr. and Meth. A355 (1995).

[14] *Proceedings of the Santa Cruz Workshop on* e^-e^- *Collisions*, Sept. 4-5, 1995, ed. C. Heusch, to be published.

[15] *Physics with* e^+e^- *Linear Colliders, Part D*, Workshops at Annecy, Gran Sasso, Hamburg, 1995, ed. P.M. Zerwas, DESY 96-123D.
Members of the working group on experimentation were: P. Bambade, W. Bartel, T. Benke, G. Blair, T. Bolognese, A. Bonissent, R. Brinkmann, J. Bürger, O. Callot, G. Coignet, P. Comas, G. Cowan, M. Danilov, P.-G. Denis, E. Elsen, M. Grünewald, D. Haidt, J.D. Hansen, J. Harton, P. Hüntemeyer, L. Jönsson, F. Kapusta, S. Katsanevas, D. Kisielewska, U. Kötz, S. Komamiya, A. Lebedev, M. Leenen, B. Löhr, K. Long, P. Mättig, J. Meyer, D. Miller, J. Milewski, R. Miquel, A. Olshevski, K. Piotrzkowski, M. Pohl, F. Richard, A. Rousarie, E. Rulikowska, H.-G. Sander, M. Schmelling, M. Schmitt, U. Schneekloth, H.-J. Schreiber, S. Schreiber, D. Schulte, R. Settles, S. Shuvalov, A. Sopczak, P. Steffen, H. Steiner, L. Suszycki, T. Tauchi, J. Thompson, I. Typakin, A. Venturi, H. Videau, A. Wagner, R. Walczak and G.W. Wilson.

[16] *Proceedings of LCWS95, the 1995 International Linear Collider Workshop at Morioka-Appi*, Sept. 8-12, 1995, World Scientific, 1996.

[17] R. Settles, et al., *Experimentation at the Linear Collider*, in Ref. [16].

[18] *International Linear Collider Technical Review Committee Report 1995*, Stanford Linear Accelerator Center Technical Publications Department, order number SLAC-R-95-471, G. Loew/SLAC(Chair) and T. Weiland/TH Darmstadt (Secreteriat).

[19] The proceedings of the studies in the USA by "DPF Long Range Planning" working groups (DPF is the Division of Particles and Fields of the American Physical Society), available on the World Wide Web under http://fermi.pha.jhu.edu/dpf/cltp/index.html

[20] D.J. Miller, *Other Collider Options*, in Ref. [16]; see Appendix A to this Conceptual Design Report.

[21] J.M. Baze, H. Desportes et al., "Design, Construction and Test of the Large Superconducting Solenoid ALEPH", IEEE Trans. on Magnetics, Vol. 24, March 1988, p. 1260-63.

[22] "The Compact Muon Solenoid (CMS) technical proposal", CERN/LHCC 94-38, LHC/P1.

[23] P. Colas, F.P. Juster, F. Kircher, "Concepts for a detector magnet for linear e^+e^- collider experiments", CEA report, to be published.

2.2 Subdetectors

2.2.1 Silicon Vertex Detector and Forward Tracker

Silicon detectors have become essential tools at fixed target and collider experiments [1, 2, 3]. The extreme accuracy of microstrip detectors [4, 5, 6] and the unique pattern recognition capability of pixel detectors [7, 8] can guarantee the full exploitation of the LC physics program for which excellent tracking and vertexing for heavy quark jet tagging are required. The silicon tracking has been designed to guarantee high quality tracking down to 100 mrad. It is divided into a vertex detector and a forward tracker.

The impact parameter resolution is the key figure of merit of the vertex detector performance. An $r\phi$ impact parameter resolution of better than $10\,\mu\mathrm{m} \oplus \frac{30\,\mu\mathrm{m\,GeV}/c}{p\ \sin^{3/2}\theta}$ has been assumed in Tab. 2.1.2 to give e.g. efficient Higgs selection. In the rz projection a similar resolution is required.

The forward tracking is important in e.g. $\mathrm{W^+W^-}$ physics for the charge identification of leptons from W decays in order to measure the W couplings. The absolute c.m.s. energy determination [9] also stresses good track measurement in the forward direction. The same is true for the measurement of the acollinearity of Bhabha events in order to determine the luminosity spectrum [10]. The benchmark for the forward tracking is therefore a momentum resolution of $\sigma_p/p < 20\,\%$ for particles in the energy range of 100 to 250 GeV and a polar angle resolution of $\sigma_\theta < 200\,\mu\mathrm{rad}$ down to the lowest possible polar angle.

2.2.1.1 Detector Layout

Vertex Detector. The impact parameter resolution is determined by both the single point precision and the detector layout. The detector technology and the radius of the innermost detector layer are constrained by the expected occupancies. These are due to both the track density in jets and the accelerator induced background. For the backgrounds, the current final focusing scheme and the 3 T magnetic field safely set the beam pipe radius at 2 cm and the first measurement plane at 2.5 cm. The track overlap in physics events at this radius is shown in Fig. 2.2.1 for the example reaction of $\mathrm{t\bar{t}}$ final states at $\sqrt{s} = 500\,\mathrm{GeV}$. The distributions show that a low level of ambiguity cannot be achieved with strip detectors. The situation is considerably better for pixel devices which are thus clearly preferred. The same conclusion can be drawn from the background hit density at $r = 2.5\,\mathrm{cm}$, where $\sim 10^{-2}\,\mathrm{hits/mm^2}$ are expected for each bunch crossing in TESLA and $\sim 1\,\mathrm{hit/mm^2}$ for each train crossing in SBLC (see Section 2.4).

Once the innermost layer radius is fixed, the interplay between the single point resolution and the lever arm to the outermost vertex detector layer determines the final impact parameter resolution; a detailed Kalman-filter based track fit, taking into

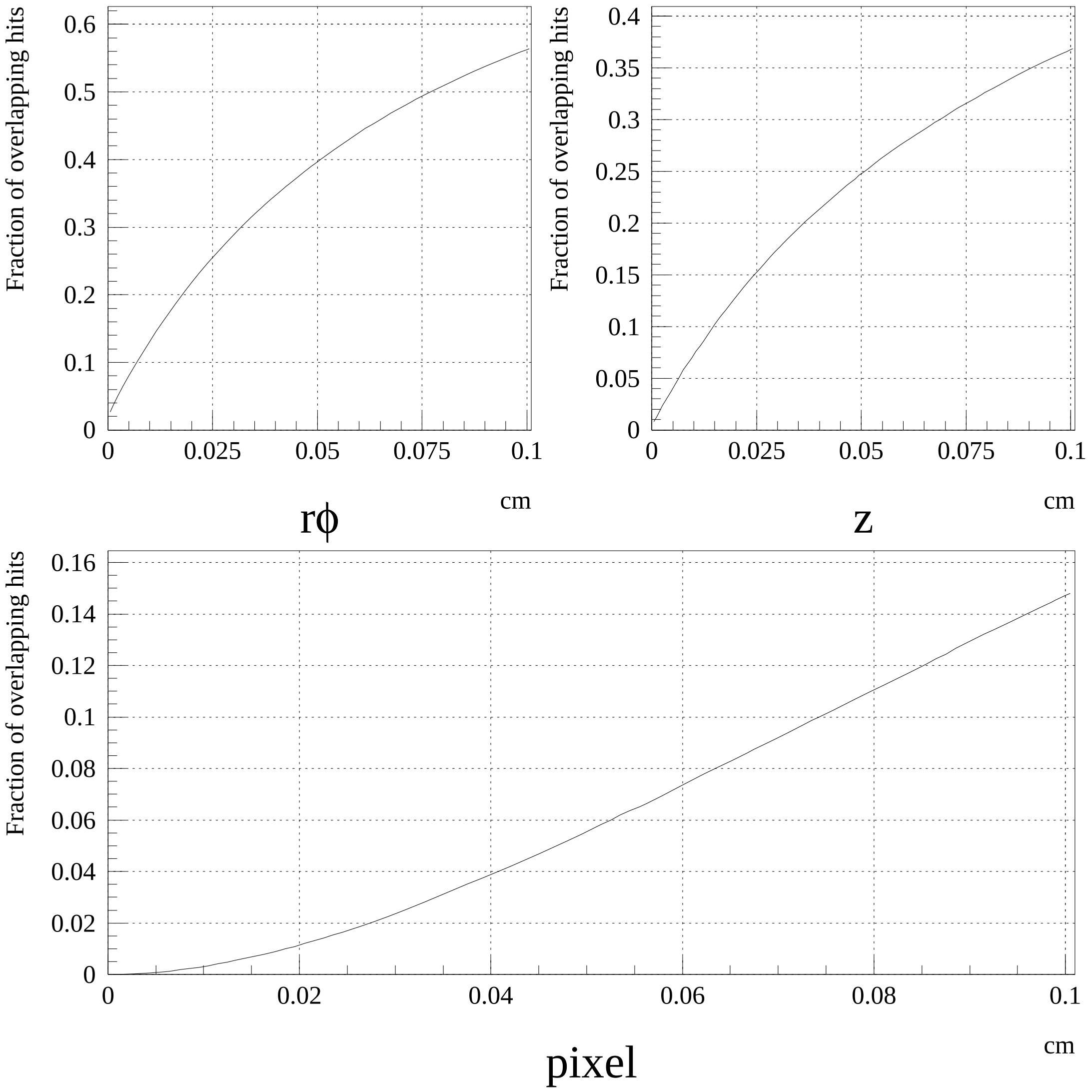

Figure 2.2.1: *Fraction of overlapping hits for the inner layer at* 2.5 cm *radius, as a function of the two-track resolution for* $r\phi$ *strips and* z *strips (upper plots) and for pixels (lower plot). The generated events were* $\mathrm{t\bar{t}}$ *final states at* $\sqrt{s} = 500\,\mathrm{GeV}$*. For the upper plots, the* $r\phi$ *strips are* 10 cm *long in* z*, and the* z *strips are* 2 cm *long in* $r\phi$*.*

account the full set of tracking chambers as specified in the subsequent sections, shows the design performance can be achieved with a single point resolution of $10\,\mu$m and a vertex detector outer layer at 10 cm radius from the interaction point.

Intermediate layers are needed to optimize the pattern recognition, and their number depends on the final detector technology:

- For Active Pixel Sensors (APS), the simplest possible geometry consists of one additional intermediate layer at 6 cm radius. A detailed simulation has shown that ambiguities at a few percent level can be obtained with a pattern recognition algorithm which starts by extrapolating a track element from the main tracker to the outermost vertex detector layer. The innermost layer extends down to 15° in polar angle, providing a precise measurement near the interaction point, in the angular region where b-tagging is effective. The mid and outer barrel layers will cover the 30° to 150° range. Each of these two layers will be complemented by an endcap, inclined by 30° with respect to the beam line and extending to the mask limit. The barrel acceptance and the cone inclination have been chosen in order to guarantee $\sigma_z \approx 10\,\mu$m also for inclined tracks. At the same time, the endcap geometry reduces the multiple scattering.

- For Charge Coupled Devices (CCD), a five layer design would allow stand-alone pattern recognition which would be desirable because of the longer readout time and the higher integrated background. A design for a CCD-based vertex detector at an X-band linear collider has recently been completed [11].

Irrespective of the detector technology, an azimuthal modularity of ~30-40° preserves the optimal $r\phi$ resolution and is also feasible for the innermost layer. Overlap between neighboring modules is foreseen for detector alignment using particle tracks.

The vertex detector has a total length of ~ 60 cm, about the same size as the LEP vertex detectors, and is mounted on the inside of the intermediate tracker (see Figs. 2.1.2 and 2.2.3). Different options for the mechanics and cooling may be conceived, depending on the detector technology. For APSs, either ladders housing cooling pipes or a homogeneous support structure acting also as a heat pipe can be imagined. For CCDs, cooling to 180 K has to be foreseen. The repeater electronics might be housed in conical cards outside the detector region. According to the present experience at LEP/SLC/HERA, survey, internal and relative alignment of the vertex detector is feasible.

Forward Tracker. The forward tracker consists of two internal disks of pixel detectors and three external disks of microstrip detectors (see Fig. 2.1.2). In the forward region the emphasis is on high momentum isolated particle tracking. It is important to have the longest possible lever arm to improve both the momentum and angular resolution.

The internal pixel detector disks complement the precision measurement of the vertex detector endcaps, providing two additional space points. These planes are located before the beginning of the mask, at $z = \pm 40$ cm and ± 50 cm, with 12 cm outer radius. The inner radius should be ≥ 4 cm to avoid entering into the envelope of particles produced by beamstrahlung.

For the external part of the forward tracker, silicon microstrips are used. In this region, projective devices can stand the track density and possible ambiguities are solved using the pixel points in the inner part of the tracker. Microstrips provide easily an extremely good point resolution with a fairly low number of channels. Furthermore, a track trigger in the angular region not covered by the inner tracker can be foreseen. Detectors are arranged in three layers, at $z = \pm$ 120, 140 and 160 cm, with an inner sensitive radius corresponding to a coverage down to the mask at about $\theta = 5°(7°)$ for TESLA (SBLC) and with an outer radius of 30 cm.

2.2.1.2 Detector Technologies for the Vertex Detector

The development of high resolution pixel detectors is currently evolving in two main directions: Active Pixel Sensors [12] and Charge Coupled Devices [13]). Both types of detectors have been successfully used in experimental apparatus [14, 15, 16] and an intense R&D program is taking place for more demanding future applications [17, 18, 19]. Both detector technologies have appealing characteristics for the linear collider environment. In the following, the main characteristics of the two options are briefly compared.

Detector thickness. In order to achieve a good signal-to-noise ratio, S/N, silicon microstrips and APS detectors have been fabricated up to now with typically 300 μm thickness. For hybrid APSs, the bump-bonded VLSI chip has also to be accounted for and adds about 300 μm to the detector. Thus the total thickness would be about 0.6 % of a radiation length, which would increase to $> 1\,\%X_0$ per layer once the mechanical support is included. The current results on low noise integrated pre-amplifiers [20] and the tiny single cell capacitance allow the possibility of reducing the detector thickness to 150 μm with a $S/N \approx 25$ [8, 21]. Back-thinning of the VSLI chip after bump bonding has been proven down to 50 μm thickness [22], so that the overall thickness would then be about $0.8\,\%X_0$ including the now dominant mechanical support.

Charge Coupled Devices built for the SLD vertex detector [14] are 150 μm thick. They are glued to a 380 μm-thick beryllium oxide mother card and support structure, giving an overall thickness of $0.36\,\%X_0$ per layer. In future, the CCDs can be thinned down to approximately 20 μm, using a procedure now being pioneered for astronomical applications. Also the mother board layout can be simplified, so that the single layer thickness can be reduced to about $0.12\,\%X_0$.

At the moment a 1 mm thick beryllium beam pipe is assumed, so that the multiple scattering term in the impact parameter design performance requires the detector thickness in the innermost layer to be $1\,\%X_0$ or less. Moreover, in order to minimize the amount of material in front of the calorimeters and to optimize the matching with the main tracker, an overall thickness of $< 3\,\%X_0$ is envisaged. Both constraints are well within the specifications of the detectors considered, either with the APS three layer geometry or the CCD five layer geometry, including the cryostat wall ($0.5\,\%X_0$) in the latter case.

Pixel size. The pixel size, the S/N and the track incidence angle determine the single point resolution. The current CCDs developed for the SLD vertex detector have a $20\times20\,\mu\mathrm{m}^2$ pixel size and provide $\sim 5\,\mu$m spatial resolution. Because of the $20\,\mu$m thick sensitive region, the resolution is not degraded for inclined tracks. For the APS solution, the pixel size is determined by the bump bonding technique and the integration scale of the readout electronics. Presently a $100 \times 100\,\mu\mathrm{m}^2$ pixel size is feasible [17]. In $r\phi$ the resolution of an effective $50\,\mu$m pitch is achieved either by utilizing $E \times B$ to induce the sharing of charge carriers between staggered adjacent rows [17] and/or by designing interleaved pixels to give analogue capacitive charge division to the nearest neighboring readout pixels [23], as in microstrip detectors [24, 25]. Assuming $S/N \approx 25$, the resolution for orthogonal tracks is $10\,\mu$m [6]. The rz resolution is affected by the incident angle, and a graded pitch similar to the DELPHI solution [26] could be used. Increasing the pixel pitch in z as $\frac{\mathrm{thickness}}{\tan(\theta)}$, the track always crosses the detector at the optimal angle, and the resolution is $\sigma_z \approx \frac{\mathrm{pitch}}{(S/N)}$ [6]. Thus the design point resolution can be obtained down to polar angles of 30°.

Readout scheme. The use of APSs at the linear collider experiment will benefit from the characteristics of the VLSI front end electronics being developed for LHC pixel detectors [17, 18]. In particular, the possibility of fast gating and time stamping the pixel hits within 25 ns would allow a considerable reduction of background hits. It would limit the background accumulation to a single bunch in TESLA; in the SBLC with 6 ns bunch spacing the background would be integrated over four bunches. Using the LHC front-end pixel electronics a simultaneous sparse data scan would allow skipping over empty pixels at a $\sim$ 1 GHz rate, while addressing fired pixels at $\sim$ 100 ns/pixel.

The CCD readout time is intrinsically limited by the charge transfer clock. Currently at SLD the readout time is $\approx$ 150 ms with a 10 MHz readout clock. For the future 50 MHz may be envisaged, so that the detector could read out between two linac cycles but with background accumulated throughout the train. The higher background from the TESLA train could be substantially reduced by a combination of fast-clearing the detector at intervals of 50 pulses ($35\,\mu$s) and pushing the beams out of collision with a kicker after a good trigger. However it may be necessary to permit a high trigger rate in order to measure novel processes with very small energy deposition in the detector (e.g. $\tilde{\chi}^+ \to \tilde{\chi}^0 + \cdots$ with small chargino/neutralino mass difference). Then it will be necessary to permit background accumulation throughout the whole train, corresponding for TESLA to $\sim 7\,\mathrm{hits/mm^2}$. In this case about 0.3 % of the innermost layer would be occupied by background hits.

Note that the CCD readout is inherently dead-time free. There is no problem in reading out any number of triggers in the train. Whether the fast clear option is implemented or not, the CCD option makes no stringent demands on the inter-bunch spacing (708 ns for TESLA down to 4 ns for the SBLC).

Radiation damage. SBLC and X-band machines can be considered friendly as far as radiation is concerned. In the case of TESLA the zero degree crossing angle has the advantage of minimizing the dead cone of the detector, but it also means that the swathe of beamstrahlung photons is dumped fairly close to the detector. A potential source of radiation damage is created due to photo disintegration neutrons which are reflected back into the detector from the dump.

Neutrons are much more damaging than electromagnetic radiation. CCDs of the type currently available for charged particle detection would be limited to $\sim 3 \cdot 10^9\,\mathrm{n/cm^2}$. Neutrons from the dump would be catastrophic ($\sim 4 \cdot 10^{11}\,\mathrm{n/cm^2 \cdot year}$), were it not for the mask in the aperture of the final quadrupoles, which reduces the flux by a factor of $\sim 10^3$. This translates to a detector lifetime in the TESLA environment of at least four years. Furthermore, there is rapid progress in hardening CCDs with respect to neutron damage (a factor 10 is likely to result from supplementary channel developments and maybe more from switching to p channel devices).

Another source is neutrons generated from the beamstrahlung background absorbed within the detector. Preliminary indications [27] are that this flux could amount to around $3 \cdot 10^9$ neutrons/cm^2·year and lead to an inadequate CCD lifetime (without the previously mentioned hardening factors). This flux estimate however depends critically on the absorbing material within the detector volume, and for example lining the mask surfaces with polyboron could give a major reduction. Detailed simulations are necessary in this area, following the prescription by the LHC collaborations.

The APSs and front end electronics for LHC are expected to stand up to 10^{15} n/cm^2 even if type inversion occurs [17, 18], so they are well suited for the linear collider environment.

Finally, the dose by the charged particle flux amounts to $\sim 10\,\mathrm{krad}$ per year (10^7 s) and is completely negligible.

2.2.1.3 Forward Tracker Technology

As mentioned earlier, backgrounds make pixels for the inner discs and strips for the outer discs the appropriate choices. The amount of material must be kept at a minimum for the measurement of Bhabha electron tracks in this angular region.

Forward tracker pixels. The discs at $z = 40$ and 50 cm (shown in Fig. 2.1.2) will use pixels. Due to the higher background and particle flux in the forward region, APS detectors are more suitable than CCD devices. APS detectors in the forward region can use a mechanical structure similar to that proposed for the vertex detector. The detectors could be mounted on a ceramic substrate which also serves as a heat pipe for the cooling components near the beam pipe.

Arrangement of the detector modules in disks perpendicular to the beam axis provides good mechanical stability. A 30° modularity as in the barrel can be achieved with trapezoidal detectors cut from standard 5″ wafers. With this geometry, forward APSs can exploit neither the track crossing angle nor the $E \times B$ effect to improve the resolution via charge sharing among different pixels. However a pixel size of 50 μm in ϕ and 200 μm in r and binary readout provide adequate resolution and two-particle separation.

Forward tracker microstrips. The outer disks at $z = 120$, 140 and 160 cm could be made of double-sided microstrip detectors or of single-sided detectors glued back to back with perpendicular orientation of the strips to provide space points in each layer. The latter solution is cheaper than double-sided detectors but contains more material, so that the choice can be made only after assessing the effect on the measurement of the Bhabha electrons. Each disk is composed of 24 detector modules, each consisting of two daisy chained microstrip detectors. The modules are supported on the inner wall of the TPC. The 20 cm spacing between the detector planes is chosen to allow the insertion of the repeater electronics cards on additional wheels interleaved with the detector wheels. Careful design work is needed to keep the amount of material low for the Bhabha measurement.

The lower angle acceptance of the detector is determined by the mask and the space needed for beam-spot monitor hardware and other services (see Section 2.4). In the TESLA design the outside mask angle is about 80 mrad, so that the forward tracker can cover the polar angles down to 5° with small gaps at appropriate positions between detectors for the services. For the SBLC the outer mask angle is about 120 mrad, and the forward trackers would cover down to 7°.

A single point resolution below 25 μm [6] can be achieved for a $S/N \approx 20$ with a 100 μm strip pitch detector, reading out every second strip to take advantage of capacitive charge division. It has been shown that silicon detectors have a time resolution sufficient to identify the bunch crossing [28, 29], and a fast readout time can be achieved by sparse data scan [30] or by integrated pipelines [31].

An interesting feature is the possibility of having a track trigger in the forward region. A first level trigger based on silicon detectors has already been realized for the HERA detectors [32, 33]. The use of microstrip detectors for trigger purposes requires the development of dedicated VLSI electronics [34, 35], and the goal looks within the reach of currently evolving microelectronics technologies.

2.2.1.4 Discussion of the Vertex Detector Options

In order to compare the CCD and APS options, the SLD algorithm ZVTOP for topological vertexing [36], which optimally disentangles the tracks associated with the primary, secondary and tertiary vertices (if any) in the jet, was used. The analysis then determines the invariant mass of the reconstructed heavy hadron decay, together with the transverse momentum, p_t, of the decay tracks with respect to the heavy hadron flight path. These kinematic quantities are combined, making allowance for missing neutral decay products, to determine the 'p_t-added mass' M_{p_t}. The vertex topology in the jet, together with the magnitude of M_{p_t}, is used to classify the jet as light-quark, c-quark or b-quark. The major challenge to achieve reasonable b/c discrimination.

It should be emphasized that this procedure is not yet completely optimized, but it already provides a valid benchmark for comparing various detector options. Further details on the present study may be found in the complete report [37].

An equal mixture of b and c jets of energy 50 GeV is generated using JETSET 7.4 with the Peterson fragmentation function, within the polar angle range $|\cos\theta| \leq 0.7$, so that the tracks from the jet are well-contained within the vertex detector aperture. The performances of the CCD and APS vertex detector options are simulated by appropriately smearing the charged particle tracks in both the $r\phi$ and rz projections, according to their momenta and directions. The smeared tracks are then processed by ZVTOP to determine the jet flavor. Knowing the generated 4-vectors for the jet permits the efficiency and purity of the flavor assignment to be determined, as a function of the cut variable M_{p_t}. Additional cuts are used for the c tag; for details see Ref. [36].

This procedure has been repeated for jet energies 100 and 200 GeV, and is found to give very similar results over this range. The results for b identification with 50 GeV jet energy are shown in Fig. 2.2.2(a) and for c identification in Fig. 2.2.2(b). It is clear that significant gains can be made by reducing the beam pipe radius, pixel size and material thickness. This may require a smaller beam pipe than in the present TESLA and SBLC designs, with consequent changes to the final-focus optics and collimation in the machine. Beauty signals are not quite so difficult to resolve, but will also be improved by having the best possible resolution.

2.2.2 Intermediate Tracker

The intermediate tracker serves to link tracks between the vertex detector and the main tracker, to detect secondary vertices for longer-lived particles, and to give a fast trigger on charged particles. As pointed out in Tab. 2.1.1, the amount of material should be minimized in the whole tracking volume because of the backgrounds from beam-beam effects; about 600 (150) photons of 1 MeV energy traverse the volume for each TESLA (SBLC) bunch crossing. Also the end flanges should be as thin as possible for the measurement of Bhabhas in the forward tracker (see Section 2.2.1.3). The multi-cellular drift chamber "Wellblechkammer", or Honeycomb chamber, made of thin-walled plastic cells in a self-supporting structure with no need for heavy flanges or massive walls, fulfills these two conditions nicely. A cross section through the intermediate detector is seen in Fig. 2.2.3.

The other technique studied for the intermediate tracker was scintillating fibers enclosing a TEC-type drift chamber as in L3 and is described in detail in Ref. [38].

Honeycomb Chamber

Prototype detectors with hexagonal shaped cells made of conductive plastic have been made and tested [39]. The cell size was 15 mm for the hexagons, and the cells were formed from foils of Makrofol KL3-1009, which is conducting and has good mechanical properties. The cell geometry was formed by pressing the foil at 180-210°C into a die consisting of groves with the desired cell pitch and having half of the hexagonal shape. Two foils were glued together to form a primary layer of cells, and these primary layers were then glued to form a block. This block can be shaped in a multiangle cylindrical form as shown in Fig. 2.2.3. Chambers of similar design are presently being manufactured for the Hera-B experiment.

This device will also be the support for the vertex detector and the four inner discs of the forward tracker. The radial thickness of the Honeycomb chamber can be kept to between 0.2 and 0.5 % X_0, depending on the number of cells chosen radially. The end flanges will be made of 2 mm of aluminum (2 % X_0). The honeycomb chamber will be mounted on the TPC inner wall as shown in Fig. 2.2.3. As indicated above, the layout for the front-end electronics, cables and cooling for vertex detector, forward-tracking detectors and intermediate tracker must be planned carefully so as not to place too much material in the path of the Bhabhas used for measuring the luminosity spectrum.

The choice of the cell size has to be optimized as function of resolution necessary and the amount of material. With a cell size of 10 to 15 mm and readout via multi hit TDCs at each end of the tube, the track coordinates will be determined with an accuracy of about 100 μm in the drift direction and about 1 cm along the wire.

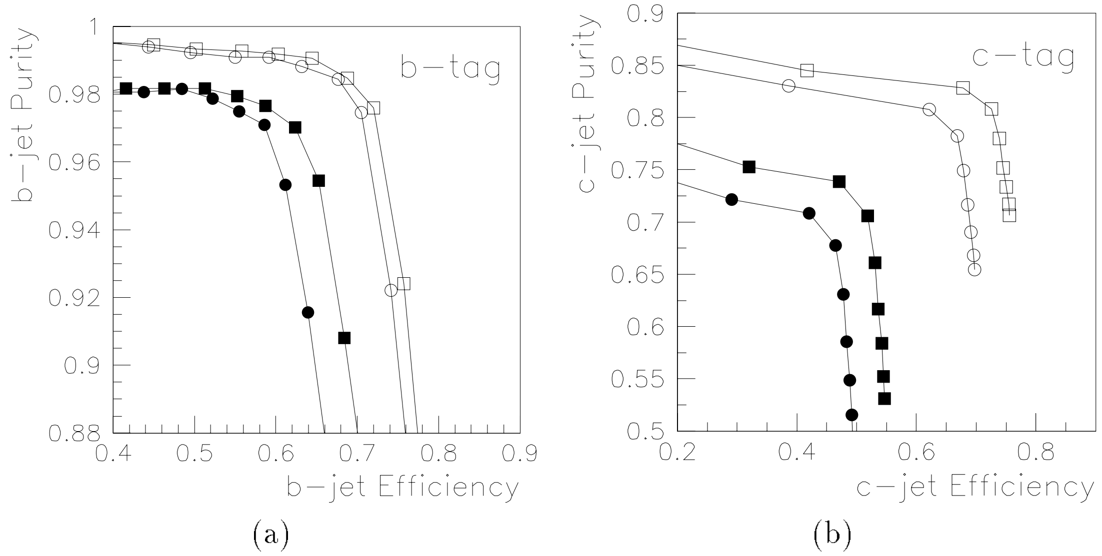

Figure 2.2.2: *Purity vs efficiency for (a) beauty and (b) charm identification in* 50 GeV *jets. Open squares and circles refer to the CCD option, with respectively* $r_{\text{beampipe}} =$ 10 *and* 22 mm. *The filled squares and circles refer to the APS option for the same* r_{beampipe} *values.*

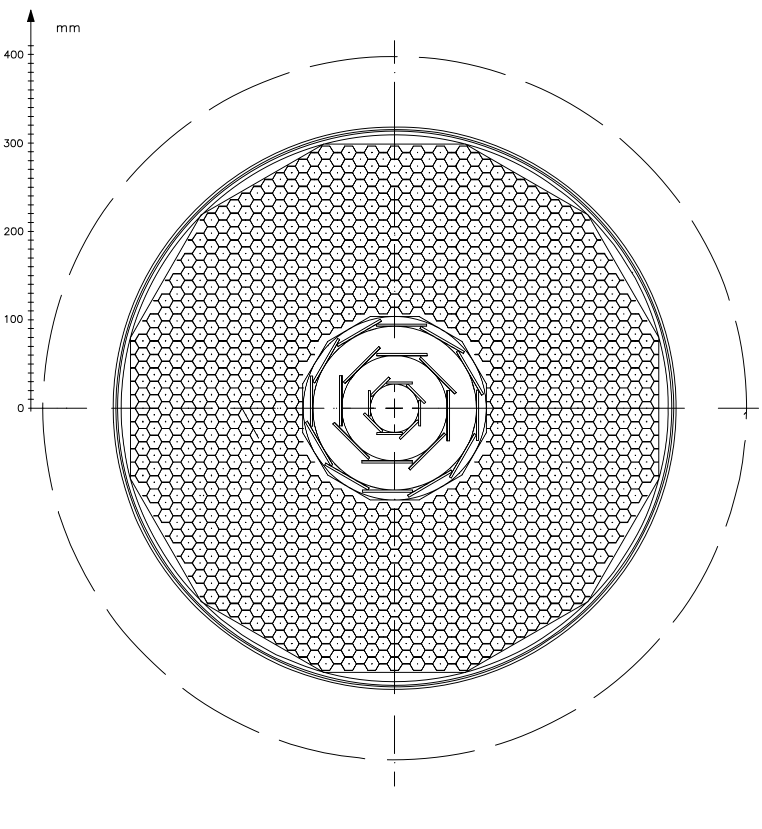

Figure 2.2.3: *$r\phi$ view of the honeycomb chamber and the vertex detector.*

2.2.3 Main Tracker

Several options were studied for the main tracking chamber: all-silicon tracking [40], an MSGC tracker [41], and a time projection chamber (TPC) [42]. The TPC was chosen as the first option in the design of the LC detector because of the excellent performance experienced at LEP [43, 44], where it proved its good momentum resolution, simple and efficient pattern recognition of complex events, and good particle identification.

2.2.3.1 The Time Projection Chamber (TPC)

The choice of a TPC is based on the experience gained in the PEP-4, TOPAZ, DELPHI and ALEPH [43] detectors and on calculations related to robustness in the background environment at the linear collider. In the following exercise, an extrapolation of the ALEPH TPC design is described, and possible areas of improvement resulting from further R&D are pointed out. The TPC offers several advantages.

- It has extremely high tracking redundancy and granularity which are important for the multijet physics at the linear collider.

- It gives good particle identification via the dE/dx ionization loss of the charged particles. This is important for the e/π separation to complement the performance of the electromagnetic calorimeter and improve the overall e/π separation to below 10^{-3} in the momentum range 1 to 50 GeV/c, for reasonable π-K-p separation, and for the energy-flow measurement [43].

- The performance profits from operation in a high B-field since the electrons drift parallel to $\vec{B}$.

- Since the wires are stretched azimuthally at end-cap sectors and thus are short ($\sim$1 m), the TPC can be long in the axial direction, to enable coverage to smaller polar angle θ.

- It is easy to maintain since the endplate is divided up into small sectors which can be readily replaced or serviced in case of problems.

On the other hand,

- it has a long memory time (50 μs), an apparent disadvantage which is more than compensated for by the high granularity (circa 10^8 3D pixel elements) as shown below;

- it does require that the B-field be well-mapped, to an accuracy of better than 10^{-3}, and that the drift volume be well-monitored with laser tracks [44].

The performance of the tracking is given by

$$\frac{\delta p_t}{{p_t}^2} = C = \frac{\sigma_{\text{point}}}{0.3\mathrm{B}(R_O - R_I)^2}\sqrt{\frac{720}{N+4}} \quad \text{for} \quad |\tan\theta| > \frac{R_O}{L}$$

$$\frac{\delta p_t}{{p_t}^2} = C \times G^2 \times \sqrt{\frac{N+4}{\frac{N}{G}+4}} \quad \text{for} \quad |\tan\theta| < \frac{R_O}{L},$$

where

$$G = \frac{R_O - R_I}{L\tan\theta - R_I},$$

with R_O and R_I being the outer and inner radii of the tracking detectors, $2 \times L$ is the length (along the beam) of the main tracker and N is the maximum number of measured points of charged particles by the tracking detectors. For the LC TPC the following choices have been made: $R_O = 1.6\,\mathrm{m}$, $R_I = 0.4\,\mathrm{m}$, $L = 2.5\,\mathrm{m}$, $N = 118$ and $B = 3.0\,\mathrm{T}$. With $\sigma_{\text{point}} \simeq 160\,\mu\mathrm{m}$ (see below), $C = 2.8 \cdot 10^{-4}$ for the TPC alone. For the ALEPH TPC alone $C = 12 \cdot 10^{-4}$, and the improvement for the LC comes from mainly the increase in B by a factor of 2 and in N by a factor of 6, which is now technologically feasible (see below).

Choosing the half-length of the chamber L to be 2.5 m means that, using the above formulae, the vertex detector + intermediate tracker + TPC will measure 200 GeV/c tracks to 30 % accuracy in the forward direction at $|\cos\theta| \simeq 0.98$, so that there is a good match to the forward tracking. This is important, for example, for the curvature measurement of muons for the determination of the anomalous couplings of the electroweak gauge bosons $\mathrm{W^+W^-}$, which are strongly forward-backward peaked. Due to the forward-peaking of $\cos\theta$, one gains rapidly in statistics at smaller angles: a factor of two in going from $|\cos\theta| = 0.94$ to $|\cos\theta| = 0.98$. The performance at small angles is even more important for other channels which will be used for the measurement of couplings and involve t-channel gauge boson fusion [45]: $\mathrm{e^+e^-} \to \mathrm{e}\nu\mathrm{W}$, $\mathrm{e^+e^-} \to \nu\bar{\nu}\gamma$, $\mathrm{e^+e^-} \to \nu\bar{\nu}\mathrm{Z}$ and $\mathrm{e^+e^-} \to \mathrm{ee\,WW}$.

2.2.3.2 Chamber Size

The chamber is situated in a 3 T magnetic field (see Section 2.1.4). The inner and outer radii of the LC TPC field cages are $\mathrm{R^{fc}_{inner}} = 0.32\,\mathrm{m}$ and $\mathrm{R^{fc}_{outer}} = 1.70\,\mathrm{m}$, and the sensitive volume of the tracking covers from $\mathrm{R^{pads}_{inner}} = 0.40\,\mathrm{m}$ to $\mathrm{R^{pads}_{outer}} = 1.60\,\mathrm{m}$. Electrons from ionizing particles drift over a length of up to $\ell_{\text{drift}} = 2.5\,\mathrm{m}$, the half-length of the chamber. Tracks can be reconstructed up to $|\cos\theta| \simeq 0.985$, using the requirement that at least four pad rows define a track.

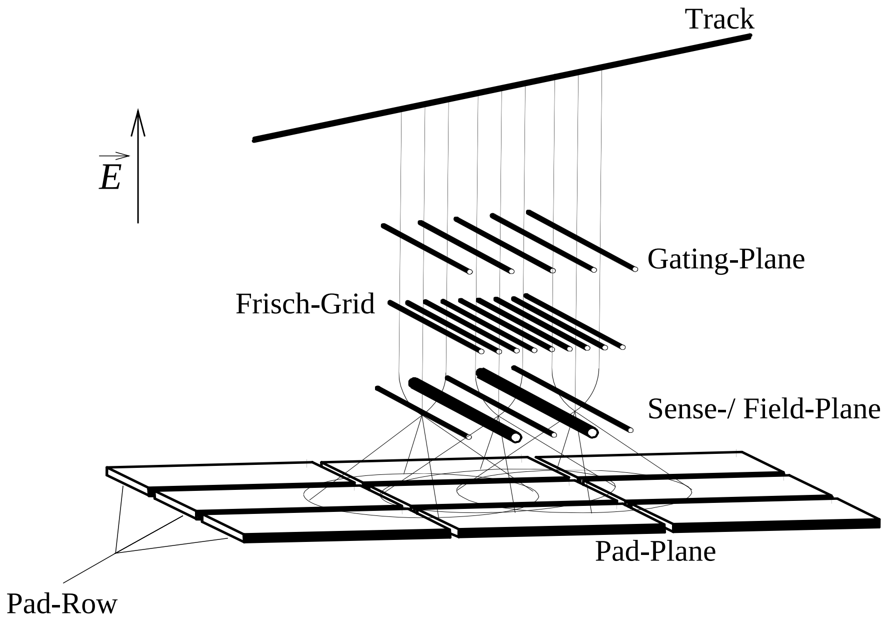

Figure 2.2.4: *Configuration for the TPC wire chamber.*

2.2.3.3 Details of the Design

The design goal is to obtain the best possible granularity by profiting from recent R&D work [46, 47]. The 3D granularity is determined by diffusion of the drifting electrons in the gas, the readout electronics and the readout-chamber technology. The relevant gas properties are the drift velocity and the longitudinal and transverse diffusion coefficients. Advances in electronics make the design of fast front-end, digitizing and buffering electronics for a large number of channels both feasible and affordable. New technologies [46, 47] for the readout chambers can also improve the granularity significantly; present possibilities are improved wire-chamber technology, micro-strip gas chamber (MSGC) [48], micromesh gaseous chamber (MICROMEGAS) [49] and gas electron multiplier (GEM) [50]. For the present, wire chamber readout technology will be studied with the gas mixture used in ALEPH to see how much the granularity can be improved. Figure 2.2.4 illustrates the configuration for the standard wire-chamber TPC readout.

Diffusion. The size of an electron cloud drifting from its point of origin to the end-cap sector is determined by diffusion in the gas. In the directions transverse and longitudinal to the drift direction, the sizes are $FWHM_T = 2.34\sigma_T = 2.34 D_T\sqrt{\ell}$ and $FWHM_L = 2.34\sigma_L = 2.34 D_L\sqrt{\ell}$, respectively, where D_T and D_L are the diffusion coefficients of the gas and ℓ the drift length. Since the electrons are drifting along the $\vec{B}$

direction, their spread is inhibited by the B-field according to $D_T(B) = \frac{D_T(B=0)}{\sqrt{1+(\omega\tau)^2}}$, where $\omega(=eB/m)$ is the cyclotron frequency and τ is the mean drift time between collisions with the gas molecules. For the gas used in ALEPH (91 % Ar, 9 % CH_4), the measured values are $\frac{\omega\tau}{B} = 5.9 \pm 0.2\mathrm{T}^{-1}$ [44], $D_T(0) = 600\,\mu\mathrm{m}/\sqrt{\mathrm{cm}}$ and $D_L = 380\,\mu\mathrm{m}/\sqrt{\mathrm{cm}}$ for a $E = 200\,\mathrm{V/cm}$ drift field, corresponding to a drift velocity of $v_D = 5.3\,\mathrm{cm}/\mu\mathrm{s}$ [46]. Thus for a 3 T B-field $\omega\tau = 17.7$, and, for a drift distance of $\ell = 250\,\mathrm{cm}$ the size of the electron cloud is $FWHM_L = 14.0\,\mathrm{mm}$ and $FWHM_T = 1.3\,\mathrm{mm}$, which translates to a volume for the 3D track pixels of $0.19\,\mathrm{cm}^3$. The volume of the TPC consists of $2{\cdot}10^9$ such 3D elements. The wire chamber readout does not exploit this fine granularity completely, as described in the following sections.

Wire chambers and pad structure. In Fig. 2.2.5, the pad structure of the TPC end plates is shown. The pads are arranged in circular rows of radial size $\Delta R = 10\,\mathrm{mm}$ and cover the entire end-plate. The pads are 2 mm wide azimuthally and the pad-to-wire distance 1 mm, corresponding to a pad-response-function width of approximately $\sigma_{\mathrm{prf}} = 1.4\,\mathrm{mm}$ [46]. (The pad response function is the form of the pulse height along a pad row induced by electrons arriving at a sense wire above.) Thus the point measuring accuracy is $\sigma_{\mathrm{point}} \simeq \sigma_{\mathrm{prf}} \times 1/\sqrt{N_{\mathrm{primaryelectrons}}} \simeq 140\,\mu\mathrm{m}$ for $N_{\mathrm{primaryelectrons}} \simeq 100/\mathrm{cm}$. There are 506 k pads in 64 pad rows in the outer sectors and 214 k pads in 54 pad rows in the inner sectors. The inner sector boundaries are arranged such that they do not point to the beam line, as shown in Fig.2.2.5, in order to have full hermeticity for the central tracking up to $|\cos\theta| \simeq 0.985$.

Electronics. The electronics can be designed such that they do not cause deterioration of the two-track resolution in the direction along the electron drift. By choosing analogue electronics with 100 ns shaping time and a clock rate for the drift-time digitization of 50 ns (giving 1000 time buckets during the 50 μs drift time for each pad), the arriving signal is broadened by the shaper by 7 % to 280 ns and is sampled six times. The information from each pad channel would be stored in a buffer, and via multiplexing of a few thousand pad channels, the number of electronic cables is reduced so as not compromise the hermeticity of the detector.

The readout granularity. As shown above, the size of an electron cloud which has drifted the full length is $FWHM_L = 14.0\,\mathrm{mm}$ and $FWHM_T = 1.3\,\mathrm{mm}$. The wire chamber readout does not capitalize completely on this fine granularity in $r\phi$ ($FWHM_T$) because the transverse readout dimension is given by in ϕ the $FWHM$ of the pad response function which is 3.3 mm and in r by the the pad height which is 10 mm. Longitudinally, the granularity will not be compromised by the readout as just explained. Thus for the readout including diffusion, the 3D volume element is $0.46\,\mathrm{cm}^3$ (ALEPH: $4.7\,\mathrm{cm}^3$) giving a total of about $7.9{\cdot}10^7$ 3D readout elements.

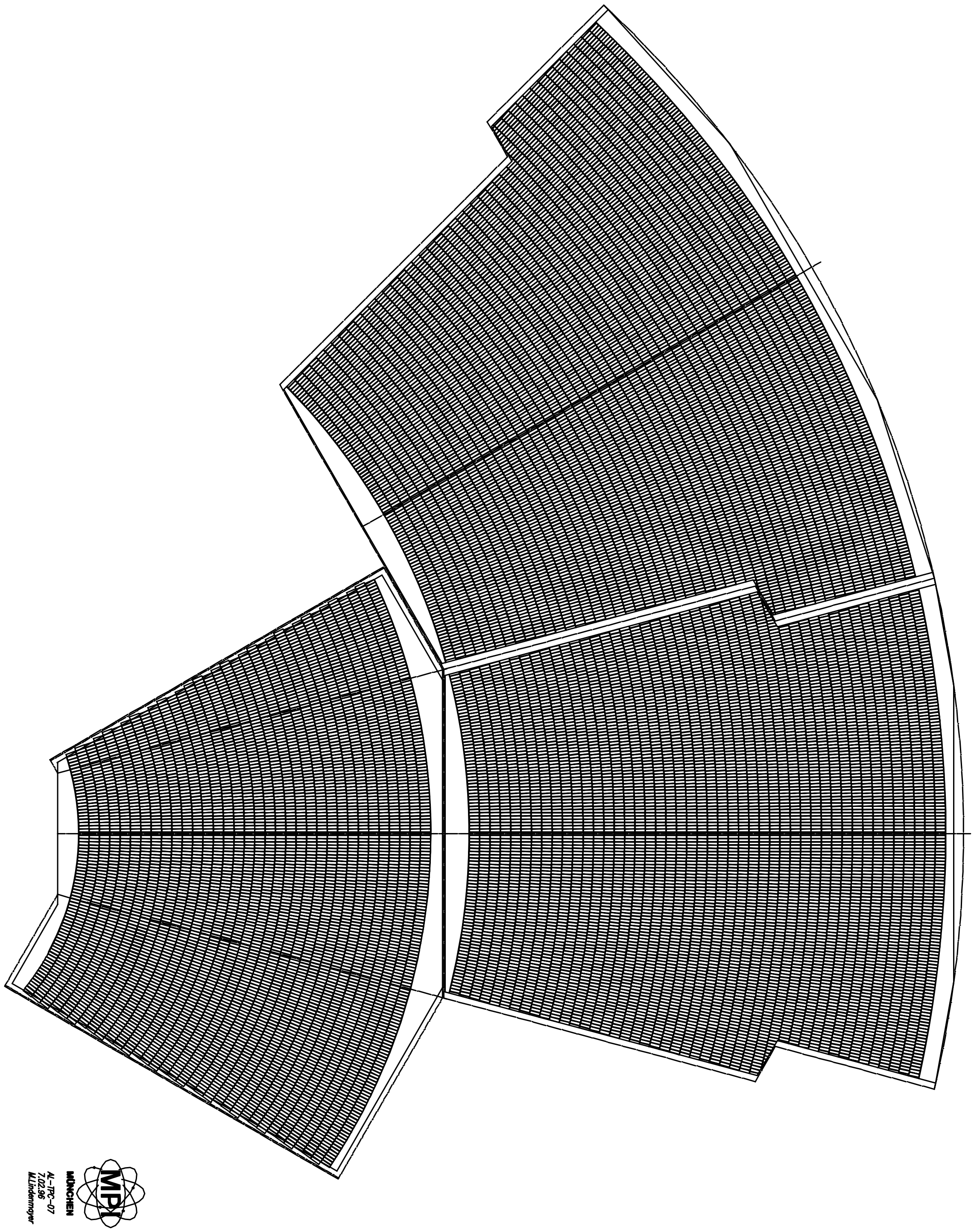

Figure 2.2.5: *TPC sectors with pad structure. The inner sector boundaries do not point to the origin.*

The dE/dx measurement and wire readout. In the ALEPH TPC, the track coordinates are measured using the pads, and the dE/dx for particle identification is measured using the signals from the wire readout. In the heavy ion experiment NA49 [51] the wires are not read out, and the dE/dx measurement is also derived from the readout of the 40 mm long pads. For the LC TPC both options are open, but it seems best to include the wire readout in the design, because then the pad and wire information can be combined to improve the coordinate measurement, the two-track resolution, the dE/dx measurement and the overall granularity, adding about $2{\cdot}10^6$ volume elements to the above figures.

Triggered gating. To reduce the background currents and positive ion build up in the TPC volume, the chamber can be operated in the triggered gating mode, by which the gate of the TPC is opened only once a good trigger is signaled. The trigger signal should arrive within $2\,\mu$s after the bunch crossing, and the final trigger rate should be less than about 20 Hz to keep the positive ions to a negligible level. It may be possible to operate in a free-running mode (gate always open), but this needs study to be sure the distortions can be corrected (see below).

Backgrounds and occupancy. As stated in Section 2.1.5, backgrounds arise from beam-beam effects, synchrotron radiation and muons from upstream sources. The main backgrounds are due to beam-beam effects: the creation in the bunch-bunch interaction of $e^{\pm}$ pairs and of photons which can scatter several times and enter the detector. The masking is designed to reduce them to an acceptable level.

It is estimated from background studies [52] that for TESLA 600 γ/bunch will cross the TPC and the average γ energy is about 1 MeV. About 2 % of the photons will undergo Compton scattering in the gas, and since the TPC integrates over 70 TESLA bunch crossings, they give rise to about 800 tightly spiraling electrons per TPC "picture". Due to the tight spiral (circa 2 mm diameter), these will be lines following the B field, each of which will affect typically 3 pads, so that the occupancy from this background will be at most 0.4 % per "picture". The background current produced per Hz of trigger rate is estimated to be 5 nA, three orders of magnitude below the operational experience ($5\,\mu$A) with the ALEPH TPC, which has been tested at another order of magnitude higher levels ($50\,\mu$A). Thus a 10 to 20 Hz trigger rate would lead to a total current of around 100 nA in the wire chamber sectors, which is small.

The situation is about the same for SBLC. The TPC integrates over a factor four more bunch crossings than for TESLA, but this is compensated by the factor four fewer γs produced per bunch due to the lower bunch charge.

The other sources of background are due to beam-beam $e^{\pm}$ pairs and slow neutrons which scatter out charged particles from the gas molecules occasionally. These backgrounds roughly double the figures above.

Distortions in the drift volume. Inhomogeneities of the electric and magnetic fields must be well controlled because they distort the paths of the drifting electrons. This leads to the tolerance on the B-field homogeneity of 10^{-3} (see Section 2.1.4), so that the correction for B-field distortions is at most a couple of mm. The experience at LEP [44] shows that the this tolerance can be met and that the B-field can be mapped to better than 10^{-4} and that the ~mm distortions can be corrected to a few tens of μm. Also this experience [53] indicates that with a good field map and the $\sim 10^6$ calibration Z events from Z-peak running, even larger B-field inhomogeneities can be handled reliably. This may be necessary for the SBLC because of the compensating solenoids surrounding the final quadrupoles.

Similarly, the LEP experience has shown the field cage can be built to keep corrections for the drift-field distortions to a negligible low level. The positive ion build up also distorts the E-field and is controlled by gating, as described above. Even here, both the DELPHI [54] and the ALEPH [55] TPCs have been operated for short periods with open gate for hardware reasons, and the effects due to the positive ions were evident but correctable. These distortions could appear if it is necessary to run at very high rates (e.g. if SUSY exists and the $\tilde{\chi}^{\pm}_j$-$\tilde{\chi}^0_i$mass difference is small) so that the gate is always open. For that case as well as for the general tracking alignment, a battery of laser tracks criss-crossing the TPC volume can correct these effects.

For the ALEPH TPC [53], the Maxwell equations for the various sources of distortion were solved and introduced into a χ^2 fit to the Z-peak data with only a very few parameters per distortion. Using these fits one is able calibrate the distortions to high accuracy and control them from year to year to a level of less than $30\,\mu$m.

Underlying events. The long memory time of the TPC does not cause a problem with underlying events, because the tracks from two bunch crossings are well separated due to the $5\,\mathrm{cm}/\mu\mathrm{s}$ electron drift velocity (or more for other gases, see below), giving a $300\,\mu$m for SBLC and 35 mm for TESLA. Thus for TESLA the situation is excellent. Even for SBLC the separation is an order of magnitude larger than the reconstruction accuracy for the primary vertex by the vertex detector and is about the same size as the bunch length. It would be easy to resolve tracks from interactions separated by two or three bunch crossings. Thus the probability for an underlying event of the kind referred to in the row labeled "Minijet ev./bunch, $p_T^{\min} = 3.2\,\mathrm{GeV}/c$" of Tab. 2.1.7 is about 0.003 for both TESLA and SBLC.

2.2.3.4 Conclusion on Standard Technology.

In conclusion, using standard TPC technologies the granularity can be increased by an order of magnitude relative to previous e^+e^- applications by employing advances in electronics and by pushing the technology of the endcap readout wire chambers further. Nevertheless, it is worthwhile to continue R&D in the direction of improving the gas and of developing new TPC readout techniques such as MSGC [46, 47, 48], MICROMEGAS [49], and GEM [50].

As an example for improving the gas, the study for the muon collider [56], for which a TPC is considered robust enough to stand more severe backgrounds than at the LC, suggests a gas 90 %He+10 %CF_4 for which the drift velocity is about twice that of the ALEPH gas (91 %Ar+9 %CH_4) while the diffusion constants are about the same. A number of factors would give reduced backgrounds and occupancy by at least a factor two: for TESLA the memory time would sum over a factor two fewer bunches; for SBLC the vertices for two successive bunches would be separated by 600 μm; recoils from neutron scattering in CF_4 are a factor $\sim$4 less energetic than in CH_4.

The application of the MSGC, MICROMEGAS or GEM technology for reading out a TPC for the LC detector is of great interest because they allow a reduction of the pad-response-function width and perhaps reduce the positive ion buildup around the gas-amplification region. For the MSGC, chambers with $\sigma_{\rm prf}$ between 0.6 and 1.4 mm have been built [47]; there is a complicated dependence of the gain on the strip geometry and on the bulk and surface resistivities which are the subject of continuing study. The MICROMEGAS have a conversion gap followed by a thin (about 100 μm) amplification gap above the anode plane which can be divided into pads; these two regions are separated by a 3 μm thick cathode mesh, the positioning of which is critical and needs further R&D. A possible solution is offered by GEM in which an intermediate cathode foil with a matrix of holes (of $\sim$ 30 μm size and $\sim$ 100 μm pitch) [57] is inserted between the two electrode planes and with suitable voltages provides an intermediate amplification region. R&D is necessary to understand how to build a large system using one of these technologies.

2.2.4 Combined Tracking Performance

The TPC is the main device for momentum measurements, but its performance is greatly enhanced by the inner tracking detectors, as displayed in Fig. 2.2.6. A very precise point determined by a layer of silicon microstrip detectors just in front of the TPC improves significantly the sagitta measurement, provided the detector can be aligned to reach an overall point precision of about 8 μm.

The resolution can be further improved by combining the data from all the tracking devices and imposing a beam constraint. The final resolution of $\sigma_p/p^2 = 0.6 \cdot 10^{-4}(\mathrm{GeV}/c)^{-1}$ allows a resolution on the mass of a pair of high momentum ($\approx$ 100 GeV) muons of a size comparable with the intrinsic Z width. This resolution requires keeping the overall systematic effects in the tracking below the 10 μm level, which represents a challenge to the tracker-builders because it is a factor of 2 to 3 smaller than achieved at LEP.

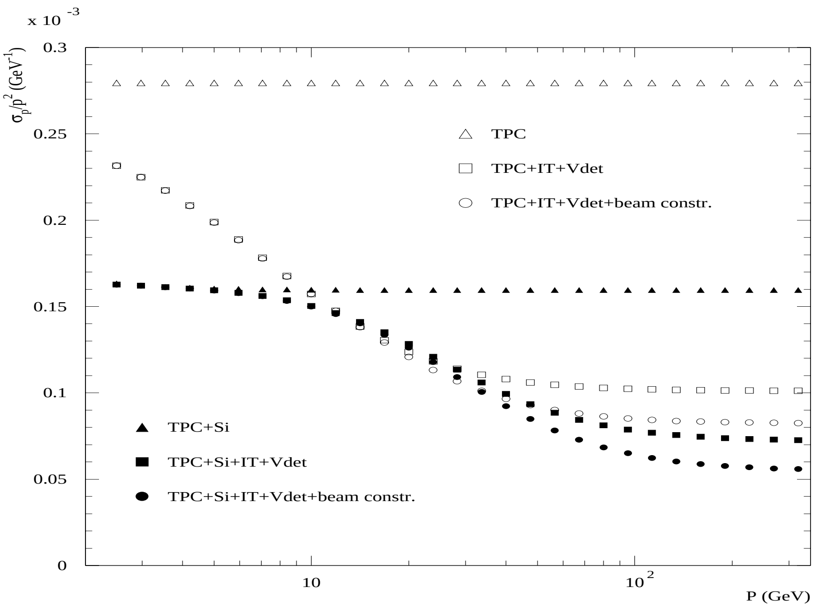

Figure 2.2.6: *Resolution of* $1/p_t$ *for* $90°$ *tracks assuming an APS vertex detector. Symbols: Vdet = vertex detector, IT = intermediate tracker, Si = intermediate silicon layer.*

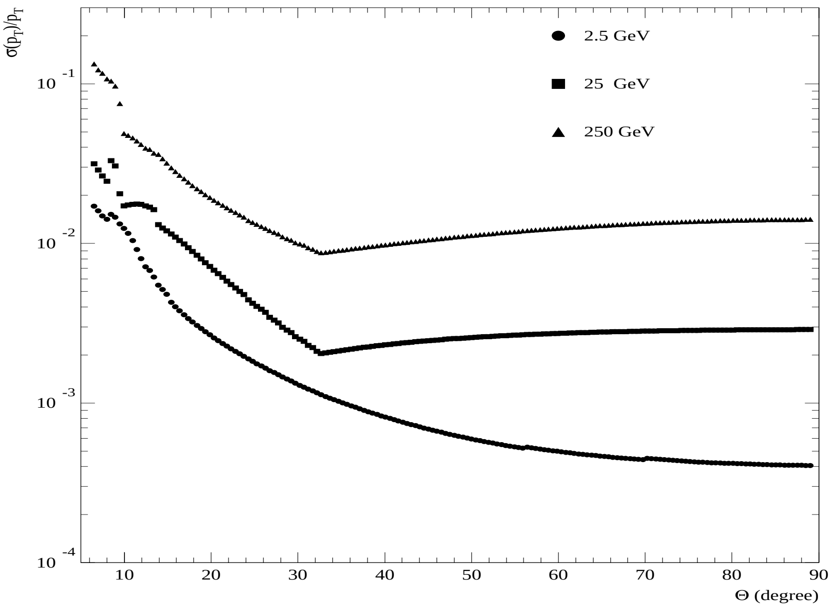

Figure 2.2.7: *Resolution of* $1/p_t$ *as a function of polar angle assuming an APS vertex detector.*

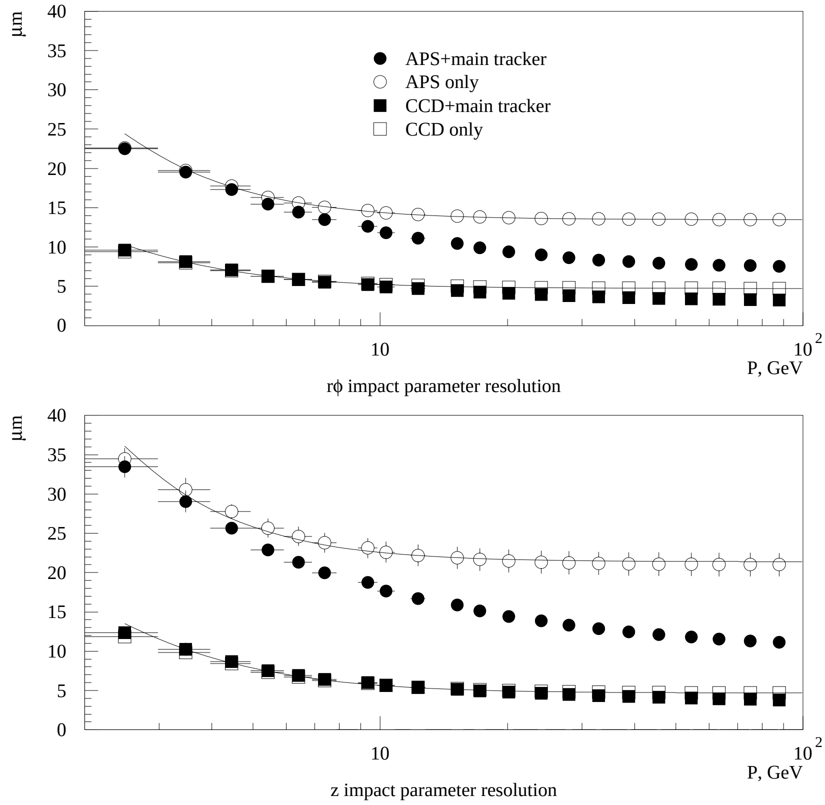

Figure 2.2.8: *Impact parameter resolution for different configurations for vertexing.*

	$\sigma_{r\phi}$ [μm]	σ_z [μm]
CCD	$4.7 \oplus 22.8/p\,_{[\mathrm{GeV}/c]}$	$4.7 \oplus 31.6/p\,_{[\mathrm{GeV}/c]}$
APS	$13 \oplus 51/p\,_{[\mathrm{GeV}/c]}$	$21 \oplus 72/p\,_{[\mathrm{GeV}/c]}$

Table 2.2.1: *Parameterization of the impact parameter resolution for the vertex detectors alone.*

At low polar angles both the projected track length and the number of TPC points decrease. It is therefore necessary to provide a precise forward tracker for momentum measurement and charge identification of energetic forward leptons. The tracking system was designed to provide a $\sigma_p/p < 30\,\%$ for tracks up to 500 GeV over the whole tracker acceptance. The performance as a function of angle is seen in Fig. 2.2.7.

The impact parameter measurement is important for the identification of decay products of short lived particles, to be used in heavy flavor tagging. Experience at LEP and SLC has shown that a gain in impact parameter measurement improves the physics capability of an apparatus (see Section 2.2.1.4). Good separation of charm from beauty requires an impact parameter resolution of at least $10\,\mu\mathrm{m} \oplus 30\,\mu\mathrm{m}/p\,[\mathrm{GeV}/c]\sin^{3/2}\theta$ in the $r\phi$ plane.

Two techniques have been studied here to achieve this performance: if the background and radiation damage rate are tolerable for very high precision CCD devices, the vertex detector can almost reach the goal with its stand-alone resolution as in the current SLD experiments at the Z peak. If the background rates exclude the use of CCDs, the APS vertex detector information can be combined with the precise TPC track information to give an impact-parameter precision for high momentum tracks of below $10\,\mu$m. The impact-parameter resolution is shown in Fig. 2.2.8. In order to compare CCDs with APSs (which have a resolution dependent on θ) an average over $30° < \theta < 90°$ has been performed. The impact-parameter resolution for the vertex detectors alone are determined assuming the momentum resolution of the TPC and yield the results in Tab. 2.2.1.

A benchmark for the forward tracking system was to achieve a precision for the polar angle determination of at least of 0.2 mrad for tracks below 10°. The silicon detectors proposed easily achieve this precision.

2.2.5 Calorimetry

2.2.5.1 Requirements

General. Calorimeters are used to measure the energy of charged and neutral particles. Longitudinal and lateral segmentation allows the location of the energy deposition, the identification of electromagnetic and hadronic components of the showers generated by the particles, and the identification of muons. Since dead material in front of the calorimeters worsens the resolution, it was decided to locate the superconducting coil, which represents approximately one nuclear interaction length (λ) of dead material, outside the calorimeter. The calorimeter must therefore be very compact.

Calorimeters are essential for measuring missing energy, the characteristic signature of SUSY particles and of neutrinos. Another example studied was the charged Higgs channel $\mathrm{H}^+\mathrm{H}^- \to \mathrm{c\bar{s}\bar{c}s}$, for which the calorimetry is important because it is sensitive to the mass resolution of the detector. A study [58, 59] of the hadronic energy resolution has shown that the goal in Tab. 2.1.2 of $\delta E/E \simeq 50\,\%/\sqrt{E} \oplus 4\,\%$ results in a good $\mathrm{H}^\pm$ detection efficiency that would not be improved much by drastically better hadronic resolution.

High resolution calorimeters. The best hadron-shower resolution is obtained in compensating calorimeters, that is, calorimeters with the electromagnetic and hadronic responses equalized, denoted $e/h = 1$. This compensation can be achieved with a U/scintillator sampling structure in which the hadronic sensitivity is increased by the nuclear fission induced by slow neutrons. For hadrons a resolution $\sigma/E \simeq 35\,\%/\sqrt{E}$ has been achieved [60]. Compensation is also achieved in lead-absorber calorimeters with resolutions of $\sigma/E \simeq 40\,\%/\sqrt{E}$ for the hadronic component and $\sigma/E \simeq 20\,\%/\sqrt{E}$ for the electromagnetic component, using a Pb/scintillator sampling ratio close to 20/5 (mm/mm) [61]. This performance results from a rather coarse-grained layer structure. A decrease of the Pb and scintillator thickness improves the electromagnetic resolution at the expense of compensation, but this degradation in compensation can be corrected for by weighting the hadronic component of the shower at the software level. This weighting technique in a multi cell Pb/LAr and Fe/LAr calorimeter [62] was shown to improve the resolution by using the iterative method described in Ref. [63]. A resolution $\sigma/E \simeq 40\,\%/\sqrt{E}$ was obtained for hadrons and $\simeq 10\,\%/\sqrt{E}$ for electrons.

The fractional resolution improves with energy as $\sqrt{E}$ but it is limited by a constant term and a noise term. The constant term dominates at energies above typically 100 GeV, whereas the noise term is important at energies around that deposited by minimum ionizing particles. To improve the resolution at high energy the constant terms will be kept as small as possible, $< 2\,\%$ for hadrons and $< 0.6\,\%$ for electrons.[1] With this performance, missing energy, a signature of new physics, can be measured very well down to a few GeV [64].

[1]These constant terms are a factor two smaller than in Tab. 2.1.2 and thus are superb goals.

2.2.5.2 Layout

Principle. The sampling thickness envisaged for the active and passive absorber layers will be kept close to that needed for compensation. However complete compensation cannot be with the electromagnetic resolution required in Tab. 2.1.2. The improved hadronic resolution due to compensation will be regained because the calorimeter granularity is fine enough to permit software energy-weighting. Good homogeneity, compactness and hermeticity can be achieved with a "Shashlik"-type tower structure in which the layers consist of a sandwich of absorber and scintillator with wavelength shifting fiber readout. The photodetectors and the readout electronics can be outside the sampling structure and cracks due to wavelength shifter layers or bars can be avoided. Such calorimeters techniques have already been tested and described [65]. They have also been proposed as an alternative to the radiation-sensitive lead tungstate crystal calorimeter for CMS [66]. Shashlik modules are also used in the STIC at DELPHI/LEP [67] and are now being built for the HERA-B detector at DESY [68].

Absorber material and thickness. For the electromagnetic section, Pb is a good candidate for the passive medium given its very short radiation length X_0. It has been observed that compensation is possible with a Pb/Scintillator sampling structure in which the volume ratio of lead to scintillator is 4/1 [60]. The LC detector will have 30 sandwich layers of 5/5 mm Pb/Scintillator sheets corresponding to $27\,X_0$, because better electromagnetic resolution at the expense of compensation is desired (see above). For the hadronic section, Cu is used because it has a short interaction length and good mechanical stiffness, which allows for smaller dimension tolerances and more precise machining. An optimal sampling structure is expected with 20/5 mm Cu/Scintillator layers. The interaction length in the hadronic section is $\lambda = 7.5\,\mathrm{cm}$ and in the electromagnetic section $\lambda = 30\,\mathrm{cm}$.

Calorimeter Structure

Supertowers. The building blocks of the barrel and endcap calorimeters are supertowers. The thinner Pb/Sci electromagnetic section in front is followed by the thicker Cu/Sci hadronic section. Supertowers are laterally divided into 4×4 hadronic towers and 8×8 electromagnetic towers. An overview of the calorimeter structure is shown in Fig. 2.2.9 and details are given in Tab. 2.2.2.

The supertowers have an angular width of $\Delta\theta = 3.5°$ at $\theta = 90°$ and a lateral size of $22.4 \times 22.4\,\mathrm{cm}$ ($26.7 \times 26.7\,\mathrm{cm}$) at the front face (end face) of the calorimeter; these dimensions are kept roughly constant over the polar angle θ. The longitudinal supertower thickness (length) is 5.4λ (114 cm) at $\theta = 90°$ and increases with θ to $\approx 8.4\lambda$ at $\theta = 30°$ and $\theta = 150°$. The weight of the supertowers varies between 600 and 850 kg.

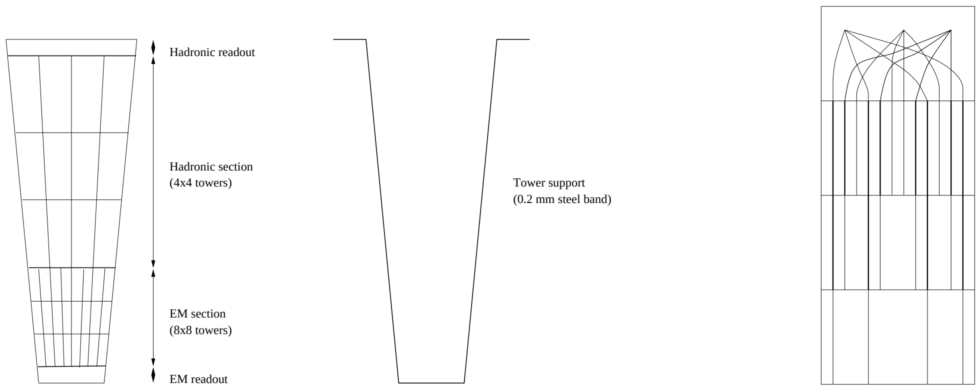

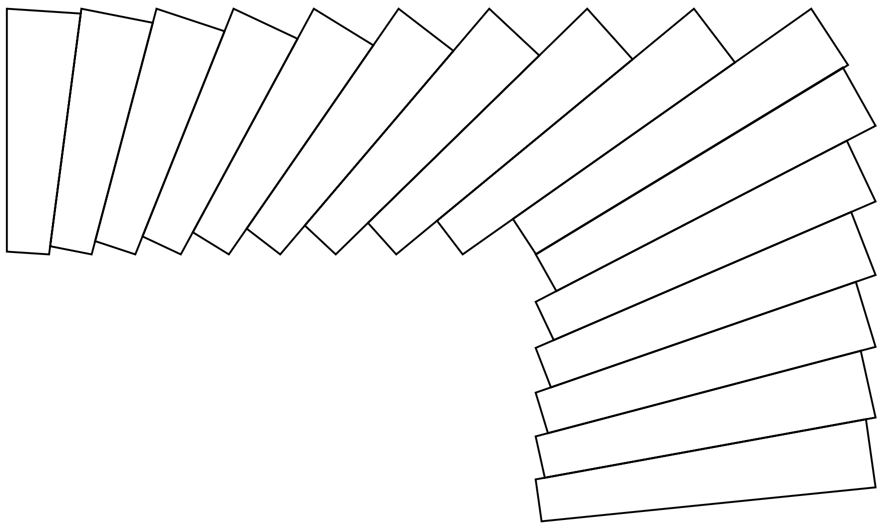

Figure 2.2.9: *Schematic drawings of a Shashlik supertower (top left), of the steel band support (top center), of the WLS readout fibers (top right) and of the arrangement of the rings of supertowers(bottom).*

Section	Radial limits (cm)	Depth (X_0, λ)	Material	Scint/Abs (mm/mm)	Number of layers	Number of longit. readout cells
Barrel						
Pre-sampler	170–172	$1.6X_0$	SciFi/Pb		2	2
ECAL	172–210	$27\,X_0$ 1.1λ	SciFi Pb WLS fib.	5/5	30	3
HCAL	210–300	4.7λ	SciFi Cu WLS fib.	5/20	33	3
Coil	300–375	0.9λ	Al Scint. pads	740/10	1	1
Tail Catcher	380–640	11λ	Fe/RP chamber	50/30 150/30	20+5	20+5
Endcaps						
ECAL	(r) 23.5–210 (z) 280–330	$27X_0$ 1λ	SciFi Pb WLS Fib.	5/5	30	3 or 4
HCAL	(r) 23.5–300 (z) 330–460	10λ	SciFi Cu WLS fib.	5/20	94	3 or 4

Table 2.2.2: *Calorimeter structure.*

Section	Angular acceptance	Number of rings	Number of super-towers	Number of readout cells	Approx. tower size (cm×cm)	Approx. tower half angle
Barrel	30°–150°	20	1000			
ECAL				192,000	2.8×2.8	0.47°
HCAL				48,000	5.6×5.6	0.94°
Coil				1,700	40×40	
TC				17,000	40×40	
Endcaps	4.85°–30° 150°–175.15°	2×6	2×174			
ECAL				66,816	2.8×2.8	0.29°
HCAL				16,704	5.6×5.6	0.58°
Grand Total				342,220		

Table 2.2.3: *Calorimeter granularity.*

Supertower rings. The whole calorimeter is made of 32 supertower rings, with 20 rings in the barrel section between 30°and 150°, and 50 supertowers making up one ring. Details are given in Tab. 2.2.3. The weight of a ring varies between 30 and 45 tons.

The calorimeter is closed by two endcaps, each consisting of 6 rings with decreasing number of supertowers down to $\theta = 4.85°$. The endcaps cover the angular range between the beam pipe and the barrel calorimeter ($4.85° < \theta < 30°$ and $150° < \theta < 175.15°$).

Supertower longitudinal sections. The outer radius of the hadronic section of the barrel calorimeter is constrained by the coil radius. The minimal depths of both electromagnetic and hadronic sections were determined by GEANT Monte Carlo simulations [69, 70]. These resulted in specifying an electromagnetic section $27\,X_0$ deep, equivalent to 30 Pb/Sci layers of 5/5 mm and a barrel hadronic section $4.4\,\lambda$ deep ($\simeq$ 84 cm.) at $\theta = 90°$. The tail catcher (see below) measures the end of the shower which leaks out through the coil.

For the endcaps, the depth of the electromagnetic section is the same as in the barrel and that of the hadronic section is $9\,\lambda$ or more. The endcap iron is also instrumented as tail catcher. The electromagnetic calorimeter starts at $z = 2.80$ m from the interaction point, and the hadronic section extends to about $z = 4.6$ m. The inner radius is 23.5 cm.

Tower sizes. The 4×4 hadronic towers in a supertower each have 5.6×5.6 cm cross section at the entrance window and cover an acceptance of 1.88° in φ and θ.

Each hadronic tower is preceded by 2×2 electromagnetic minitowers of 2.8×2.8 cm ($\Delta\theta = 0.94°$). This size is well adapted to the lateral size of the electromagnetic shower (Moliere radius $\simeq 2$ cm).

In the endcaps, the supertower and tower sizes are approximately the same as those in the barrel calorimeter. Due to the larger distance from the interaction point, the angular granularity of the hadronic tower improves to $\Delta\theta \simeq 2\ 1.2°$.

Cell segmentation. The electromagnetic section will be longitudinally segmented into at least three readout cells. To permit a good e/π separation, three cells of depths of 4, 12, and 11 X_0 can be used. For the hadronic section, longitudinal segmentation into at least three cells is also needed in order to have the information for software compensation. In the present design the hadronic towers are divided into three cells of equal depth of about $1.5\,\lambda$ ($\simeq 28$ cm); the optimization of individual cell depths will be the subject of further Monte Carlo studies.

In the endcap calorimeters, there are also three longitudinal cells for both the electromagnetic and hadronic sections at the moment. The number and depths of these cells still need to be optimized by Monte Carlo simulations.

Cracks. The energy leaking through cracks can be avoided in a design where the supertowers do not point directly to the interaction vertex. Therefore an alignment offset of 3° is built into the system. In addition, support and signal cables for the electromagnetic section will not run between the supertowers or the rings. They will be run in front of the electromagnetic section and exit the detector through two non-pointing cable slits at 30° and 150° between the barrel and endcap calorimeter.

Photodetectors. The photodetectors must be insensitive to the strong magnetic field and, in order to fulfill the calorimeter compactness requirement, must be very short. Stability and insensitivity to temperature changes are essential requirements. They are envisaged to operate in front of the electromagnetic section, where the shower development has not yet started and beyond $5.4\,\lambda$, where most of the shower energy is already absorbed. The development of vacuum phototriodes and phototetrodes [71], avalanche silicon photodiodes (AVPs) [72] and proximity focused multichannel hybrid PMTs (HPMT) [73] is progressing rapidly.

Coil Calorimeter and Tail-Catcher Sections

The superconducting coil calorimeter section is considered separately for optimization. The coil is a single absorber layer, mainly aluminum ($0.9\,\lambda$), in a 75 cm deep cryostat, and the readout being considered is one scintillator layer just outside the cryostat. Laterally it could be segmentated into pads with dimensions approximately the same as the dimensions of a supertower end face; a scintillator thickness of 1 cm should be sufficient. The light could be wavelength shifted in double-cladded WLS readout fibers and transported to photomultipliers via clear optical fibers.

The tail (a few percent) of the hadronic shower leaks out of the back of the hadron calorimeter and the coil, and the iron surrounding the superconducting coil is instrumented to act as tail catcher. A detailed description is given in Section 2.2.6. Similar tail catcher structures already exist in several large experiments, e.g. H1 [74].

Presampler

The presampler improves the measurement of electron and photon lateral position, π^0 reconstruction and e/γ separation. The present idea is to use two superlayers of fibers sandwiched with $1.6\,X_0$ of Pb. Each layer would consist of 10^5 radiation-hard, double-cladded blue scintillation fibers of 1 mm diameter, arranged in stereo layers and running roughly parallel to the beam. The inner superlayer would be made of six staggered layers of 10^4 fibers each, with a pitch of 1.07 mm, and would give an $r\phi$ resolution of $50\,\mu$m. The outer superlayer would consist of four staggered layers and give an $r\phi$ resolution of $80\,\mu$m. The presampler would be mounted directly in front of the electromagnetic barrel calorimeter on the outer wall of the TPC, have a length of 2×280 cm and cover the polar angle range $33° < \theta < 148°$. Further details can be found in Ref. [75].

More simulation of the shower development in the magnetic field will be done to optimize the structure of the presampler and improve further the measurement of the shower energy.

2.2.5.3 Calorimeter Electronics

Signal boxes. The photodetectors and associated electronics are located at the top and bottom of the supertowers. The details of the readout depend on the choice of the photodetector and are still being specified. The monitoring of the gain of each cell can be done with LED or laser light, injected via optical fibers from outside the detector. Only one injection fiber per supertower is needed.

Trigger and readout. Calorimeter-based triggers are a key element to the Level-1 trigger and will be based on:

- total tower multiplicity,
- total electromagnetic energy,
- total hadronic energy,
- total global energy,

– energy leakage from barrel calorimeter,

– missing energy,

– missing transverse energy.

The 6 ns SBLC bunch spacing makes it necessary to use a pipeline to readout the data, the time being too short for a final trigger decision. The 708 ns bunch spacing of TESLA allows for enough time to make a reasonable trigger decision before readout.

Underlying events are a minimal problem for the calorimeter since the time resolution is approximately 1 ns, depending on the photodetectors and amplifiers used.

2.2.5.4 Performance

As mentioned in the previous sections, several effects contribute to degrading the sampling energy resolution of the calorimeter. The final resolution receives a contribution from a noise term and a constant term. The noise term includes white and coherent noise which must be kept small in order to allow a precise calibration with cosmic and halo muons. This can be achieved with the use of low-capacitance photodetectors, optimal electronic amplifier design and proper grounding. The constant term, which dominates at high energy, can be reduced by minimizing the amount of dead material in front of the calorimeter and between the supertowers and by avoiding cracks. Stable response can be optimized by keeping the temperature and the supply voltages constant, by minimizing rate effects and by permanent gain monitoring. Further reduction of the constant term can be gained by software-weighting the individual signal samples to make the e/h ratio as close to unity as possible. As other experiments have shown [76], it is possible to make the constant term smaller than 0.6 % in the electromagnetic calorimeter and smaller than 2 % in the hadronic calorimeter [77].

Calorimeter depth optimization.

Parameterized shower profiles. Several options for the structure of the calorimeter were studied; energy resolutions used were parameterization of those measured in previous experiments.

For various sampling layer structures, the intrinsic resolution was studied as a function of the global depth of the calorimeter within the superconducting coil, as well as a function of the relative depths of the electromagnetic and hadronic sections.

The longitudinal profile of a hadronic shower was parameterized as in Ref. [78]. The fraction of hadronic energy deposited in each calorimeter section was calculated by integrating the shower profile in the corresponding section and smeared according to experimentally measured intrinsic resolutions [79]. Electromagnetic showers were assumed to be fully contained in the $27\,X_0$ deep electromagnetic section of the

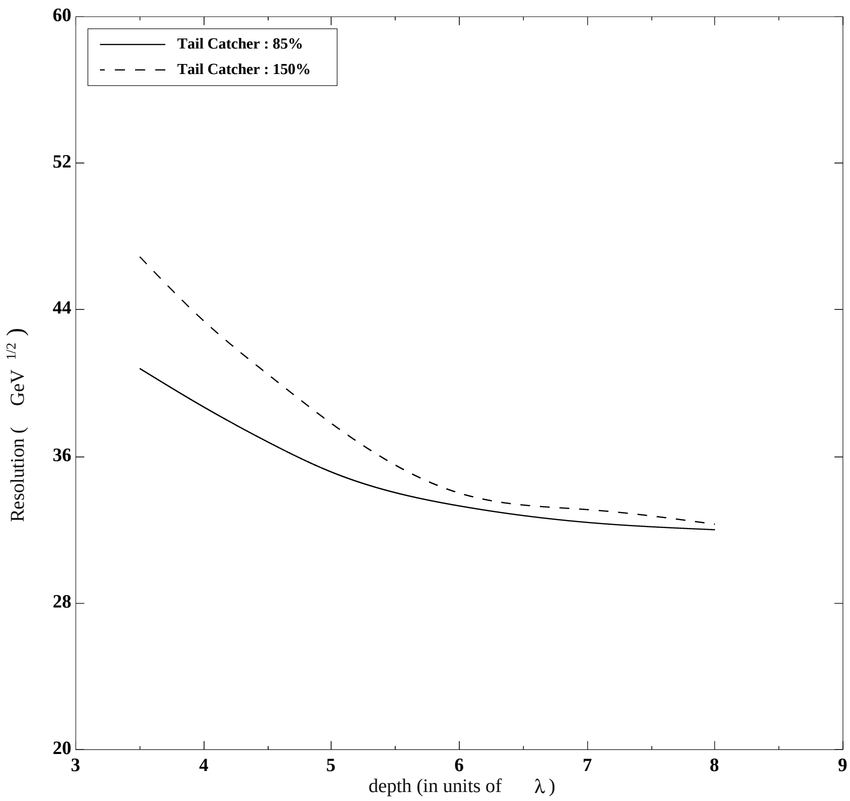

Figure 2.2.10: *Dependence of the intrinsic energy resolution* $(\sigma/E)\sqrt{E}$ *as a function of the depth (in units of interaction length) of the calorimeter inside the coil volume for two different tail-catcher resolutions.*

calorimeter and the energy deposit was merely smeared. To study the variation of the calorimeter performance, $e^+e^- \to W^+W^-$ events were generated with PYTHIA at 800 GeV center-of-mass energy and the energy of the particles in W jets was deposited in the calorimeter using different depths, materials, structures and resolutions. For the study, a single-particle resolution of $\sigma/E = 0.145/\sqrt{E}$ was assumed for the electromagnetic calorimeter for photons and electrons, and a hadronic resolution of $\sigma/E = 0.445/\sqrt{E}$ for the combined electromagnetic and hadronic sections. For the coil calorimeter section, a resolution of $\sigma/E = 1.5/\sqrt{E}$ was postulated. Two cases have been studied for the tail catcher: one with resolution $\sigma/E = 0.85/\sqrt{E}$ and the other with $\sigma/E = 1.5/\sqrt{E}$. Under these conditions, the resolution of the total energy of the particles in W jets was calculated for various depths of the calorimeter, the total depth being kept constant ($10\,\lambda$) for the sake of simplicity.

The jet-energy intrinsic resolutions $(\sigma/E)\sqrt{E}$ are shown in Fig. 2.2.10. Two important qualitative features are to be noted for a depth of the calorimeter inside the coil of greater than $5.4\,\lambda$. First, the energy resolution varies little as the depth increases; second, an improvement of the resolution of the tail catcher does not improve significantly the overall resolution of the calorimeter. It follows from these simulations that the depth of $5.4\,\lambda$ proposed in this report is sufficient from an energy resolution standpoint. More details about these simulations can be found in Ref. [69].

GEANT simulation. The second more detailed approach [70], relies on a complete GEANT simulation of the electromagnetic and hadronic shower development in a calorimeter similar to that discussed above. Results are obtained for the energy resolution for electrons (3 to 100 GeV), positive pions (3 to 100 GeV) and W jets generated by PYTHIA. The energy range covered by the W jets is 10 to 200 GeV. The particles and jets are assumed to hit the calorimeter at normal incidence and the dead material in front of the calorimeter consists of the beam pipe and the TPC. In what follows, results are presented for a $5.4\,\lambda$ deep calorimeter, including the electromagnetic section. Electromagnetic showers are completely absorbed in the nearly $27\,X_0$ deep lead-scintillator calorimeter section.

Pions deposit little energy in the electromagnetic section on average, since the latter is only $1\,\lambda$ deep. The energy resolution is determined by the structure and the depth of the hadronic section of the calorimeter. For a full containment of the shower, the coil calorimeter layer and the tail catcher are necessary. Figure 2.2.11 shows the calorimeter response to 30 GeV single pions for two cases: one in which only the calorimeter is taken into account and one in which all sections are included (i.e. calorimeter, coil calorimeter and tail catcher). Without the coil calorimeter and tail catcher, the measured pion energy is on average 28.7 GeV, with an RMS of 4.8 GeV, the distribution showing a long tail at lower energies. In contrast, the inclusion of the tail catcher and the coil layer increases the mean measured energy to 29.5 GeV and reduces the RMS down to 3.7 GeV, corresponding to a relative resolution of about 13 %. Energy fluctuations larger than 10 GeV are observed only at the 0.1 % level, fluctuations larger than 15 GeV are negligible. Such a calorimeter would allow good measurement of, and efficient triggering on, missing energy.

The electromagnetic energy resolution is shown in Fig. 2.2.12. An energy resolution of

$$\frac{\sigma}{E} = \frac{0.103}{\sqrt{E}} + 0.006$$

is possible in the absence of cracks between the towers and of noise. The relative energy

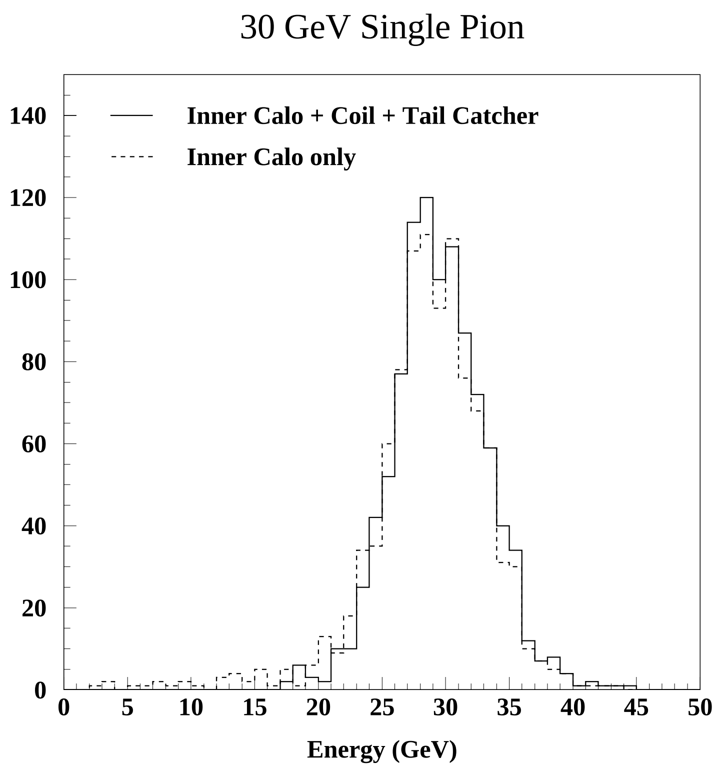

Figure 2.2.11: *Comparison of the energy deposit of* 30 GeV *pions in the calorimeter with (dashed lined) and without (solid line) the tail catcher.*

resolution for single pions can be parameterized by

$$\frac{\sigma}{E} = \frac{0.405}{\sqrt{E}} + 0.042$$

The resolution and particularly the constant term can be improved with appropriate software energy weighting which compensates for the difference in electromagnetic and hadronic response. The energy resolution for jets is given in Fig. 2.2.12 and can be parameterized by

$$\frac{\sigma}{E} = \frac{0.566}{\sqrt{E}} + 0.006$$

Fig. 2.2.13 shows the measured energy distribution of 1000 jets, all of them having an energy of 100 GeV. The average reconstructed jet energy is 99.5 GeV, with an RMS of 7.1 GeV. Seven events have a missing energy in excess of 20 GeV, three events have a missing energy greater than 30 GeV and only one event has a missing energy above 40 GeV.

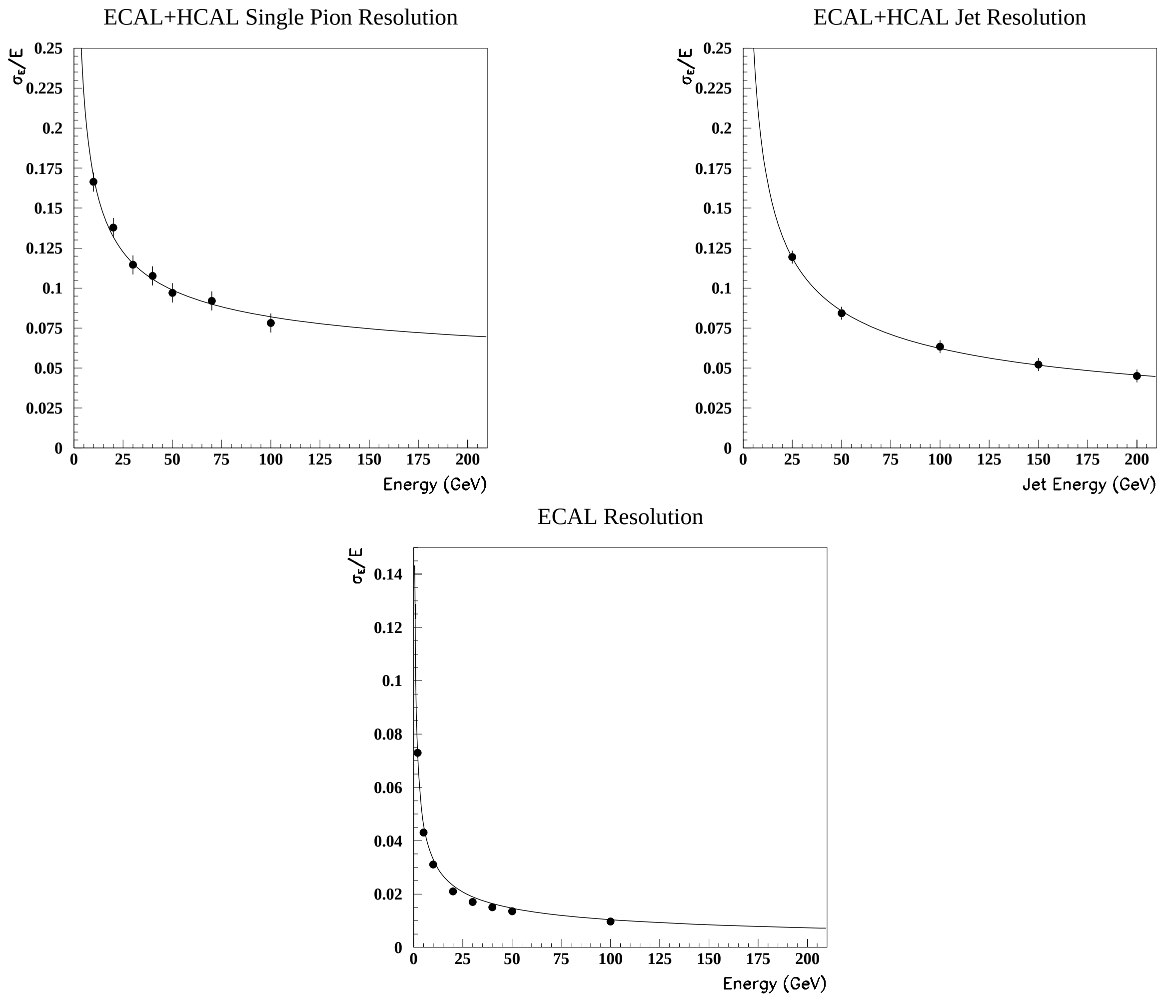

Figure 2.2.12: *Single-pion energy resolution (top left), jet energy resolution(top right) and electromagnetic energy resolution (bottom).*

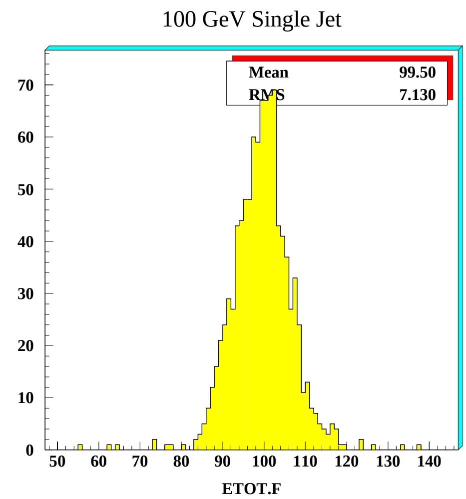

Figure 2.2.13: *Calorimeter jet energy distribution for* 100 GeV *incident jets.*

Other aspects of the performance.

Energy weighting. Energy weighting has not been applied in any of the approaches discussed above. However, this technique has proven successful in improving the energy resolution of existing calorimeters. The method was first used in the CDHS experiment [80]. The H1 collaboration at HERA applies such "software compensation" in their fine-grained Pb/LAr (electromagnetic) and Fe/LAr (hadronic) calorimeter. Results from early beam tests are described in [76, 77]. The sampling energy resolution reached is $11\,\%$ $(50\,\%)$ $/\sqrt{E}$ for electrons (pions) with a constant term of $\leq 0.6\,\%$ $(2\,\%)$ for electromagnetic (hadronic) showers. The jet-energy resolution is $44\,\%/\sqrt{E}$ and can be improved for jets having a large electromagnetic fraction [63]. The improvement which can be gained by applying such weighting methods for the proposed structure will be studied by Monte Carlo simulation in the near future.

Energy flow. The main aim of an energy flow reconstruction algorithm is to provide the energy and the directions of hadronic jets. Two approaches to date have been (*i*) a purely calorimetric method, as generally used in pp or ep colliders, and (*ii*) a method that exploits all subdetectors and particle identification capabilities, as used for example by ALEPH[81].

The present LC detector has been designed assuming method (*ii*) will be used. The charged particle momenta are measured by the tracking to determine the energy and directions of all charged particles. Low-to-medium energy jets have usually a large enough spatial spread to give rise to well-separated calorimeter clusters originating from the particles in the jets. The calorimetric energy deposited by identified muons and electrons can be isolated due to the fine transverse granularity of the calorimeters. Photons in jets can often be identified via their characteristic transverse shower profile. Similarly for isolated neutral hadrons (i.e., ones not linked to the extrapolation of a charged particle track): the fine transverse granularity of the calorimeter and the high magnetic field allow neutral hadrons to be identified if their clusters are separated. For isolated particles, the energy measurements from the tracking and the calorimeters can be combined for an improved measurement. Finally, the four-momenta of all particles thus detected are used in jet-clustering algorithms.

The total energy-momentum conservation in e^+e^- collisions can be used to constrain the jet energies, and for this the jet directions play a major rôle since they are usually measured better than the jet energies. Due to the magnetic field, the charged particles that reach the calorimeter deposit their energies at angles quite different from the original particle directions. This degrades the jet angular resolution for the purely calorimetric method (*i*), while method (*ii*) corrects for this effect. In ALEPH typical values for the jet angular resolution are 35 mrad for method (*i*) and 18 mrad for method (*ii*). For the LC detector, the measurement using method (*i*) will be dominated by the spreading by the magnetic field, while method (*ii*) should be much improved with respect to ALEPH.

Method (*ii*) has been shown [81] to give better results than method (*i*) for measuring jet directions because it includes the curling low momentum charged particles that do not reach the calorimeters and the muons which cannot be measured calorimetrically; these are two important losses in the calorimetric method (*i*).

Further simulations with the present set-up are needed to optimize the energy flow algorithm and measurement, especially in light of the superior performance of the calorimeters and the higher jet energies at the LC compared to LEP1. For example, careful studies of the calorimeter must be done to minimize the loss of resolution due to neutral particles having clusters that overlap with other clusters in the calorimeter and due to the broadening of the calorimeter showers in the magnetic field. Then, in the barrel region, the tracker dominates the energy measurement, while in the endcap below polar angles of about 0.4 rad the tracker resolution gets worse and the calorimeter dominates, and studies will help understand and improve the energy flow measurement in this transition region. Other points to optimize are the tower size, cracks between towers, longitudinal segmentation and software compensation, the coil calorimeter and tail-catcher sections, the particle identification via dE/dx and kink recognition in the tracking, the transition region between barrel and end-cap in trackers and calorimeters, the transition region between main tracker and forward tracker, to mention a few.

Clearly how to handle the jet-jet resolution problem is one of the lessons being learned right now at LEP2 and is more difficult than most people imagined. Thus is a reason for the emphasis on better energy-flow tools for the LC detector.

Angular resolution. The proposed cell sizes at the entrance to the towers are $2.8 \times 2.8\,\mathrm{cm}$ ($5.6 \times 5.6\,\mathrm{cm}$) for the electromagnetic (hadronic) calorimeter, as described earlier. From simulation studies and measurements with similar cell sizes a resolution in $\sigma_{r\phi}$ of $\sim 4\,\mathrm{mm}/\sqrt{E} + 1\,\mathrm{mm}$ can be expected [82], leading, for energies $\geq 10\,\mathrm{GeV}$ to an angular resolution of $\sim$ 0.9 (0.6) mrad at 90° (170°). Presampling with 1 mm fibers improves the resolution to $\sim 50\,\mu\mathrm{m}$ [75].

The angular resolution for hadronic jets is dominated by the large cluster width of the individual showers. However, combining tracks and clusters, as described in the previous section, can improve the jet angular resolution. Again, more Monte Carlo studies are needed to quantify the improvement.

e/π separation. For the reconstruction of certain final states, it is vital to have the best possible pion and electron identification. For this purpose, information about the spatial shower development, both laterally and longitudinally, must be used, and this in turn requires a very fine cell granularity to allow for a good measurement of the first and second moments of the shower shape.

The H1 liquid-argon calorimeter has a sampling structure very similar to that proposed here and gives a rejection power for 30 GeV pions of 2 to $5{\cdot}10^3$ with 95 % of the electrons being correctly identified [83]. Further improvement of the electron identification by a factor of 2 to 4 can be achieved with the 1 to 2 X_0 thick presampler [75]. A similar factor can be gained using the dE/dx information from the TPC [43].

2.2.5.5 Calibration and Monitoring

The absolute energy measurement and resolution achievable with the calorimeter are strongly dependent on the absolute precision of the energy calibration and the stability of the relative gain monitoring. Approximately 300,000 cells must be

- calibrated,
- adjusted in response relative to each other, and
- the e/π-response measured as a function of the angle of incident particles.

Whereas rough energy calibration values are sufficient for online performance, monitoring and trigger thresholds, precise calibration constants for the electromagnetic (hadronic) calorimeter have to be determined to an accuracy of better than 0.6 % (2 %). The calibration measurement has to be performed before installation and must be monitored closely during operation.

In addition to extensive measurements at a high-energy test beam, it is proposed to use a cosmic-muon test facility for the calibration of the assembled rings before installation. The energy deposit of a minimum-ionizing particle is approximately

40 MeV/cm(10MeV/cm) in the electromagnetic (hadronic) sections and has to be corrected for the incidence angle of the muon track traversing the cell. The determination of the e/h ratio should be done with medium-energy pion beams (up to 30 GeV), but the required precision in the knowledge of the calibration constants implies using a tail catcher calorimeter in order to tag and correct the energy leakage. The measurement of the electromagnetic response in the 3-cell deep hadronic sections requires electrons of an energy of about 6 GeV with an impact angle of 20 to 30°. The effect of the magnetic field would have to be studied using Monte Carlo simulations. These measurements and studies should permit the determination of the calibration constants including the crack effects with the required precision.

During operation of the experiment, minimum-ionizing cosmic and halo muons are always present. Using special triggers they could be recorded for continuous calibration and gain-stability monitoring.

The online electromagnetic calibration is more difficult to carry out, the rate of hard-scattered electrons being very low. Low energy neutral pions, could be used via their decay into two photons. Very good calibration conditions could be obtained from a dedicated run at the Z pole, from which at least $2{\cdot}10^6$ Z events are expected. Other possibilities for calibration include using radiative-return events and track-cluster comparisons. The latter approach would work well only in the case of well-separated clusters, and this within the limits imposed by the steeply falling transverse momentum distribution.

Gain variations resulting from temperature, power supply or amplifier drifts, aging or radiation damage of the optical components of the calorimeter, as well as rate or pedestal effects can be monitored by an external pulsed LED or laser calibration system. The stability of the light sources has to be monitored with a precision better than 1 %. The light can enter the detector via a few flexible and radiation-hard quartz fibers which have an attenuation length of several meters. The comparison of the response of each cell with the calibration light source signal would permit the monitoring of the gain.

2.2.5.6 Construction, Assembly and Installation

The electromagnetic and hadronic cells are combined into supertowers. These supertowers are assembled as one unit, with individual tiles of absorber and scintillator whose sizes increase with depth. The 2 cm scintillator tiles are tailored to the tower dimensions. (As an alternative, the lateral resolution envisaged is achieved with tiles having the dimensions of the whole supertower cross section but with a shorter – a few cm – attenuation length). The individual scintillator cells are mirror-coated before assembly. During assembly, the position of the scintillator and absorber tiles can be fixed by insertion of stiff steel fibers in 1 mm diameter pre-drilled holes for the WLS readout. The fiber density needed is approximately 0.5–1 fiber/cm^2. Prototype tests have to be carried out to optimize the resolution. The WLS fibers collect light from the corresponding calorimeter cell. The fibers are mirror-coated and blackened where they traverse the neighboring cells (Fig. 2.2.9.)

The assembled supertowers are machined and polished to 0.1 mm tolerance and wrapped in reflector foils to ensure light tightness. This way, inhomogeneities in the structure and cracks can be kept very small.

The front and back absorber plates of a supertower carry the photodetectors and the readout electronics for the electromagnetic and hadronic towers. The supertower is held together by a 0.2 mm stainless steel band (see Fig. 2.2.9) which also allows handling, transportation and installation. The supertowers are inserted into 6 m diameter cylinders made of stainless steel which can be rotated during assembly. In the endcap calorimeters, the installation of the supertowers is much easier and can be made in 1/4 or 1/2 disks. This is helpful, since the weight of these supertowers is larger than that of the barrel supertowers. After installation of the supertowers, the signal boxes can be installed and tested.

2.2.5.7 Future Studies

Further research and development must be undertaken to answer questions which have not yet been addressed. These include

- the improvement of the energy resolution of the electromagnetic section by an optimized choice of sampling and/or crystals,
- the investigation of software weighting to achieve good compensation,
- the optimization of the calorimeter cell sizes with respect to compensation,
- the study of readout performance and lateral resolution of scintillator layers with reduced light attenuation length,
- the optimization of WLS readout fiber density (between 0.2 and 2 fibers per cm^2),
- GEANT Monte Carlo simulations to optimize the cell granularity for very high energy jets (up to 1 TeV) in the forward region of the endcap calorimeter,
- further development of photodetectors,
- study of calibration monitoring.

2.2.6 Instrumented Iron

The iron return yoke, as shown in Fig. 2.2.14(a), is instrumented to supplement calorimetric measurement of hadronic energy flow and to allow the detection and identification of penetrating muons over the polar angle range $4^\circ < \theta < 176^\circ$ and the entire azimuth. As the return yoke is preceded by the electromagnetic and hadronic calorimeters and the superconducting coil, a total of about six interaction lengths of material, the hadronic energy deposited in the tail catcher is not large. Calorimetric measurements with accuracy $\Delta E/E \sim 0.85/\sqrt{E}$ (E in GeV) are thus adequate. They may be used in two ways:

- to improve the energy flow measurements in all events in which there is hadronic energy;
- to identify a sample of events in which no energy leaked through the hadronic calorimeter, allowing the most accurate possible measurement of hadronic energy.

The identification of high momentum muons allows the study of much interesting physics. It is thus important that the instrumented iron provide highly efficient muon identification for muons with a momentum greater than about 5 GeV. In general, the determination of the charge and momentum of these muons may be done accurately in the vertex and inner tracking detectors and in the TPC; no independent measurement is necessary within the iron. Hence, while the accuracy of measurements in the iron must be sufficient to allow unambiguous association of penetrating muons with tracks in the central tracking system, it does not need to reach the precision necessary for momentum measurements. An accuracy of the order of 1 cm in two coordinate directions is adequate. Higher accuracy instrumentation of parts of the end-cap regions is foreseen to facilitate the determination of muon charge and momentum using accurate tracking through the end-cap iron. This includes accurate measurement at the inner face of the end-caps in order to use optimally the available lever arm for muon charge and momentum determination before the muons enter the iron. Toroidal spectrometers surrounding the beam pipe outside the iron end-caps permit the study of muons at the extremes of the polar angular range.

A further requirement is that the muon system provide a trigger signal. This has two uses, firstly to indicate the presence of a muon with high momentum during the physics operation of the detector and secondly to provide a cosmic ray trigger to facilitate calibration and testing. As aspects of the instrumentation of the barrel and end-cap sections of the yoke are different, they are considered separately in the following.

2.2.6.1 Barrel

The barrel section of the iron return yoke is dodecagonal in shape, that is, it has twelve-fold symmetry. The total thickness of the iron is 180 cm. Experience at the LEP [43, 84, 85] and HERA detectors [86] and at the SLD [87] has shown that the required energy resolution can be obtained in a calorimeter with iron as passive material if sampling is done about every 5 cm (the interaction length of iron, $\lambda_{\rm Fe}$, is 16.8 cm). However, it is not necessary to make calorimetric measurements throughout the entire yoke, which presents about $11\lambda_{\rm Fe}$ to particles at normal incidence. For muon identification purposes, adequate reconstruction of the path of a penetrating muon can be performed if the position of the muon is determined every $\lambda_{\rm Fe}$. The yoke is therefore constructed from 20 layers of 5 cm thick iron, followed by 5 layers of 15 cm thick iron and a final layer of thickness 5 cm.

The measurement of the hadronic energy deposited in the iron and the tracking of muons is done using resistive plate chambers (RPCs) [88]. These are inserted in 3 cm wide slits between the iron layers. In addition, two layers of RPCs are inserted between the cryostat housing the coil and the iron, providing calorimetric readout and a space point on muon tracks. The following twenty slits each contain one layer of chambers. These allow for calorimetric readout and the determination of, alternately, the ϕ and z coordinates of muon tracks. The iron layer following the twentieth slit is the first which is 15 cm thick. This is followed by a slit of width 3 cm which houses a chamber instrumented to provide ϕ and z coordinates on muon tracks. This pattern is repeated four more times until the final 5 cm thick iron layer is reached. The last layer ensures that the outermost chamber is adequately shielded from any low energy background in the surrounds of the experiment. The above configuration, illustrated in Fig. 2.2.14, leads to a total thickness of the iron structure of 2.55 m.

The proposed RPC design is as illustrated in Fig. 2.2.14(b). Each chamber consists of two layers of bakelite between which there is a 2 mm gas gap. The outer surfaces of the bakelite are painted with a conducting graphite layer and the inner surfaces are treated with linseed oil. Adjacent to the graphite layers are printed circuit boards on the external faces of which are the readout strips or pads. These give coordinate and calorimetric information, respectively. The readout strips are of width 2.75 cm and pitch 3 cm and the pads are of dimensions varying from about $30 \times 30\,\mathrm{cm}^2$ to $60 \times 60\,\mathrm{cm}^2$. Smaller pads with digital readout have been successfully used by the E771 Collaboration [89]. Chambers required to measure space points on muon tracks are equipped with two sets of orthogonal strips, those required to provide calorimetric information and one coordinate have one pad and one strip layer. Contact with the strips is made at the edges of the chamber, that with the pads via cables running over the surface of the printed circuit boards. A PVC foil covers the outer faces of the pads and strips. Improved mechanical stability is achieved by mounting the chambers in an aluminum foam sandwich, with aluminum supports at the chamber edges. Connections

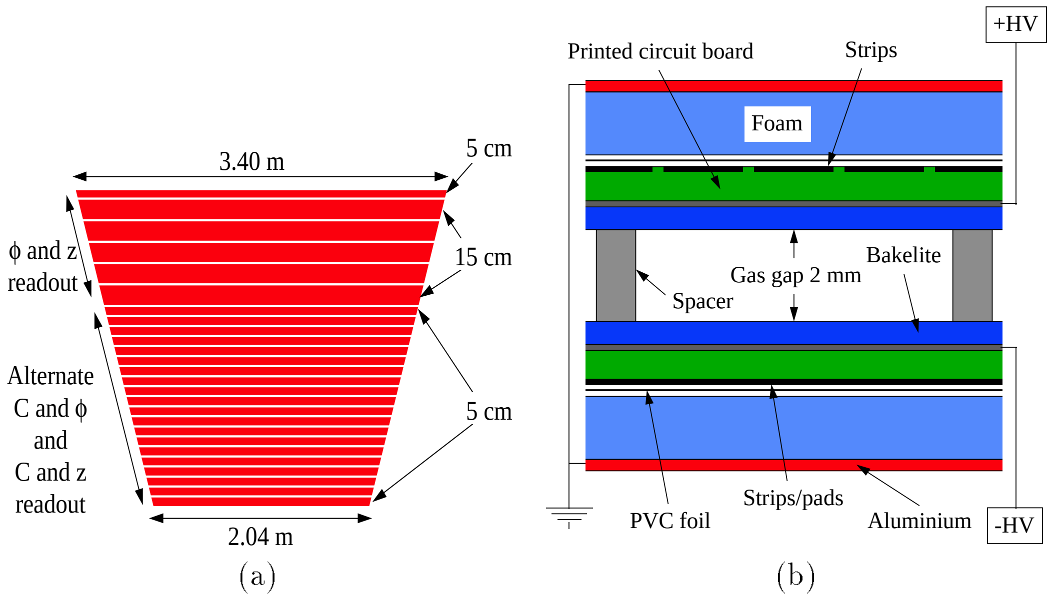

Figure 2.2.14: *(a) Cross section through one of the twelve symmetrical segments of the barrel of the iron return yoke showing the slits into which the resistive plate chambers are inserted; these are instrumented with calorimetric (C), ϕ and z readout as indicated. (b) Cross section through a resistive plate chamber.*

to the gas and high voltage supplies are made at these edges. The total thickness of the chambers is 2.2 cm.

Research is underway as to the desirability of using materials such as phenolic-melanine instead of bakelite, of increasing the size of the gas gap to about 6 mm [90], or of using a multi-gap structure [91]. The iron slits are wide enough to accommodate such chambers. In addition, tests of the performance of analogue pad readout of RPCs must be made.

The sizes and locations of the chambers are chosen to ensure that no dead solid angle is generated due to the inevitable loss of chamber efficiency around the spacers. The pad sizes and locations are similarly chosen to provide a projective tower structure matching the towers in the electromagnetic and hadronic calorimeters.

2.2.6.2 Endcaps

The instrumentation proposed for the end-caps of the iron yoke is similar to that described for the barrel, with the exception that at two depths within the end-caps the standard RPCs are replaced with chambers allowing more accurate position measurement, perhaps RPCs with finer strip pitch and incorporating ADC readout. These help determination of muon charge and momentum. Studies are still underway of the necessary chamber resolutions and best locations,which depend on the details of the magnetic field configuration in the end-caps. Further information on the charge and momentum of muons in the end-cap region is obtained using the end-cap muon tracker. This consists of two orthogonal sets of five planes of hexagonal straw tubes, similar to those described in [39] and used in the inner tracker of the LC detector. The end-cap muon tracker chambers are of width 1 cm and maximum length 3 m. High voltage and gas distribution is done at the outer end of the tubes. Readout is via TDCs at each end of the tube using electronics similar to that of the inner tracker. This allows determination of the coordinates of a muon track with an accuracy of about 100 μm in the drift direction and about 1 cm along the wire. A study is being performed of the levels of background these chambers will experience and the consequences this has for their operation. Furthermore, the possibility of using inductive strip readout to extract more accurately the position of a hit along the wire is under investigation [92].

2.2.6.3 Toroidal Spectrometers

These spectrometers each consist of a toroidal magnet sandwiched between layers of straw tube chambers. The iron magnets, similar to those used in the H1 detector [93], have inner radius 0.4 m, outer radius 3.0 m and a depth of 1.5 m. Current carrying coils are wound around the iron, producing a magnetic field of a strength of about 2 T. The hexagonal straw tubes described above are used here also, three sets of five planes of tubes, with wires at 0° and $\pm 60^\circ$ to the vertical, being placed before and after the magnets. This system allows the determination of the charge of muons with momenta of up to about 250 GeV in the polar angle region given by $2^\circ < \theta < 14^\circ$.

2.2.6.4 Readout and Trigger

The RPC strips are read out digitally, the pads using analogue electronics. The total number of strips is about 200 000. The pad signals are summed to give a measure of the energy deposited in the inner 10 and outer 11 layers of each tower, resulting in a total number of about 7 000 channels.

A trigger signal is formed using the strip readout. Two trigger modes are foreseen. In the first the trigger logic searches for hit patterns corresponding to the signals expected from high momentum muons coming from close to the interaction point. In the second, designed for test and calibration purposes, much less stringent directional criteria are required in the trigger.

The chambers described above have a time resolution of about 1 ns. In addition to the benefits this provides when used as a trigger, either for electron-positron annihilation or cosmic ray studies, this enables rejection of halo muons using the differences between their time of arrival and those of muons from electron-positron interactions.

2.2.7 Luminosity Calorimeter

Two separate aspects of the luminosity measurement at the linear collider are (a) the luminosity spectrum measured using the forward tracking (see Section 2.3) and (b) the integrated luminosity measured using the detector described in this section. A precise measurement of the integrated luminosity will be required for the determination of the top mass from the $t\bar{t}$ cross section at threshold, as well as for the measurement of the W boson couplings from the W^+W^- cross section. The experience of the LEP luminosity monitors (luminometers) show that Bhabha scattering $e^+e^- \to e^+e^-(n\gamma)$ at very low angles should be considered as the reference process for the following reasons:

- it is a QED process and consequently the cross section can be simulated with great accuracy;
- it provides a large sample of events which can be tagged with high efficiency and purity within a well defined geometrical acceptance.

As at LEP, a calorimetric selection of the events is the best choice in order to accept radiative Bhabhas and to be less sensitive to the upstream material. Two modules (forward and backward) of the electromagnetic calorimeter can be placed inside the tungsten mask in the angular range between about 30 (30) and 55 (85) mrad around the TESLA (SBLC) beam line. The exact placement will depend on the final layout of the mask.

The small angle luminometers at LEP have measured the integrated luminosity to better than 0.1 % by establishing a well defined angular acceptance which could be simulated in very precise theoretical Monte Carlo calculations of the Bhabha cross section, including radiative corrections. There are two possible obstacles to doing a similar job for the linear collider:

i) The flood of radiation from the intersection point. It is estimated that the equivalent of 10^4 photons of 1 MeV will enter the mask at every beam crossing. Exactly where they fall, and their fluctuations, will affect the precision of measurements of the high energy showers from Bhabha scattering. The soft x-rays from the showers they produce in the inner mask may penetrate some distance into the calorimeter, distorting shower profiles.

ii) The tight geometrical constraints which may limit the containment of showers and the readout of the detector.

A radiation-hard technology exists which should enable a suitable calorimeter to be built. Considerable R&D has already been done with a view to developing a precision tracker for the LHC [94]. The calorimeter would have alternate planes of lead and of glass capillaries filled with liquid scintillator, read out via clear glass fibers to APDs

[95] or HPDs [96]. Successive planes of capillaries would be rotated by 60° to give good position resolution. The systematic precision on the inner cut-off angle for the Bhabha sample should be controllable to better than 50 microns - background radiation allowing - which would permit the integrated luminosity to be measured with comparable accuracy to that achieved at LEP. The longitudinal segmentation of the readout would allow careful systematic checks to be made of the shower reconstruction.

As well as giving the integrated luminosity, the small angle calorimeter will serve as a tagger for gamma-gamma events. It will also have an important role in completing the electromagnetic hermeticity of the whole detector down to very small angles - assuming that the tungsten mask can itself be instrumented.

2.2.8 Infrastructure

2.2.8.1 Hall layout

The underground experimental hall must accommodate the detector and allow convenient installation and maintenance procedures for the whole lifetime of the experiment and for all foreseeable circumstances.

The experimental hall of rectangular cross section is divided by the beamline into a short and a long section. The long section of the hall will allow a complete detector installation or in a later phase upgrade of the detector with the installation area shielded by movable concrete blocks against radiation from accelerator operation. Commissioning of the linac is therefore completely independent of the detector status. The short section of the hall is designed to house one of the muon filter-shells with the detector in the interaction region and in the open position to access the inside areas of the barrel toroid.

The detector size and the various modes of operation (detector-assembly, detector-test in a parking position, detector-data taking in the interaction region) lead to the following approximate hall dimensions: width 30 m, length 82 m, beam height 9 m above floor, crane-hook 20 m above floor.

2.2.8.2 Detector assembly and Maintenance access to detector systems in the beam position

The detector consists of three independent parts moving on rails; a central part mounted around the beam pipe and two symmetric half shells which can be moved independently perpendicular to the beam line. The steel rails are installed in the floor of the hall and extend over the full length of the installation area and interaction region. The modular concept allows a simultaneous assembly of the various detector systems during the installation phase and a fast and easy access to detector components while the detector is in the interaction region. Two cranes are foreseen for the installation of heavy pieces.

The detector electronics is located in a 3 stories electronic trailer coupled to the detector and moving on the rail system. Figure 2.2.15 shows a cross section through the detector arrangement perpendicular to the beam.

The linac section between tunnel entrances and the detector – rolled into the beam position and closed for data taking – are shielded with movable concrete blocks. The detector is designed to be self-shielding. A layer of about 1 m concrete is mounted on the outer detector-shell to stop slow neutrons. Figure 2.2.16 is an isometric view of the closed detector with one detector quadrant cut out and part of the shielding removed to show the structure of the detector arrangement in the interaction region.

The detector design allows the outer shell of the detector to be split in two and moved apart leaving the central part in the beam position with the detector beam pipe permanently connected to the machine vacuum.

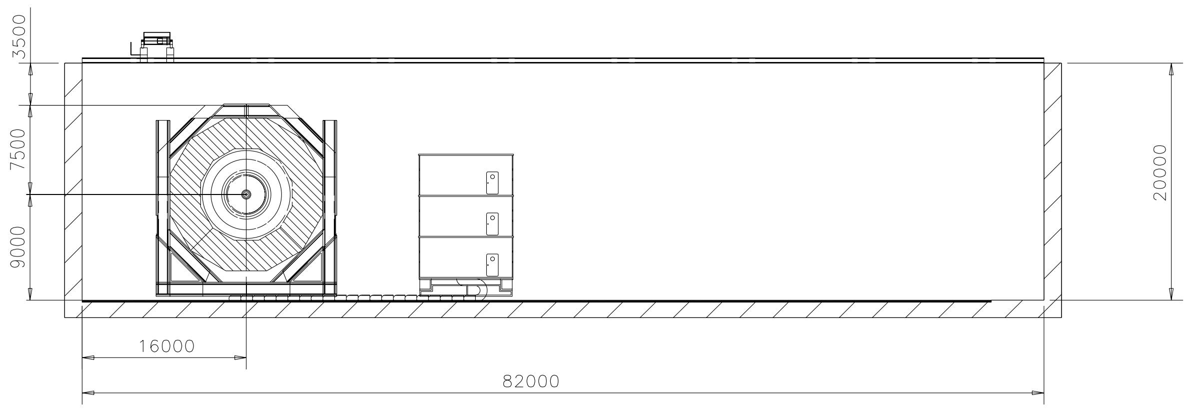

Figure 2.2.15: *Cross section through the detector arrangement perpendicular to the beam.*

To access the inner detector elements the calorimeter end cap discs are movable along the beam direction to storage positions on specially provided support frames. Figure 2.2.17 shows the detector with the calorimeter discs opened, Fig. 2.2.18 shows the detector arrangement during installation or maintenance work with the beam region shielded by concrete blocks.

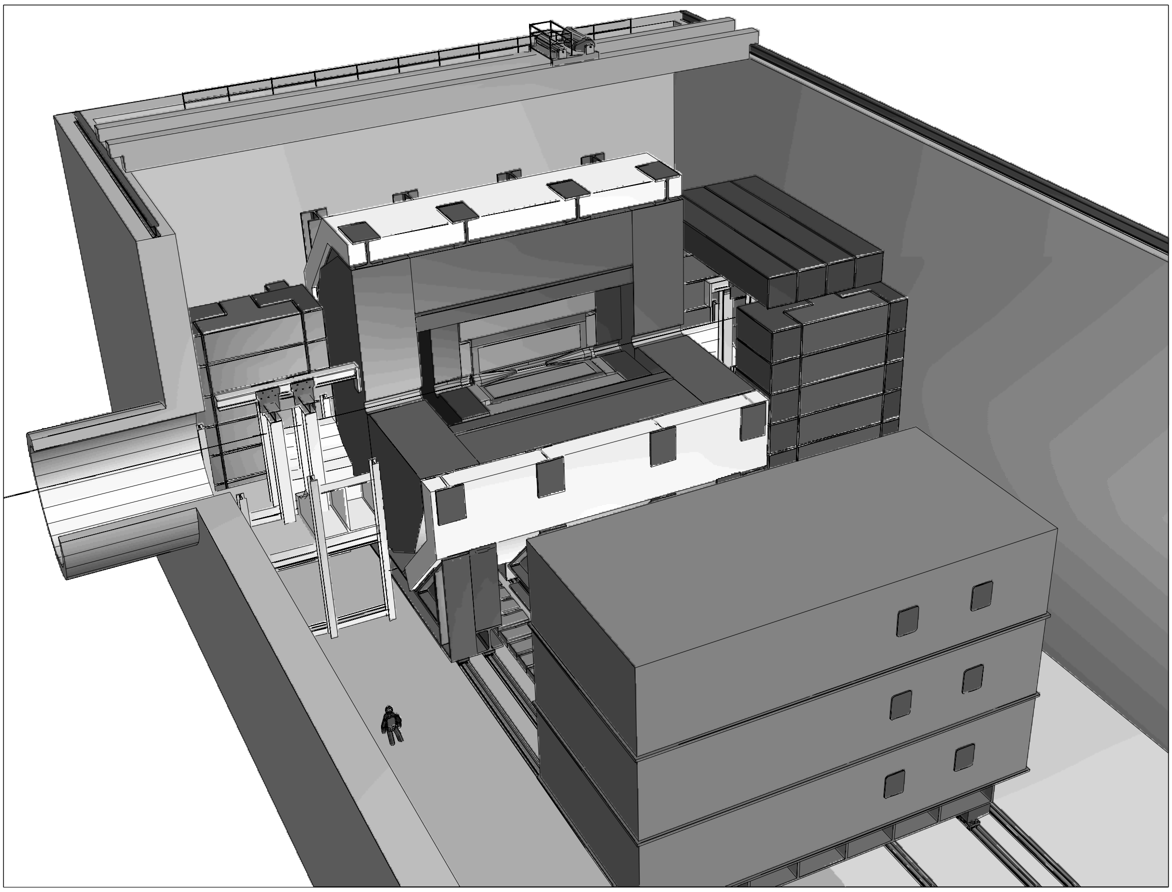

Figure 2.2.16: *Isometric view of the closed detector with one detector quadrant cut out and part of the shielding removed. For clarity the toroids are not shown.*

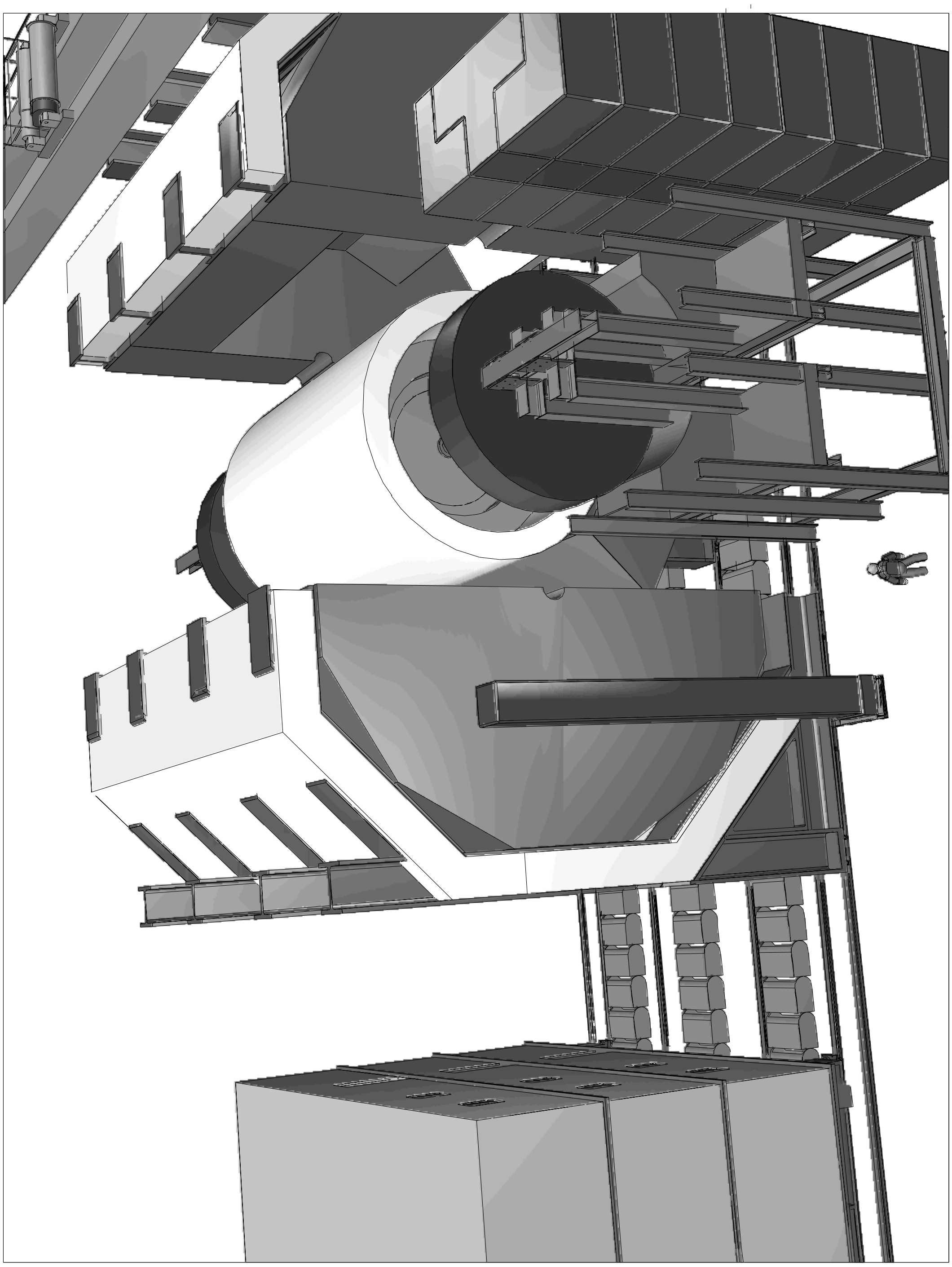

Figure 2.2.17: *Detector with the calorimeter discs opened.*

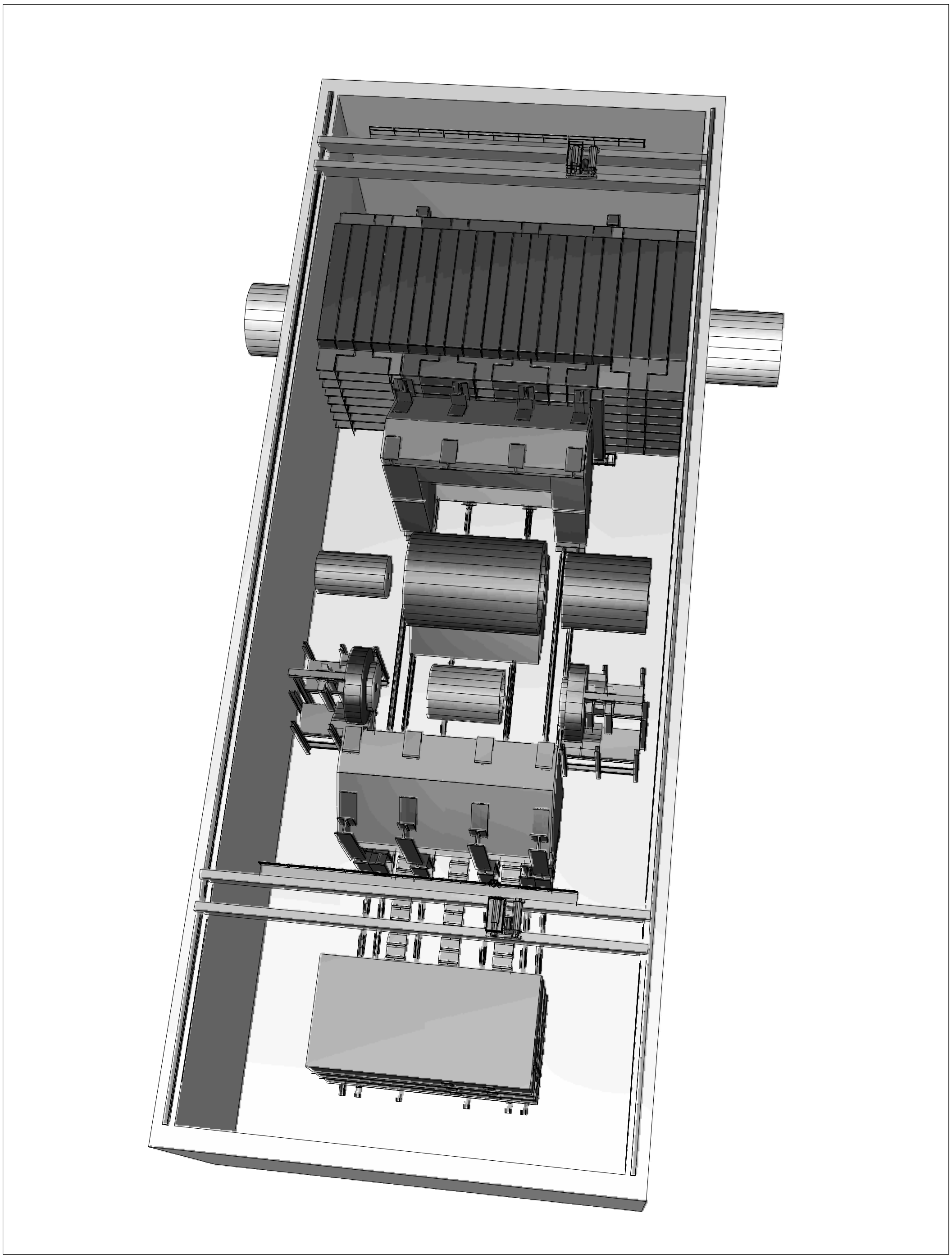

Figure 2.2.18: *Detector arrangement during installation with the beam region shielded by concrete blocks.*

Bibliography

[1] A.S. Schwarz, "Heavy Flavour Physics at Colliders with Silicon Strip Vertex Detectors", Phys. Rep. 238 (1994) 1-133.

[2] M. Adamovich et al., "WA92: a fixed target experiment to trigger on and identify beauty particle decays ", CERN/PPE 96-066.

[3] G. Bellini et al., "A microstrip vertex detector to identify heavy flavour decays", Nucl. Instrum. and Meth. A305 (1992) 395.

[4] C. Troncon, "Measurement of spatial resolution and charge collection in double sided double metal Silicon microstrip detectors", Nucl. Phys. Proc. Suppl. 44 (1995) 287-291.

[5] J. Straver et al., "1-micron spatial resolution with Silicon strip detectors", CERN/PPE 94-026.

[6] R. Turchetta, "Spatial resolution of Silicon microstrip detectors", Nucl. Instrum. and Meth. A335 (1993) 44-58.

[7] E.H.M. Heijne, P. Jarron, "Development of Silicon pixel detectors: an introduction", Nucl. Instrum. and Meth. A275 (1989) 467-471.

[8] G.D. Hallewell, "Development of active pixel vertex detectors for high luminosity particle physics applications", Nucl. Instrum. and Meth. A348 (1994) 388-398.

[9] G. Wilson, contribution to Ref. [97].

[10] M.N. Frary and D.J. Miller, in: *e^+e^--Collisions at 500 GeV: The Physics Potential, Parts A and B*, Workshops at Munich, Annecy, Hamburg, 1991, ed. P.M. Zerwas, DESY 92-123A&B (1992), p.379.

[11] C.J.S. Damerell and D.J. Jackson, "Vertex detector technology and jet flavour identification at the future e^+e^- collider", Proc. 1996 Snowmass Workshop, "New Perspectives in High Energy Physics", to be published.

[12] Proceedings of the *III International Workshop on Semiconductor Pixel Detectors for Particles and X-rays*, March 24-27 1996, Bari, Italy, to be published on Nucl. Instrum. and Meth.

[13] C.J.S. Damerell, "CCD vertex detectors in particle physics", Nucl. Instrum. and Meth. A342 (1994) 78-82.

[14] The SLD collaboration, "VXD3: the SLD vertex detector upgrade based on a 307 Mpixel CCD system", SLAC-PUB 95-6950.

[15] M. Caccia et al., "Progress in the construction of the DELPHI pixel detector", DELPHI 96-56 MVX 14, to be published on Nucl. Instrum. and. Meth.

[16] F. Antinori et al., "Experience with a 30 cm^2 Silicon Pixel plane in the CERN experiment WA97", Nucl. Instrum. and Meth. A360 (1995) 91-97.

[17] The CMS collaboration, "Technical Proposal", CERN/LHCC 94-38.

[18] The ATLAS collaboration, "Technical Proposal", CERN/LHCC 94-43.

[19] C.J.S. Damerell, "Vertex Detectors at linear collider (Present and Future)", RAL-94-096.

[20] CERN RD19 collaboration (E.H.M. Heijne et al.), "LHC 1: a semiconductor pixel detector readout chip with internal, tunable delay providing a binary pattern of selected events", CERN/ECP 96-03.

[21] CERN RD19 collaboration (E.H.M. Heijne et al), "First operation of a 72k element hybrid Silicon micropattern pixel detector array", Nucl. Instrum. and Meth. A349 (1994) 138-155.

[22] G. Kramer et al., "Development of pixel detectors for SSC vertex tracking", SLAC-PUB 91-5518.

[23] M. Pindo, "Correlated noise in pixel detectors with analogue readout", Nucl. Instrum. and Meth. A378 (1996) 443-450.

[24] J.B.A. England et al., "Capacitive charge division readout with a Silicon strip detector", Nucl. Instrum. and Meth. 185 (1981) 43.

[25] U. Kotz et al., "Silicon strip detectors with capacitive charge division", Nucl. Instrum. and Meth. A235 (1985) 481.

[26] V. Chabaud et al., "The DELPHI silicon strip microvertex detector with double sided readout", Nucl. Instrum. and Meth. A368 (1996) 314-332.

[27] D. Schulte, private communication.

[28] A. Rudge, "Comparison of charge collection in semiconductor detectors and timing resolution using sub-ns transimpedance amplifier", Nucl. Instrum. and Meth. A360 (1995) 169.

[29] M. Menichelli et al., "Fast pre-amplifier for TOF silicon strip detectors operating in the temperature range from 20°C to −55°C", Nucl. Instrum. and Meth. A360 (1995) 177.

[30] S. A. Kleinfelder et al., IEEE Trans. Nucl. Sci. 35 (1989) 171.

[31] R. Horisberger and D. Pitzl, "A novel readout chip for silicon strip detectors with analog pipeline and digitally controlled analog signal processing", Nucl. Instrum. and Meth. A326 (1993) 92.

[32] F. Benotto et al., "The LPS trigger system", DESY 96-045, March 1996.

[33] H. Henschel et al., "A silicon backward tracking detector and trigger for the H1 experiment at the ep collider HERA", IEEE Trans. Nucl. Sci. 40 (1993) 692.

[34] B. Foster et al., "Second level trigger for the SDC silicon tracker detector", Nucl. Instrum. and Meth. A360 (1995) 325.

[35] R. Dzelyadin et al., "RD21: test of a silicon dta driven trigger processor", Nucl. Instrum. and Meth. A351 (1994) 228.

[36] C.J.S. Damerell and D.J. Jackson, SLAC-PUB-7215 (1996), to be published in Nucl. Instrum. and Meth.

[37] C.J.S. Damerell and D.J. Jackson, contribution to Ref. [97].

[38] R. Nahnhauer and M. Pohl, contribution to Ref. [97].

[39] J. F. Schottmüller, "Driftzeitmessung mit einer Wabenkammer", PITHA 94/41, unpublished Diplomarbeit (in German), III. Physikalischen Institut, Aachen University, Germany, October 1994.

[40] B. King, contribution to Ref. [97].

[41] C. Vander Velde, W. Vandoninck and F. Udo, contribution to Ref. [97].

[42] D.R. Nygren, "The time-projection chamber – a new 4π detector for charged particles", PEP Note 144, in 1974 PEP Summer Study, (PEP 137).

[43] ALEPH Collab., D. Decamp et al., Nucl. Instrum. and Methods A294 (1990) 121; ALEPH Collab., D. Buskulic et al., Nucl. Instrum. and Methods A360 (1995) 481.

[44] The ALEPH Handbook 1995, Vol.1, ed. Chris Bowdery, ISBN 92-9083-072-7, CERN(1995).

[45] A. Miyamoto, in: *Workshop on Physics and Experiments with Linear e^+e^- Colliders, Vols.I and II*, Waikoloa, Hawaii, 1993, eds. F.A. Harris, S.L. Olsen, S. Pakvasa and X. Tata, World Scientific, Singapore, 1993, p.141.

[46] H. Wieman et al., RD-32 Status Report, CERN/DRDC 94-10.

[47] J. Bartke et al., RD-32 Final Report, CERN/DRDC 96-16.

[48] A. Oed, Nucl. Instrum. and Methods A263 (1988) 351;
A. Oed, Nucl. Instrum. and Methods A367 (1995) 34;
W.G. Gong, et al., Nucl. Intrum. and Methods A374 (1996) 144.

[49] P. Colas, contribution to Ref. [97];
Y. Giomataris, Ph. Rebourgeard, J.P. Robert and G. Charpak, Nucl. Instrum. and Meth. A376 (1996) 29.

[50] R. Bouclier et al., "The Gas Electron Multiplier (GEM)", CERN PPE 96-177.

[51] V. Eckart, private communication.

[52] D. Schulte, Ph.D. Thesis, U. Hamburg (1996).

[53] W. Wiedenmann, private communication.

[54] F. Richard, private communication.

[55] R. Settles, private communication.

[56] "Design Study for a 4 TeV $\mu^+\mu^-$ Collider",
http://www.cap.bnl.gov/~cap/mumu/book.html.

[57] F. Bartol, et al., J. Phys. III 6 (1996) 337.

[58] A. Sopczak, contribution to Ref. [97].

[59] A. Sopczak, in: *Workshop on Physics and Experiments with Linear e^+e^- Colliders, Vols.I and II*, Waikoloa, Hawaii, 1993, eds. F.A. Harris, S.L. Olsen, S. Pakvasa and X. Tata, World Scientific, Singapore, 1993, p.666;
A. Sopczak, Zeitschr. f. Phys. C65 (1995) 449.

[60] A. Bernstein et al., Nucl. Instrum. and Meth.A336 (1993) 23.

[61] E. Bernardi et al., Nucl. Instrum. and Meth.A262 (1987) 229.

[62] H1 Collaboration, Nucl. Instrum. and Meth.A386 (1997) 310;
H1 Collaboration, Nucl. Instrum. and Meth.A386 (1997) 348 and references therein.

[63] W. Braunschweig et al., Nucl. Instrum. and Meth.A265 (1988) 419;
H. Greif, Ph.D. Thesis, MPI-PAE/Exp El.229.

[64] I. Abt et al., Nucl. Phys.B396 (1993) 3.

[65] Calorimetry in HEP, BNL 1994, 177 and references therein.

[66] CERN internal note CMS TN/96-305

[67] IEE NS43 (1996) 1496.

[68] H1 Collaboration, DESY PRC-94/02, 108-117.

[69] S. Aïd, V. Korbel, contribution to Ref. [97].

[70] P. Checchia, C. Luci, M. Mazzucato, F. Simonetto, contribution to Ref. [97].

[71] OPAL Collaboration, Nucl. Instrum. and Meth.A305 (1991) 275;
CERN PPE/95-194.

[72] "CMS Technical Proposal", CERN LHCC/94-38, CMS TN/95-077, CMS TN/95-135.

[73] Calorimetry in HEP, BNL 1994, 470 and references therein.

[74] DESY H1-10/91-197, internal note; and DESY H1-2/94-344, internal note.

[75] R. Nahnhauer et al., contribution Ref. [97].

[76] H1 Calorimeter Group, Nucl. Instrum. and Meth.A350 (1994) 57.

[77] B. Andrieu et al., Nucl. Instrum. and Meth.A336 (1993) 499.

[78] R.K. Bock et al. Nucl. Instrum. and Meth.186 (1981) 533.

[79] V. Korbel, contribution to Ref. [97].

[80] H.Abramowicz et al., Nucl. Instrum. and Meth.A180 (1981) 429.

[81] ALEPH Collaboration, Nucl. Instrum. and Meth.A360 (1995) 481.

[82] T.Nicholls et al., Nucl. Instrum. and Meth.A374 (1996) 149.

[83] B.Andrieu et al., Nucl. Instrum. and Meth.A344 (1994) 492.

[84] "Performance of the DELPHI Detector", P. Abreu et al. (DELPHI Collaboration), CERN-PPE/95-194.

[85] K. Ahmet et al. (OPAL Collaboration), Nucl. Instrum. and Meth. A305 (1991) 275.

[86] "The H1 Detector at HERA", I. Abt et al. (H1 Collaboration), DESY H1-96-01.

[87] A.C. Benvenuti et al., Nucl. Instrum. and Meth. A290 (1990) 353.

[88] R. Santonico and R. Cardorelli, Nucl. Instrum. and Meth. A187 (1981) 377;
R. Santonico and R. Cardorelli, Nucl. Instrum. and Meth. A263 (1988) 20.

[89] G. Cataldi et al. (E771 Collaboration), Nucl. Instrum. and Meth. A337 (1994) 350.

[90] I. Crotty et al. Nucl. Instrum. and Meth. A360 (1995) 512;
A. Ceron Zeballos et al. Nucl. Instrum. and Meth. A373 (1996) 35.

[91] C. Bacci et al. Nucl. Instrum. and Meth. A352 (1995) 350;
E. Cerron Zeballos et al. Nucl. Instrum. and Meth. A374 (1996) 132.

[92] Stan Majewski et al., Nucl. Instrum. and Meth. A348 (1994) 307.

[93] "The H1 Forward Muon Spectrometer", I.R. Kenyon et al., DESY 93-020 (1993).

[94] S. V. Golovkin et al., "Radiation damage studies on new liquid scintillators and liquid-core scintillating fibers", Nucl. Instrum. and Meth. A362 (1995) 283.

[95] E. Lorenz et al., "Fast readout of plastic and liquid scintillators by avalanche photodiodes", Nucl. Instrum. and Meth. A344 (1994) 64.

[96] R. De Salvo et al., "First results on the hybrid photodiode tube", Nucl. Instrum. and Meth. A315 (1992) 375.

[97] "ECFA/DESY Study of Physics and Detector for a Linear Collider", http://www.desy.de/conferences/ecfa-desy-lc96.html, proceedings to be published as DESY 97-123E.

2.3 Detector Performance

In order to assess the physics capabilities of the detector described earlier in this document, a few reference reactions have been analyzed in detail:

- $e^+e^- \rightarrow t\bar{t}$ at threshold
- $e^+e^- \rightarrow H^0Z^0$ at $\sqrt{s} = 360, 500\,\mathrm{GeV}$
- $e^+e^- \rightarrow HA$ at $\sqrt{s} = 800\,\mathrm{GeV}$
- $e^+e^- \rightarrow WW \rightarrow \ell\nu q\bar{q}$ at $\sqrt{s} = 500\,\mathrm{GeV}$,
- $e^+e^- \rightarrow \tilde{\chi}_1^+\tilde{\chi}_1^-$ at $\sqrt{s} = 500\,\mathrm{GeV}$
- $e^+e^- \rightarrow \tilde{\mu}_R\tilde{\mu}_R$ at $\sqrt{s} = 800\,\mathrm{GeV}$

The rationale for choosing the reactions listed above can be summarized as follows:

- The study of top production at threshold tests the ability of the detector to cope with multijet events and to reconstruct the invariant masses needed to identify top events; furthermore, the beamstrahlung associated with the beam-beam interaction at the IP, has to be evaluated and shown not to spoil the expected mass resolution for the top quark mass measurement.
- Higgs production and branching ratio measurements are connected with b-tagging and tracking performances of the experimental set-up.
- Again H and A bosons detection requires good b detection together with jets energy and direction determination in order to form jet-jet invariant masses.
- WW production allows to determine the optimal angular coverage of the detector as the W-pair angular distribution peaks in the very forward region.
- Sleptons and/or charginos detection tests the di-jet mass resolution, the capability of the detector in the measurement of missing energy, and lepton identification.

In addition to these processes, the measurement of the luminosity and of the center of mass energy has been also studied since their precise knowledge is crucial for the other measurements. In the following the performance of the detector subsystems is analyzed in some detail: the relevant processes were simulated with generators, which are thought reasonably accurate as of now; detector smearing was obtained with SIMDET code [1]. This software package returns momenta and energies of isolated particles; charged prongs and/or neutral entering the calorimeters with relative distances smaller than the proposed granularity are combined into *energy clusters*. The isolation cut is hence set by the cell geometry of the proposed calorimeters. Particle clusters undergo separate smearing for the e.m. and hadronic components of the energy. Smeared energies are then combined into *total cluster energy.* Minimum energy/momentum cuts are set at 200 MeV/c (p_t tracking) and 100/300 MeV for the e.m./hadronic calorimeters. Misidentifications π/μ and π/e were implemented at the usual level. Complete GEANT simulation was used if the details of the detector response were believed important (e.g. heavy flavor tagging). The detail of the analyses and the results are discussed in the following paragraphs.

2.3.1 Precision Measurement of Luminosity and $\sqrt{s}$

2.3.1.1 Motivation

To realize the full physics potential of the linear collider, for example in accurate measurements of the W boson and top quark masses, it will be necessary to develop precise techniques for measuring the integrated luminosity, the center of mass energy and the luminosity spectrum as a function of $\sqrt{s}$. External spectrometers (see section 2.4.6.2) for the outgoing beam can be used to measure the energies of the un-interacted beams, but they can not measure the true spectrum at interaction. Beamstrahlung spreads the luminosity over a range of energies and shifts the peak value of $\sqrt{s}$ at interaction away from precisely $2E_{\mathrm{beam}}$. These effects can only be monitored reliably by analyzing samples of calibration events taken from the same datasets as the events used for physics studies.

2.3.1.2 Absolute Energy Measurement

The most useful quantity available for calibrating the energy is the mass of the Z-boson [2]; measured at LEP with a precision of a few MeV. The cross section for $\mathrm{e^+e^-} \to \mathrm{Z}\gamma$ is comparable with the WW cross section and significantly larger than that for $\mathrm{t\bar{t}}$. The most precise determination of energy will come from kinematic fits to events with $\mathrm{Z} \to \mu^+\mu^-$ and with the radiated photon lost along the beam direction. There is an inescapable error from the width of the Z boson:

$$\frac{\Delta(\sqrt{s})}{\sqrt{s}} = \frac{5 \cdot 10^{-4} \times (\sqrt{s}/161)}{\sqrt{f_{\mathrm{acc}}\mathcal{L}(\mathrm{fb}^{-1})}} \tag{2.3.1}$$

where f_{acc} is the fractional acceptance of the detector for $\mathrm{Z} \to \mu^+\mu^-$. With the outer cone of the forward shielding mask at 83 mrad, $f_{\mathrm{acc}} \simeq 1$ for $\sqrt{s} \leq 500$ GeV and drops to 0 for $\sqrt{s} \simeq 2$ TeV. This gives $\Delta(\sqrt{s})/\sqrt{s} = 1.6 \cdot 10^{-4}$ for 10 fb^{-1} at $\sqrt{s} = 161$ GeV. For each event the contribution to the error from the angular resolution on the muon tracks must be kept below a half of the contribution from the width of the Z, requiring an angular resolution of 3 mrad on muons at $\theta \simeq 60°$ for $\sqrt{s} = 161$ GeV, or 200 μrad at

$\theta \simeq 190\,\mathrm{mrad}$ for $\sqrt{s} = 1\,\mathrm{TeV}$. These measurement errors can easily be achieved with the detector described in this chapter, using the intermediate silicon layer and TPC for large angle muons or the forward silicon tracker for muons close to the shielding mask.

2.3.1.3 Integrated Luminosity Measurement

Because of the large flux of soft electrons and gamma rays coming from the interaction point it is not clear that the small-angle luminosity monitors (see section 2.2.7), inside the shielding mask, will be able to perform as well as the equivalent detectors in the LEP experiments which are now achieving systematic errors of much less than 1 per mille. This is one of the R&D projects which needs to be pursued as the design develops. Such a small angle monitor is needed for a number of physics reasons, especially for tagging gamma-gamma scattering events and to give the best possible hermeticity for high energy electrons and gamma rays. But away from the Z boson peak it may also be possible to normalize on larger angle Bhabha scatters. The number of events with e^+e^- going outside the mask is much higher than any physics channel, so statistics will not be a significant limitation on the precision of measuring the integrated luminosity. Studies at CLEO [3], however, have shown that the systematic errors on the theoretical cross sections limit the precision available at the present time to a little less than 1 %. But the same was true for the Bhabha cross sections at small angles when LEP1 first began using them for luminosity measurement and significant improvements have since been made which have almost matched the improvements in experimental errors. Theorists [4] who have worked on the LEP luminosity have no doubt that similar improvements can be made to the cross section calculations for larger angles. This will require a substantial effort from the theory community.

2.3.1.4 Measuring the Luminosity Spectrum

The spread of $\sqrt{s}$ due to beamstrahlung, initial state radiation and the momentum spread in the linacs can be directly related [5] to the distribution of the acollinearity of the e^+ and e^- in Bhabha scattering events outside the shielding cone. Recent studies at KEK [6] have confirmed that the effects of realistic beamstrahlung distributions can indeed be resolved in this way. In order to achieve the precision needed for measuring the top quark mass to better than 200 MeV in the scan over the $t\bar{t}$ threshold (see section 2.3.2.2) it will be necessary to measure the angle θ of the e^+ and e^- tracks to better than $250\,\mu\mathrm{rad}$ for $\theta \simeq 180\,\mathrm{mrad}$ or to better than 1 mrad for $300 < \theta < 800\,\mathrm{mrad}$; similar requirements to those mentioned above in the discussion of energy measurement (section 2.3.1.2). They should be easily achieved in this detector, as long as the amount of material in front of the precision detectors is kept to a small fraction of a radiation length so that electrons do not shower before their tracks can be measured. Good electron identification will be needed in the endcaps.

2.3.2 Top Physics

One of the main physics topics for the next generation colliders (both e^+e^- and hadronic) will be the production and properties of the top quark. An e^+e^- collider is particularly suited to study in detail top quark physics thanks to the extreme cleanliness of the leptonic environment. Top quarks will be copiously pair-produced at such a machine and, since they are heavier than the intermediate vector bosons, (maybe even heavier than the Higgs boson), their properties will be different from the ones of the lighter quarks; as a matter of fact they might shed some light on the mechanism of mass generation and provide valuable information for the understanding of flavor symmetries. The dominant top production channel goes through the e^+e^- annihilation to a virtual photon or Z, which subsequently decays to a $t\bar{t}$ pair. The $t\bar{t}$ production cross section is about 650 fb at $\sqrt{s} = 500\,\mathrm{GeV}$. At the foreseen luminosities of 10^{33} to $10^{34}\,\mathrm{cm}^{-2}\mathrm{s}^{-1}$ (or 10 to $100\,\mathrm{fb}^{-1}$ per year) the sample will allow quite detailed studies of this fermionic species. In the Minimal Standard Model (MSM) the top decays 100 % to a bottom quark and a W. Depending on the decays of the two W's present in the event, the $t\bar{t}$ event will consist of six jets (44 %); four jets, a high-momentum lepton and a neutrino (44 %); or two jets, two high-momentum leptons and two neutrinos (11 %). In all decays at least two b-flavored jets will be present. The total top quark width is given approximately by $\Gamma_t \sim 0.18\,\mathrm{GeV}(m_t/M_W)^3$: about 1.4 GeV for $m_t = 175\,\mathrm{GeV}$.

2.3.2.1 Detector Requirements for Top Physics

In $t\bar{t}$ physics the six jet final state is the hardest to reconstruct. Simulations were performed where the energy, momentum and angular resolutions of the detectable particles were varied. The granularity of a hadron calorimeter was also varied in the simulation. The resolution functions were parametrized as a sum of two Gaussian distributions in order to simulate deviations from simple Gaussian resolutions ($1\,\sigma + 5\,\sigma$). Previous studies [7, 8] have shown that of the currently available jet finding algorithms LUCLUS, which was used here, performs best. The performance of a hadron calorimeter was found to be of greatest importance, but a significant contribution to the resolutions of the reconstructed properties of the top quarks and the jets was found to be due to the jet finding algorithm.

2.3.2.2 Threshold Scan Studies

The large decay rate of the top quark carries as a consequence that toponia bound states do not form: this is the very first case in which *E*-*W*interactions lead to a decay rate faster than the strong ones. The top width Γ_t acts as an effective cut-off energy for non-perturbative QCD effects. This facilitates the theoretical predictions, in particular, near the $t\bar{t}$ production threshold. An energy scan around the $t\bar{t}$ threshold will yield a very precise measurement of the top quark mass. Three observables can be used:

- The total production cross section $\sigma_{\mathrm{t\bar{t}}}(s)$ which is particularly sensitive to m_{t}. This observable, however, is also quite sensitive to the strength of the $\mathrm{t\bar{t}}$ binding potential.
- The top momentum distribution $d\sigma/dp(s)$ which again can be linked to the top mass and $\alpha_s(m_{\mathrm{t}})$.
- The forward-backward asymmetry $A_{\mathrm{FB}}(s)$ which, due to the interference of S- and P-wave amplitudes, allows an independent although less sensitive evaluation of the top mass.

The cross section shape at threshold is distorted by initial state radiation effects (ISR) and energy smearing due to beamstrahlung (BS). The last effect is particularly important and leads to a smoother threshold behavior of the cross section. The results quoted in the following refer to beam energy spectra expected for the TESLA option: as one might anticipate both ISR and BS cause an effective loss of analyzing power toward the top mass measurement. The other two observables (momentum spectrum and forward backward asymmetry) are also affected although to a smaller extent. The threshold scan will only be effective for these studies if the spread of the beam momentum and the beamstrahlung are small and the detector is capable of making precise measurements of the luminosity spectrum, as has been discussed in the previous section. These three requirements are built into the machine and detector designs presented in this conceptual design report.

a) Event Selection

As mentioned before both the signal ($\mathrm{e^+e^-} \rightarrow \mathrm{t\bar{t}}$) and background ($\mathrm{e^+e^-} \rightarrow \mathrm{Z}\gamma$, $\mathrm{e^+e^-} \rightarrow$ ZZ, and $\mathrm{e^+e^-} \rightarrow \mathrm{W^+W^-}$) events were smeared according to the SIMDET algorithm. The smeared events were put through some selection and analysis as discussed below. For the $\mathrm{t\bar{t}}$ cross section measurement events with six jets or four jet plus a prompt lepton were selected; in the six jets case the following requirements had to be satisfied:

- Thrust smaller than 0.85.
- Charged multiplicity greater than 20 ($p_t > 500\,\mathrm{MeV}/c$).
- Total reconstructed energy greater than 65 % $E_{\mathrm{c.m.}}$.
- At least six jets.

All the events which did satisfy these cuts were required to be reconstructed as six jets with the JADE algorithm. At this stage they were selected as top candidates if two W's were found within a bound of 30 GeV w.r.t the nominal W mass, the reconstructed top mass was within 60 GeV of its nominal value and at least one of the assumed b-jets was tagged as such. These requirements selected a sample of $t\bar{t}$ events with $\approx 23\,\%$ efficiency and a background contamination of $\approx 10\,\%$. The four-jet plus lepton sample was selected requiring that the JADE jet-finding algorithm found 5 jets; one of those had to contain a lepton with momentum greater than 20 GeV/c. The total energy of the *leptonic* jet should not exceed the lepton energy by more than 10 %. Top candidates were furthermore required to have a reconstructed W mass within 20 GeV of the nominal value, a reconstructed top mass within 50 GeV of the nominal value and, again, at least one of the assumed b-jets tagged as such. The overall efficiency came out to be 18.5 % while the remaining background in this sample was below 3 %. Events with one leptonic decay of the W were selected in a different way to measure the top momentum spectrum and charge asymmetry: in these events one of the top quark charge is unambiguously tagged by the leptonic decay of the W, the *other* top is momentum analyzed. The following criteria were used in this case, the purpose of which was to reduce backgrounds as much as possible. Briefly, the following additional requirements were imposed: a reconstructed total energy between 200 and 350 GeV, charged multiplicity below 5 in the *leptonic* jet and a total multiplicity of charged track and energy clusters smaller than 35 in the event, a positive anti-tag the two W-forming jets as b and reconstructing the W mass with those to better than 10 GeV were imposed. After this, 9.4 % of all top events were kept and no background remained. Assuming an integrated luminosity of 5 fb^{-1} per energy point, the top momentum was reconstructed with a resolution which ranged from about 30 % for the lowest energies to 18 % for the highest. The peak position of the top momentum distribution could be estimated with a relative precision ranging from $\Delta(p_{\mathrm{peak}})/p_{\mathrm{peak}} \simeq 12\,\%$ to 4 % as the machine energy is increased. Figure 2.3.1 shows how, in spite of the fact that detector effects do change appreciably the shape of the momentum distribution, its peak position remains quite stable. The probability of charge mislabelling, relevant for A_{FB}, has been found to be at the few per cent level. Figure 2.3.1 shows the top invariant mass as reconstructed after this selection. Table 2.3.1 summarizes the efficiencies and backgrounds obtained. These figures show a marked improvement with respect to the ones quoted in previous studies [9]: both better hardware performance and more sophisticated analyses are responsible for the overall upgrade in physics results.

b) Overall Energy Scan Results

The total cross section, the most probable top momentum and the forward-backward asymmetry are the three variables whose variation with center of mass energy, close to threshold, is most sensitive to the top mass. The most probable top momentum is the

Cross section measurement

	Efficiency	Background
6-jet	23 %	7 fb
4-jet	18.5 %	1.4 fb
TOTAL	41.4 %	8.4 fb

Top momentum measurement

	Efficiency	Background
4-jet	9.4 %	nihil

Table 2.3.1: *Summary of the selection efficiencies and background cross sections as obtained for $E = E_{\mathrm{CM}} - 2m_{\mathrm{t}} = 0$ with the analyses explained in the text.*

parameter which exhibit a smaller dependence on beam effects and uncertainties in the $\mathrm{t\bar{t}}$ binding potential with respect to the total cross section. The three observables are used in a χ^2-fit assuming a nine-point scan around $\sqrt{s} = 350\,\mathrm{GeV}$ with an integrated luminosity of $5\,\mathrm{fb}^{-1}$ per point[2]. An additional measurement below threshold is foreseen ($5\,\mathrm{fb}^{-1}$) to directly evaluate backgrounds. The fit has two free parameters: the top quark mass and $\alpha_s(M_{\mathrm{Z}}^2)$, which appears in the QCD $\mathrm{t\bar{t}}$ potential. The results are shown in Fig. 2.3.2. The overall precision expected in the top quark mass and the strong coupling constant are:

$$\begin{aligned} \Delta m_{\mathrm{t}} &\leq 110\,\mathrm{MeV} \\ \Delta\alpha_s &\simeq 0.003 \end{aligned}$$

although their correlation is rather big. Most of the sensitivity comes from the total cross section measurement, (which alone leads to about $\Delta m_{\mathrm{t}} \simeq 140\,\mathrm{MeV}$ and $\Delta\alpha_s \simeq 0.0040$). Adding the constraint from the momentum distribution gives a significant improvement on the determination of m_{t} and helps to reduce the correlation with $\alpha_s(M_{\mathrm{Z}}^2)$. The forward-backward asymmetry retains a much smaller analyzing power. The same data can be exploited to determine the top quark width. The forward-backward asymmetry does have some analyzing power for the width through the interference of the S- and P-wave amplitudes. Again a χ^2 fit to the same observables can be performed: the overall precision in the top quark total width will be around 18 %, once m_{t} and α_s are determined.

[2]This scan strategy has not been optimized. As a matter of fact, the cross section has the largest sensitivity to the top mass and α_s just at the rising edge of the $1S$ *peak*, about 2 to 3 GeV below the kinematical threshold. By concentrating the scan in that region, the results might improve by a fair amount.

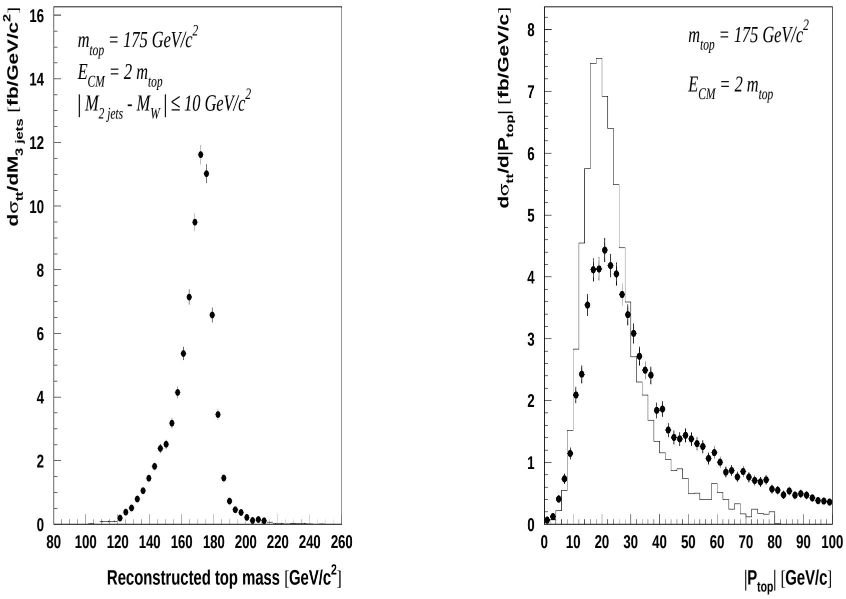

Figure 2.3.1: *The top invariant mass and the top momentum distribution as reconstructed with the 4-jet events selected for the momentum study. The solid line corresponds to the generated distribution.*

2.3.2.3 Other Measurements involving Top Quarks

Complete simulations involving other interesting measurements on top quarks physics, such as the study of top rare decays, the determination of the top form factors and its Yukawa coupling are in progress. Preliminary studies, however, carried out in previous workshops [10, 11, 12] indicate that the detector described in this chapter would cope with the demands that physics pose. There are also important possible effects of flavor violation in top quark processes (via the coupling $Z \rightarrow t\bar{c}$) which can be looked for very sensitively in the proposed detector, giving results which will complement those expected from the LHC [13]. To summarize this section, no limitation can be anticipated from the detector performance on the study of top quark physics. The results obtained show that, an e^+e^- collider running close to the top threshold can yield, with the proposed detector, a determination of the top mass better than 0.1 % and measure the strong coupling constant to better than 3 % accuracy.

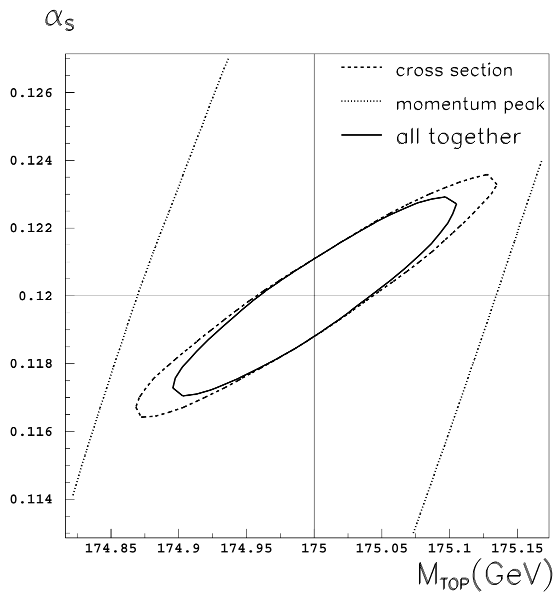

Figure 2.3.2: $1\,\sigma$ *contours in the top mass versus α_s plain which can be obtained with the measurement of the cross section and the top momentum distribution in a threshold scan.*

2.3.3 Higgs Physics

The discovery and study of Higgs bosons are among the primary goals for the very high energy program in particle physics. At an e^+e^- collider operating around half a TeV Higgs particles can be produced and studied in a completely unbiased way by means of the Z H associate production. This mechanism allows the absolute determination of the production cross section and, as a by product, the measurement of absolute branching ratios. Wherever a Higgs is first found, measurements of its decay branching ratios will be needed to confirm that it is indeed a Higgs particle and to identify which theory of electroweak symmetry breaking fits its properties. The measurement of the Higgs decay branching fractions to different fermionic species represents a crucial test of the Higgs sector in Standard Model (SM) [14]. A precise determination of the branching ratio for the decay $H \to b\bar{b}$ may allow to distinguish between the SM neutral Higgs boson H and its counterpart h^0 in the minimal supersymmetric SM extension (MSSM). Moreover, it has been suggested that the ratio of branching ratios $\frac{BR(H\to c\bar{c}+gg)}{BR(H\to b\bar{b})}$ may provide an evaluation of the CP-odd A boson mass, in the kinematical region not directly accessible in the first phase of operation of the e^+e^- linear collider [15].

In the following the results obtained for the search for a neutral Higgs boson, the determination of its production cross-section and of the branching ratios for its decays into hadronic final states are presented: simulations were run at two c.m. energies 360 GeV and 500 GeV. Z H events were generated with two different Higgs mass values of 120 GeV and 140 GeV. The signal $e^+e^- \to ZH$; $Z \to q\bar{q}$, $\ell^+\ell^-$, $\nu\bar{\nu}$ events and background (mainly Z Z) were generated using PYTHIA 5.702 and JETSET 7.405 tuned with the LEP data for the electroweak and QCD variables and with the CLEO and LEP data for the heavy flavor decays and including initial state radiation and beamstrahlung. The minimum luminosity necessary to obtain a statistical significance $S/\sqrt{B}$ greater than five on the Higgs signal at 360 GeV is compatible with what is required to carry out the top physics program. For the higher energy running, an integrated luminosity of 50 fb^{-1} is assumed in the error estimates for the branching ratios: this corresponds to about one year of running at the nominal luminosity.

The study of the Higgs boson production and decays requires good detector performances both in the energy/momentum determination and in the vertexing of charged tracks. Good resolution in the jet-jet invariant mass is needed, which in turn demands precise determination of the energy and the directions of the hadronic jets. Finally good momentum determination for high energy leptons from $Z \to \ell^+\ell^-$ is required in order to achieve good missing mass resolution. For adequate jet flavor tagging, stringent requirements for tracking and vertexing are to be met. From all of the above requirements it follows that precision study of the Higgs boson decays represent a hard challenge and set quite a number of benchmarks for the global performance of the detector.

The energies and momenta of generated particles which fall within the geometrical acceptance are smeared according to the expected detector resolutions. Tracking efficiency and impact parameter resolution are evaluated by using GEANT simulation of the silicon vertex tracker. Full pattern recognition, track refit, misassociation of vertex detector hits and background from the accelerator are included in the simulation in order to have a realistic assessment of tracking and vertex determination.

2.3.3.1 Higgs Observation and Determination of the $e^+e^- \to$ ZHCross Section

As it will be shown below, the Higgs signal at an e^+e^- machine can be observed already with a limited integrated luminosity provided that the Higgsstrahlung process holds ($\sqrt{s} \geq m_Z + m_H$). The cross section for this type of production can be determined with high accuracy without explicit assumptions on the Higgs decay modes. As already stressed before, this feature extends the sensitivity to non-standard types of Higgs bosons and reduces the experimental uncertainties in the determination of the Higgs decay branching ratios through the direct measurement of the Higgs production rate.

To measure the $e^+e^- \to ZH$ cross section σ_{ZH}, inclusive of all decay channels, the main technique consists in selecting events with two isolated fast charged particles consistent with $Z \to \ell^+\ell^-$ and then computing the mass recoiling against them. This

Reaction	Luminosity needed (fb^{-1})	
	Recoil Mass Technique	Invariant Mass Technique
$e^+e^- \rightarrow \ell^+\ell^- q\bar{q}$	10	10
$e^+e^- \rightarrow \nu\bar{\nu} q\bar{q}$	–	1
$e^+e^- \rightarrow \tau\bar{\tau} q\bar{q}$	80	80
$e^+e^- \rightarrow 2q2\bar{q}$	3	3
$e^+e^- \rightarrow 3q3\bar{q}$	50	50

Table 2.3.2: *Integrated luminosity required to observe an* H *signal with* $S/\sqrt{B} \sim 5$ *or better. The* H *mass is assumed to be* 140 GeV *and* $\sqrt{s} = 360$ GeV.

technique has already been used in previous analyses [17]. Here, the guidelines of these for the reconstruction method were used, while the selection criteria have been improved and further constraints were explicitly imposed, when appropriate, in order to achieve better experimental resolution [18]. For instance, a beam constraint fit on the particle tracks was performed in order to obtain the best possible momentum resolution and furthermore the resulting missing mass was reevaluated by forcing the candidate lepton pair to the Z mass.

Figure 2.3.3 shows the result for a Higgs boson mass of 140 GeV with $\sqrt{s} = 360$ GeV and an integrated luminosity of 50 pb^{-1}. The signal is clearly visible over the background which is dominated by $e^+e^- \rightarrow ZZ$ with $Z \rightarrow \ell^+\ell^-$. The irreducible background for the $H \rightarrow W^+W^-$ channel, for which no Monte Carlo event generator exists, has been estimated to be small and has been neglected. The cross-section σ_{ZH} is measured to a precision of $\sim 6\,\%$, for this Higgs boson mass where the $H \rightarrow b\bar{b}$ rate is roughly equal to the $H \rightarrow W^+W^-$ one. A similar analysis for a 120 GeV Higgs mass, where $H \rightarrow b\bar{b}$ dominates, gives a precision on σ_{ZH} of $\sim 5\,\%$.

To measure the branching ratios of the Higgs boson it is necessary to split up the cross section σ_{ZH} into its topological subchannels. In each channel a search is made for the Higgs boson peak above background, either in the directly measured invariant mass of the Higgs boson decay products or in the recoil mass distribution, calculated as for Fig. 2.3.3. Table 2.3.2 shows the result for a Higgs boson mass of 140 GeV in terms of the integrated luminosity required at $\sqrt{s} = 360$ GeV to observe the peak in each topology with a significance of $S/\sqrt{B} \sim 5$ or better. In the table for each listed 4-body final state, all diagrams at tree level have been considered. In particular, the $\tau^+\tau^-\, q\bar{q}$ final state involves also the $H \rightarrow \tau^+\tau^-$ contribution. For some of these final states, like for instance $\nu\bar{\nu}\, q\bar{q}$, other production mechanisms like the WW fusion, do

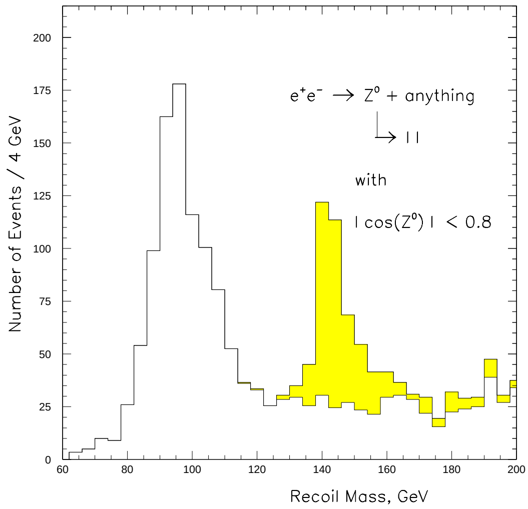

Figure 2.3.3: *The dilepton recoil mass distribution showing the signal of a* 140 GeV *Higgs boson produced together with the* Z *at* $\sqrt{s} = 360\,\mathrm{GeV}$ *for an integrated luminosity of* $50\,\mathrm{fb}^{-1}$.

play a relevant rôle and hence, the resulting luminosity does not follow the simple Z branching ratio expectation.

2.3.3.2 Measuring Higgs Hadronic Decay Branching Ratios

The accuracy with which a given Higgs decay branching fraction can be measured depends on the experimental capability of identifying the different fermionic species in the decay. Since the decay $\mathrm{H} \to \mathrm{b\bar{b}}$ is the dominant decay mode for Higgs masses up to about 130 GeV, an efficient b-tagging capability is a prerequisite of this analysis. Moreover, the large $\mathrm{b\bar{b}}$ yield requires also efficient anti-b tagging in order to reject b jets in the study of the Higgs boson decays into lighter quark or gluon pairs. For the measurement of the Higgs decay branching ratios, Higgs decays to hadronic final states are reconstructed using both four jet ($jjjj$), two jet and two lepton ($jj\ell\ell$), and two jet plus missing energy ($jj\nu\nu$) topologies in the process $\mathrm{e^+e^-} \to \mathrm{HZ}$. The details of the selection criteria applied can be found in [19]. After the jet clustering, the energies of the reconstructed jets are rescaled imposing energy and momentum conservation at $\sqrt{s}$. Then the jets are paired and a final cut is applied, imposing compatibility with the $\mathrm{e^+e^-} \to \mathrm{ZH}$ hypothesis using the reconstructed jet-jet masses. The selection efficiency for $\mathrm{e^+e^-} \to \mathrm{ZH}$, $\mathrm{Z} \to$ anything, $\mathrm{H} \to \mathrm{q\bar{q}}$ and gg are summarized in Tab. 2.3.3 for two values of the $\sqrt{s}$ energy and of the Higgs boson mass m_{H}. To measure the branching ratios $\mathrm{BR}(\mathrm{H} \to \mathrm{b\bar{b}})$ and $\mathrm{BR}(\mathrm{H} \to \mathrm{c\bar{c}} + \mathrm{gg})$, the quark content of the di-jet system originating from the Higgs decay needs to be tagged. Methods of quark flavour tagging at $\mathrm{e^+e^-}$ colliders have been developed and successfully applied at LEP and SLC to study the hadronic decays of the Z boson. At a high energy linear collider, these

$\sqrt{s}$ (GeV)	360	360	500	500
m_{H} (GeV)	120	140	120	140
H Z Efficiency	22 %	20 %	26 %	24 %

Table 2.3.3: *The efficiency obtained for the reconstruction of the* $\mathrm{e^+e^-} \to \mathrm{ZH}$*;* $\mathrm{Z} \to$ *anything,* $\mathrm{H} \to \mathrm{q\bar{q}}, \mathrm{gg}$.

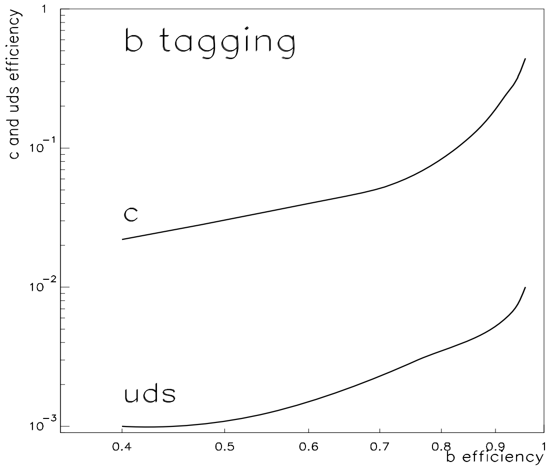

Figure 2.3.4: *The probability of classifying a* $\mathrm{c\bar{c}}$ *(upper curve) or a lighter* $\mathrm{q\bar{q}}$ *pair (lower curve) as* $\mathrm{b\bar{b}}$ *plotted as a function of the efficiency of tagging* $\mathrm{b\bar{b}}$ *pairs from Higgs decays.*

techniques can be further improved by exploiting the favourable kinematics and the performance of an optimized detector for tagging heavy quarks. In particular the large boost to the short-lived (b and/or c) hadrons and the extremely good tracking accuracy, which the silicon vertex tracker will provide, allows the use of inclusive algorithms for the identification of their decays. In the present analysis the impact parameters of both tracks and the invariant mass of the candidate decay products have been used to distinguish b's from non-b hadronic jets. Briefly, the impact parameter tagging tests the compatibility of the charged tracks in a jet to be originating from a common primary vertex, comparing their impact parameters with the estimated impact parameter error, which includes multiple scattering and the position and width of the luminous spot, which in a linear collider is extremely small and very well defined $\mathcal{O}(10\,\mu\mathrm{m})$. Due to the relatively long decay distances of beauty and charm hadrons, the probability distribution for this hypothesis exhibits a sharp peak at zero (b and c jets); u, d and s jets generate a flat spectrum between 0 and 1. In addition, b jets are characterised by the relatively high mass of the decaying b hadrons. An inclusive algorithm is used to select the candidate products of b and c decays in a jet and to estimate the invariant mass of the secondary particles jet by accounting for the invariant mass of the selected particles, their energy, the jet energy and the b quark fragmentation function. The various kinematic quantities computed for each jet are combined for the di-jet system representing the candidate H decay once that the jets are b- (or anti b)-tagged.

The performance of the $\mathrm{b\bar{b}}$ tagging algorithm is shown in Fig. 2.3.4 where the probability for a $\mathrm{c\bar{c}}$ and a light $\mathrm{q\bar{q}}$ pair to be tagged as $\mathrm{b\bar{b}}$ is plotted as a function of the efficiency for identifying a genuine $\mathrm{b\bar{b}}$ di-jet from the Higgs decay for different tagging criteria. The use of the jet mass algorithm provides an efficient mean of reducing the charm contamination in the b-tagged sample while retaining a significant efficiency for $\mathrm{H} \to \mathrm{c\bar{c}}$ decays with an anti-tag against b quarks. As a matter of fact, the reconstruction of the non-$\mathrm{b\bar{b}}$ decays of the Higgs is affected by a significantly larger background as compared to the $\mathrm{b\bar{b}}$ channel. Since the main interest of the study of these decays is the determination of the ratio $\frac{\mathrm{BR(H\to c\bar{c}+gg)}}{\mathrm{BR(H\to b\bar{b})}}$, events with an anti-tag against b quarks are used for the measurement of non-$\mathrm{b\bar{b}}$ hadronic Higgs decays without attempting to separate $\mathrm{c\bar{c}}$ from the other modes. The background contribution to each candidate sample is estimated from the simulated background events and from the misassignemet probability for genuine Higgs decays and subtracted. By combining the $jjjj$ and $jj\ell\ell$ with the $jj\nu\nu$ channels an experimental accuracy on the measurement of $\sigma_{\mathrm{ZH}}\mathrm{BR(H \to b\bar{b})}$ of better than 4.0 % can be obtained for a Higgs mass of 120 GeV at both 360 GeV and 500 GeV centre-of-mass energy. The ratio $\frac{\mathrm{BR(H\to c\bar{c}+gg)}}{\mathrm{BR(H\to b\bar{b})}}$ can be determined with an accuracy of 20 % for $m_{\mathrm{H}} = 120\,\mathrm{GeV}$, or about 50 % if $m_{\mathrm{H}} = 140\,\mathrm{GeV}$ (see Tab. 2.3.4). The above figures should be compared with the theoretical uncertainties on the same quantities, about 3 % for the $\mathrm{b\bar{b}}$ mode and 11 % for $\mathrm{c\bar{c}}$ plus gg, due to less than perfect knowledge of α_s and the quark masses.

The significance of these results in the study of the properties of a neutral Higgs boson is exemplified by defining the region of the m_{H}, $\tan\beta$ plane where the MSSM h^0 boson can be distinguished from the SM Higgs boson. It is assumed, in the following, $M_{\mathrm{SUSY}} = 1\,\mathrm{TeV}$, $m_{\mathrm{t}} = 180\,\mathrm{GeV}$ and maximal squark mixing. A comparison of the ratio $\frac{\mathrm{BR(H^0_{SM}\to b\bar{b})-BR(h^0_{MSSM}\to b\bar{b})}}{\mathrm{BR(H^0_{SM}\to b\bar{b})}}$ with the fractional error on the absolute branching ratio $\mathrm{BR(H \to b\bar{b})}$ measured from the total Higgsstrahlung cross section and the $\sigma \times \mathrm{BR}$

$m_{\rm H}$ (GeV)	120	140
$\Delta(\sigma_{\rm ZH}\,{\rm BR}({\rm H}\to {\rm bb}))$	3.8 %	6.2 %
$\Delta(\sigma_{\rm ZH}\,{\rm BR}({\rm H}\to {\rm c\bar{c}, gg}))$	19 %	47 %
$\Delta(\frac{{\rm BR}(H\to {\rm c\bar{c}, gg})}{{\rm BR}({\rm H}\to {\rm bb})})$	20 %	48 %

Table 2.3.4: *Relative accuracy Δ on the determination of the branching ratios for the Higgs hadronic decay modes. The experimental accuracy corresponds to an integrated luminosity of* $50\,{\rm fb}^{-1}$ *at either* $\sqrt{s} = 360\,{\rm GeV}$ *or* $500\,{\rm GeV}$.

for the bb channel allows a discrimination between the SM Higgs and the MSSM one. Experimental errors are obtained combining two data sets, at 360 GeV and 500 GeV ($50\,{\rm fb}^{-1}$ each). The theoretical uncertainty is also taken into account and convoluted with experimental errors. Figure 2.3.5 shows the region in which the SM and MSSM hypotheses can be distinguished at the 90 % confidence level. The constraints from the theoretical upper bound on the h^0 mass in the MSSM including radiative corrections and the expected exclusion region from the LEP 2 data at $\sqrt{s} = 192\,{\rm GeV}$ are folded in. The results from the $b\bar{b}$ branching ratio measurement cover most of the region of the plane; the area left uncovered is minimal. A high energy e^+e^- collider will yield an uncontroversial assessment of the H^0 nature.

2.3.4 Production of the HA Final State

A typical final state which can be expected in the MSSM is the associated production of H and A Higgs bosons. This process has been simulated in detail with the goal of determining the precision on the mass and production cross section the linear collider would yield, in a direct measurement. The following sets of MSSM parameters were assumed for the analysis:

$$M_{\rm A} = 260 \text{ or } 300 \text{ or } 340 \text{ GeV}$$

with

$$\begin{aligned} \tan\beta &= 50 \\ \mu &= 551\,{\rm GeV} \\ M_2 &= 185\,{\rm GeV} \end{aligned}$$

In such a scenario the lowest lying Higgs boson h will have a mass of $\approx 110\,{\rm GeV}$ and would be almost standard model like. The associate production h A and Z H will be suppressed, therefore direct evidence of the MSSM Higgs sector can be achieved

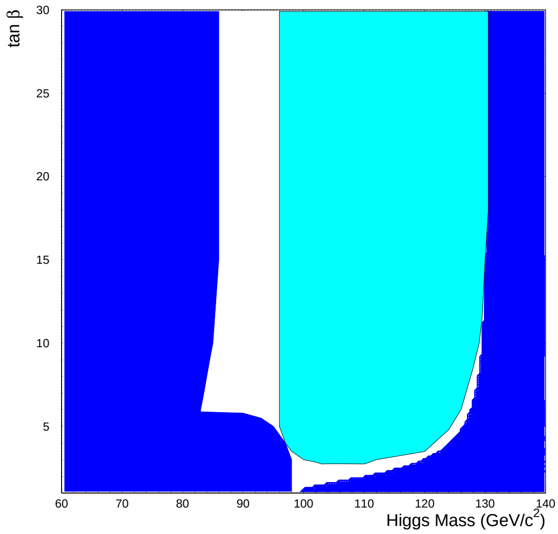

Figure 2.3.5: *The region of the* m_{H}, $\tan\beta$ *plane where the MSSM neutral Higgs boson* h^0 *can be distinguished from the SM boson* H *(gray area). This plot has been obtained for* $m_{\mathrm{t}} = 180\,\mathrm{GeV}$, $M_{\mathrm{SUSY}} = 1\,\mathrm{TeV}$ *and maximal squark mixing. The LEP 2 expected exclusion region is shown in dark at the left. The constraint from the theoretical upper bound on the* h^0 *mass in the MSSM including radiative corrections is shown in dark at the right.*

studying this particular final state. With the parameters listed above H and A have similar masses, branching ratios ($\mathrm{b\bar{b}} \approx 90\,\%, \tau^+\tau^- \approx 10\,\%$) and widths ($\approx 15\,\mathrm{GeV}$). The mass range was chosen in order to be above the threshold of A and H production at $\sqrt{s} = 500\,\mathrm{GeV}$ and below the threshold for the decay $\mathrm{A/H} \to \mathrm{t\bar{t}}$. The cross section is expected to be 7.8, 5.6 and 2.4 fb respectively for the three mass hypotheses. An integrated luminosity of $\mathcal{L} = 200\,\mathrm{fb}^{-1}$ at $\sqrt{s} = 800\,\mathrm{GeV}$ was assumed.

2.3.4.1 Simulation and Event Selection

6000 $\mathrm{e^+e^-} \to \mathrm{HA}$ events at each mass value (i.e. between four and twelve times the expected amount of data) were generated using the HZHA code [20]. Signal events produce final states with four jets, so that standard processes expected to contribute to the four-jet topology as background sources are:

- $\mathrm{e^+e^-} \to \gamma/\mathrm{Z} \to \mathrm{f\bar{f}}$
  $\mathrm{f\bar{f}}$ s channel production via γ/Z was generated using PYTHIA [7]. After the

selection, the only surviving events in this sample were the $\mathrm{t\bar{t}}$ ones and, to get better statistical significance, a special set of these events were generated with JETSET.

- $\mathrm{e^+e^- \to ZZ/WW \to f\bar{f}\,f\bar{f}}$ and $\mathrm{e^+e^- \to f\bar{f}\,f\bar{f}}$
  4-fermion events were generated using PYTHIA with double vector boson production and EXCALIBUR [21]. The two generators were found to be compatible. The only relevant background was found to come from $\mathrm{e^+e^- \to b\bar{b}\,b\bar{b}}$, $\mathrm{e^+e^- \to b\bar{b}\,c\bar{c}}$, and $\mathrm{e^+e^- \to cscs}$ for which special samples were generated.

The generated events were processed through the SIMDET code to add detector effects in the event reconstruction. All particles with energy greater than 1 GeV and $|\cos\theta| < 0.95$ were used as input for the jet reconstruction algorithm. The reconstructed particles were clustered into four jets according to the JADE algorithm. Jets with at least 5 charged particles were classified as *hadronic* and jets with 1 or 3 charged particles and an invariant mass lower than 3 GeV as *leptonic*. Only topologies with 4 hadronic jets (corresponding to 4b-decays) or 2 hadronic and 2 leptonic jets (corresponding to $\mathrm{bb}\tau\tau$ decays) were initially considered. The energies of the four jets were afterward rescaled imposing the total energy-momentum conservation with the assumption that the four jet velocities $\bar{\beta}_i = \bar{p}_i/E_i$ were measured correctly. Compatibility of the events with the four body hypothesis was enforced requiring all the recomputed energies be positive. The requirements of positive energies after rescaling, and of a four-jet topology, were effective in reducing background coming from channels which did not have just four hard jets, such as $\mathrm{e^+e^- \to t\bar{t}}$ (6 jets or 4 jets plus a prompt lepton) or $\mathrm{e^+e^- \to q\bar{q}\,gg}$ (2 leading jets and two soft gluon jets) and yielded a reasonably high ($\approx 60\,\%$) efficiency for the $\mathrm{e^+e^- \to HA}$ signal. After the kinematical fit, jets were paired and di-jet invariant masses were computed from the rescaled energies. To reject $\mathrm{e^+e^- \to ZZ/WW \to f\bar{f}\,f\bar{f}}$ background, events with at least one di-jet combination with both di-jet masses lower than 120 GeV were discarded. $\mathrm{t\bar{t}}$ contamination was further reduced rejecting events with at least one di-jet combination with distance from the point $(m_\mathrm{t}, m_\mathrm{t})$ lower than 50 GeV. At this stage of the analysis, since the 2 hadronic and 2 leptonic jets sample had a relevant background from $\mathrm{e^+e^- \to q\bar{q}\,gg}$ events, with gluon jets having low multiplicity and low invariant mass, only topologies with 4 hadronic jets were further considered. A b-tagging algorithm based on lifetime probability tag [22, 23, 24] was then performed, using two dimensional track impact parameter significance. As the most important background was found to be $\mathrm{t\bar{t}}$ production, which contains always two (and only two) b jets, the sum of the two highest jet probabilities was used as discriminating variable, requiring also all the four jets to have a significant probability to come from a b quark. A summary of the selection criteria is displayed in Tab. 2.3.5 for the signal and for the surviving backgrounds, $\mathrm{t\bar{t}}$, $\mathrm{b\bar{b}\,b\bar{b}}$, and $\mathrm{b\bar{b}\,c\bar{c}}$ only. The $\mathrm{f\bar{f}}$ sample included also the $\mathrm{t\bar{t}}$ which yielded the only two fermions

	HA (260, 300, 340 GeV)	$t\bar{t}$	4b	2b2c
Cross section [fb]	7.8, 5.6, 2.4	280	6.2	12.5
Generated events	6000, 6000, 6000	30000	5000	5000
4 hadronic jets	.81	.49	.22	.21
Kinematic fit	.61	.36	.15	.15
WW,ZZ rejection	.61	.36	.05	.08
m_t compatibility	.59	.20	.04	.07
b-tagging	.21	.001	.01	.002

Table 2.3.5: *Summary of the generated events (signal and background) and their selection efficiencies at the various stages of the selection.*

surviving events. Out of the cscs sample, no event survived the selection criteria, giving us confidence on the goodness of the method. An efficiency of 21 %, with a purity of 69 % was obtained for $m_A = 300$ GeV. This figure can be substantially improved without a significant loss of efficiency if a cut on the di-jet invariant masses is applied (this technique is discussed in the next section). More details about this selection can be found in [25].

2.3.4.2 Masses and Cross Section Determinations

The A and H masses can be measured exploiting the fact that, in the scenario discussed, they are almost mass-degenerate, therefore only one mass need to be determined. From the selected event sample a dijet invariant mass distribution was formed, choosing the combination with minimal difference between the two masses and discarding the combination in which the two most energetic jets were paired together. The distribution obtained (Fig. 2.3.6), shows a mass peak with a width of 15 GeV; such width comes mostly from hadronization effects. With a calorimeter segmentation two times worse than the one proposed (in this case the energy flow algorithm was less effective) the mass resolution was $\approx$ 20 % worse. Once a peak is established in the di-jet mass distribution (or if the mass is already known by other means, e.g. LHC), it is also possible to reduce the number of wrong pairings, choosing the di-jet mass combination with better compatibility to the central value of the peak (Fig. 2.3.7). The overall error on the H and A bosons masses, using this technique, comes out to be 1.5 GeV, approximately independent of the mass. By the same token, the purity of the event sample can be improved to obtain a more precise measurement of the production cross section, selecting the di-jet combinations. For instance, a minimum invariant mass requirement of 200 GeV would yield a sample with an efficiency and purity of 20 % and

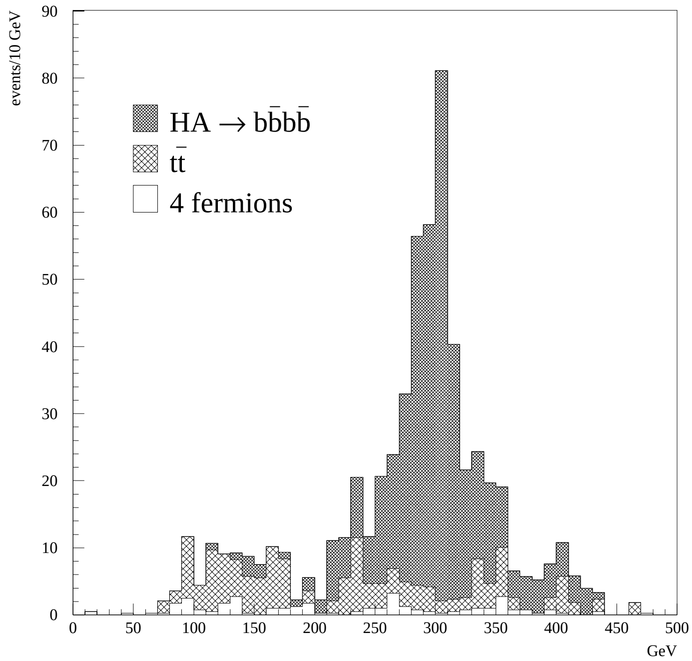

Figure 2.3.6: *Distribution of the di-jet invariant mass for the jet pair combination with the smallest mass difference.*

80 % respectively. This, in turn, allows a determination of $\sigma(\mathrm{e^+e^-} \to \mathrm{HA}) \times \mathrm{BR}(\mathrm{A} \to \mathrm{bb}) \times \mathrm{BR}(\mathrm{H} \to \mathrm{bb})$ with a relative accuracy of 7 %, for $m_{\mathrm{A,H}} = 300\,\mathrm{GeV}$. The same technique was applied to the other masses and was found to provide accuracies on $\sigma(\mathrm{e^+e^-} \to \mathrm{HA}) \times \mathrm{BR}(\mathrm{A} \to \mathrm{bb}) \times \mathrm{BR}(\mathrm{H} \to \mathrm{bb})$ of 5 % and 11 % for $m_{\mathrm{A,H}} = 260$ and 340 GeV respectively. In conclusion, the reaction $\mathrm{e^+e^-} \to \mathrm{HA}$ can be isolated and studied in detail without any experimental limitation coming from the proposed detector. With simple selection criteria a clean event sample can be obtained with a manageably small background. The b-tagging performance of the proposed detector is essential in selecting an event sample which can be used to give precise measurements of both the mass and the cross section. For a luminosity of $\mathcal{L} = 200\,\mathrm{fb}^{-1}$ at $\sqrt{s} = 800\,\mathrm{GeV}$ the expected statistical accuracy is:

$$\Delta m_{\mathrm{A,H}} \approx 1.5\,\mathrm{GeV},$$

$$\Delta\sigma(\mathrm{e^+e^-} \to \mathrm{HA}) \times \mathrm{BR}(\mathrm{A} \to \mathrm{bb}) \times \mathrm{BR}(\mathrm{H} \to \mathrm{bb}) \approx 5 - 11\,\%.$$

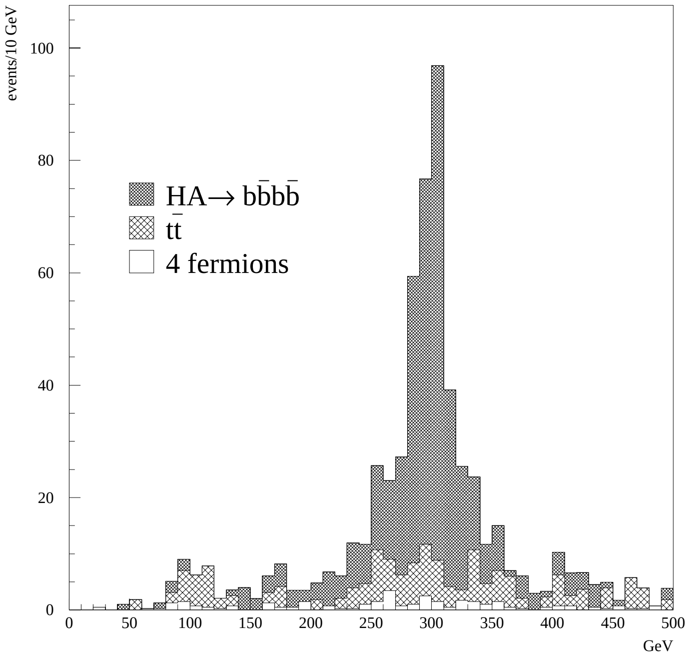

Figure 2.3.7: *Distribution of the di-jet invariant mass for the jet pair combination with better compatibility to the central value of the peak.*

Even with a reduced integrated luminosity of $\mathcal{L} = 50\,\mathrm{fb}^{-1}$, the signal to background ratio $S/\sqrt{B}$ is still ≈ 10 for the more unfavorable case of $m_{\mathrm{A,H}} = 340\,\mathrm{GeV}$ (expected cross section 2.4 fb), thus making this type of reaction clearly detectable by the combination of the proposed machine/experimental apparatus.

2.3.5 $\mathrm{e^+e^-} \rightarrow \mathbf{WW}$

W-pair production in $\mathrm{e^+e^-}$ annihilation is described at the lowest order in the Standard Model by three diagrams: two in the s channel containing the triple gauge boson couplings and one in the t channel with ν_e exchange; the latter gets contributions from left-handed electrons only. Different generators are available to simulate this process: at first, the compatibility of various codes with the Born approximation of CompHEP [26] has been checked. In Fig. 2.3.8 the CompHEP result is presented as a full line. In the same plot the results of different generators ([27],[28],[29],[21]) at $\sqrt{s} = 360$, 375, 500, 800 and 1600 GeV are shown.

variable	cut num.	value (e sel.)	eff.	cut num.	value (μ sel.)	eff.
$\cos\theta_l$	1	≤ 0.9848+lumi	0.91	1	≤ 0.95	0.60
p_l	2	$\geq 20\,\mathrm{GeV}$	0.90	2	$\geq 20\,\mathrm{GeV}$	0.56
α_{iso}	3	$\geq 23°$	0.87	3	$\geq 30°$	0.55
E_{had}	4	$\geq 0.2 * \sqrt{s}$	0.77			
M(lmiss)	5	50 - 110 GeV	0.54	5	60 - 100 GeV	0.46
M(jj)	6	60 - 100 GeV	0.48	6	60 - 100 GeV	0.45

Table 2.3.6: *Selection cuts as used in the* WW *analysis.*

All cross-sections were calculated for resonant W diagrams without beamstrahlung or initial state radiation (ISR) and without any selection or cuts. All cross-sections agree within few percent. Once the initial state radiation and beamstrahlung effects are included, the total cross section is $\approx 8\,\mathrm{pb}$ at 500 GeV. An event sample of $50\,\mathrm{fb}^{-1}$ luminosity will contain 400 k WW-pairs. To determine triple gauge boson couplings from WW events in $\mathrm{e}^+\mathrm{e}^-$ annihilation, the charge of the W has to be identified. This is readily done by measuring the charge of the daughter-lepton. The leptonic branching ratio for the W ($\mathrm{W}^- \to \mathrm{e}^-\nu$ and $\mathrm{W}^- \to \mu^-\nu$) will then give about 40 k events of each type.

2.3.5.1 Generation of W Pairs and Background Reactions

W pairs were generated with two different generators ERATO [27] and WOPPER [28]: in both cases the couplings were set to the Standard Model values. Initial state radiation and beamstrahlung were simulated through the CIRCE code [30] in its TESLA implementation.

The detection efficiency is essentially dependent on the polar angle of the produced lepton (θ_l or $\cos\theta_l$).

About 30 k WW-pairs decaying to $\mu^\pm\nu\mathrm{q}\bar{\mathrm{q}}$ were generated for resonant W diagrams using the ERATO code; approximately the same number of W pairs decaying each into electron and muon final states were generated from resonant and non-resonant W diagrams using the WOPPER code.

Table 2.3.6 summarizes selection cuts and efficiencies for the two lepton species. In this simulation, the muon coverage includes only the tracking solid angle while electrons are assumed to be detected and identified also in the calorimeters (including the luminosity monitor). The isolation criteria for muons require the closest jet to be 30° away from the lepton. For electrons, the requirement is having a jet energy of less than 10 GeV in a cone of 23° centered in the lepton track. The selection efficiency for the electron final states is 0.480 ± 0.003, for muons 0.450 ± 0.003.

In the present analysis background events can be split in two classes: background

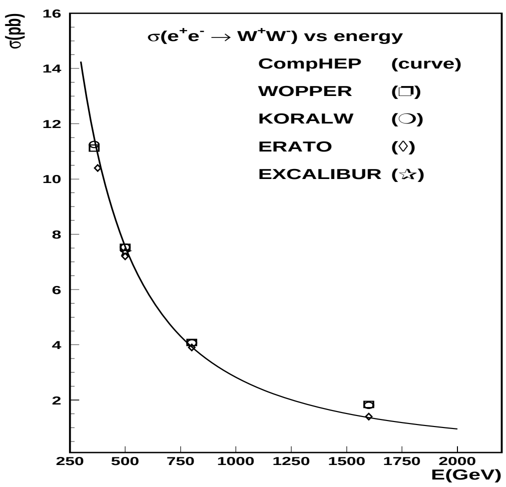

Figure 2.3.8: *Total cross-section of* WW *pair production.*

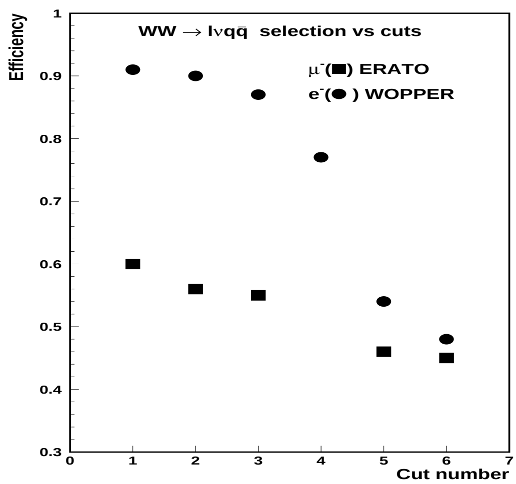

Figure 2.3.9: *Selection efficiencies as a function of the selection cuts.*

from the other W decay and background from processes which do not involve primary W's (e.g. $e^+e^- \to ZZ, t\bar{t}, q\bar{q}$). All these processes were generated at 500 GeV using PYTHIA [7], including ISR and beamstrahlung. The background contamination for the various sources is summarized in Tab. 2.3.7. The selected sample purity is high: only 2.24 % background contamination is allowed in.

2.3.5.2 Experimental Resolutions

The resolution on the lepton momenta as a function of momentum and as a function of $\cos\theta_l$ is shown in Fig. 2.3.10. A minimum momentum 20 GeV/c was required to cut-out leptons coming from semileptonic decays of heavy quarks.

The expected momentum resolution for selected leptons is $\approx 2\,\%$. The above figure applies to the entire inner tracker coverage ($|\cos\theta_l| \le 0.83$), so that no charge mislabelling is expected for these events.

Selected events were then forced to have two jets according to the Durham algorithm [31]. A kinematical fit was performed after the event selection requiring four-momentum conservation and equal masses of the two W bosons. The W invariant mass reconstructed from the hadronic decay is the one which is better determined.

Figure 2.3.12 shows the mass plots for the invariant jet-jet mass for the electron and Fig. 2.3.13 for the muon final state.

Reaction $e^+e^- \to$	cross-section pb	events after cuts	rate %
$WW \to q\bar{q}\,q\bar{q}$	3.6	–	–
$\ell\nu\,\ell\nu$	0.8	–	–
$\tau^-\nu\,q\bar{q}$	0.6	260	1.8
$q\bar{q}$	12.0	3	0.02
$t\bar{t}$	0.6	3	0.02
ZZ	0.4	50	0.4
all			2.24

Table 2.3.7: *Background contributions to* $e^+e^- \to W^+W^- \to \ell\nu q\bar{q}$ *events from the different reactions, corresponding to the integrated luminosity of* $50\,\mathrm{fb}^{-1}$.

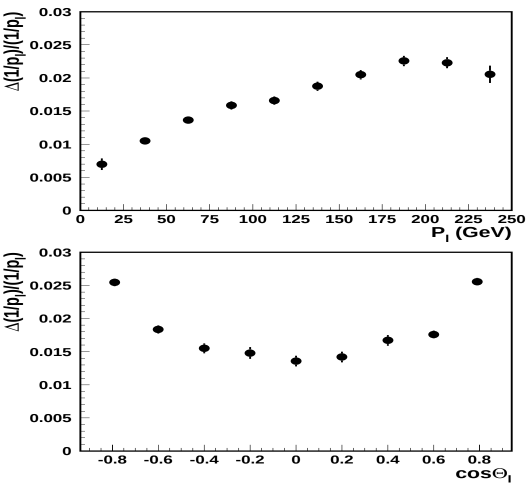

Figure 2.3.10: *Lepton momentum resolution as a function of the momentum (upper plot) and* $\cos\theta_l$ *(lower plot).*

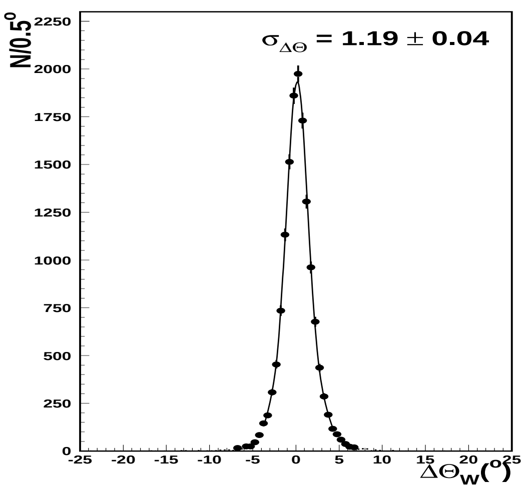

Figure 2.3.11: *Angular resolutions for* θ_W *as reconstructed from the two jets.*

The invariant mass distributions obtained, have been fit with a convolution of a Breit-Wigner and a Gaussian according to:

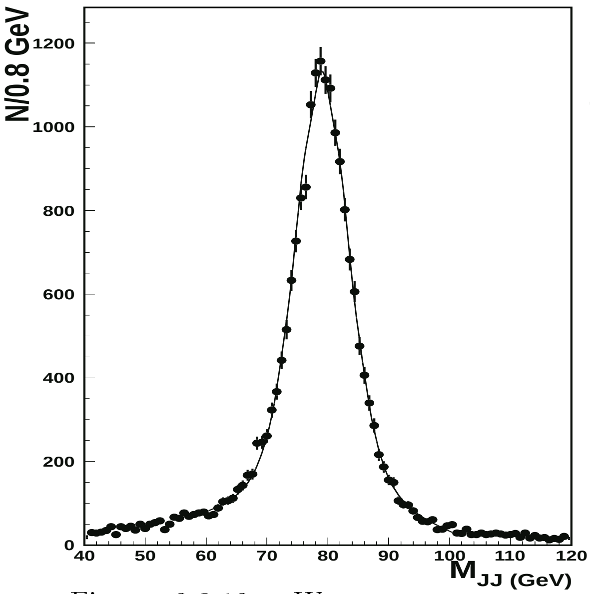

Figure 2.3.12: W *mass spectrum from invariant jet-jet mass for the electron final state.*

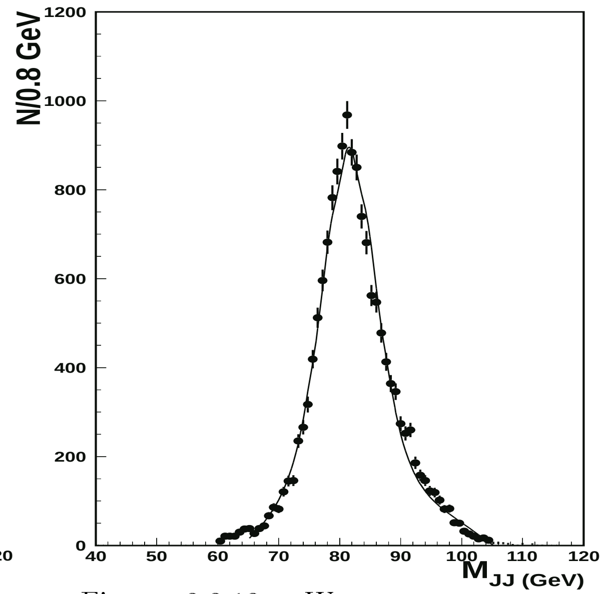

Figure 2.3.13: W *mass spectrum from invariant jet-jet mass for the muon final state.*

$$N(m, m_{\mathrm{W}}, \Gamma_{\mathrm{W}}, \sigma) = \int_{y_1}^{y_2} BW(y; m_{\mathrm{W}}, \Gamma_{\mathrm{W}}) G(y - m, \sigma) dy. \tag{2.3.2}$$

The width of the Breit-Wigner was chosen to be the width of the W in the Monte Carlo generator. The width of the Gaussian parameterizes detector effects. The fitting procedure resulted in an experimental width of 3.6 GeV for electron and muon final states. The integration limits were set at four σ's.

A systematic shift of the fitted mass toward lower than the nominal value was observed in the case of hadronic decays. This effect can be explained as wrong assignments of particles inside a jet, loss of some jet-energy outside of the acceptance of the detector and detector thresholds; a correction on a statistical basis can be applied to the data a posteriori.

The best accuracy one might envisage on m_{W} is given by the distribution width scaled by $\frac{1}{\sqrt{N}}$, N being the total number of W's in the mass plot. Taking into account all semileptonic final states and their efficiency a statistical error of ≈ 15 MeV can be expected for $50\,\mathrm{fb}^{-1}$. Systematics however, set in before the statistical limit is reached. A preliminary investigation of systematic effects results in an expected error of 15 MeV leading to 20 MeV on the W mass. More sophisticated analyses of the systematics are in progress; some improvement could come from these. The resolutions on θ_{W}, $\cos\theta_l$,

resolution of	μ sel.	e sel.
$\cos\Theta_W$	0.0083	0.0082
Θ_W	1.20	1.19
$\cos\Theta_q$	0.026	0.027
Θ_q	2.5	2.6
ϕ_q	3.0	2.8
$\cos\Theta_l$	0.050	0.067
Θ_l	2.7	2.6
ϕ_l	4.0	3.9

Table 2.3.8: *Resolutions for* W *production angle and its decay products angles in the* W *rest frame (the angles are measured in degrees).*

and ϕ_l as well as $\cos\theta_q$ and ϕ_q play an important role in the determination of the anomalous couplings. Table 2.3.8 summarizes the results of the simulations.

2.3.5.3 Limits on the Anomalous Couplings

A maximum likelihood fit has been used to evaluate the sensitivity to measure anomalous couplings. The matrix element M_i for each event was calculated with the ERATO generator using the 4-momenta of the lepton, neutrino and two jets after the constrained fit. The minimization function is given by:

$$-\log \prod_{i=1}^{N_{\text{events}}} \frac{|M_i|^2}{\sigma_{\text{tot}}}. \tag{2.3.3}$$

The fact that the quark flavor is not identified, has been taking into account by the proper symmetrization of the matrix element squared to be evaluated for each event. The total measured cross-section is denoted by σ_{tot}. It will be parameterized according to Ref. [32] as:

$$\sigma_{\text{tot}} = S_0 + S_1 \cdot \alpha + S_2 \cdot \alpha^2, \tag{2.3.4}$$

where α denotes generically any of the anomalous couplings under study.

The muon channel, with its selection cuts was used to evaluate the total cross section; one parameter fits were performed for different anomalous couplings. The

Model	Coupling	Value
$\hat{O}_{B_\phi}$	$x_\gamma \equiv \Delta\kappa_\gamma$	-0.0889 ± 0.0029
$\hat{O}_{W_\phi - B_\phi}$	$\delta_z \equiv \frac{\Delta g_Z^1}{\tan\theta_W}$	-0.1474 ± 0.0045
$\hat{O}_{W_\phi}$	$x_\gamma \equiv \Delta\kappa_\gamma$	-0.0420 ± 0.0017
$\hat{O}_W$	λ_γ	0.0654 ± 0.0017

Table 2.3.9: *Results on accuracy of TGB coupling estimation from ERATO for different models with just one free parameter.*

overall results are given in the Tab. 2.3.9 following the notation of [33] and [34]. The fact that the extracted couplings have a systematic bias is well understood and can be, in principle, corrected for by using the Monte Carlo predictions.

The proposed facility will cope with the demands W physics impose: limits on anomalous couplings of the order of 10^{-3} and W mass determination with accuracies better than 20 MeV are foreseen.

2.3.6 Study of $e^+e^- \to \chi_1^+ \chi_1^-$

Among the supersymmetric signal, chargino pair production $\chi_1^+ \chi_1^-$ at a linear collider operating at $\sqrt{s} = 500\,\mathrm{GeV}$ is one of the most interesting. Discovery strategies at a linear collider have been discussed elsewhere [35, 36]. Here, the goal is to assess whether the anticipated detector performance poses any limitations to precisely determine the chargino mass $\chi_1^\pm$, and the mass of its supersymmetric decay product, the neutralino χ_1^0. Chargino production occurs via intermediate vector bosons γ, Z in the s channel and via electron-sneutrino exchange $\tilde{\nu}_e$ in the t channel. The reference reaction, the decay modes and the relevant SUSY mass parameters are

$$e^+e^- \to \chi_1^+ \chi_1^- \;, \tag{2.3.5}$$

$$\chi_1^\pm \to \chi_1^0 \ell^\pm \nu \qquad \mathrm{BR} = 34.5\,\% \quad \ell = \mathrm{e},\ \mu,\ \tau \;, \tag{2.3.6}$$

$$\to \chi_1^0 q\bar{q}' \qquad \mathrm{BR} = 65.5\,\% \;,$$

$$m_{\chi_1^\pm} = 168.2\,\mathrm{GeV} \;, \tag{2.3.7}$$

$$m_{\chi_1^0} = 88.1\,\mathrm{GeV} \;, \tag{2.3.8}$$

$$m_{\tilde{\nu}_e} = 304.0\,\mathrm{GeV} \;. \tag{2.3.9}$$

The neutralino escapes detection, thus the experimental signature is a final state with an isolated lepton e or μ, two hadronic jets and missing energy. The cross section exhibits a typical threshold behavior proportional to β while the angular distribution is dominated by the very asymmetric t channel process: $d\sigma/d\cos\theta\chi_1^+$ is largest for $\cos\theta\chi_1^+ = -1$ and drops by a factor of ~ 5 at $\cos\theta\chi_1^+ = +1$. This behavior is quite different from Standard Model processes which may constitute a background to reaction (2.3.5). The shape of the angular distribution is essentially the same for the daughter-lepton and hadron-jets.

2.3.6.1 Simulation and Event Selection

Events are generated with the Monte Carlo program SPYTHIA [37], the supersymmetric extensions of PYTHIA with the JETSET fragmentation model. The center of mass energy is $\sqrt{s} = 500\,\mathrm{GeV}$ and the integrated luminosity is assumed to be $\mathcal{L} = 50\,\mathrm{fb}^{-1}$. Radiative corrections as well as beamstrahlung effects [30] are taken into account in the simulation. Charged particles are measured over the polar angle acceptance $|\cos\theta_{ch}| < 0.95$ with a momentum resolution of $\Delta p_\perp/p_\perp = 1.5\cdot 10^{-4}\,p_\perp\,[\mathrm{GeV}]$ and angular resolutions of $\Delta\theta = \Delta\phi = 0.001\,\mathrm{rad}$. The calorimetry extends over $|\cos\theta| < 0.99$ with an electro-magnetic energy resolution of $\Delta E_e/E_e = 0.10/\sqrt{E_e\,[\mathrm{GeV}]} \oplus 0.01$ and $\Delta E_h/E_h = 0.50/\sqrt{E_h\,[\mathrm{GeV}]} \oplus 0.04$ for hadrons. The event selection requires an isolated electron or muon, $\ell = \mathrm{e}$ or μ, and exactly two hadronic jets reconstructed with the JADE algorithm ($y_{\mathrm{cut}} = 0.01$). The event selection criteria for unpolarized $\mathrm{e}^\pm$ beams are listed in Tab. 2.3.10.

variable	accepted range
topology	one isolated lepton + two hadron jets
lepton $\ell = \mathrm{e}$ or μ	$5\,\mathrm{GeV} < E_\ell < 150\,\mathrm{GeV}$
	$-0.90 < Q_\ell\cos\theta_\ell < 0.50$
hadron jets	$5\,\mathrm{GeV} < E_j < 150\,\mathrm{GeV}$
	$|\cos\theta_j| < 0.90$
di-jet system	$10\,\mathrm{GeV} < E_{jj} < 175\,\mathrm{GeV}$
	$-0.90 < -Q_\ell\cos\theta_{jj} < 0.50$
	$m_{jj} < m_{\mathrm{W}} - 10\,\mathrm{GeV}$
recoil against di-jet system	$|m_{\mathrm{recoil}-jj} - m_{\mathrm{W}}| > 10\,\mathrm{GeV}$
missing momentum	$|\cos\theta_{\vec{p}_{\mathrm{miss}}}| < 0.90$

Table 2.3.10: *Event selection criteria for the reaction* $\mathrm{e}^+\mathrm{e}^- \to \chi_1^+\,\chi_1^-$, *leptons* $\ell = \mathrm{e}$ *or* μ.

The main background was found to come from

$$e^+e^- \rightarrow W\,W \rightarrow \ell\,\nu\, q\bar{q}' \qquad \ell = e,\ \mu,\ \tau \quad . \tag{2.3.10}$$

Cascade decays $W \rightarrow \tau\,\nu$ with subsequent decays $\tau \rightarrow \mu\,\nu$ or $e\,\nu$ are included. The background from $e^+e^- \rightarrow W\,W$ production can be effectively suppressed by cuts on the signed lepton and quark polar angles (due to the V-A structure the $W^\pm$ and its decay fermions tend to be aligned along the $e^\pm$ direction, opposite to the preferred hemisphere of chargino production), on the di-jet mass and on the mass recoiling against the di-jet system around the W mass. The missing momentum vector $\vec{p}_{\rm miss}$ has to point into the detector acceptance in order to ensure good containment and to remove background from intermediate γ^*, Z decays produced by high energy radiated photons. The cross sections and efficiencies for the reference and background reactions are given in Tab. 2.3.11. The observable cross section for $e^+e^- \rightarrow \chi_1^+\,\chi_1^-$ leads to comfortable event rates. The acceptance of $\epsilon_{\ell\,jj} = 11.7\,\%$ is reasonably high, the biggest reduction factor originates from the decay branching fractions. The only relevant background from $e^+e^- \rightarrow W\,W$ amounts to $\sim 10\,\%$, other sources are negligible.

process	σ [fb]	BR($\ell\,\nu$ $q\bar{q}'$)	$\epsilon_{\ell\,jj}$	$\sigma_{\rm acc}$ [fb]
$e^+e^- \rightarrow \chi_1^+\,\chi_1^- \rightarrow \chi_1^0\,\ell\,\nu\ \chi_1^0\, q\bar{q}'$	245	0.293	0.117	28.7
$e^+e^- \rightarrow W\,W \rightarrow \ell\,\nu\ q\bar{q}'$	8000	0.292	$4{\cdot}10^{-4}$	3.2

Table 2.3.11: *Production cross sections, branching ratios, efficiencies and visible cross sections of the reference and background reactions, $\ell = e$ or μ.*

2.3.6.2 Mass Determination of $m_{\chi_1^\pm}$ and $m_{\chi_1^0}$

a) Di-jet Energy Spectrum

The masses of the chargino $m_{\chi_1^\pm}$ and the neutralino $m_{\chi_1^0}$ can be determined through the analysis of the di-jet system energy spectrum [36]. The SUSY parameters are chosen such that the chargino decays according to Eq. (2.3.6) via a virtual W into a three-body final state. The di-jet energy spectrum ranges between $25\,\text{GeV} \leq E_{jj} \leq 156\,\text{GeV}$. Here the situation is a bit more complicated with respect to the case of the scalar muon $e^+e^- \rightarrow \tilde{\mu}_R\,\tilde{\mu}_R$ discussed in the next section, where the two body decay implies that the endpoints from a flat energy distribution $\tilde{\mu}_R \rightarrow \chi_1^0\,\mu$ yield a better analyzing power toward the mass measurements. The observable di-jet energy spectrum, shown in Fig. 2.3.14, is distorted due to the event selection criteria, detector resolutions and initial state radiation, but still retains the characteristic features. The experimental energy resolution is expected to vary between $3\,\mathrm{GeV} \lesssim \Delta E_{jj} \lesssim 9\,\mathrm{GeV}$. Here again initial state radiation has practically no influence on the energy spectrum and mass determination; the photons carry away, on the average, very little energy with a rms spread of 3.4 GeV. Tails, however, are quite sizeable. Beamstrahlung effects are more important: they account for a sizeable c.m. energy reduction (CIRCE [30]) $\langle\sqrt{s}\rangle = 492.4\,\mathrm{GeV}$ with a rms width of 10.2 GeV at 500 GeV nominal value. The mass determination of $m_{\chi_1^\pm}$ and $m_{\chi_1^0}$ is obtained with a two parameter maximum likelihood fit to the di-jet energy spectra of Fig. 2.3.14; signal and background reactions (2.3.5) and (2.3.10) are included in the fitting procedure. The mass correlation with one and two standard deviation contours is displayed in Fig. 2.3.15. The result of the analysis is

$$\begin{aligned} m_{\chi_1^\pm}(\mathrm{obs},\ E_{jj}) &= 167.6 \pm 1.1\,\mathrm{GeV} \\ m_{\chi_1^0}(\mathrm{obs},\ E_{jj}) &= 88.2 \pm 0.6\,\mathrm{GeV}. \end{aligned}$$

The input values of Eqs. (2.3.7) and (2.3.8) are well reconstructed within the errors. With an integrated luminosity of $\mathcal{L} = 50\,\mathrm{fb}^{-1}$ the masses of the chargino $\chi_1^\pm$ and the neutralino χ_1^0 can both be measured with a statistical accuracy of $\Delta m/m \simeq 0.7\,\%$.

b) Threshold Energy Scan

Here, the chargino mass $m_{\chi_1^\pm}$ can be measured by determining the $\chi_1^+\chi_1^-$ production cross section close to the kinematic threshold. The cross section for $e^+e^- \to \chi_1^+\chi_1^-$ around the threshold including initial state radiation and beamstrahlung, but neglecting the finite chargino width, is shown in Fig. 2.3.16. The excitation curve rises steeply $\propto \beta$. It is assumed to collect $\mathcal{L} = 10\,\mathrm{fb}^{-1}$ at five different c.m. energies to cover the range from $\sqrt{s} = 336\,\mathrm{GeV}$ to $\sqrt{s} = 341\,\mathrm{GeV}$. A χ^2 analysis of the threshold scan yields a statistical sensitivity to the chargino mass of

$$m_{\chi_1^\pm}(\mathrm{obs, scan}) = 168.2 \pm 0.100\,\mathrm{GeV}\ .$$

The scanning strategy has not been optimized concerning the luminosity weighting. A cross section measurement at the kinematic threshold offers the possibility to improve the precision attainable on the chargino mass $m_{\chi_1^\pm}$ by an order of magnitude already with a moderate integrated luminosity.

c) Polarized Beams

Longitudinally polarized beams offer great advantages for the study of SUSY phenomenology. The linear collider might provide polarizations up to $P_L(e^-) = \pm 0.90$ and

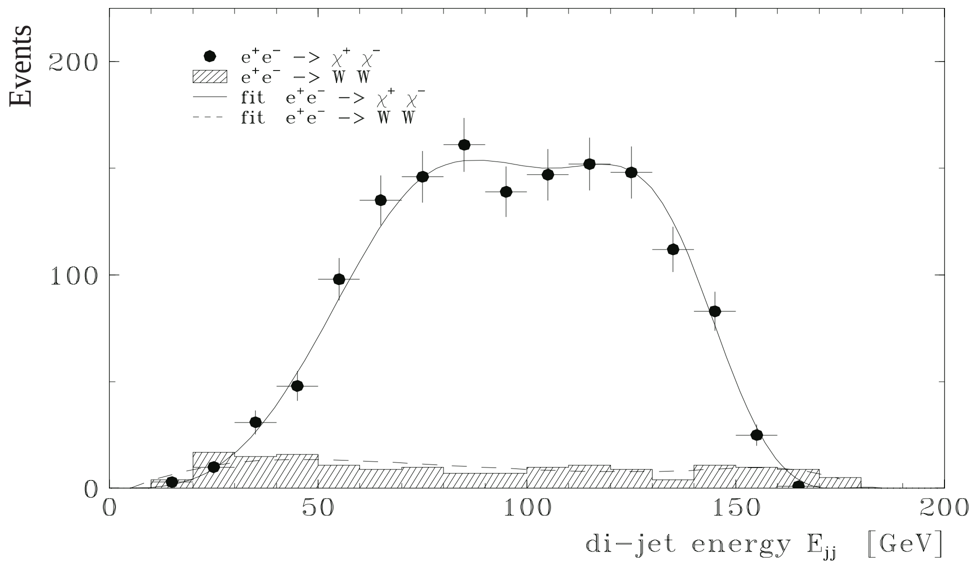

Figure 2.3.14: *Di-jet energy spectra E_{jj} of the reaction* $e^+e^- \to \chi_1^+\chi_1^-$ *(• and —) and the background reaction* $e^+e^- \to \mathrm{W\,W}$ *(histogram and −−), assuming* $\mathcal{L} = 50\,\mathrm{fb}^{-1}$.

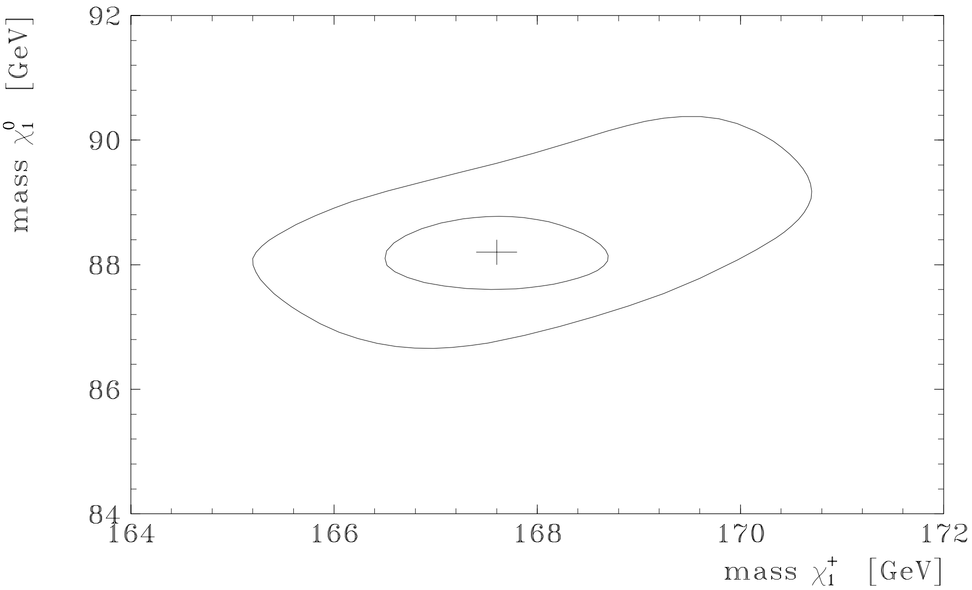

Figure 2.3.15: *Correlation of $m_{\chi_1^0}$ versus $m_{\chi_1^\pm}$ from a two parameter mass fit. The reconstructed masses are indicated by the cross, the contours show the one standard deviation and two standard deviations measurements.*

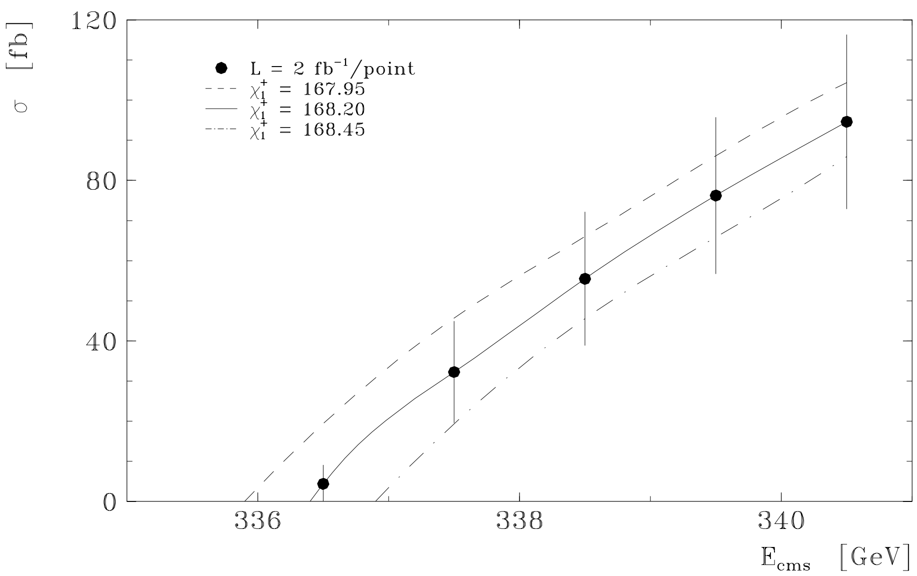

Figure 2.3.16: *Cross section for* $e^+e^- \to \chi_1^+\chi_1^-$ *around the kinematic threshold with initial state radiation and beamstrahlung, assuming* $\mathcal{L} = 2\,\mathrm{fb}^{-1}$ *per measurement (•). The curves indicate chargino masses of* $m_{\chi_1^\pm} = 168.2 \pm 0.25\,\mathrm{GeV}$.

$P_L(e^+) = \pm 0.60$. In terms of background rejection chargino production does not benefit from polarization as the scalar lepton production does. For left-handed electrons the cross section σ_L increases by a factor of ~ 1.7, while for right-handed electrons the cross section σ_R decreases by almost an order of magnitude. This is due to the fact that, for the chosen set of SUSY parameters, $\chi_1^+\chi_1^-$ production is dominated by $\tilde{\nu}_e$ t channel exchange, which couples only to left-handed electrons. The W W cross section scales by approximately the same amount. Polarization, however, is indeed useful because it offers the possibility of disentangling the s and t channel diagrams and to determine the gaugino and higgsino components of the chargino: $\chi_1^\pm = \alpha\,\tilde{\mathrm{W}}^\pm + \beta\,\tilde{\mathrm{H}}^\pm$, where the higgsino couples only to right-handed electrons. With a luminosity of $\mathcal{L} = 10\,\mathrm{fb}^{-1}$ the cross section σ_L can be measured with a statistical accuracy of $\Delta\sigma_L \sim 4.5\,\%$ and σ_R with a statistical error of $\Delta\sigma_R \sim 15\,\%$. Thus, precise measurements of σ_L and σ_R will allow the chargino mixing parameters to be determined. Doing this at the same time as measuring the sparticle masses will give important tests of the predictions of SUSY-GUT theories.

The masses of the chargino and neutralino can be determined by a study of the reaction $e^+e^- \to \chi_1^+\chi_1^-$. The event signature is an isolated lepton $\ell = e$ or μ and two hadron jets. The detection efficiency is reasonably high and clean event samples can be obtained. The main background from $e^+e^- \to W\,W$ is small. The energy spectrum of the di-jet system provides a powerful tool to measure the chargino and neutralino masses. With an integrated luminosity of $\mathcal{L} = 50\,\mathrm{fb}^{-1}$ at a center of mass energy $\sqrt{s} = 500\,\mathrm{GeV}$ the expected accuracy is

$$\begin{aligned} \Delta m_{\chi_1^\pm} &\simeq 1.1\,\mathrm{GeV}\ , \\ \Delta m_{\chi_1^0} &\simeq 0.6\,\mathrm{GeV}\ . \end{aligned}$$

A more accurate chargino mass $m_{\chi_1^\pm}$ may be obtained by a $\chi_1^+\,\chi_1^-$ production cross section measurement around the kinematic threshold. The expected sensitivity is $\Delta m_{\chi_1^\pm} \sim \mathcal{O}(100\,\mathrm{MeV})$, depending on the collected statistics. No experimental limitation is expected with the experimental apparatus described in this report.

2.3.7 Study of $e^+e^- \to \tilde{\mu}_R\,\tilde{\mu}_R$

The last reaction to be discussed in this section is the production of scalar muons $\tilde{\mu}_R$. Previous studies concentrated on the discovery potential of lepton colliders at $\sqrt{s} = 500\,\mathrm{GeV}$ [35]. Here, the main thrust is in trying to devise methods to precisely determine the mass of the scalar muon $\tilde{\mu}_R$ and of its (supersymmetric) decay product, the neutralino χ_1^0. The reference reaction and the relevant SUSY mass parameters are

$$e^+e^- \to \tilde{\mu}_R^+\,\tilde{\mu}_R^-\ , \tag{2.3.11}$$
$$\tilde{\mu}_R \to \mu\,\chi_1^0 \qquad \mathrm{BR} = 99.5\,\%\ , \tag{2.3.12}$$
$$m_{\tilde{\mu}_R} = 275.1\,\mathrm{GeV}\ , \tag{2.3.13}$$
$$m_{\chi_1^0} = 88.1\,\mathrm{GeV}\ . \tag{2.3.14}$$

The neutralino escapes detection, thus the experimental signature is an acoplanar $\mu^+\,\mu^-$ pair and missing energy. The cross section exhibits a typical threshold behavior $\propto \beta^3$ and has a characteristic polar angle distribution $\propto \sin^2\theta$, quite different from Standard Model processes which may constitute a background to reaction (2.3.11).

2.3.7.1 Simulation and Event Selection

Events are generated with the Monte Carlo code SPYTHIA [37], which includes supersymmetric extensions of PYTHIA; the JETSET fragmentation model is included. The center of mass energy is $\sqrt{s} = 800\,\mathrm{GeV}$; the assumed integrated luminosity is $\mathcal{L} = 125\,\mathrm{fb}^{-1}$. QED radiative corrections as well as beamstrahlung effects [30] are taken into account. The detector simulation follows the proposed design and assumes μ detection over 95 % of the total solid angle ($|\cos\theta_\mu| < 0.95$) with a momentum resolution of $\Delta p_\perp/p_\perp = 1.5\cdot 10^{-4}\,p_\perp$ [GeV] and an angular resolution of $\Delta\theta_\mu = \Delta\phi_\mu = 0.001$ rad. The event selection requires an acoplanar $\mu^+\,\mu^-$ pair (the acoplanarity is defined as the difference between the lepton azimuthal angles ϕ_μ measured in the plane perpendicular to the $e^\pm$ beams) and nothing else in the detector. The event selection criteria for unpolarized $e^\pm$ beams are listed in Tab. 2.3.12. The following background sources

variable	accepted range
topology	$\mu^+\,\mu^-$ pair + nothing else in detector
radiative γ veto	$E_\gamma > 1\,\mathrm{GeV} \quad \lvert\cos\theta_\gamma\rvert < 0.985$
lepton polar angle	$\lvert\cos\theta_\mu\rvert < 0.95$
at least one lepton	$Q_\mu\,\cos\theta_\mu < 0.75$
acoplanarity	$\lvert\phi_{\mu^+} - \phi_{\mu^-}\rvert < 145^\circ$
missing momentum	$\lvert\cos\theta_{\vec{p}_\mathrm{miss}}\rvert < 0.90$
lepton energy	$45\,\mathrm{GeV} < E_\mu < 375\,\mathrm{GeV}$
di-lepton mass	$\lvert m_{\mu^+\mu^-} - m_\mathrm{Z}\rvert > 10\,\mathrm{GeV}$
recoil mass	$\lvert m_\mathrm{recoil} - m_\mathrm{Z}\rvert > 15\,\mathrm{GeV}$

Table 2.3.12: *Event selection criteria for the reaction* $e^+e^- \to \tilde{\mu}_R\,\tilde{\mu}_R$.

are considered in the analysis

$$e^+e^- \to \gamma/\mathrm{Z} \to \mu^+\,\mu^-\,(\gamma)\ , \tag{2.3.15}$$

$$e^+e^- \to \mathrm{Z\,Z} \to \mu^+\,\mu^-\,\nu\,\nu\ , \tag{2.3.16}$$

$$e^+e^- \to \mathrm{W\,W} \to \mu^+\,\nu\,\mu^-\,\nu\ . \tag{2.3.17}$$

Cascade decays γ, $\mathrm{Z} \to \tau\,\tau$ and $\mathrm{W} \to \tau\,\nu$ with subsequent decays $\tau \to \mu\,\nu$ are included. The missing momentum vector $\vec{p}_\mathrm{miss}$ has to point to the sensitive area of the detector in order to ensure good containment and to suppress background from intermediate Z decays produced by high energy radiated photons. Further reduction of Z background is obtained with cuts on the di-lepton invariant mass and on the recoil mass close to the Z pole. Background from $e^+e^- \to \mathrm{W\,W}$ production can be effectively suppressed by cuts on the signed lepton polar angle (due to the V-A structure the $\mathrm{W}^\pm$ and its decay $\mu^\pm$ tend to be aligned along the $e^\pm$ direction) and on the acoplanarity. The cross sections and efficiencies for the reference and background reactions are given in Tab. 2.3.13. The observable cross section for $e^+e^- \to \tilde{\mu}_R\,\tilde{\mu}_R$ leads to comfortably large and clean event rates, the acceptance, $\epsilon_{\mu^+\mu^-} = 50\,\%$, being reasonably high. The most prominent background contamination comes from $e^+e^- \to \mathrm{W\,W}$ and amounts to $\sim 10\,\%$, the other backgrounds are negligible.

process	σ [fb]	$\epsilon_{\mu^+\mu^-}$	$\sigma_{\rm acc}$ [fb]
$e^+e^- \to \tilde{\mu}_R^+ \tilde{\mu}_R^- \to \mu^+ \chi_1^0 \, \mu^- \chi_1^0$	15.2	0.50	7.6
background			
$e^+e^- \to \gamma/Z \to \mu^+ \mu^- (\gamma)$	850	$< 3 \cdot 10^{-5}$	< 0.03
$e^+e^- \to Z\,Z \to \mu^+ \mu^- \, \nu \nu$	5.9	$1.3 \cdot 10^{-2}$	0.08
$e^+e^- \to W\,W \to \mu^+ \nu \, \mu^- \nu$	210	$3.8 \cdot 10^{-3}$	0.8
total			~ 0.9

Table 2.3.13: *Production cross sections, efficiencies and visible cross sections of the reference and background reactions. Cascade decays γ, $Z \to \tau\,\tau$, $W \to \tau\,\nu$ and $\tau \to \mu\,\nu$ are included.*

2.3.7.2 Mass Determination of $m_{\tilde{\mu}_R}$ and $m_{\chi_1^0}$

The masses of the scalar muon $\tilde{\mu}_R$ and the neutralino χ_1^0 can be evaluated by analyzing the energy spectrum of the final state leptons $\mu^\pm$. The scalar muon decays isotropically according to the decay mode (2.3.12) and the simple two-body kinematics results in a flat energy distribution of the observable muon. The endpoint energies $E_\mu^{\rm min}$ and $E_\mu^{\rm max}$ can be related to the masses of the scalar muon and the neutralino via

$$\frac{m_{\tilde{\mu}_R}}{2}\left(1-\frac{m^2_{\chi_1^0}}{m^2_{\tilde{\mu}_R}}\right)\gamma\,(1-\beta) \;\leq\; E_\mu \;\leq\; \frac{m_{\tilde{\mu}_R}}{2}\left(1-\frac{m^2_{\chi_1^0}}{m^2_{\tilde{\mu}_R}}\right)\gamma\,(1+\beta)\;, \qquad (2.3.18)$$

$$49.1\,\mathrm{GeV} \;\leq\; E_\mu \;\leq\; 309.8\,\mathrm{GeV}\;,$$

where $\gamma = \sqrt{s}\,/\,(2\,m_{\tilde{\mu}_R})$ and $\beta = \sqrt{1-\gamma^{-2}}$. The observable lepton energy spectrum, shown in Fig. 2.3.17, is distorted due to the event selection criteria, detector resolution and initial state radiation, but still maintains the characteristic features. The experimental energy resolution is expected to vary between $0.5\,\mathrm{GeV} \lesssim \Delta E_\mu \lesssim 15\,\mathrm{GeV}$. Initial state radiation has very little influence on the shape of the energy spectrum and the mass determination ($\langle\sqrt{s}\rangle = 799.8\,\mathrm{GeV}$, rms spread $3.6\,\mathrm{GeV}$ with a very long tail). However, the beamstrahlung effects are more important and must be kept under control. In the present version of CIRCE [30] the mean center of mass energy is reduced to $\langle\sqrt{s}\rangle = 788.9\,\mathrm{GeV}$ with a rms of $17.4\,\mathrm{GeV}$. The mass determination of $m_{\tilde{\mu}_R}$ and $m_{\chi_1^0}$ has been obtained by performing a two parameter maximum likelihood fit to

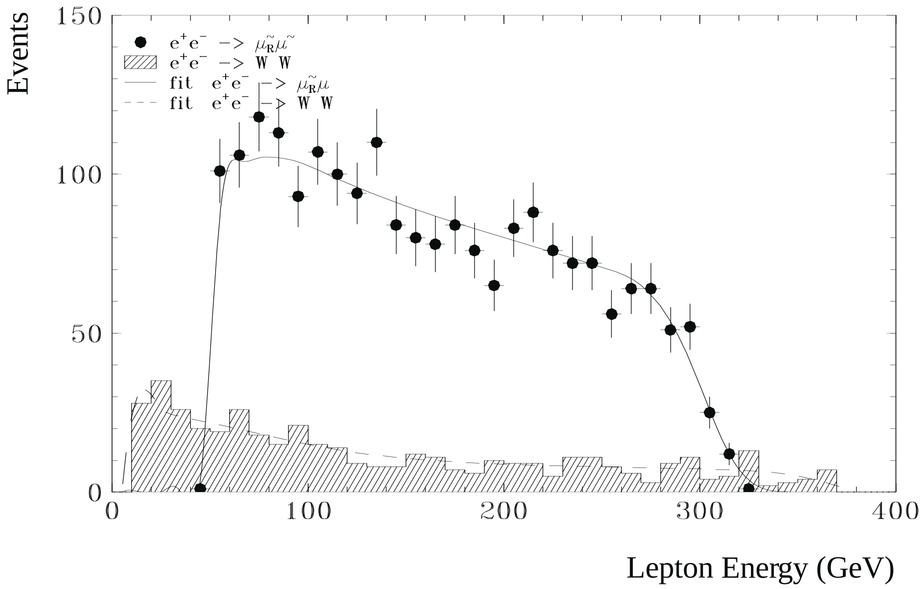

Figure 2.3.17: *Energy spectra of the final state* $\mu^{\pm}$ *for the reaction* $\mathrm{e^+e^-} \to \tilde{\mu}_R\,\tilde{\mu}_R$ *(•) and the background* $\mathrm{e^+e^-} \to \mathrm{W\,W}$ *(histogram), assuming* $\mathcal{L} = 125\,\mathrm{fb}^{-1}$*.*

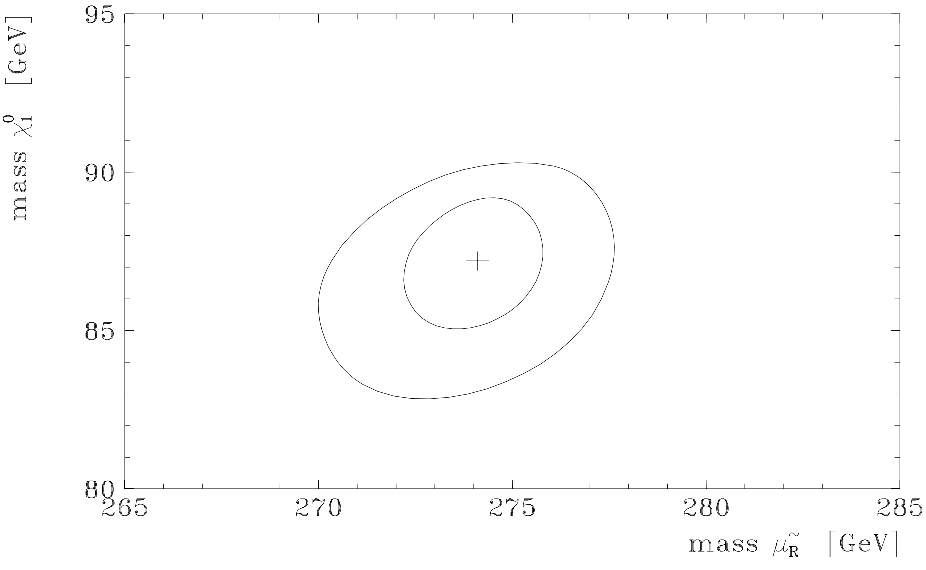

Figure 2.3.18: *Correlation of* $m_{\chi_1^0}$ *versus* $m_{\tilde{\mu}_R}$ *from a two parameter mass fit using unpolarized beams. The reconstructed masses are indicated by the cross, the contours show the one standard deviation and two standard deviation measurements.*

the lepton spectra of Fig. 2.3.17 including the signal and background reactions (2.3.11) and (2.3.17). The mass correlation with one and two standard deviation contours is shown in Fig. 2.3.18. The final result is

$$\begin{aligned} m_{\tilde{\mu}_R}(\text{obs}) &= 274.1\,^{+1.7}_{-1.9}\,\text{GeV}\,, \\ m_{\chi^0_1}(\text{obs}) &= 87.2\,^{+2.1}_{-2.4}\,\text{GeV}\,. \end{aligned} \tag{2.3.19}$$

Comparing this mass determination with the input values of Eqs. (2.3.13) and (2.3.14) one observes a small shift towards lower masses, but well within the errors. With a luminosity of $\mathcal{L} = 125\,\text{fb}^{-1}$ the masses of the scalar muon $\tilde{\mu}_R$ and the lightest neutralino χ^0_1 can be measured with a statistical accuracy of $\Delta m_{\tilde{\mu}_R}/m_{\tilde{\mu}_R} \simeq 0.7\,\%$ and $\Delta m_{\chi^0_1}/m_{\chi^0_1} \simeq 2.5\,\%$.

a) Use of Polarized Electrons

The linear collider offers the possibility of accelerating longitudinally polarized electrons: this technique carries enormous advantages for the study of SUSY phenomenology. A right-handed electron with a degree of polarization $P_L(\text{e}^-) = +0.90$ (such a large polarization might be attainable by the time the linear collider is completed) enhances the cross section $\sigma(\text{e}^+\text{e}^-_\text{R} \to \tilde{\mu}_R\,\tilde{\mu}_R)$ by a factor of ~ 1.6. At the same time the most severe background, W pair production, is suppressed by an order of magnitude. The background suppression allows, in turn, the cuts to be relaxed on the polar angle of the signed lepton and on the acoplanarity, increasing the acceptance to $\epsilon_{\mu^+\mu^-} \simeq 0.60$. Overall, the gain is equivalent to almost doubling the integrated luminosity. The muon energy spectrum, displayed in Fig. 2.3.19, is more uniform than in the unpolarized case. Such an event sample, essentially background free, would allow the mass errors to be reduced, in particular for the scalar muon. The expected precision is

$$\begin{aligned} m_{\tilde{\mu}_R}(\text{obs}, \text{e}^-_R) &= 275.3\,^{+0.9}_{-0.7}\,\text{GeV}\,, \\ m_{\chi^0_1}(\text{obs}, \text{e}^-_R) &= 88.2\,^{+1.8}_{-1.6}\,\text{GeV}\,. \end{aligned}$$

The masses correlation with one and two standard deviation contours is shown in Fig. 2.3.20.

b) Alternative Determination of $m_{\tilde{\mu}_R}$

An alternative to determine the scalar muon mass $m_{\tilde{\mu}_R}$ is to measure the $\tilde{\mu}_R\,\tilde{\mu}_R$ production cross section close to the kinematic threshold with a similar technique as proposed for the WW and $\text{t}\bar{\text{t}}$ pair production. The lepton energy spectrum becomes almost monochromatic, a spectacular signature. A threshold scan has the additional advantage that the signal reaction is not spoiled by complicated cascade decays, which otherwise may be kinematically allowed. The cross section for $\text{e}^+\text{e}^-_\text{R} \to \tilde{\mu}_R\,\tilde{\mu}_R$ around the

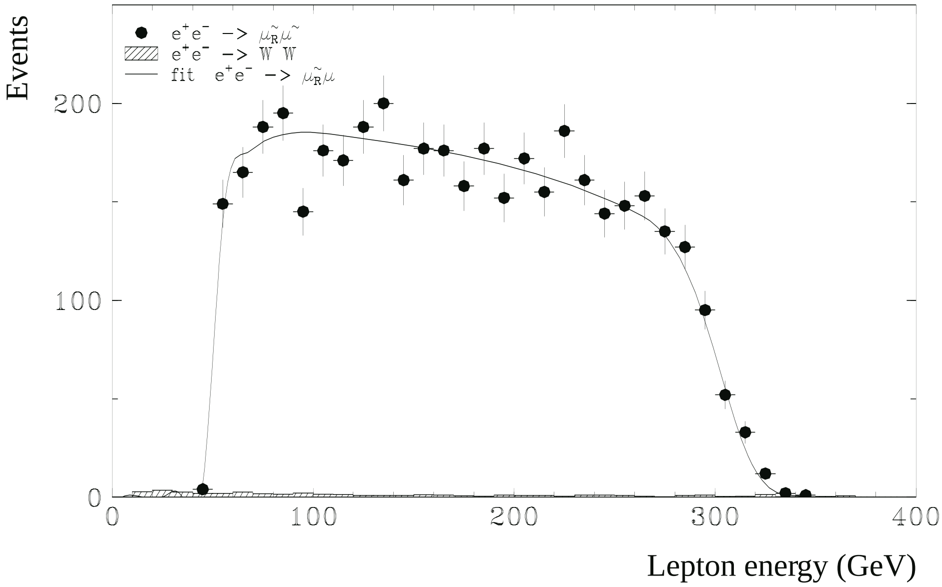

Figure 2.3.19: *Energy spectra of the final state* $\mu^{\pm}$ *for the reaction* $\mathrm{e}^+\mathrm{e}^-_{\mathrm{R}} \to \tilde{\mu}_R\,\tilde{\mu}_R$ *(•) and the background* $\mathrm{e}^+\mathrm{e}^-_{\mathrm{R}} \to \mathrm{W\,W}$ *(histogram), assuming* $\mathcal{L} = 125\,\mathrm{fb}^{-1}$.

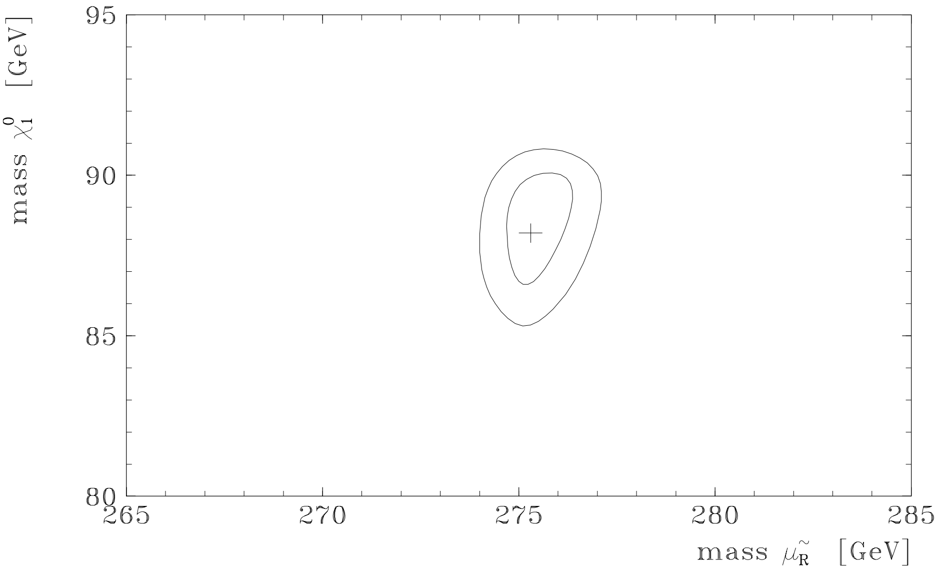

Figure 2.3.20: *Correlation of* $m_{\chi_1^0}$ *versus* $m_{\tilde{\mu}_R}$ *from a two parameter mass fit using a polarized* e^-_R *beam. The reconstructed masses are indicated by the cross, the contours show the one standard deviation and two standard deviation measurements.*

threshold using right-handed electrons ($P_L = +0.90$) and ignoring beamstrahlung is shown in Fig. 2.3.21 a). The excitation curve rises as β^3, slower than for spin 1/2 particles. An event sample of $\mathcal{L} = 100\,\mathrm{fb}^{-1}$ integrated luminosity equally shared between 10 measurements in the center of mass energy range $\sqrt{s} = 550\,\mathrm{GeV}$ to $\sqrt{s} = 560\,\mathrm{GeV}$ is assumed. A χ^2 analysis of the threshold scan, results shown in Fig. 2.3.21 b), yields a statistical sensitivity to the scalar muon mass of

$$m_{\tilde{\mu}_R}(\mathrm{obs},\, \mathrm{e}^-_R) \;\; = \;\; 275.1\; ^{+0.35}_{-0.30}\,\mathrm{GeV}\ .$$

No attempt has been yet done to optimize the choice of beam energy settings and integrated luminosities; also, beamstrahlung effects have not be taken into account. Nevertheless, a cross section measurement at the kinematic threshold without significant background allows an improvement on the the scalar muon mass measurement $m_{\tilde{\mu}_R}$ of a factor between two and three with respect to the other technique discussed.

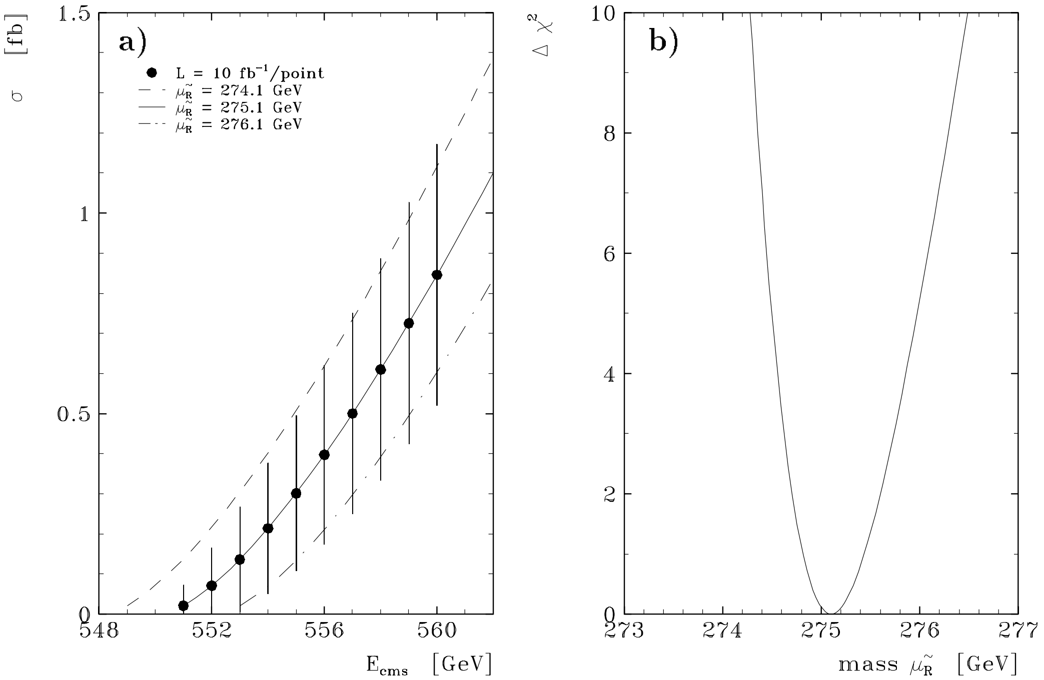

Figure 2.3.21: *a) Cross section for* $\mathrm{e}^+\mathrm{e}^-_\mathrm{R} \to \tilde{\mu}_R\,\tilde{\mu}_R$ *around the kinematic threshold without beamstrahlung effects, assuming* $\mathcal{L} = 10\,\mathrm{fb}^{-1}$ *per measurement (•). The curves indicate scalar muon masses of* $m_{\tilde{\mu}_R} = 275.1 \pm 1.0\,\mathrm{GeV}$. *b) Result of a* χ^2 *analysis versus* $m_{\tilde{\mu}_R}$.

To summarize, the study of the reaction $\mathrm{e}^+\mathrm{e}^- \to \tilde{\mu}^+_R\,\tilde{\mu}^-_R \to \mu^+\,\chi^0_1\,\mu^-\,\chi^0_1$ carried out with the proposed detector will lead to the precise determination of the scalar muon $\tilde{\mu}_R$ and neutralino χ^0_1 masses. With simple selection criteria a reasonably high detection efficiency and clean event samples can be obtained; the background is expected to be small and manageable. The energy spectrum of the decay lepton provides a very powerful tool to measure masses. Collecting a luminosity of $\mathcal{L} = 125\,\mathrm{fb}^{-1}$ and using unpolarized beams at a center of mass energy of $\sqrt{s} = 800\,\mathrm{GeV}$ the expected mass accuracy is $\Delta m_{\tilde{\mu}_R} \simeq 1.8\,\mathrm{GeV}$ and $\Delta m_{\chi_1^0} \simeq 2.3\,\mathrm{GeV}$. The use of right-handed polarized electrons turns out to be extremely valuable. The signal can be enhanced by almost a factor of two and the main background (W pair production) can be suppressed by an order of magnitude. The same integrated luminosity, with e_R^- beam 90 % right-handed polarized, would allow mass determinations with a precision of

$$\begin{aligned} \Delta m_{\tilde{\mu}_R} &\simeq 0.8\,\mathrm{GeV}\ , \\ \Delta m_{\chi_1^0} &\simeq 1.7\,\mathrm{GeV}\ . \end{aligned}$$

An even more accurate mass measurement of the scalar muon $\tilde{\mu}_R$ may be obtained by a $\tilde{\mu}_R\,\tilde{\mu}_R$ production cross section scan around the kinematic threshold. Again polarized electrons are very important. The expected sensitivity is $\Delta m_{\tilde{\mu}_R} \sim \mathcal{O}\,(350\,\mathrm{MeV})$. More sophisticated simulations, including beamstrahlung, for the threshold scan are in progress. The physics reach for this measurement is not limited by detector performances. Beamstrahlung effects, however, might be more dangerous in impairing the physics reach of this measurement and other relying on reconstructing threshold behavior of the cross section.

2.3.8 Conclusions

The design of the detector for the next generation of electron colliders, as described in this chapter was tested evaluating its performances through detailed Monte Carlo simulations. Five different reactions were selected on the basis of both physics relevance and experimental peculiarities:

- The study of top production and decay at threshold, a topic of great physics relevance: the expected experimental reach of the linear collider will give a $\approx$ 0.1 % precision in the mass measurement. From the experimental point of view this process depends upon the ability of the apparatus to reconstruct multijet events and extract invariant masses of combinations of jets. A reasonable capability for tagging detached vertices is needed. Beamstrahlung phenomena have to be kept under control and measured during data taking. The proposed set-up should be able to measure the top mass to better than 110 MeV; the total top width is expected to be measured with a relative precision smaller that 20 %. As a by-product of this measurement, α_s would be measured to a relative precision better than 3 %. The luminosity required is of the order of $50\,\mathrm{fb}^{-1}$.

- If the Higgs boson mass is in the region below the WW threshold the linear collider will have important contributions to make. This study has shown that our chosen detector can measure the total cross section for production of the standard model Higgs boson in this region with good precision, and recognize its decay products. The quality of the vertex detector and the tracking system are particularly important for measuring branching ratios to discriminate between the Higgs bosons predicted by different models.

- The associate production of H and A bosons was chosen also to check the capabilities of the detector both on detached vertices identification and on jet detection and reconstruction. The proposed apparatus will detect and identify the H A production in the mass range up to 340 GeV if the collider will deliver $\approx 200\,\mathrm{fb}^{-1}$ at 800 GeV total energy; the H A signal can, however, be identified also at reduced luminosity ($50\,\mathrm{fb}^{-1}$) with a less precise measurement of the production cross section.

- W pair production, with its very forward peaked angular distribution, requires good angular coverage and good resolution on the momentum (and charge where possible) of tracks going into the forward regions, especially leptons. With the proposed detector and integrated luminosity of $50\,\mathrm{fb}^{-1}$ at 500 GeV E_{cm} limits on the anomalous couplings of the order of 10^{-3} will be reached.

- The linear collider will be particularly suited to the study of lepton and gauge boson superpartners, at whatever mass they are to be found. These studies have shown that if smuons and/or charginos are kinematically accessible at any part of the energy range of the machine then they can be identified and their masses can be measured to better than 1 %.

The overall performance of the detector described in section 2.2 is, on the basis of this selected set of reference reactions, more than adequate to give a uniquely important programme of measurements. Most of the studies have shown that the sensitivity will be limited either by statistics or by such unavoidable features of the detector as the loss of particles close to the forward direction. There is still scope for more detailed studies, including other physics processes and using full GEANT simulation in places, to refine the design and point to regions where further detector R & D will be needed.

Bibliography

[1] H.J. Schreiber, code SIMDET, available upon request from "schreibe@ifh.de"

[2] G.W. Wilson, talk to the ECFA/DESY workshop at MPI-Munich, 16-17 September 1996.

[3] G. Crawford et al. (the CLEO II collaboration), "Luminosity measurement with the CLEO II detector", Nucl. Instrum. and Meth. A345 (1994) 429-439.

[4] S. Jadach and B. Ward, private communication.

[5] M.N. Frary, D.J. Miller, "Monitoring the Luminosity Spectrum", DESY 92-123A, p. 379.

[6] N. Toomi, J. Fujimoto, S. Kawabata, Y. Kurihara, "Luminosity measurement in future e^+e^- linear colliders using large angle Bhabha events", KEK-CP-051, November 1996.

[7] T. Sjöstrand, Comp. Phys. Comm. 84 (1994) 74.

[8] S. Bethke, Z. Kunszt, D.E. Soper, W.J. Stirling, "New Jet Algorithms: Next-to-leading Order QCD and Hadronization Corrections", CERN-TH 6222/91.

[9] P. Comas et al., "The physics of the e^+e^- threshold scan" in: Proceedings of the Workshop on e^+e^- collisions at TeV energies: the Physics Potential, Annecy, Gran Sasso, Hamburg, February to September 1995, ed. P.M. Zerwas, DESY Report 96-123d, pp. 57–66.

[10] A. Venturi, in: Proceedings of the Workshop on e^+e^- Collisions at 500 GeV: The Physics Potential Munich, Annecy, Hamburg, November 1992 to April1993, ed. P.M. Zerwas, DESY Report 93-123c, pp. 269–281.

[11] M. Schmitt, "Top Production and Decay Form Factors" in: Proceedings of the Workshop on e^+e^- collisions at TeV energies: the Physics Potential, Annecy, Gran Sasso, Hamburg, February to September 1995, ed. P.M. Zerwas, DESY Report 96-123d, pp. 67–74.

[12] M. Martinez and S. Orteu, "Direct measurement of the top quark Yukawa coupling", in: Proceedings of the Workshop on e^+e^- collisions at TeV energies: the Physics Potential, Annecy, Gran Sasso, Hamburg, February to September 1995, ed. P.M. Zerwas, DESY Report 96-123d, pp. 75–82.

[13] G. Blair, to appear in DESY 97-123E.

[14] P.M. Zerwas, in: Proc. of the International Conference on High Energy Physics, Marseille, 1993;
A. Djouadi, Int. Mod. Phys. A10 (1995) 1.

[15] J. Kamoshita et al., in: Proc. of the Workshop on Physics and Experiments with Linear Colliders, Vol. II, World Scientific, Singapore 1996.

[16] A. Djouadi, M. Spira and P.M. Zerwas, DESY 95-210.

[17] P. Grosse-Wiesmann, D. Haidt and H.J. Schreiber, DESY 92-123A;
P. Janot, LAL 93-38;
H.D. Hildreth, T.L. Barklow and D.L. Burke, Phys. Rev. D49 (1994), 3441.

[18] M. Sachwitz, H.J. Schreiber and S. Shichanin, to appear in DESY 95-123E.

[19] M. Battaglia and R. Vuopionperä, to appear in DESY 97-123E.

[20] P. Janot, "The HZHA generator", in Physics at LEP2, Eds. G.Altarelli, T. Sjostrand and F. Zwirner, CERN 96-01, Vol.2, p. 309.

[21] F.A. Berends, R.Kleiss and R. Pittau, Nucl. Phys. B424 (1994) 308; Nucl. Phys. B426 (1994) 344.

[22] C.Troncon, "Tagging Heavy Flavours with Vertex Detectors at e^+e^- Colliders", Proceedings of 5^{th} International Workshop on Vertex Detectors, VERTEX 96, Chia, Cagliari, Italy, 16/21 June 1996, to be published on Nucl. Instrum. and Meth.

[23] D. Brown, M. Frank, "Tagging b hadrons using track impact parameters", ALEPH 92-135, PHYSIC 92-124;
ALEPH Collab., D. Buskulic et al., Phys. Lett. B313 (1993), 535.

[24] DELPHI Collab., P. Abreu et al., Zeitschr. f. Phys. C65 (1995), 555;
DELPHI Collab., P. Abreu et al., Nucl. Instrum. and Meth. A378 (1996) 57;
G.V.Borisov, "Lifetime Tag of events $Z \to b\bar{b}$ with the DELPHI Detector", DELPHI 94-125/PROG 208, 1994.

[25] A. Andreazza and C. Troncon, to appear in DESY 97-123E.

[26] E. Boos et al., Moscow State University preprint SNUTP-94-116, Oct. 1994 and Korean Physical Society meeting, Oct. 21 1994, hep-ph/9503280.

[27] C. Papadopoulos, DEMO-HEP-96/02 and hep-ph/96099320, September 1996.

[28] H. Anlauf et al., Manual of WOPPER version 1.5.

[29] M.S. Skrypzek et al., Comp. Phys. Comm. 94 (1996) 216.

[30] T. Ohl, IKDA 96/13, hep-ph/9607454, July 1996.

[31] Z. Kunszt, Phys. Lett. 99B (1981) 429.

[32] C. Papadopoulos, Phys. Lett. B352 (1995) 144.

[33] M. Bilenky et al., Nucl. Phys. B409 (1993) 22.

[34] "Physics at LEP2", Vol.1, CERN 96-01 Yellow Report, edited by G. Altarelli, T. Sjöstrand and F. Zwirner, Geneva, February 1996.

[35] Proceedings of the Workshop on e^+e^- Collisions at 500 GeV: The Physics Potential, Munich, Annecy, Hamburg, November 1992 to April 1993, ed. P.M. Zerwas, DESY Report 93-123 A+B and DESY 93-123 C.

[36] T. Tsukamoto et al., Phys. Rev. D 51 (1995) 3153.

[37] S. Mrenna, "SPYTHIA, A Supersymmetric Extension of PYTHIA 5.7", ANL-HEP-PR-96-63 and hep-ph/9609360;
T. Sjöstrand, "PYTHIA 5.7 and JETSET 7.4, Physics and Manual", CERN-TH 7712/93.

2.4 Interface between Collider and Experiment

This section is devoted to the accelerator components or beam related aspects which either influence the design of the detector or are imposed by the detector performance. The machine and beam parameters are taken from the TESLA design, with SBLC parameters given in parentheses.

2.4.1 Beam Delivery System

The beam delivery system shown in Fig. 2.4.1 is the transfer line which transports the beam from the linac exit to the interaction point (IP) of the collider. The linac position with respect to the tunnel is shown in Sections 3.10 and 4.10 for TESLA and SBLC. The main function of the beam delivery system is to demagnify the beams and to bring them to collisions with spot sizes of $845\,\mathrm{nm}\times 19\,\mathrm{nm}$ ($335\,\mathrm{nm}\times 16\,\mathrm{nm}$) at the center of the detector. The overall demagnification from linac to IP is mostly produced by a strongly focusing quadrupole doublet 3 m (2 m) distant from the IP, integrated in a 140 m (125 m) long telescopic final transformer.

Even with the small, around $30\,\mu$rad, angular divergence of the beam at the IP, the chromaticity of this last doublet, roughly given by the ratio $\hat{\sigma}_{\mathrm{Q}}/\sigma^*$ of the maximum beam size in the last doublet to the beam size at the IP, is too large in comparison with the expected relative energy spread of 10^{-3} ($3.5{\cdot}10^{-3}$) of the incoming beam. The final transformer is therefore preceded by a 330 m (380 m) long S-shaped Chromatic Correction Section (CCS) where sextupoles, located in dispersive regions, create the necessary quadrupole correction for the off-energy particles. The energy bandwidth of this correction determines the energy acceptance of the whole system.

The transverse beam tails passing through the doublet quadrupoles produce synchrotron radiation which in turn can be a source of background in the detector. The photon energies and angles are maximum in the last doublet where masking is difficult. The beam halo and the low energy tail, possibly generated in the linac, are therefore scraped off in the collimation section by collimators placed at maxima of the horizontal and vertical betatron and dispersion functions. The 390 m (610 m) long collimation section, also S-shaped, is located upstream from the CCS and separated from it by about 210 m (330 m) of straight beam instrumentation and tuning sections.

This beam delivery system has been designed to allow for an adiabatic upgrade of the collider beam energy from 250 to 400 GeV for TESLA (250 to 500 GeV for SBLC) by simply increasing the magnet strengths without changing the geometry of the beam line nor the magnets.

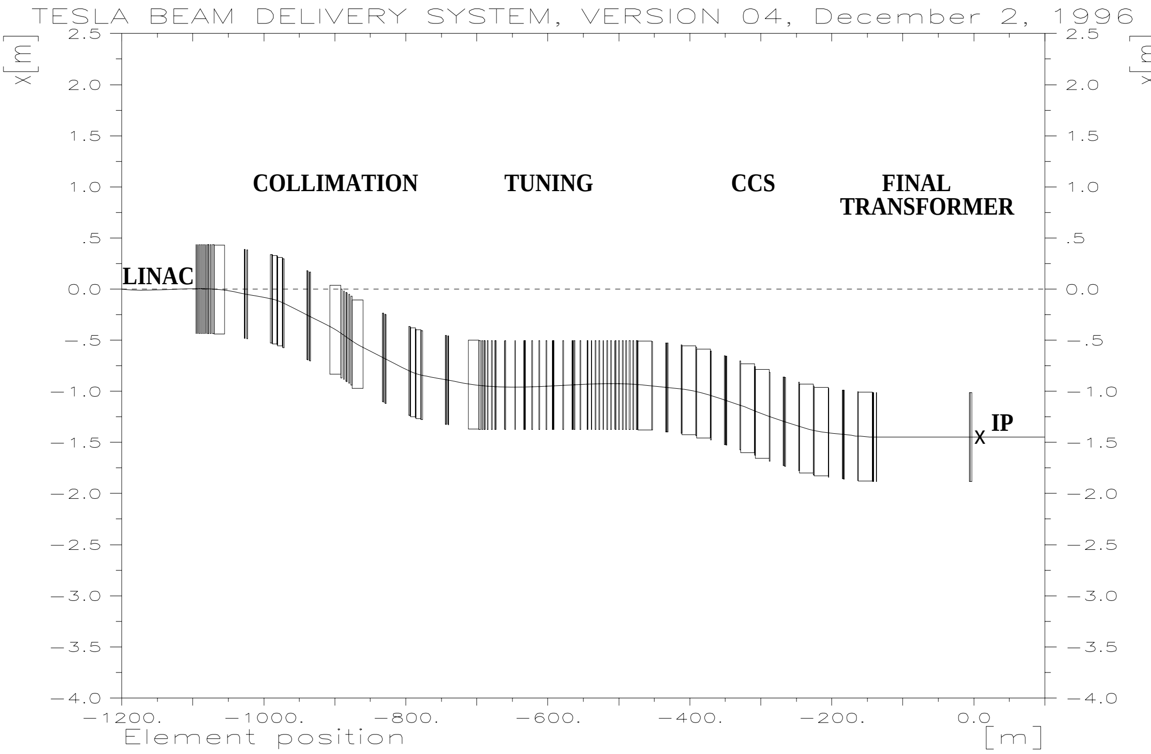

Figure 2.4.1: *Magnet layout and horizontal view of the TESLA beam delivery system from the Linac exit ($s = 0\,\mathrm{m}$) to the interaction point ($s = 1100\,\mathrm{m}$). The boxes indicate the position of the magnets.*

2.4.2 Interaction Region Layout

The interaction region layout is shown in Fig. 2.4.2 for TESLA. Since the doublet quadrupoles and cryostat are inside of the detector, the 3 T detector solenoid field is superimposed over the quadrupole field which precludes the use of an iron yoke to contain the quadrupole stray fields. For a quadrupole gradient of 250 T/m, the magnetic field reaches 8.4 T at its maximum on the conductor, and is only $5{\cdot}10^{-3}$ T at 600 mm radius [1]. The inner radius of the beam pipe inside the quadrupole is 24 mm, the outer radius of the cryostat 148 mm. The two 4.25 m long cryostats, facing each other on both sides of the IP, are separated by 5.5 m, the quadrupoles by 6 m.

The quadrupoles are covered by tungsten masks to suppress background from particles hitting the quadrupoles. Inside the masks the beam pipe reaches its smallest inner radius of 18 mm, while the radius is 40 mm at the tip of the mask (see Fig. 2.4.10). At the position of the vertex detector the radius is decreased to 20 mm – a more detailed

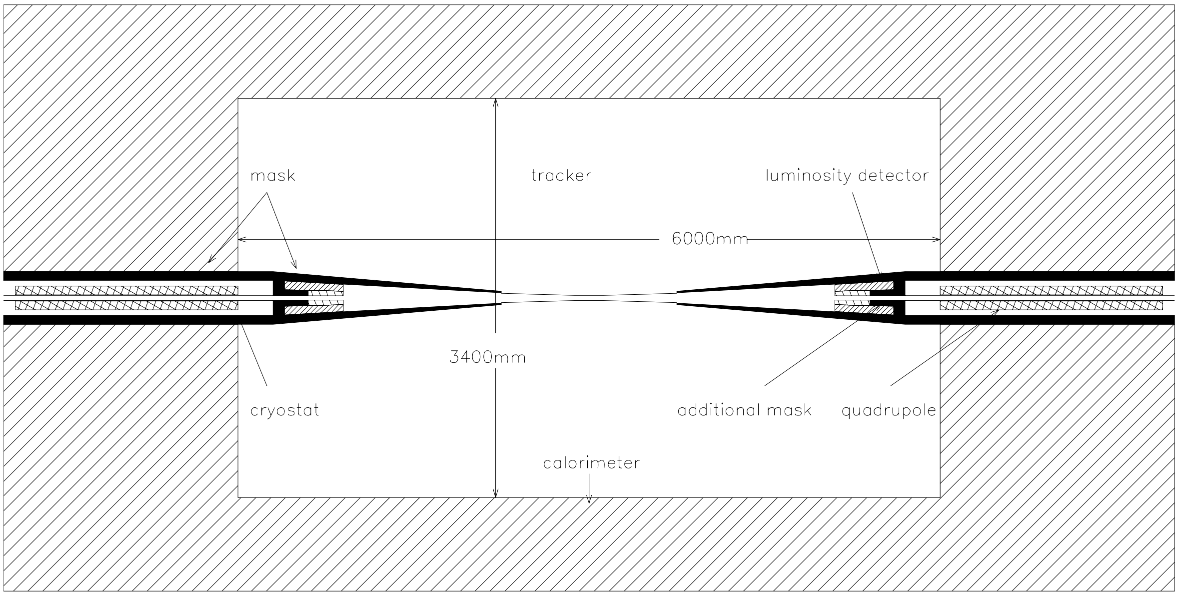

Figure 2.4.2: *TESLA (*500 GeV *c.m.) interaction region layout. The inner region is reserved for tracking. The hatched area represents the calorimetry (outer dimensions are arbitrary).*

description is given in section 2.4.4.

2.4.3 Accelerator Backgrounds

2.4.3.1 Synchrotron Radiation

Synchrotron radiation photons emitted by the incoming beam in the magnetic field of the last doublet quadrupoles has been identified as a major source of detector background at the SLC [2]. Although the average emitted power is only 35 W for TESLA (37 W for the SBLC), the average photon critical energy of 3.6 MeV (4.3 MeV) in the last quadrupole, is above the pair creation threshold. These photons are therefore difficult to shield and particularly harmful if they hit the inner part of the detector.

As can be seen from Fig. 2.4.3 the stay clear condition for the diverging photon flux is more constraining than the stay clear of the incoming beam itself. Requiring that all synchrotron radiation photons clear the exit aperture of the opposing doublet and the exit face of the detector implies that the incoming beam transverse tails do not extend beyond $14\,\sigma_x \times 46\,\sigma_y$ ($7\,\sigma_x \times 18\,\sigma_y$). For a circular aperture of TESLA, the collimation requirement for rectangular collimator apertures $n_x \times n_y$ in unit beam

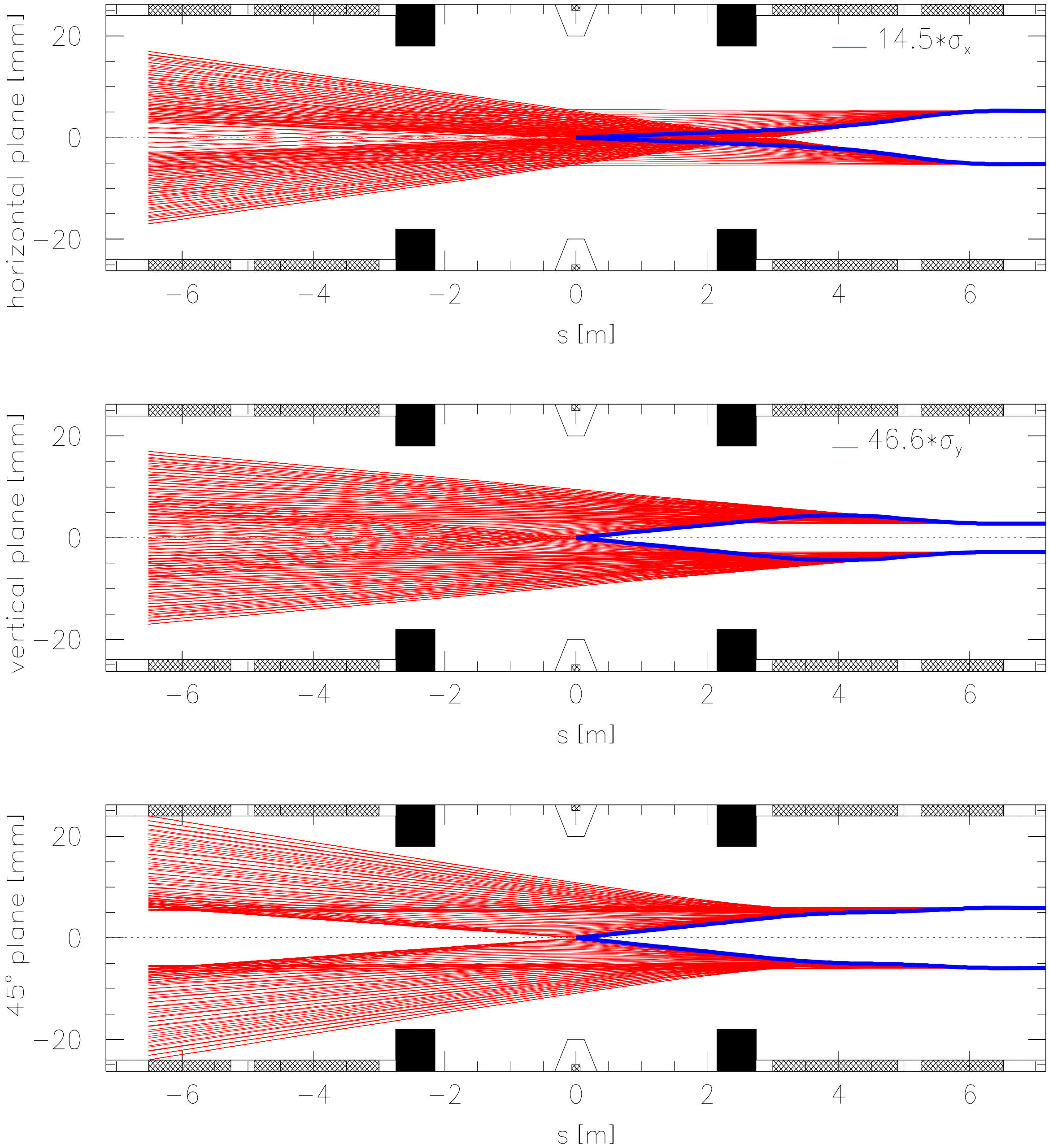

Figure 2.4.3: *Envelopes of synchrotron radiation photons emitted along the TESLA (500 GeV c.m.) last doublet quadrupoles through the vertex detector and opposing doublet apertures. Thick lines represent the envelopes of the incoming beam (entering from the right).*

sigmas, is actually given by

$$(n_x/14)^2 + (n_y/46)^2 = 2$$

in such a way that the photon flux fills a rectangle inscribed in the beam pipe aperture circle. Compared to the SLC beam collimation of $5\,\sigma_x \times 9\,\sigma_y$, these collimation requirements are quite loose. In fact, for the beam population considered, only non-gaussian tails can populate the beam at such numbers of sigmas. Generation of such tails in the linac is difficult to model. Therefore the proportion of beam intercepted by the collimators is difficult to predict, as is the background from muons produced at the collimator discussed in the following section.

Other sources of synchrotron radiation include the upstream quadrupoles of the final telescope and the last bending magnet of the CCS. The collimation requirements concerning the upstream quadrupoles are about 3 times looser than for the final doublet. In the case of TESLA, the photon flux originating from the last CCS dipole has a critical energy of 1.3 MeV. It must be horizontally collimated to fit through the detector inner beam pipe aperture. To achieve this, it is intended to use the beamstrahlung main collimator with 4 mm aperture radius located half-way of the final telescope, as shown in Fig. 2.4.5.

In conclusion, the collimation system can be designed such that no synchrotron radiation photon hits, directly or indirectly, any part of the detector.

2.4.3.2 Muons

In e^+e^- linear colliders muons produced in electro-magnetic beam-nucleon interactions in the beam delivery system can contribute an intolerable background in the detector. When electrons or positrons strike beam-line elements, e.g. the beam-halo collimators, muons are produced by a variety of mechanisms:

- Bethe-Heitler process with $\gamma \mathrm{Z} \to \mu^+\mu^-\mathrm{Z}$
- photo-production of pions $\gamma \mathrm{Z} \to \pi(\to \mu\nu) + \mathrm{anything}$
- direct e^+e^- annihilation, $e^+e^- \to \mu^+\mu^-$.

Of these, the most important muon source is the Bethe-Heitler process which produces about an order of magnitude more muons than the other processes.

The estimation of the muon background expected in the detector takes into account the beam-line elements of the TESLA and SBLC beam delivery systems (see section 2.4.1), the transverse dimensions of the corresponding tunnels and the positions of the beams as indicated in Fig. 2.4.1. Two independent programs were used, one developed at SLAC [3] and adapted for this study, and the other based on the CERN package GEANT [4][5], so that some confidence on the reliability and an idea

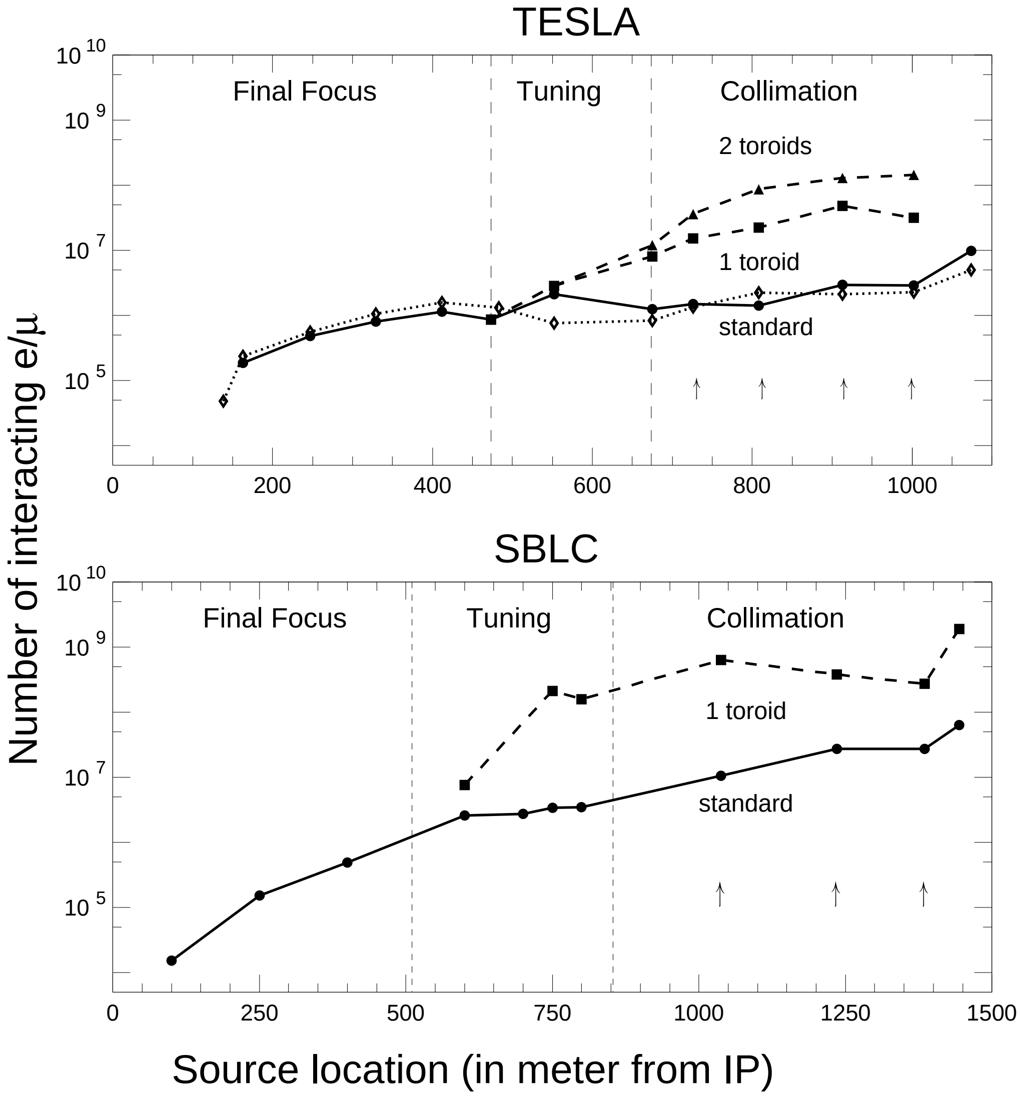

Figure 2.4.4: *The number of beam particles required to hit the source in order to produce one muon in the detector as a function of the source location for TESLA and SBLC (*500 GeV *c.m.). The arrows indicate the locations of the collimators, the dotted line is calculated using the GEANT based program developed for this study [5], the other lines are calculated using a program developed at SLAC [3].*

of the systematic errors have been obtained. The detector is approximated by a disk of 5 m radius, centered at the interaction point. All muons which hit the detector are counted, irrespective of their energy. The source of the muons has been placed anywhere between the beginning of the collimation part and the IP. The muons have been produced randomly according to theoretical momentum and angular distributions [6] and tracked through the beam delivery system taking into account multiple coulomb scattering, energy loss, decay and bending in the magnetic fields, until they stop or reach the detector.

Figure 2.4.4 shows for the TESLA and SBLC designs the number of beam particles $N_{\rm int}$ which have to interact in order to produce one muon in the detector, as a function of the muon source location. Interactions of beam particles are likely to happen in the beam-halo collimators (spoilers) which are located several hundreds of meters upstream of the IP. Muon fluxes resulting from these positions are indicated by arrows in Fig. 2.4.4. Averaging over the spoiler positions yields $N_{\rm int} = 2 \cdot 10^6$ for TESLA and $N_{\rm int} = 2 \cdot 10^7$ for SBLC. The difference between TESLA and SBLC arises mainly from the different beam line positions in the tunnel and the material to be installed.

Beside this direct muon production, muons can also be produced by interactions of electro-magnetic shower particles (photons, electrons, positrons) created when the beam strikes a spoiler. These particles are to a great extent absorbed in the iron absorbers positioned further downstream. Their rates and energy distributions in the absorber have been calculated and, in turn, used as input of the muon production and tracking programs. The rate of such muons has been found to be very similar to that of the "directly produced" muons.

Finally, the allowed fractional beam loss on the spoilers $\epsilon_{\rm lost}$, in order to have less than one muon in the detector, is given by the ratio of tolerable number of intercepted beam particles $N_{\rm int}/2$, where the factor of 2 accounts for the electro-magnetic showers, to the total number of particles in the two beams $2N_{\rm e}N_{\rm b}$, where $N_{\rm e}$ is the number of particles per bunch and $N_{\rm b}$ is the number of bunches. For TESLA with its large bunch spacing no pile-up of muons is expected and $N_{\rm b} = 1$, while for the SBLC design, a detector read out time of 100 ns is assumed, thus $N_{\rm b} = 17$, in such a way that

$$\begin{aligned} \epsilon_{\rm lost} &= 1.4 \cdot 10^{-5} \qquad \text{(TESLA)} \\ \epsilon_{\rm lost} &= 2.8 \cdot 10^{-5} \qquad \text{(SBLC).} \end{aligned}$$

If, for some unexpected reasons, the muon rate will be intolerably large, additional devices like magnetized iron toroids [3] or nested magnetized iron cylinders with opposite-polarity azimuthal magnetic fields [7] positioned downstream of the muon source are able to reduce the muons considerably. An example of such muon rate reduction is also shown in Fig. 2.4.4: here, one or two iron toroids of 9 m length each have been installed in the final focus section relatively close to the IP. They add one to two orders of magnitude of protection.

2.4.3.3 Beam-Gas

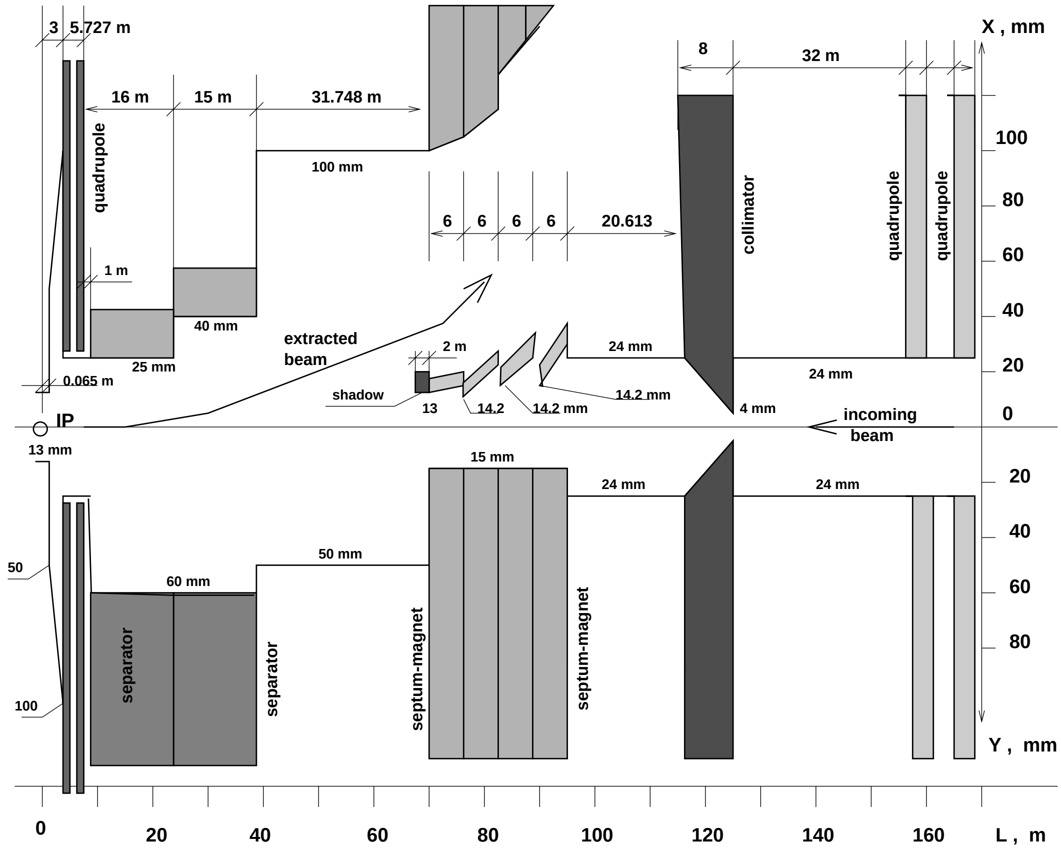

Figure 2.4.5: *TESLA (800 GeV c.m.) beam line aperture.*

The contribution to the background rates in the detector due to beam-gas interactions has been calculated using the same approach as [8, 9] for the TESLA 800 GeV design. Background rates for the 500 GeV design can be scaled down linearly with the energy. Interactions of the 400 GeV electron beam with residual gas, induced electro-magnetic showers, production of muons and hadrons and their transport are simulated with the latest version 13(96) of the MARS code [10]. Along with the detailed geometry and magnetic field description and advanced tracking algorithms for electro-magnetic and hadronic showers, the calculations include prompt muon production by electrons and photons (Bethe-Heitler pairs $\gamma Z \to Z\mu^+\mu^-$ and direct positron annihilation $e^+e^- \to \mu^+\mu^-$), muon production in π, K, charmed, and vector meson decays and the dimuon continuum, hadron production in photo-nuclear and deep inelastic muon interactions. The cut-off energies for particles in these calculations are 1 MeV for charged hadrons, muons and $e^\pm$, 0.2 MeV for photons and 0.5 eV for neutrons. The gas pressure is

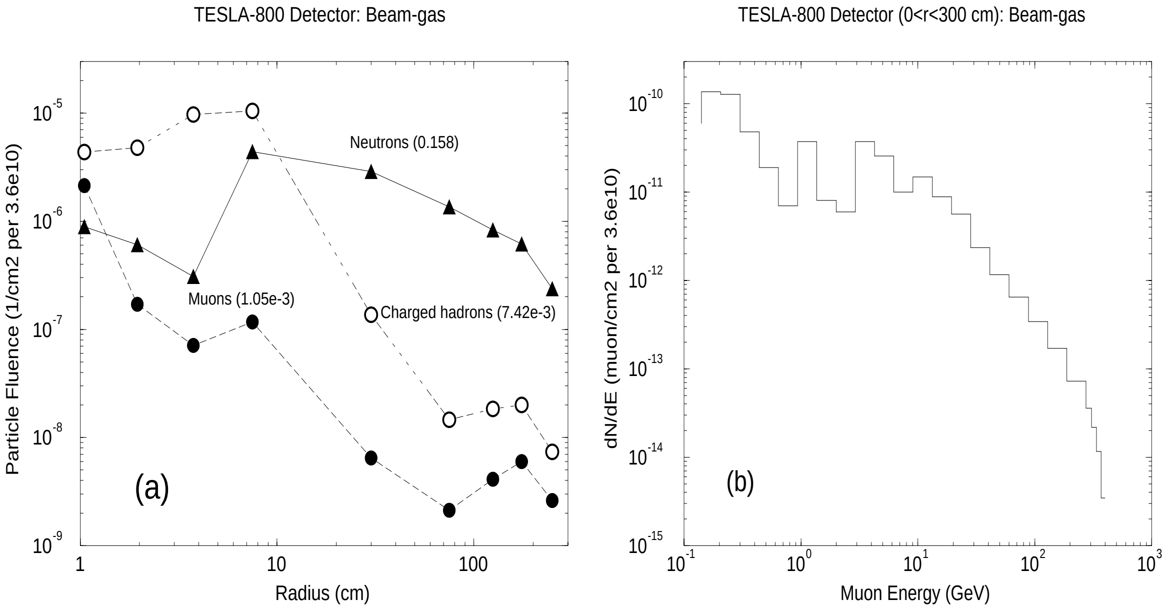

Figure 2.4.6: *TESLA (800 GeV c.m.) interaction region: (a) Muon, charged hadron, and neutron flux* ($1/\mathrm{cm}^2$) *per bunch due to beam-gas interactions in the final focus, as a function of the radius from the center of the detector. Indicated in the parenthesis are the integrated numbers of particles at the detector. (b) Radially averaged muon spectrum at the detector due to beam-gas interactions.*

assumed to be 10^{-7} mbar, and results can be linearly rescaled for other pressures. The geometry of the TESLA-800 beam line layout as it is used for the MARS simulations is shown in Fig. 2.4.5. Three-dimensional geometry and material descriptions of the final-focus quadrupoles, separators, septum magnets, shadow, collimator and drifts in the 170 m region from the IP are taken into account in the simulations. Magnetic fields in the final-focus quadrupoles (250 T/m) and septum magnet (0.08 and 0.12 T) are included as well. No detailed description of the detector, tunnel and experimental hall is included in the model at this stage.

Particle fluxes coming to the detector due to 400 GeV electron beam interactions with the residual gas in the 170 m long region in the IP vicinity are presented in Fig. 2.4.6(a) as a function of the distance from the beam axis. Charged hadrons dominate at small radii, but at $r \geq 10$ cm the main contribution is due to low-energy neutrons. Although the entire region is responsible for the production of background particles, soft neutrons are mostly produced in the few meter vicinity of the IP where details of the detector, tunnel and experimental hall geometry might affect the results. The energy spectrum of muons coming to the detector due to beam-gas interactions is shown in Fig. 2.4.6(b).

For the foreseen vacuum level of better than 10^{-8} mbar at the interaction region and 10^{-7} mbar in the beam delivery system, background from beam-gas interaction is negligible. The numbers given can be scaled linearly for different beam energies, bunch charges and vacuum pressure.

2.4.4 Beam-Beam related Backgrounds and Masking

The high charge density of the colliding beams produces strong electro-magnetic fields which bend the trajectories of the particles of the oncoming bunch. This focusing effect reduces the effective beam size and enhances the total luminosity. However, at these high energies, this beam-beam interaction also induces an intense emission of hard "beamstrahlung photons" which degrades the energy distribution of the beams during collision. The resulting dilution the luminosity spectrum is shown in Fig. 2.4.7 for the TESLA 500 GeV parameters. Keeping this dilution acceptable for the experiment sets a lower limit on the horizontal spot size, which in turn limits the luminosity.

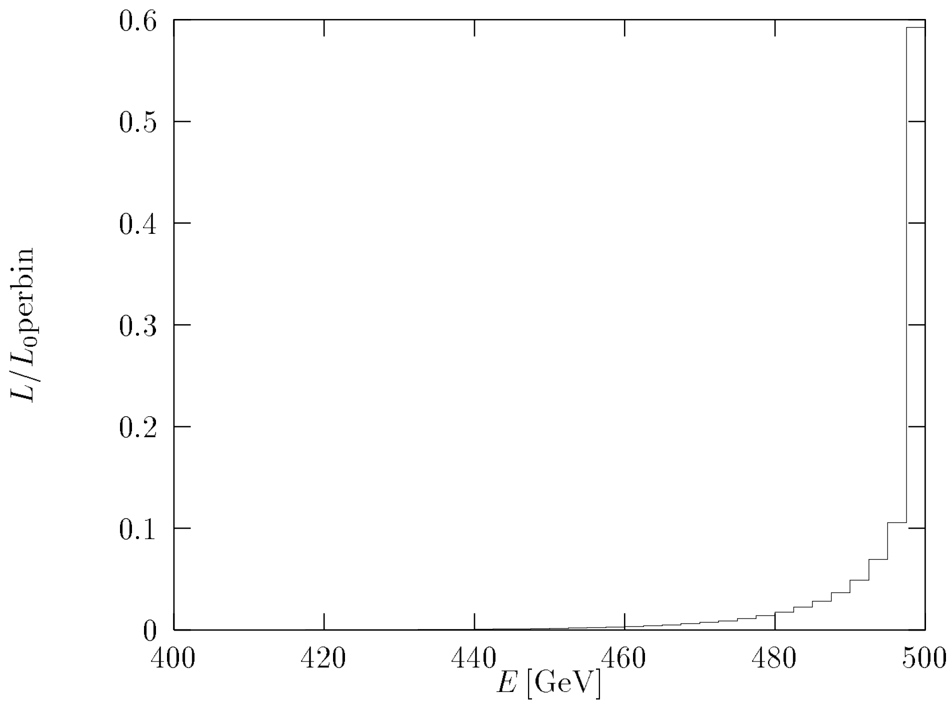

Figure 2.4.7: *Luminosity spectrum for TESLA (*500 GeV *c.m.) parameters, as resulting from beamstrahlung alone.*

The lowest part of the outgoing beam energy spectrum is plotted in Fig. 2.4.8 and their average energy loss δ, of the order of a few percent, is given in Table 2.4.1 for two sets of TESLA and SBLC parameters. As shown in Fig. 2.4.8, the outgoing beam energy spectrum is dominated by the bremsstrahlung spectrum, discussed later, for particle energies below 100 GeV. Tracking simulations show that, despite the emittance degradation, the outgoing beam particles originating from the IP lie within the acceptance of the opposing doublet as long as the particle energy is larger than 90 GeV.

One of the main background sources in the detector is the production of electron-positron pairs via coherent or incoherent processes in the beam-beam interaction. In

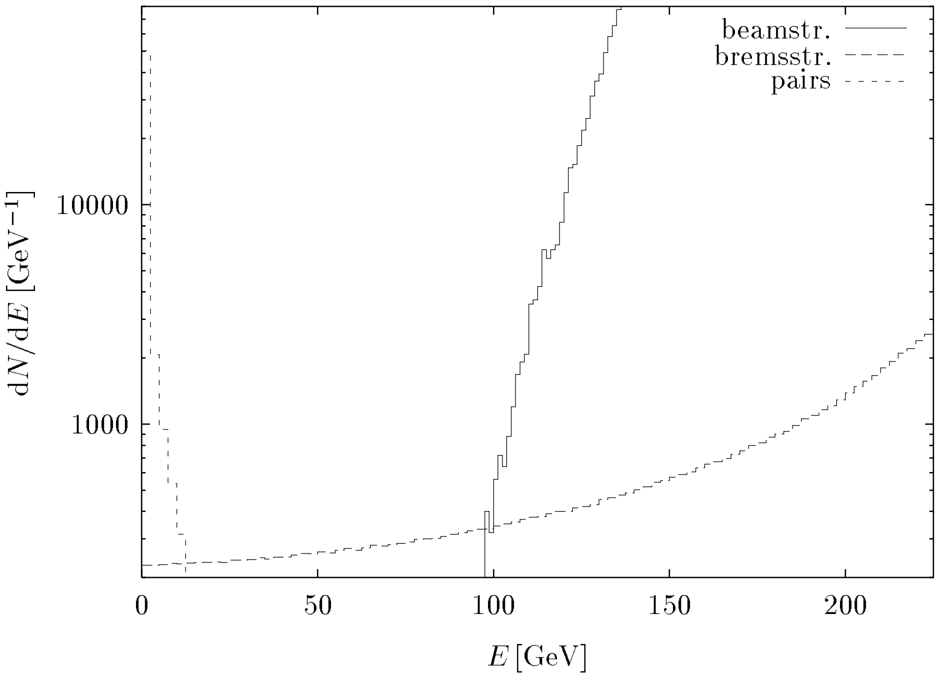

Figure 2.4.8: *The energy spectrum of the outgoing beam due to beamstrahlung effects and bremsstrahlung, and the spectrum of the particles due to pair production, for TESLA (*500 GeV *c.m.) parameters.*

addition beam particles can emit bremsstrahlung photons hard enough that the remaining low energy particle is lost inside the quadrupoles. Also relatively low energy hadronic events contribute to the background. The beamstrahlung is emitted into a very narrow cone of less than 0.5 mrad for the core and thus exits the detector safely without producing any direct background. It only enhances the production of pairs and hadrons due to beam-beam interaction.

In principle pairs can be produced via coherent and incoherent processes[3]. The coherent ones can be neglected if the beamstrahlung parameter Υ is smaller than

[3]The production of muon pairs is strongly suppressed compared to electrons due to their larger mass.

		TESLA		SBLC	
E_{cm}	[GeV]	500	800	500	750
L	$[10^{33}\,\mathrm{cm}^{-2}\mathrm{s}^{-1}]$	6.0	5.7	5.3	5.5
δ	[%]	2.5	5.2	2.8	4.8
N_P	$[10^3]$	96	180	24	70
E_P	$[10^3\,\mathrm{GeV}]$	164	650	53	290
$N_\perp$		31	46.5	7.1	17
N_{Hadr}		0.13	0.46	0.04	0.17
N_{MJ}	$[10^{-2}]$	0.3	1.6	0.1	0.66

Table 2.4.1: *Luminosity L, average energy loss δ, and background for different TESLA and SBLC parameter sets. N_P pair particles with a total energy of E_P are produced per bunch crossing of which $N_\perp$ have transverse momentum in excess of* $20\,\mathrm{MeV}/c$ *and an angle with respect to the beam axis of more than* $150\,\mathrm{mrad}$. *The number of hadronic events is N_{Hadr} including N_{MJ} minijet pairs with a transverse momentum of more than* $3.2\,\mathrm{GeV}/c$.

0.3 [11], as is the case for TESLA and SBLC. Three main processes contribute to the incoherent production of electron-positron pairs $\mathrm{ee} \to \mathrm{ee}(\mathrm{e}^+\mathrm{e}^-)$, $\mathrm{e}\gamma \to \mathrm{e}(\mathrm{e}^+\mathrm{e}^-)$ and $\gamma\gamma \to \mathrm{e}^+\mathrm{e}^-$, where the real photons arise from beamstrahlung. The first two processes can be calculated using the equivalent photon approximation, in which the electrons (and positrons) are replaced by a spectrum of photons. Most of the particles are produced at a small angle but are strongly deflected by the fields of the beams. If the particles move initially in the direction of the beam with the same charge, they are over-focused, if they move into the opposite direction they are bent outwards. The maximal angle the particles can receive from the deflection is a function of their energy. Only a small number of particles is produced at a larger angle. The production and deflection of the pairs is simulated with the program GUINEA-PIG [12].

The number of particles produced with the standard TESLA parameters (the first column in Table 2.4.1) is about 10^5 per bunch crossing with a total energy of $1.6 \cdot 10^5$ GeV. Figure 2.4.9 shows the angle and transverse momentum of the pair particles after the bunch crossing. The numbers for the other parameter sets are listed in Table 2.4.1.

Another process that produces low energy particles is bremsstrahlung. In this process a beam particle emits a hard photon in the field of a single particle of the other bunch. The photon escapes through the beam pipe, while the remnant beam particle contributes to the background. It is calculated using the equivalent photon approximation. The resulting spectrum of low energy beam particles is almost flat for small energies. These particles deposit a total energy of about $2{\cdot}10^5$ GeV per bunch

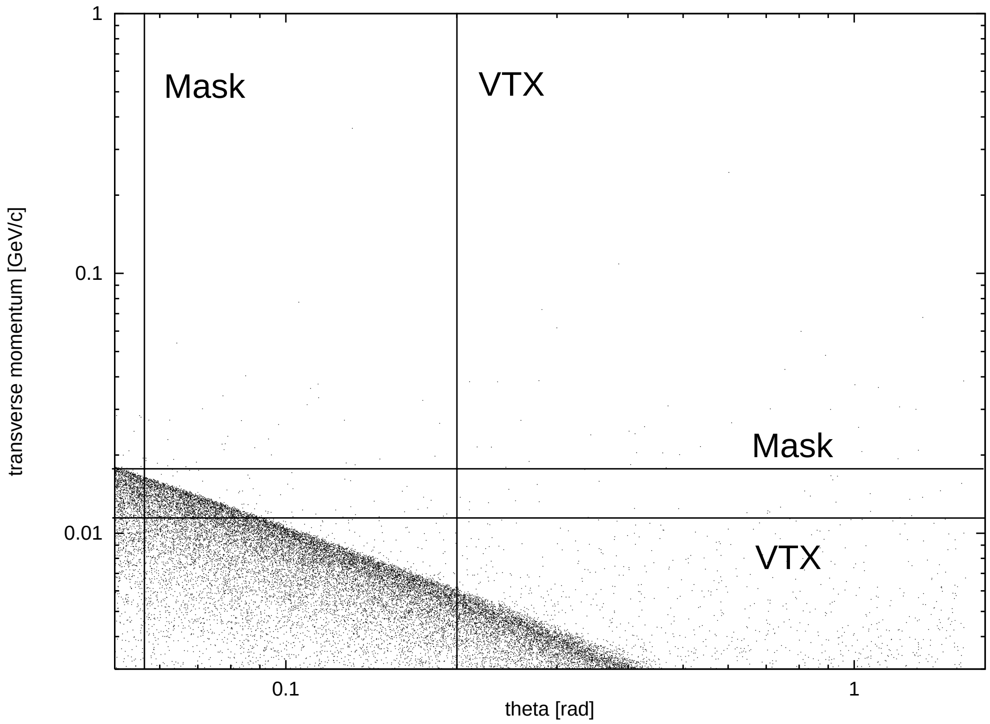

Figure 2.4.9: *Distribution after the interaction of the angle theta with respect to the beam axis and the transverse momentum of the particles from pair creation for TESLA (*500 GeV *c.m.) parameters. Indicated are the geometrical inner boundaries of the mask and the vertex chamber (VTX).*

crossing in the quadrupoles. The energy spectra of the pairs, and of the beam particles due to bremsstrahlung and beamstrahlung is shown in Fig. 2.4.8.

To estimate the background induced by the pairs and bremsstrahlung a detector simulation was performed on the basis of GEANT using the mask described below.

The large number of particles hitting the final quadrupoles leads to a high number of backscattered photons in the detector if it is not protected. The protection can be achieved with a conical mask mounted to a cylindrical one, as shown in Fig. 2.4.10. If the cone was extended its tip would be at the interaction point. The inner opening angle of the mask of 55 mrad is determined by the space requirement of the cryostat, which has a radius of 148 mm and starts at $|z| = 2750$ mm. The mask starts at $|z| = 750$ mm with an inner radius of $r_i = 41.7$ mm to let pass all the particles below the edge in Fig. 2.4.9 safely. The outer opening angle of 83 mrad is chosen to achieve the required thickness of the cylindrical part.

To minimize the thickness of the mask it is made of tungsten. In the electro-

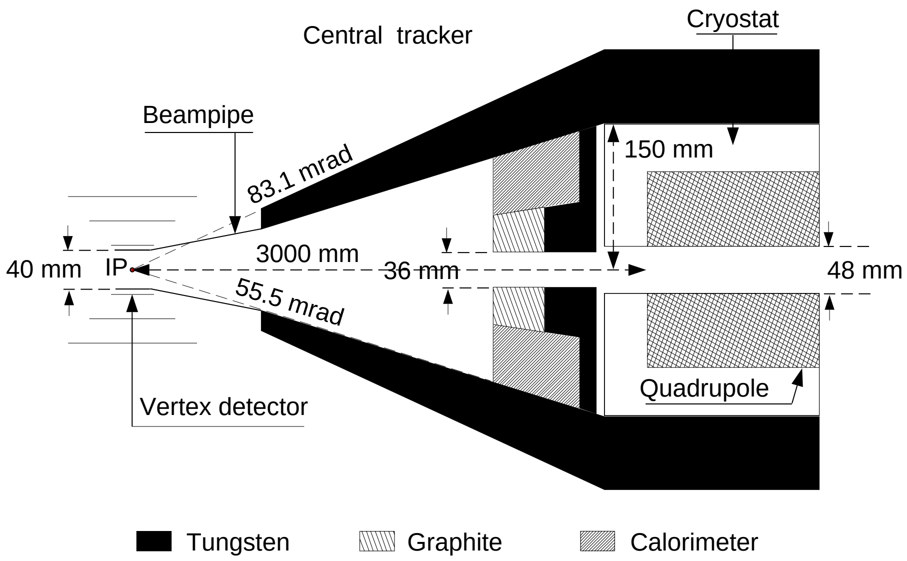

Figure 2.4.10: *Possible mask layout to suppress the background from pair creation for TESLA (*500 GeV *c.m.).*

magnetic showers a large number of photons is produced that are scattered out of the quadrupoles. While the spectrum of these photons peaks at a few hundred keV the most dangerous are those with energies of a few MeV since their total cross section in matter is small. The total energy of all photons outside the mask at a position $|z| < 5\,\mathrm{m}$ is about 400, 55, 10 or 2 GeV for mask thicknesses of 25, 50, 75 or 100 mm, respectively. A thickness of 75 mm was chosen to have a photon energy of less than 10 GeV outside the mask. For this thickness, about 600 photons per bunch crossing have to be expected in the drift chamber. This number depends on the design of the luminosity monitor which increases the effectiveness of the mask. A significant part of these photons is produced by the electrons and positrons which do not enter the mask but are rather trapped outside of it. The number of these particles is about 37 per bunch crossing for TESLA and most of them hit the mask on the outside producing secondary photons.

A number of particles is produced at larger angles and transverse momenta. These can hit especially the vertex detector. Figure 2.4.11 shows the number of charged particles hitting the inner layer of the vertex detector. The radius of this layer is varied but the angular coverage of $|\cos\theta| < 0.98$ is kept constant. Below a radius of about 10 mm the number of hits increase drastically. In this case, the detector would be hit by particles that received their angles and transverse momentum by the deflection of the beams.

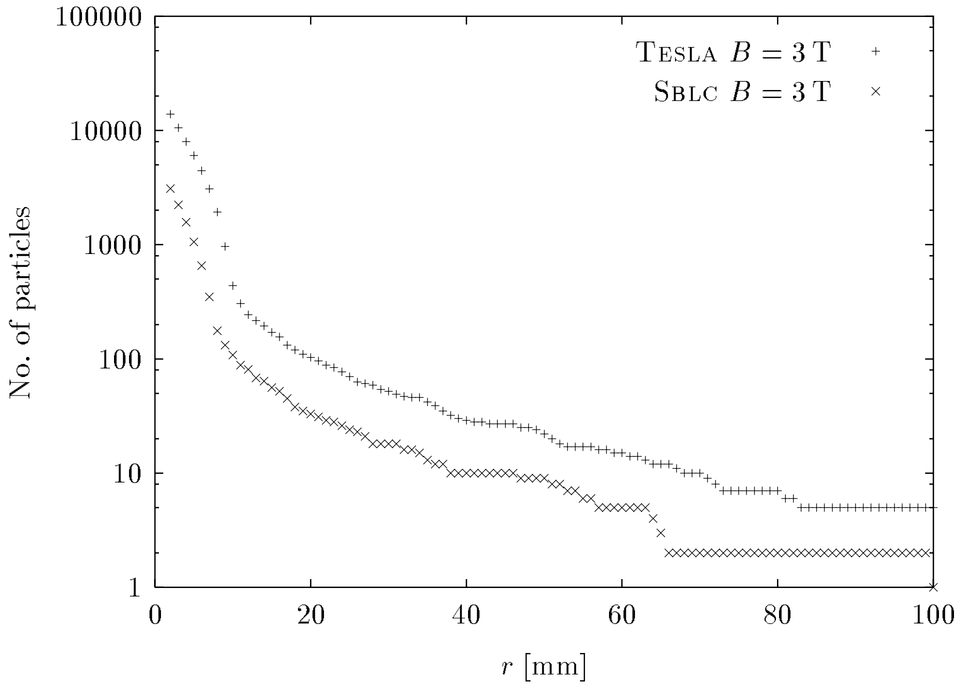

Figure 2.4.11: *The number of particles hitting the inner layer of the vertex detector as a function of its radius for an angular coverage of* $|\cos\theta| < 0.98$ *(for the* $500\,\mathrm{GeV}$ *c.m. parameters).*

The longitudinal and azimuthal distribution of the hits in the vertex detector layers is almost uniform with the center of the barrel showing a slightly higher hit density than the ends, see Fig. 2.4.12.

Almost all particles due to pair creation are lost inside the quadrupoles where the strong magnetic field bends their trajectories. At the ends of the quadrupoles facing the interaction point, the combined magnetic field of the outer main solenoid and quadrupole points towards the aperture. Soft charged particles produced in this region that leave the material of the quadrupole are led by these field lines back into the interaction point. The detector simulation shows that this can increase the number of hits in the vertex detector by an order of magnitude.

To suppress the backscattered charged particles an additional mask is used inside the main one. It consists of a material with a long radiation length (graphite) towards the interaction point to avoid particles scattering back at the mask. The other side is made of tungsten to reduce the background from the neutrons produced in the beamstrahlung collimator. The inner radius of the additional mask is set by the collimation system. The collimation is chosen such that no particle of the remaining tails could emit a photon in the final doublet that can hit the final doublet on the opposite side.

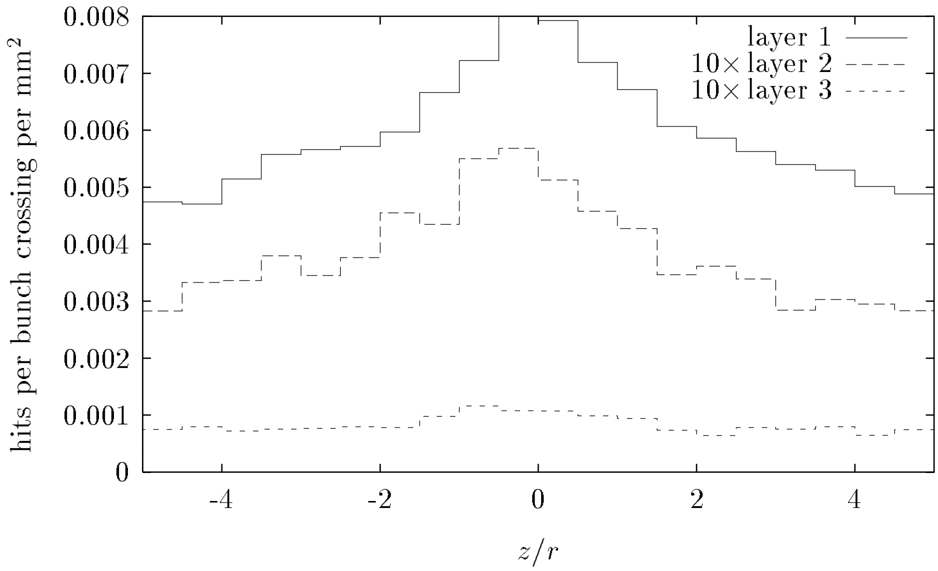

Figure 2.4.12: *The longitudinal distribution of the hits in the vertex detector for TESLA (*500 GeV *c.m.). The numbers for the layers two and three are enhanced by a factor ten. The azimuthal distribution is flat.*

In order to avoid that the additional mask can be hit by these photons its radius has to be at least 18 mm with the present collimation system (see Fig. 2.4.3). The radius of the beam pipe at the IP has to exceed the radius of the inner mask to achieve the suppression. It should therefore be at least 20 mm which leads to a minimal radius of the vertex detector of about 25 mm.

If it turns out to be desirable from the physics point of view to further reduce the beam-pipe radius at the interaction point in order to allow for a smaller radius for the vertex detector, this could be achieved by improving the collimation section and reducing the radius of the mask.

To avoid that the beam pipe is hit by a large number of particles which can emit bremsstrahlung photons its radius increases from 20 mm at $|z| = 125$ mm to 40 mm at $|z| = 750$ mm. In the simulation the inner most part of the beam pipe consists of a 1 mm thick beryllium tube while the outer parts are 1.5 mm thick. The detector simulation shows that the described mask suppresses the backscattering of charged particles to a negligible level.

At the radius of the vertex detector of 25 mm with an angular coverage of $|\cos\theta| < 0.98$ one finds about 230 hits per bunch crossing for TESLA which, including a safety factor of 1.5, leads to a hit density of about 10^{-2} mm^{-2}. For SBLC, the number of hits per bunch is 70, which leads to 1 hit per mm^2 and per bunch train.

As indicated in Fig. 2.4.10, low angle taggers will be incorporated inside the mask.

These could consist of tungsten calorimeters similar to those that are used presently for luminosity measurements. For TESLA, the simulation shows that the showers from the pair particles lead to soft photons with a total energy of about 250 GeV per side and bunch crossing in such low angle taggers. A single pair particle with an energy of more than 20 GeV would hit the tagger directly once per about 600 bunch crossings.

Photons in the electro-magnetic showers can produce neutrons via the giant resonance process. These neutrons have typical energies of around 1 MeV. For initial electrons with an energy of more than about 100 MeV the neutron yield is almost linear with the particle energy. In copper one neutron is produced per about 6 GeV, in tungsten per 2.5 GeV. The particles from pair production and bremsstrahlung produce about $6 \cdot 10^4$ neutrons per bunch crossing. In hydrogen rich material as for example scintillator low energy neutrons can produce slow protons which deposit their energy in a small distance via ionization.

An additional source of background is the production of hadrons by two colliding photons $\gamma\gamma \to \mathrm{X}$. In this process the photons fluctuate into hadrons with the same quantum numbers (usually ρ-mesons) and interact hadronically. The cross section for this process can be approximated as [13]

$$\sigma_H = 211\,\mathrm{nb} \cdot \left(\frac{s}{\mathrm{GeV}^2}\right)^{0.0808} + 297\,\mathrm{nb} \cdot \left(\frac{s}{\mathrm{GeV}^2}\right)^{-0.4525} \tag{2.4.1}$$

The hadronic content of the photon is suppressed if it has a significant virtuality. In the simulation this is taken into account by allowing for a maximal $Q^2 \leq 1\,\mathrm{GeV}^2$. For TESLA, the number of hadronic events with a center of mass energy in excess of 5 GeV is about 0.13 per bunch crossing. An event deposits on average an energy of 10 GeV at angles larger than 100 mrad in the detector.

Some of the hadronic events contain so-called minijets. These low energy jets can be produced via the direct process $\gamma\gamma \to \mathrm{q\bar{q}}$. Photons that interact as hadrons can also produce minijets if individual partons scatter either on the other photon (once-resolved process) or another parton from the other photon, which also interacts as a hadron (twice-resolved process), producing two minijets. The remnant part of the hadrons also forms jets with a small transverse momentum, the so-called spectator jets. While the cross section for the direct process decreases for higher photon-photon center of mass energies it increases for the once- and twice-resolved process, they can exceed the total hadronic cross section according to equation 2.4.1. This is not in contradiction if one assumes that at high center of mass energies the number of minijets per event increases rather than the number of events.

The simulation is performed using the parametrization of the partonic contents of the photon according to M. Drees and K. Grassie [14] as well as with the photon parametrization according to M. Glück, E. Reya and A. Vogt [15], which are compatible with measurements at HERA [16]. In TESLA the expected rate of minijets with a transverse momentum of 2.0 (3.2, 10) GeV/c is $(0.3, 0.0075) \cdot 10^{-2}$ per bunch crossing using the latter parametrization and thus significantly smaller than the total rate of hadronic events.

An additional background source are the beamstrahlung collimators which are located at a distance of about 120 m from the interaction point. These collimators are hit by around 200 kW of beamstrahlung photons, which produce about $8 \cdot 10^{13}$ neutrons per second adding both sides. Assuming a point-like source the neutron flux at the detector position is about $4.4 \cdot 10^4\,\mathrm{cm}^{-2}\mathrm{s}^{-1}$ or about $4.4 \cdot 10^{11}\,\mathrm{cm}^{-2}$ per year. The detector can be shielded from these neutrons by a concrete wall but this has to have an inner hole to let the beams and the beamstrahlung photons pass. The effect of the inner mask on the neutron flux has been calculated using a simulation based on the GEANT/MICAP-interface and results in a suppression by three orders of magnitude for neutrons with an energy of less than about 100 MeV. Thus, the neutron flux is several orders of magnitudes lower than expected in the inner vertex detector layer of the proposed ATLAS experiment at LHC [17], which is around $6 \cdot 10^{13}\,\mathrm{cm}^{-2}$ neutrons per year.

The tungsten of the inner mask can be instrumented to measure the total energy deposition of the pair particles, which is about 9000 GeV per side and bunch crossing. This signal can be helpful for tuning the machine to achieve higher luminosity.

2.4.5 Ground Motion Detection and Feedback

Fast beam steering at the interaction point, which relies on the beam-beam effect of colliding bunches, is a powerful tool to relax nanometer tolerances for final focus quadrupoles in linear colliders. These tolerances are determined by the vertical spot size which is 16 to 19 nm in the case of SBLC or TESLA. One stringent requirement for such a feedback, which corrects the bunch train offset in the IP is, that the beam pulse is long compared to the overall processing time of the detected signal from the beam position measurement (BPM) to the kicker magnet. Due to the low frequency approach and especially in case of a superconducting linac this is naturally fulfilled.

Parameters that influence this delay are the distance of the beam position monitor to the IP, the processing time of the feedback loop and the required magnetic field strength compared to the available peak power of the amplifier. The amplitude of pulse to pulse ground motion which can be expected from measurements done in the HERA tunnel, which is a tunnel under the city of Hamburg with an colliding beam facility, [18, 19] is approximately 70 nm rms for frequencies above 1 Hz which is roughly 5 times the design vertical beam size. In order to limit the luminosity reduction to 5 %, the jitter at the IP should be smaller than 30 % of the beam size, which is roughly 5 nm in our case. A list of the interaction region parameters can be found in the machine chapter of this report. Additional measurements in an existing experimental hall in HERA (Hall West) over a typical distance of a linear collider final doublet of 4 to 6 m have been done. The correlation decreases significantly at frequencies higher than

10 Hz but integrated from here, the measured rms amplitudes are at least an order of magnitude smaller. Therefore the IP jitter during collision driven by uncorrelated motion of quadrupoles is expected to be much smaller than 70 nm.

One possibility to achieve this tolerance is to design a passive support system that keeps the final doublets at a given position over a time scale much larger than the repetition rate of the accelerator. This is certainly a challenging task for the technical design of the quadrupole supports which are part of the experiment in a linear collider. Independent of other methods for feedback, this design task should be fulfilled as good as possible to avoid additional complications like, for example, resonances induced by the support structure itself.

For a round beam the beam-beam force of two colliding bunches is proportional to the separation of the two bunches over approximately one sigma. Operating with an aspect ratio ($=\sigma_x/\sigma_y$) of 20 (or more) as it is foreseen in linear colliders to reduce the beamstrahlung, produces an almost linear beam-beam force over approximately $10\,\sigma_y$. According to the beam-beam simulations the kick angle per σ_y separation of the two colliding beams is given by approximately 30 to $60\,\mu$rad which can easily be measured with a BPM 2 to 3 m downstreams. At this position the beam offset in the monitor would be $100\,\mu$m per σ_y separation at the IP, which is easy to measure as compared to the $4\,\mu$m resolution being required for the rest of the linac BPMs.

A method based on beam-beam deflections to measure precisely the offset of the two colliding beams has been used for single bunch operation in the SLC from pulse to pulse already [20]. While at TESLA a bunch to bunch measurement of the beam position can be used for both outgoing beams within one pulse, in case of the SBLC, a combination of both methods is proposed which uses a pilot bunch in one of the two colliding beam pulses and only a single BPM in combination with a single kicker magnet [21]. A much more detailed discussion on the SBLC and TESLA feedback systems which are foreseen in the interaction regions can be found in this report in the sections where instrumentation and diagnostics are discussed.

2.4.6 Beam Related Measurements

2.4.6.1 Fast Luminosity Measurement

The normal operation of the collider requires on-line measurement of the luminosity in order to rapidly detect beam detuning at the IP. A fast re-tuning of the beam beam delivery system (BDS), by means of horizontal spot size and luminosity optimization, will also be integrated in the machine control. A relative luminosity measurement, eventually cross-calibrated with a slower but absolute measurement of large angle Bhabha pairs in the central detector, should be able to resolve luminosity variations of the order of 1% ideally within one bunch train: this would require a counting rate of about 10 events per bunch crossing for TESLA.

Low-angle Bhabha pairs emitted along the beam pipe, unless detected inside of the last quadrupole doublet, cannot be measured against the 200 kW of beamstrahlung photons emitted in a forward cone of about 1 mrad. This is why the fast luminosity monitor, like at the SLC [22], is based on the detection of the radiative Bhabha electrons and positrons. As shown by Fig. 2.4.8, in order to provide a clear signal, the energy of these particles, produced in the forward direction relative to the same-sign incoming beam, should range from about 20 GeV, above the pair-created background, to 100 GeV where the beamstrahlung spectrum starts to dominate.

As a result of a simulation taking into account the action of the opposite beam coherent electro-magnetic field as well as the weaker effect of the main solenoid on the emitted radiative Bhabha particles, Fig. 2.4.13 shows the rates of lost particles within

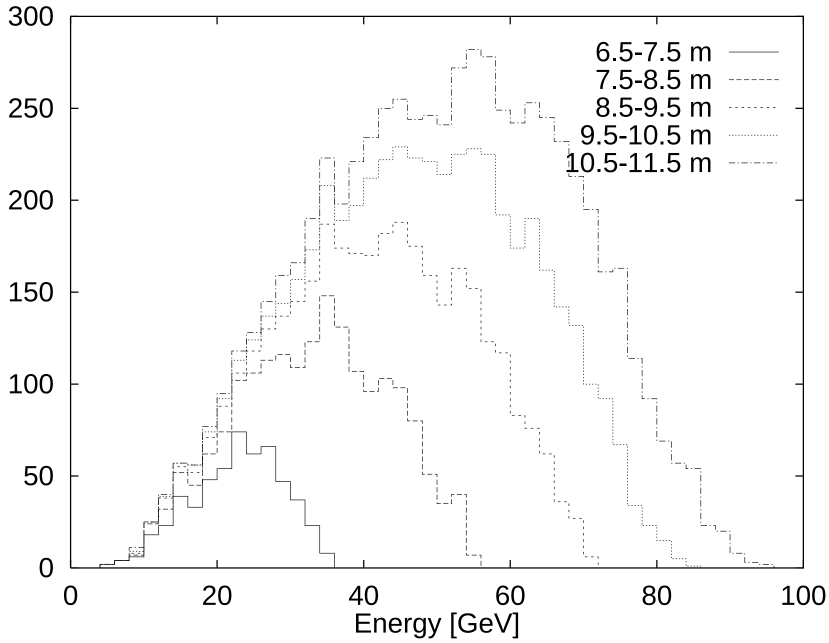

Figure 2.4.13: *Counting rates for radiative Bhabha electrons and positrons lost in the given z-ranges per bunch crossing for TESLA (*500 GeV *c.m.)*

different 1 m longitudinal ranges after the last doublet exit. Due to the peculiarities of the beam-beam and quadrupole focusing forces, all of these particles are lost in the horizontal plane. Located between 8.5 and 9.5 m, a luminosity detector would intercept particles around 50 GeV in energy and would be free from the background of outgoing beam particles with energies higher than 80 GeV, lost downstream.

The present ALEPH-BCAL calorimeter [23], designed to detect 45 GeV horizontal Bhabha pairs at LEP, would therefore be a good prototype for such a detector. Al-

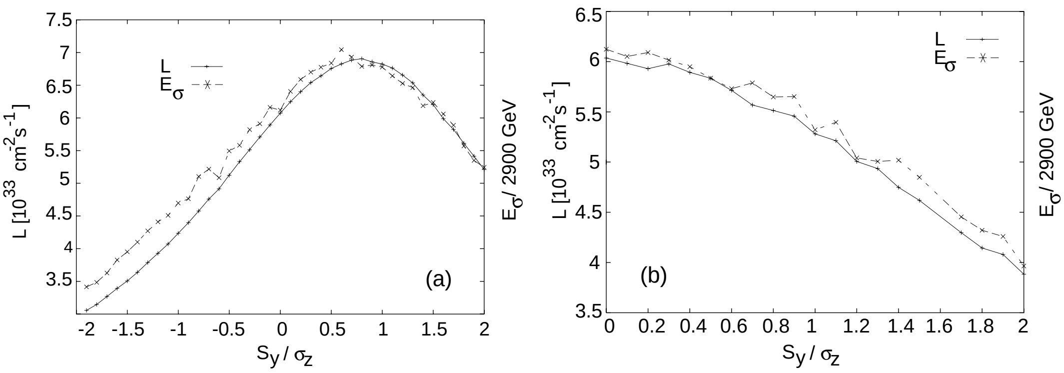

Figure 2.4.14: *Comparison of luminosity L and energy E_σ deposited by the* e^+e^- *pairs in the inner part of the mask if (a) the two vertical waists are symmetrically shifted by S_y with respect to the collision point along the beam axis and (b) for two coinciding vertical waists which are shifted with respect to the collision point, for TESLA (*500 GeV *c.m.) parameters.*

though its insertion and actual acceptance has not been calculated precisely, the total rate of about 5500 electrons and positrons lost in the 8.5 to 9.5 m range with an energy higher than 30 GeV suggests that the 1 % relative accuracy may be a realistic goal.

By instrumenting the inner part of the mask as a calorimeter one can use the total energy deposited by the pairs in this region to optimize luminosity. The signal depends on the produced photon spectrum, the luminosity and the deflection of the pairs by the beams. For constant bunch length, width and charge the spectrum and deflection are almost constant with a very weak dependence on the vertical bunch size. The deposited energy then depends only on the number of produced pairs which is proportional to luminosity.

One reason for a decreased luminosity is a shift of the vertical waists of the beams. In this case the position where the beam reaches its smallest vertical size lies either before ($S_y > 0$) or behind ($S_y < 0$) the collision point. Figure 2.4.14(a) shows the dependence of the luminosity and the pair energy deposited in the inner mask for two symmetrically shifted vertical waists. Optimal luminosity is reached if both beams are focused slightly before the collision point. Figure 2.4.14(b) shows the dependence of the luminosity and energy deposition if the two waists are at the same position but are shifted with respect to the collision point.

The achievable resolution has to be studied in detail. The main error may be due to changing bunch properties like the horizontal and longitudinal dimensions. With knobs to tune the vertical waist shift only, the relative signal can be used to maximize luminosity.

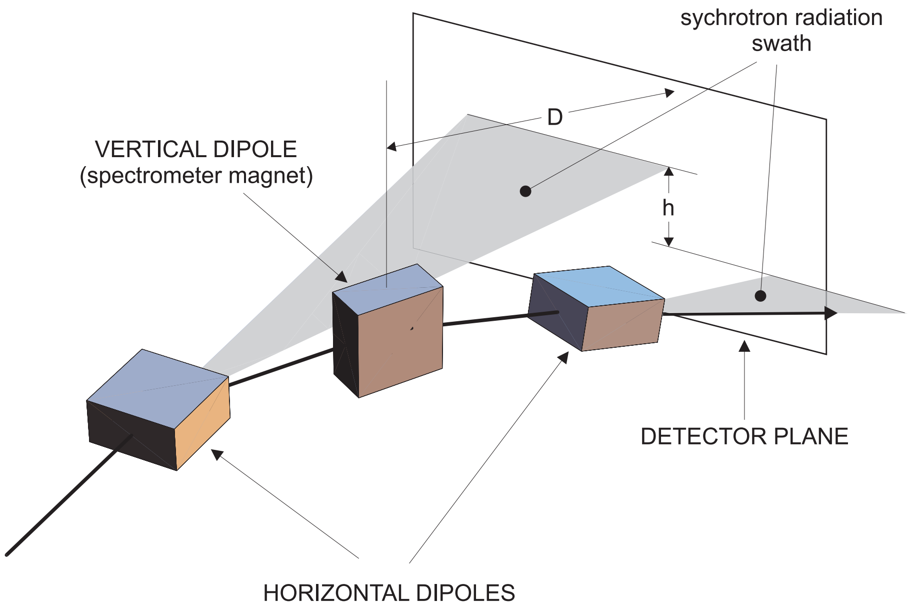

Figure 2.4.15: *Energy Spectrometer Concept (as used at the SLC/SLD). The vertical bend acts as the spectrometer magnet, while the two horizontal dipoles produce swaths of synchrotron light which are detected a distance D downstream. The bend angle (and hence the momentum) of the beam is given by h/D [not to scale].*

2.4.6.2 Energy Measurement

It is intended to place two precision spectrometers in both the electron and positron extraction lines to order to determine the absolute energy of each beam with a resolution of 10^{-4}. Since the beams are expected to loose some 3 % of their energy during the beam-beam interaction, it will be necessary to turn one beam off in order to make a measurement of the pre-collision energy of the other beam. Spectrometers based on the same design currently used at the SLC with a $5{\cdot}10^{-4}$ resolution will be used [24], a schematic of which is shown in Fig. 2.4.15. The spectrometer consists of a single high precision spectrometer magnet, either side of which are two small synchrotron light generating dipoles whose deflecting angles are in the opposite plane to the spectrometer magnet. The separation of the two bands of synchrotron light generated is measured by a suitable synchrotron radiation detector placed an accurately known distance downstream from the spectrometer magnet. The separation is proportional to the bend angle of the spectrometer magnet and hence the energy of the beam. At 250 GeV, a spectrometer magnet of length 5 m and field 0.24 T generates a bend angle of approximately 1.5 mrad. The energy loss from the magnet is approximately 25 MeV or 0.01 % which is acceptable given the required resolution.

Another method for measuring the absolute center of mass energy, based on radiative Z boson production and the precise knowledge on the Z mass, is described in section 2.3.1.2 of this chapter.

2.4.6.3 Polarization Measurement

The longitudinal polarization of the electron beam, expected to be about 80 %, can be measured with a Compton polarimeter similar to the ones already used at SLAC [25] and DESY [26]. The longitudinal polarization P_e of the electron beam is extracted from the asymmetry between 2 measurements of Compton scattering with parallel (+) or anti parallel (−) polarization of the electron and Laser beams. Kinematics and cross-sections of Compton scattering of 250 GeV electrons on 2.33 eV photons, corresponding to a green ($\lambda = 532\,\mathrm{nm}$) Nd:YAG laser, are shown in Figs. 2.4.16 and 2.4.17 from Ref. [27] where 1064 nm IR and 248 nm UV lasers have also been studied. As can be seen, the asymmetry is maximum when the photons are recoiling along the electron axis with the maximum energy of 225 GeV.

The time t needed to measure the electron polarization to an accuracy $\Delta P_e/P_e$ is given by

$$t = \frac{1}{\mathcal{L}\ \left(\frac{\Delta P_e}{P_e}\right)^2\ P_e^2 P_\gamma^2}\ \frac{1}{A^2}\ \frac{1}{\sigma(k'_{\gamma,\mathrm{min}})} \tag{2.4.2}$$

where $\mathcal{L}$ is the luminosity, A is the measured asymmetry and $\sigma(k'_{\gamma,\mathrm{min}})$ the total cross-section above a photon energy detection threshold $k'_{\gamma,\mathrm{min}}$. For TESLA, assuming a electron beam spot size of 20 μm, a 1 W cw laser and a 10 mrad electron-laser crossing angle, the luminosity has been estimated to be about $5 \cdot 10^{26}\,\mathrm{cm}^{-2}\mathrm{s}^{-1}$. For a completely polarized laser $P_\gamma = 1$, the time needed for a 1 % accurate polarization measurement is then of the order of 15 min. This time could be considerably reduced by using a pulsed laser with a higher peak power synchronized with the electron bunch train. In this case, one could even pulse the laser every few bunch trains for a precise determination of the background.

The insertion of the Compton polarimeter has not been studied yet. Locating the Compton interaction point after the e^+e^- collision point would allow to measure the polarization of the electron beam with and without collisions in such a way that the depolarization due to the beam-beam forces, predicted to be negligible, could be detected. Locating it in front of the separator would allow to analyze the recoiling electron momentum in the separator deflecting field, as is done at SLAC [25], rather than the very high energy photon scattered in the forward direction. Locating the polarimeter downstream the extraction line would require a precise knowledge of the spin transport optics as well as that of the electron beam transverse polarization to reconstruct the longitudinal polarization at the IP.

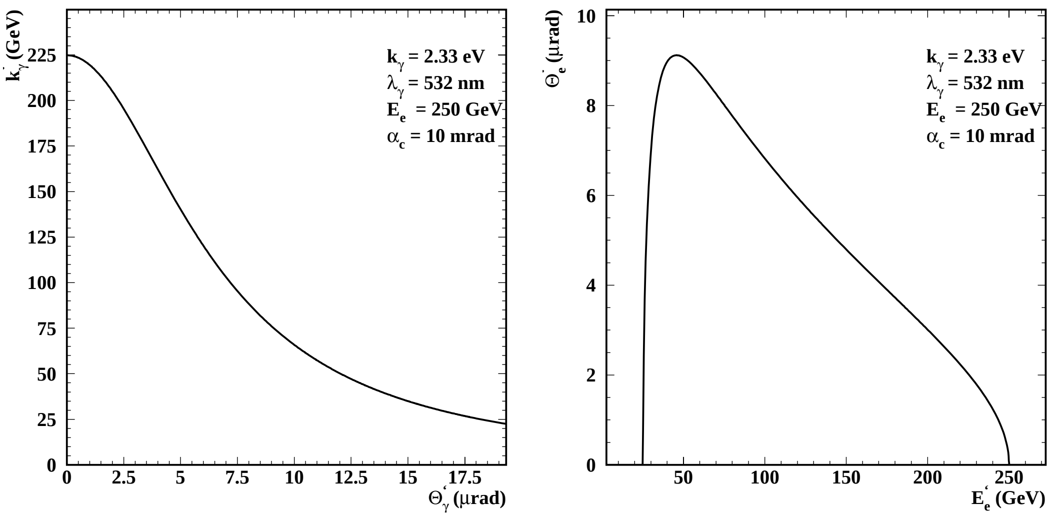

Figure 2.4.16: *Kinematic of the Compton scattering. Scattered γ energy k'_γ as a function of scattered γ angle θ_γ (left). Scattered* e$^-$ *energy E'_e as a function of scattered* e$^-$ *angle θ_e (right).*

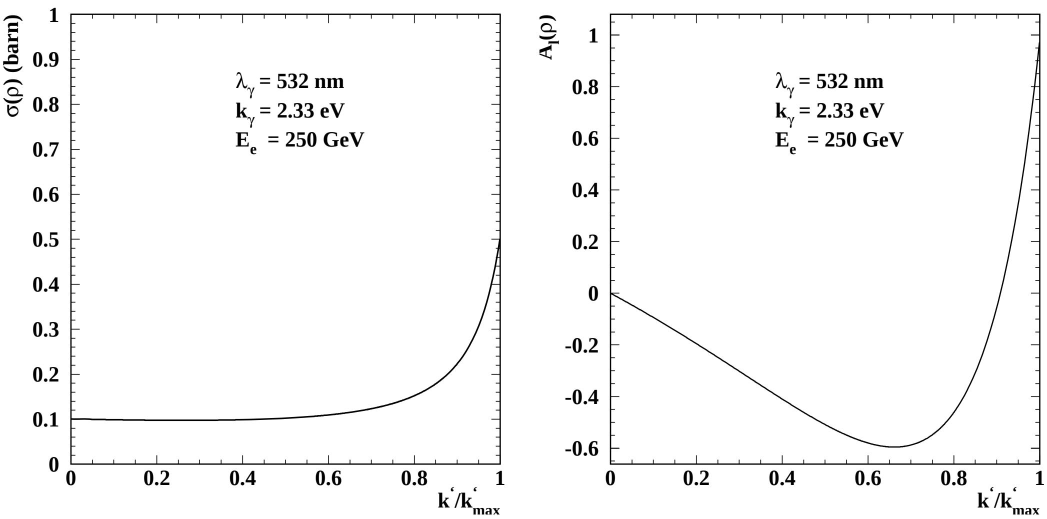

Figure 2.4.17: *Compton unpolarized differential cross section and longitudinal asymmetry as a function of the scattered photon energy k'_γ.*

2.4.6.4 Beam Size Measurement

The beam sizes to be measured at the interaction point (IP) are extremely small: less than 20 nm vertical and less than 1 μm horizontal. The precision should be better than 10 %. Beam sizes as small as 70 nm have already been measured at the Final Focus Test Beam (FFTB) at SLAC [28] with a Shintake-Monitor [29]. At SLD, a laser wire is used to measure beam sizes down to 1 μm [30]. It is planned to use both techniques at the IP: the Shintake-Monitor for the vertical beam size and the laser wire for the horizontal beam size.

Shintake-Monitor The Shintake-Monitor uses the two arms of a split laser beam to generate an interference pattern at the location of the electron beam. The spacing between the fringes is a few times larger than the beam size to be measured. The electron beam is swept over the pattern using a steering magnet. The rate of Compton scattered photons N_γ is measured as a function of the beam displacement y. The result is a modulated signal, where the modulation depth is a direct measure of the beam size. Figure 2.4.18 shows the principle components of the system.

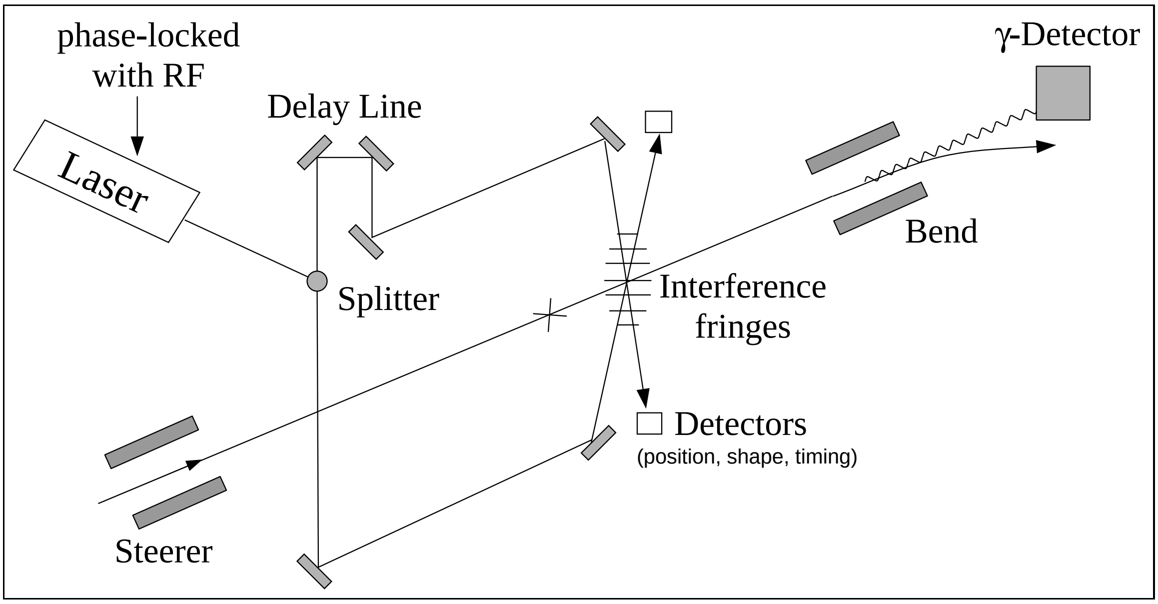

Figure 2.4.18: *Shown are the principal components of the Shintake-Monitor at the interaction point. The electron or positron beam is swept over the fringe pattern generated by the two arms of the split laser beam. The Compton scattered photons are measured as a function of the sweep.*

The advantage of this technique is the precise knowledge of the fringe pattern. The distance d between the fringes is only a function of the laser wavelength λ, if the angle θ between the laser arms is chosen to be close to 180°: $d = \lambda/(2\sin(\theta/2))$. A quite large misalignment in the angle of 1° would result in an uncertainty of the beam size of only 1 %.

The measured modulated Compton rate $N_\gamma(y)$ is fitted to a sine-function in order to determine the modulation depth $M = (N_{\max} - N_{\min})/(N_{\max} + N_{\min})$ (see Fig. 2.4.19a). The modulation depth is a function of the beam size σ [29]:

$$M(\sigma) = K|\cos\theta|\mathrm{e}^{-2(\frac{2\pi}{\lambda}\sin\frac{\theta}{2})^2\sigma^2}$$

For realistic assumptions, the correction factor K is 0.996 for TESLA and 0.994 for SBLC. It accounts for a power imbalance of the two laser beam arms of 10 % and the finite laser beam spot size in z of $w = 10\,\mu$m. The latter correction is small and depends only weakly on σ, since the laser beam waist w is small compared to the beta-function of the electron beam ($\beta_y^\star = 700\,\mu$m for TESLA and $450\,\mu$m for SBLC). In order to keep the traveling wave component small, θ should be close to 180°. For practical reasons and the necessity to monitor the outgoing laser beams, $\theta = 175°$ is chosen.

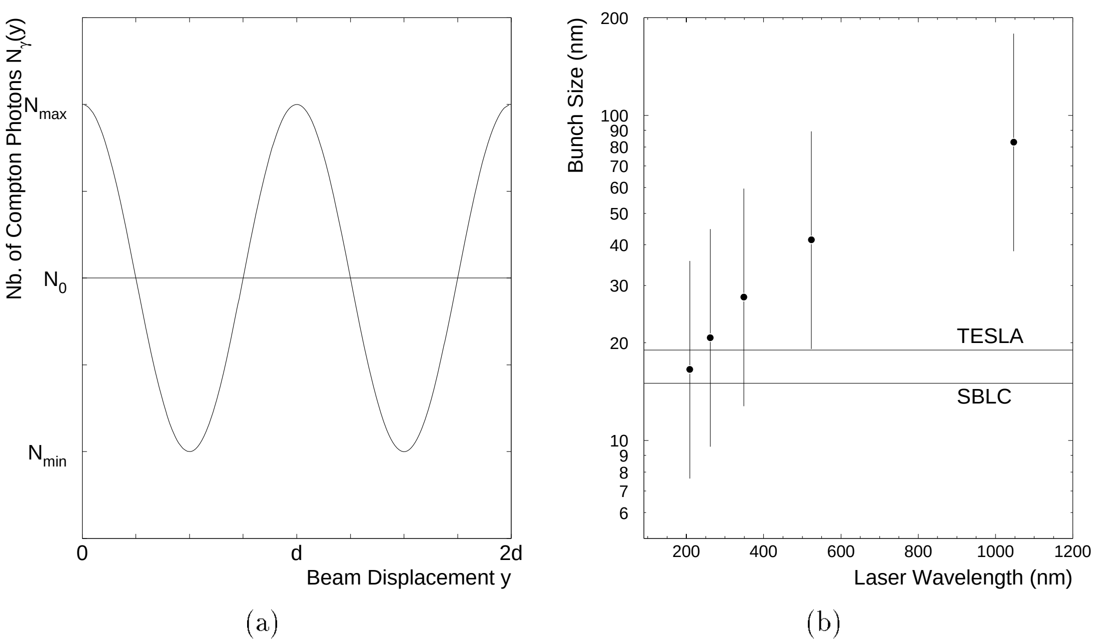

Figure 2.4.19: *(a) Modulated signal N_γ as a function of the beam displacement y; d is the fringe distance. (b) The lines indicate accessible beam size ranges for the different wavelengths of a Nd:YLF laser. The black dots are for a modulation depth M of* 0.61 *(best sensitivity), the range indicated is for M between* 0.1 *and* 0.9 *($\theta = 180°$).*

The best sensitivity for a given beam size is achieved, when the laser wavelength is chosen such, that the modulation depth M depends strongest on the beam size: $\mathrm{d}M/\mathrm{d}\sigma$ is maximal when $\lambda = 4\pi\sigma\sin(\theta/2)$. In the following, $\theta = 180°$ is assumed. The optimal wavelengths for bunch sizes of 16 and 19 nm are 201 and 239 nm resp. Common lasers for these wavelengths are Excimer lasers (ArF 193 nm, KrF 248 nm) and higher harmonics of Nd doped lasers like Nd:YLF (209 nm and 262 nm).

The expected measurement error depends mainly on the signal-to-noise ratio of the measured Compton photons. Other sources contributing to the systematic error are the position jitter and injection angle of the electron beam, and a misalignment and a non-uniformity of the laser beam. At the FFTB, these parameters have been controlled in a way that the beam size measurement error was about 7 % [28]. The electron position jitter has to be much smaller than the bunch size to be measured. It is expected that for TESLA and SBLC this is the case at least during one bunch train.

The dynamic range of the Shintake-Monitor is small: taking the measurement error of the modulation depth from the FFTB of $\mathrm{d}M = 0.02$, the relative error in the beam size is less than 10 % for a modulation depth M in the range of 0.1 and 0.9. Using e.g. a laser wavelength of 262 nm, beam sizes between 10 and 45 nm can be measured within this range. Figure 2.4.19b shows the accessible beam size ranges for some harmonics of a Nd:YLF laser. A laser based on Nd:YLF[4] would cover the beam sizes from 8 to 180 nm. Therefore, it is planned to use at least the fundamental, the second and fourth harmonic in order to be able to measure larger than nominal beam sizes as well. To extend the range to 1 μm, a CO_2 laser ($\lambda = 10\,\mu$m) may be used, or the angle θ between the laser arms may be reduced e.g. to the cone opening angle of 200 mrad.

The expected mean number of Compton scattered photons per bunch N_γ can be estimated from

$$N_\gamma = \sigma_c N_e n_{\mathrm{ph}} L$$

The Compton cross section is $\sigma_c = 1.7{\cdot}10^{-24}\,\mathrm{cm}^2$ for a beam energy of 250 GeV and a laser wavelength of 262 nm. The product of the laser photon density and the target length $n_{\mathrm{ph}}L$ can be expressed by $n_{\mathrm{ph}}L = \sqrt{\frac{2}{\pi}}\frac{P}{c^2 h}\frac{\lambda}{w}$ assuming gaussian distributions for the laser beam. P is the power of the laser, w the laser beam waist. With $\lambda = 262$ nm and $w = 10\,\mu$m we get

$$N_\gamma = 600 \cdot N_e/(10^{10}) \cdot P/(MW)$$

To achieve approximately the same photon yield per bunch as the FFTB, 0.2 MW of laser power are required. The correction due to the gaussian shape of the electron beam reduces the rate by 15 %.

For the photo injector of the Tesla Test Facility (TTF) a laser is being built [31], which fulfills most of these requirements. This laser will deliver a train of more than

[4]Lasers based on materials doped with Nd like Nd:YAG, Nd:YLF or Nd:Glass have all similar wavelengths.

800 pulses spaced by $1\,\mu$s with a repetition rate of 10 Hz. The pulse length is about 10 ps. It is straightforward to modify this laser to reflect the TESLA bunch structure. To generate the SBLC bunch structure would not impose principle problems, only the laser power per pulse must be at least doubled, since the 5^{th} harmonic is preferred for a bunch size of 16 nm. Table 2.4.2 shows the numbers of expected Compton scattered photons for a TTF type laser system.

The laser pulses are synchronized with the electron bunches, and will allow a bunch-to-bunch measurement. Within a bunch train, a full sweep over the interference pattern will be measured. The laser pulse repetition rate in the train should be half the electron bunch rate allowing the determination of the background every second bunch.

λ (nm)	P (MW)	N_γ (TESLA)	N_γ (SBLC)
1047	15	25500	7730
523.5	7.5	14450	4380
262	3	6440	1950
209	1	2200	670

Table 2.4.2: *Shown are the expected number of Compton scattered photons N_γ per bunch for a TTF-type laser system. The laser is focused to a waist of $w = 10\,\mu$m. The laser power P for the different wavelengths λ are the expected performances of the TTF laser.*

Since the laser pulses are short (in the order of 10 ps), the requirements on the timing and alignment of the laser beams are tight. The path length difference of the two arms has to be smaller than 1 mm. A remotely controlled delay line, motorized mirrors, and suitable fast detectors are required to adjust and stabilize the beams.

For stability reasons, the last optical elements, the mirror and focusing optics will be mounted onto the detector mask, which itself is a heavy rigid structure. Incorporating most of the optics into the mask reduces additional dead material inside the detector to a minimum. The laser will be housed outside the detector. The split laser beams of the different wavelengths will be transported into the detector with a mirror system [32]. The system will be installed on both sides of the detector. The mask will not extend to the interaction point. Therefore, the electron or positron beam focus has to be shifted from the IP about 800 mm up- and downstreams.

Special attention has to be taken on the laser beam intensity at the mirror surfaces: the peak intensity on the last mirror is about 100 MW/cm^2 per MW laser beam power in one arm. For several MW of laser power, the intensity comes close to damage thresholds of common dielectric mirrors, which are in the order of 1 GW/cm^2. Therefore, critical parts of the laser beam line should be evacuated to a pressure of less than 10^{-6} mbar to avoid dust particles on the mirror surfaces. Therefore, it is planned to include the last critical mirrors for the Shintake Monitor as well as for the laser wire into the vacuum of the beam pipe (see Fig. 2.4.20).

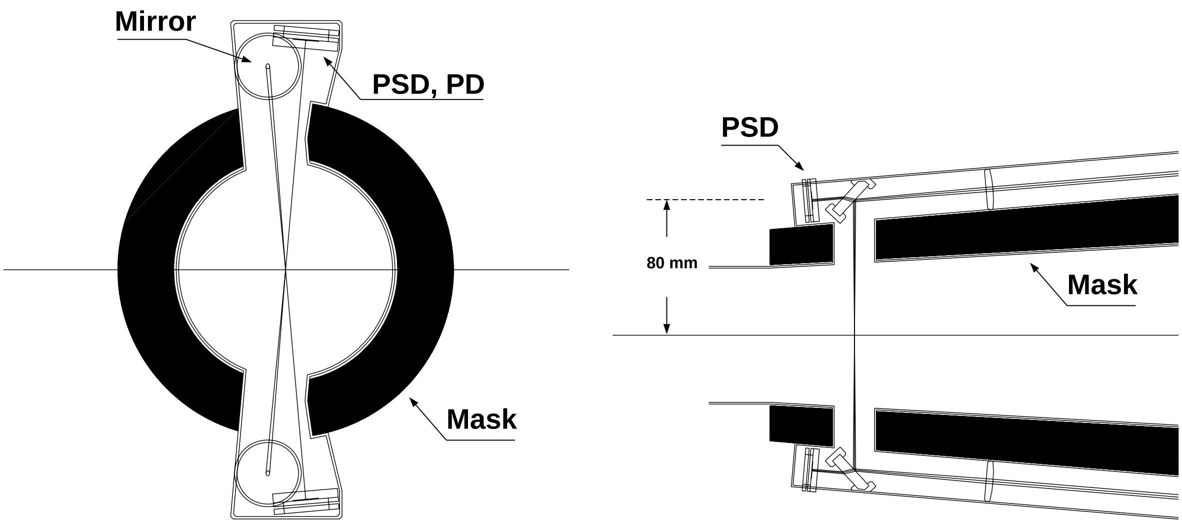

Figure 2.4.20: *Possible mechanical implementation of the optics for the Shintake Monitor. On the left, the $r\phi$-view is shown, indicating a position sensitive device (PSD) and a fast diode (PD) for timing. The z-view on the right shows how the beam is guided along the mask.*

Laser Wire The laser beam is used in a similar way as a wire in wire scanners. The beam is swept over a strongly focused laser beam. From the measured rate of Compton-scattered photon N_γ as a function of the beam displacement y, the size of the beam can be determined by unfolding the signal with the shape of the laser beam. In order to reduce potential systematic errors due to the uncertainties in the laser beam shape, the laser spot should be smaller than the beam size. Assuming a perfect gaussian transverse laser beam (TEM_{00}-mode), the waist $w = 2\sigma_r$ at the focal spot is given by $w = \lambda/\pi\theta$, where θ is the far field divergence angle of the laser beam with a wavelength λ. To estimate the achievable spot size, the geometrical constraints at the IP have to be considered. The last optical elements for the laser wire will be mounted onto the detector mask at a distance of about 1 m from the IP. At this location, the last focusing mirror will be at a distance from the electron beam line of about $l = 100\,\text{mm}$. Allowing a laser spot diameter at the last mirror of $D = 30\,\text{mm}$, the smallest achievable waist would be $w = \frac{\lambda}{\pi}/\arctan(\frac{D}{2l}) \approx 2\lambda$. Choosing the 4^{th} harmonic of a Nd:YLF laser (262 nm), a spot size down to 560 nm could be realized for perfect conditions.

This is smaller than the TESLA horizontal beam size of 845 nm, but still larger than the SBLC beam size of 335 nm. Either the smallest transmittable wavelength through air has to be chosen (ArF-Excimer with 193 nm) or the Shintake-technique may be used. However, for $\theta = 180°$, the optimal wavelength would be 4210 nm, where no common laser source exists. But reducing the angle between the two laser beams to $\theta = 29°$, a standard Nd-doped laser material could be used.

The number of scattered Compton photons N_γ can be estimated assuming gaussian shapes for the electron bunch as well as for the laser bunch: for a laser wavelength of 262 nm and a laser spot size of $w = 600$ nm one gets for TESLA, if both beams are centered,

$$N_\gamma = 3000 \cdot N_e/(10^{10}) \cdot P/(MW)$$

which is sufficient for a reasonable measurement.

Compton-Detector For the Shintake-Monitor and the laser wire the detector for the Compton scattered photons will be far behind the bend of the beam delivery system at a distance of about 100 m from the IP (see Fig. 2.4.1). Most of the scattered photons will have 70 to 90 % of the beam energy. Their angle with respect to the beam axis is proportional to $1/\gamma$ and in the order of 10 μrad. This is small enough to pass through the beam pipe and the collimators.

2.4.7 Luminosity expectation for a calibration run on the Z^0-pole

The aspects of running the TESLA collider on the Z^0-pole, corresponding to a center of mass energy of 91.2 GeV well below the design energy, have not been studied in any detail. The following considerations are therefore preliminary.

The main uncertainty in the luminosity of a dedicated run on the Z^0-pole comes from the positron intensity. The present design of the positron source relies on using the high energy electron beam, captured after the collision, as the primary beam for intense production of photons in a long wiggler. The photons are then converted into positrons on a target. This concept requires a primary beam energy above 150 GeV to produce the desired positron intensity. Below this energy, an auxiliary classical positron source is needed whose performance has not been fully analyzed yet.

However the luminosity obtainable in the Beam Delivery System (BDS) at 91.2 GeV as compared to 500 GeV c.m. energy can be analyzed, if one assumes 1) that the beam normalized transverse emittances are identical for both energies (this may require the use of bypass beam lines to extract both beams at 45.6 GeV from the linacs), 2) that the BDS magnet strengths can be powered down linearly with the energy in such a way that the Twiss parameters are essentially identical along the BDS, keeping the freedom to re-match the beta-functions at the IP with the quadrupoles of the beta matching section, 3) that the electron bunch train matches the positron one both in time structure and in beam size.

Then, the luminosity scales according to the following expression

$$\mathcal{L} \propto \frac{I^+ N^-}{\sigma_x^* \sigma_y^*} \times H_D$$

where I^+ is the positron current, N^- the electron bunch charge, σ_x^* and σ_y^* are the transverse beam sizes and H_D is the pinch enhancement factor.

The electron bunch charge N^-, which is $3.6{\cdot}10^{10}$ for the 500 GeV design, can probably be raised up to $5{\cdot}10^{10}$, as in a previous parameter list.

In view of the uncertainty in the positron bunch population, the pinch factor, which is equal to 1.65 in the 500 GeV design, must be assumed equal to unity.

The vertical beam size σ_y^* is fixed by the hour-glass condition $\beta_y^* = \sigma_z$, where σ_z is the bunch length. It therefore scales like the square-root of the energy up to $\sigma_y^* = 44.5\,\mathrm{nm}$. This implies that the beam divergence Θ_y^* at the IP, and hence the 1-sigma beam size in the last doublet, is also increased by the same factor. However, this has a detrimental impact neither on the Oide effect which scales like $(\Theta_y^* \cdot \gamma)^5$ and therefore gets weaker, nor on the synchrotron radiation background which is governed by the product $(N_y^{\mathrm{coll}} \cdot \Theta_y^*)$ where N_y^{coll} is the collimation condition in units of σ_y. Assuming that the vertical collimator gaps are identical for both energies, N_y^{coll} scales inversely with the square-root of the energy, and therefore the synchrotron radiation stay-clear is identical (with a reduction in the photon numbers and photon energies, strongly dependent on the beam energy).

The horizontal beam size is the only parameter which can be used to sizeably increase the luminosity on the Z^0-pole. The above discussion for the vertical beam size shows that it is safe to scale σ_x^* with the square-root of the energy up to $\sigma_x^* = 2\,\mu\mathrm{m}$. The constraint on the large aspect ratio from the beamstrahlung is of course relaxed at the low energy: even at the nominal bunch population of $3.6{\cdot}10^{10}$ for both beams, the beamstrahlung energy loss is of the order of 1 % for $\sigma_x^* = 1\,\mu\mathrm{m}$. Therefore, σ_x^* can be decreased as long as a higher level of synchrotron radiation background, or alternatively a higher level of muon background by tightening the horizontal collimators, can be accepted for the Z^0-pole running experiment.

The above discussion shows that the luminosity would simply scale linearly with the energy if the positron intensity $I^+(46.5\,\mathrm{GeV})$ at the Z-pole could be maintained at the same level as $I^+(250\,\mathrm{GeV})$ at 500 GeV c.m. energy. It would also benefit from a larger pinch enhancement factor due to the stronger pinch effect at low energy. For a reduced positron intensity, the above arguments suggest that the luminosity is given by

$$\mathcal{L} \simeq 9.1 \cdot 10^{32}\,\mathrm{cm}^{-2}\mathrm{s}^{-1} \cdot \frac{I^+(46.5\,\mathrm{GeV})}{I^+(250\,\mathrm{GeV})} \cdot \frac{2\,\mu\mathrm{m}}{\sigma_x^*}$$

The target value of $10^{32}\,\mathrm{cm}^{-2}\mathrm{s}^{-1}$ luminosity, which corresponds to about 11,000 Z^0 per hour, could therefore be achieved with a factor 10 (for $\sigma_x^* = 2\,\mu\mathrm{m}$) or 20 (for $\sigma_x^* = 1\,\mu\mathrm{m}$) reduction in the positron intensity. Intensity reduction factors of the order of 100 would lead to luminosities in the range of $10^{31}\,\mathrm{cm}^{-2}\mathrm{s}^{-1}$.

Bibliography

[1] O. Napoly, E. Klein and J.M. Rifflet, "TESLA Final Focus System with Superconducting Magnets in the Interaction Region", Saclay Preprint, DAPNIA/94-10 (1986).

[2] R. Jacobsen et al., "Detector background conditions at linear colliders", SLAC-PUB-5205 (April 1990).

[3] L.P. Keller, SLAC-PUB-5522 (April 1991);
L.P. Keller, SLAC-PUB-6385 (October 1993).

[4] CERN Program Library, GEANT 3.15, W5013.

[5] M. Sachwitz, H.J. Schreiber, "Muon Background in a 500 GeV TESLA Linear Collider", DESY Print, November 1994, TESLA 94-27.

[6] Yung-Su Tsai, Rev. Mod. Phys. 46 (1974) 815.

[7] E. Kushnirenko, in Proc. of the International Workshop on Final Focus and Interaction Regions of Next Generation Linear Colliders, SLAC-405, (1992).

[8] N.V. Mokhov, "Comparison of Backgrounds in Detectors for LHC, NLC and $\mu^+\mu^-$ Colliders", Fermilab-Conf-96/062 (1996).

[9] A.I. Drozhdin, M. Huhtinen and N.V. Mokhov, "Accelerator Related Background in the CMS Detector at LHC", Fermilab-Pub-96/113 and CERN-CMS-TN/96-056 (1996); to be published in Nucl. Instrum. and Meth.

[10] N.V. Mokhov, "The MARS Code System User's Guide", Version 13(95), Fermilab-FN-628 (1995).

[11] K. Yokoya and P. Chen, "Beam-beam phenomena in linear colliders", KEK Preprint 91-2 (1991).

[12] D. Schulte, "Study of Electromagnetic and Hadronic Background in the Interaction Region of TESLA", Ph.D. thesis, University of Hamburg 1996.

[13] T. Sjoestrand, “What is a photon and how should it diffract?”, Talk given at Photon 95.

[14] M. Drees and K. Grassie, “Parametrizations of the photon structure and applications to supersymmetric particle production at Hera”, Zeitschr. f. Phys. C, 28 (1985) 451–462.

[15] M. Glück, E. Reya, and A. Vogt, “Photonic parton distributions”, Physical Review D, 46 (1992) 1973.

[16] J.M. Butterworth, “Photon Structure as seen at HERA”, DESY 95-043, March 1995.

[17] ATLAS collaboration, “Technical proposal for a general-purpose experiment at the large hadron collider at CERN”, CERN/LHCC/94-43 (1994).

[18] V. Shiltsev, B. Baklakov, P. Lebedev (Novosibirsk, IYF), C. Montag, J. Rossbach (DESY), “Measurements Of Ground Vibrations And Orbit Motion At HERA”, DESY-HERA-95-06, June 1995, 64pp.

[19] R. Brinkmann, J. Rossbach (DESY), “Observation Of Closed Orbit Drift At Hera Covering Eight Decades Of Frequency”, Nucl. Instrum. and Meth. A350 (1994) 8-12.

[20] P. Bambade, R. Erickson, “Beam-Beam Deflections as an Interaction Point Diagnostics for the SLC”, SLAC-PUB-3979, May 1986.

[21] G.A. Voss, R. Brinkmann, N. Holtkamp. “A Beam Based Interaction Region Feedback for an SBLC Linear Collider”, Linac 96, Linac Conference, Aug. 1996, CERN, Geneva, to be published.

[22] R.C. Field, private communication.

[23] E. Fernandez et al., “A very forward luminosity monitor for the ALEPH detector at LEP”, Nucl. Instrum. and Meth. A297 (1990) 153.

[24] Mark II Collaboration and the SLC Final Focus Group, SLAC-SLC-PROP-2 (1986).

[25] G. Shapiro et al., “The Compton Polarimeter at the SLC”, Proc. of the “1993 IEEE Particle Accelerator Conference”, May 17-20, 1993, Washington DC, p. 2172.

[26] D.P. Barber et al., “The HERA polarimeter and the first observation of electron spin polarization at HERA”, Nucl. Instrum. and Meth. A329 (1993) 79.

[27] G. Bardin, C. Cavata and J.P. Jorda, “Compton Polarimeter studies for TESLA”, DESY Print, TESLA 97-03.

[28] V.A. Alexandrof et al., “Results of Final Focus Test Beam”, Proc. of the “1995 IEEE Particle Accelerator Conference”, May 1–5, 1995, Dallas (Texas), p. 2742.

[29] T. Shintake, “Proposal of a nanometer beam size monitor for e^+e^- linear colliders”, Nucl. Instrum. and Meth. A311 (1992) 453.

[30] D. Arnett et al., “SLC/SLD Laserwire”, Proc. of the “6th Intern. Workshop on Linear Colliders LC95”, ed. J. Urakawa, March 27–31, 1995, Tsukuba, Japan, KEK proceedings 95-5, p. 1525.

[31] “Tesla Test Facility Linac – Design Report”, Ed.: D.A. Edwards, DESY Print, March 1995, TESLA 95-01.

[32] see e.g.: O. Biebel et al., “The Laser System for Calibration and Monitoring of the OPAL Jet Chamber”, Nucl. Instrum. and Meth. A320 (1992) 183.

2.5 Conclusion on Particle Physics and Experiments

The search for the fundamental constituents of matter and their interactions has led to a coherent picture of the structure of matter. This picture is known as the Standard Model. It encompasses the matter particles, leptons and quarks, classified in three families with identical symmetries. Their electroweak and strong interactions are successfully described by gauge theories in which the forces are carried by so called gauge bosons. These features are well established experimentally. A third component of the Standard Model is the still hypothetical Higgs mechanism through which the masses of the particles of the Standard Model may be generated.

This Standard Model has been tremendously successful in predicting the properties of new particles and the structure of their interactions. In many of its facets it has been tested to better than 1 %. However, no direct evidence for the Higgs mechanism has yet been seen.

Despite these important successes the Standard Model cannot be considered to be the ultimate theory of matter but rather as an empirical description of a part of physical reality which is itself part of a larger picture yet to be discovered. In the Standard Model none of the fundamental parameters, the masses and couplings or the symmetry patterns are derived from elementary principles but must be put in from observation. Furthermore, gravity, the interaction responsible for the large scale structures in the universe, is not included in the Standard Model. An ultimate theory should be able to predict the masses and couplings of all particles from one or a very few basic principles and it should include gravity in such a way that the evolution of the world from the time of the "big bang" to the present can be understood in detail.

Two strategies can be followed to gain insight into the physics beyond the Standard Model. First, the particles and forces of the Standard Model must be affected by the interactions at higher energies. Precision measurements can thus provide clues to this physics. Second, if the energies available in the laboratory are high enough to cross the thresholds, the new phenomena may be seen directly and thoroughly studied. These are the primary reasons for any new accelerator for particle physics research.

For several years the physics potential of a future Linear Collider has been studied in considerable detail. This work has been summarized in Chapter 1. Key elements of the research are the detailed study of the top quark, the understanding of the dynamics of the electroweak gauge bosons, the search for Higgs particles, and the search for signals of a more comprehensive and fundamental theory. Here, the next generation of colliders is certain to uncover striking new phenomena of fundamental interest. In comparing the physics programme of the LHC proton-proton collider and the e^+e^- collider, it became clear that their roles are complementary and both will be needed for a robust description of Nature that can extend far beyond the Standard Model of today. There exists a significant overlap in their capabilities but neither can gather the complete picture alone.

In Chapter 2 a high performance detector is presented which is needed to realize the full particle physics potential of the linear collider. Detailed studies have shown that a large, general purpose detector, incorporating the basic design features of typical e^+e^- collider detectors would provide the necessary performance and be able to deal with event and background rates associated with the projected luminosity.

The most essential components of such a detector are a very high resolution tracking detector close to the interaction point to measure the decays of short lived particles, a high resolution, large solid angle tracking detector to measure the topology and momenta of all charged particles, a high-field solenoid to provide the necessary magnetic field volume and bending power, a calorimeter to measure the energy and direction of neutral particles and to detect possible missing energy, and a segmented iron return yoke with embedded tracking detectors. While most of these features exist in current e^+e^- collider detectors, the challenge is to make them work at much higher energies and in the background environment characteristic of a linear collider. To meet this challenge intense R&D work is needed in a number of areas, such as high resolution solid state pixel detectors. Extensive work has gone into the study of all possible sources of background and methods to protect the experiment from it. In order to assess the physics capabilities of the detector, a few reference reactions have been analyzed in detail. It was found that the performance is fully adequate for the processes which were studied so far.

In conclusion, it should be emphasized that already today an experiment can be designed which would allow the full exploitation of the rich physics potential of a linear collider. Nevertheless, further research and development is needed to arrive at an optimized, robust technical design and an even better understanding of the physics reach.

LC DETECTOR GROUP: ADDRESSES

S. Aïd [15], A. Andreazza [22], P. Bambade [24], G. Bardin [14], T. Barklow [29], W. Bartel [15], M. Battaglia [16], R. Bellanzzini [12], S. Bertolucci [11], G. Blair [30], R. Brinkmann [15], I. Brock [7], R. Brown [10], J. Bürger [15], P.J. Bussey [13], M. Caccia [21], C. Cavata [14], P. Checchia [25], G. Coignet [2], P. Colas [14], P. Clarke [19], C. Damerell [10], G. Daskalakis [3], M. David [14], A. De Roeck [15], S. Drozhdin [9], E. Elsen [15], E. Fernandez [4], Y. Giomataris [14], T. Greenshaw [18], R. Heuer [12], C. Heusch [28], N. Holtkamp [15], P. Hüntemeyer [15], D. Jackson [29], P. Janot [24], L. Jönsson [20], J.-P. Jorda [14], A. Juste [14], F.P. Juster [4], B.J. King [31,15], F. Kircher [14], U. Kötz [15], V. Korbel [15], Y. Kurihara [17], A. Kyriakis [3], P. Le Du [14], M. Leenen [15], W. Lohmann [32], C. Luci [27], L. Mandelli [21], C. Markou [3], M. Martinez [4], H.U. Martyn [1], M. Mazzucato [25], C. Meroni [21], J. Meyer [15], D.J. Miller [19], N. Mokhov [9], R. Nahnhauer [32], R. Nania [6], O. Napoly [14], H. Nowak [32], R. Orava [16], M. Piccolo [11], M. Pohl [33], D. Reed [12], F. Richard [24], I. Riu [4], A. Rousarie [14], M. Sachwitz [32], H.-G. Sander [21], D. Saxon [13], U. Schneekloth [15], H.J. Schreiber [32], S. Schreiber [15], D. Schulte [15,a], R. Settles [23], R. Shanidze [32], C. Shepherd-Themistocleous [15,a], S. Shichanin [32], F. Simonetto [25], E. Simopoulou [3], K. Sinram [15], A. Skillman [19], A. Sopczak [32], P. Steffen [12,15], H. Steiner [5], J. Steuerer [15], G. Tonelli [26], M. Tonutti [1b], C. Troncon [22], C. VanderVelde [8], G. Vegni [22], R. Vuopionperä [16], A. Wagner [15], N. Walker [15], M. Weber [1b], W. Wiedenmann [23], G.W. Wilson [15], K. Zapfe-Düren [15].

———————————

[1]I. Physikalisches Institut, RWTH Aachen, Physikzentrum, D–52056 Aachen; [1b]III. Physikalisches Institut, RWTH Aachen, Physikzentrum, D–52056 Aachen; [2]Laboratoire d'Annecy le Vieux de Physique des Particules, LAPP, IN2P3-CNRS, BP-110, F–74941 Annecy-Le-Vieux CEDEX; [3]Institute of Nuclear Physics, NRCPS "Demokritos", GR–15310 Attiki; [4]I.F.A.E., Universidad Autónoma de Barcelona, E–08193 Bellaterra; [5]Lawerence Berkeley National Laboratory, USA–Berkeley, CA 94720; [6]Dipartimento di Fisica, Università degli Studi di Bologna, I–40126 Bologna; [7]Rheinische Friedrich-Wilhelms-Universität Bonn, Physik Inst., D–53115 Bonn; [8]Service de Physique des Particules Elémentaires, Univ. Libre de Bruxelles, B–1050 Bruxelles; [9]FNAL, Fermilab, P.O. Box 500, Batavia IL 60510; [10]Particle Physics, Rutherford Appleton Laboratory, Chilton, GB–Didcot OX11 0QX; [11]LNF, Istituto Nazionale di Fisica Nucleare (INFN), I–00044 Frascati; [12]CERN, CH–1211 Genève 23; [13]Department of Physics, University of Glasgow, GB–Glasgow G12 8QQ; [14]CE Saclay, F–91191 Gif/Yvette CEDEX; [15]DESY, Deutsches Elektronen-Synchrotron, D–22603 Hamburg; [16]Helsinki Institut of Physics, FIN–00114 University of Helsinki; [17]KEK, National Lab. for High Energy Physics, 1–1 Oho, Tsukuba-shi, Ibaraki-ken 305; [18]Department of Physics, University of Liverpool, GB–Liverpool L69 3BX; [19]Department of Physics and Astronomy, University College London, GB–London WC1E 6BT; [20]Physics Department, University of Lund, S–22362 Lund; [21]Institut für Physik, Johannes-Gutenberg-Universität, D–55099 Mainz; [22]Dipartimento di Fisica, Università degli Studi di Milano and INFN, I–20133 Milano; [23]Werner-Heisenberg-Institut, Max-Planck-Institut für Physik, D–80805 München; [24]LAL, Université de Paris–Sud, F–91405 Orsay Cedex; [25]Dipartimento di Fisica, Università di Padova, I–35131 Padova; [26]INFN, Sezione di Pisa, San Piero a Grado, I–56010 Pisa; [27]INFN, Sezione di Roma I and Dipartimento di Fisica, Università di Roma I "La Sapienza", I–00185 Roma; [28]Institute for Particle Physics, UC Santa Cruz, USA–Santa Cruz, CA 95064; [29]SLAC, Stanford University, USA–Stanford CA 94309; [30]Department of Physics, Royal Holloway and Bedford New College, University of London, GB–Surrey TW20 OEX; [31]Brookhaven National Laboratory, USA–Upton, NY 11973–5000; [32]Institut für Hochenergiephysik, DESY, D–15738 Zeuthen; [33]Labor für Hochenergiephysik, ETH, CH–8093 Zürich; [a]now at CERN.